

POLITECNICO DI TORINO

**Department of Mechanical, Aerospace
and Automotive Engineering**

Master's Degree in Automotive Engineering



Master's Degree Thesis

**Development of Control Logic for
Common Pressure Rail Architecture in
Hybrid Excavators**

Supervisors

Prof. Daniela MISUL

Prof. Massimo RUNDO

PhD. Federico MIRETTI

Candidate

Gabriele MOFFA

ACADEMIC YEAR 2023/24

Acknowledgements

I would like to express my deepest gratitude to my supervisors, Professors Massimo Rundo and Daniela Misul, whose expertise, understanding, and patience, added considerably to my graduate experience.

I would also like to thank PhD. Federico Miretti for his support and encouragement, whose deep insight into the subject matter was instrumental in this thesis.

Abstract

The use of mobile machinery is widespread across all industrial sectors; however, their low energy efficiency, primarily due to hydraulic architecture, presents a significant problem. The hydraulic excavators available on the market predominantly adopt the Load Sensing architecture, which offers good operational capabilities but exhibits very low energy efficiency, with the net work of the actuators amounting to only 4% of the chemical energy of the fuel. The causes of these energy losses lie in various components of the circuit, such as the internal combustion engine, the hydraulic pump, and the actuators, but the main contribution is attributable to the hydraulic distributor.

The objective of this thesis was the creation of a model of a hydraulic excavator based on the Common Pressure Rail architecture, an architecture studied over the past decades that has proven to be highly advantageous in terms of fuel consumption. Specifically, the focus of the thesis was the development of the control system for the Common Pressure Rail architecture, capable of managing the access of the actuator chambers to the different pressure lines and determining the modulation of the proportional valve located upstream of each actuator based on external system conditions. This ensures the execution of the digging cycle and the generation of movement of the linear actuators and the hydraulic motor based on the inputs provided by the operator via joystick.

The optimization of this controller and the proper design of the hydraulic components for a 9-ton excavator resulted in a 50% reduction in fuel consumption compared to the Load Sensing architecture. Furthermore, the performance of the controller achieved a maximum error of 5% in the displacements of the actuators relative to the joystick inputs.

In conclusion, the Common Pressure Rail architecture has proven to be valid and effective, offering lower energy consumption and reduced economic costs compared to other solutions. With some architectural modifications, it can achieve performances similar to the traditional counterpart, offering a significant advantage and proving to be competitive.

Sommario

L'utilizzo di macchinari mobili è ampiamente diffuso in tutti i settori industriali, tuttavia, la loro bassa efficienza energetica, principalmente dovuta all'architettura idraulica, costituisce un problema rilevante. Gli escavatori idraulici presenti sul mercato adottano prevalentemente l'architettura Load Sensing, la quale offre buone capacità operative, ma presenta un'efficienza energetica molto bassa, con il lavoro netto degli attuatori pari solamente al 4% dell'energia chimica del combustibile. Le cause di queste perdite energetiche risiedono nei diversi componenti del circuito, quali il motore termico, la pompa idraulica e gli attuatori, ma il contributo principale è attribuibile al distributore idraulico.

L'obiettivo della tesi è stato la creazione di un modello di escavatore idraulico basato sull'architettura Common Pressure Rail, un'architettura studiata negli ultimi decenni che ha dimostrato essere molto vantaggiosa in termini di consumo di carburante. In particolare, il focus della tesi è stato lo sviluppo del sistema di controllo dell'architettura Common Pressure Rail, in grado di gestire l'accesso delle camere degli attuatori alle diverse linee di pressione e determinare la modulazione della valvola proporzionale situata a monte di ogni attuatore in funzione delle condizioni esterne al sistema. Questo garantisce l'esecuzione del ciclo di scavo e la generazione del movimento degli attuatori lineari e del motore idraulico in funzione degli input forniti dall'operatore tramite joystick.

L'ottimizzazione di questo controller e il corretto design delle componenti idrauliche per un escavatore da 9 tonnellate hanno permesso di ridurre il consumo di carburante del 50% rispetto all'architettura Load Sensing. Inoltre le prestazioni del controller hanno permesso di raggiungere un errore massimo del 5% negli spostamenti degli attuatori rispetto agli input dei joystick.

In conclusione, l'architettura Common Pressure Rail si è dimostrata valida ed efficace, offrendo un consumo energetico inferiore e costi di implementazione ridotti rispetto ad altre soluzioni. Con alcune modifiche architetturali, essa può raggiungere prestazioni simili alla controparte tradizionale, offrendo un notevole vantaggio e mostrandosi competitiva.

Contents

Abstract	IV
Sommario	VI
List of Tables	XI
List of Figures	XIII
Introduction	1
1 Hydraulic Excavator	3
1.1 Excavator Types, Sizes, and Purposes	3
1.1.1 Types of Excavators	4
1.1.2 Excavator Size and Purpose Classification	4
1.2 Subsystems and Equipment Configuration	6
1.2.1 Hydraulic System	6
2 Principles, Classification, and Review of Valve-Controlled and Valve-Less Hydraulic Circuits	10
2.1 Valve-Controlled Hydraulic Systems	11
2.1.1 Non-hybrid - Load Sensing Hydraulic System	13
2.1.2 Non-hybrid - Electronic Flow Matching System	17
2.2 Valve-Less Hydraulic Systems	18
2.2.1 Steam - the Concept	19
3 Development of Simulation Models for Load Sensing and Common Pressure Rail Architectures	22
3.1 Load Sensing-Based Excavator Model Layout	22
3.1.1 Hydraulic Subsystems - Flow Generation Unit	24
3.1.2 Hydraulic Subsystems - Actuators and Turret Motor	27
3.2 Common Pressure Rail-Based Excavator Model Layout	32
3.2.1 Engine Subsystem	32

3.2.2	Hydraulic Subsystems - Flow Generation Unit	34
3.2.3	Hydraulic Subsystems - Energy Storage Units and Pressure Levels	37
3.3	Duty Cycles	42
3.3.1	Dig and Dump	43
3.3.2	Air Grading	47
4	Development of Control Logic for Common Pressure Rail Archi- tecture	54
4.1	Actuator Force Signals - PSD, FSA and Low-Pass Filter Design . .	55
4.1.1	Characteristics of Actuator Forces in the Load Sensing Model	55
4.1.2	Design of Low-Pass Filters	56
4.2	Insights into Control of Linear Actuators	66
4.2.1	Linear Actuator Operating Modes	69
4.2.2	Controller Details	72
4.2.3	Implementation and Analysis of Chokes Integration in the Simulink Model	85
4.2.4	Implementation of Low-Pass Filter for Actuator Control . .	88
4.3	Insights into Control of the Hydraulic Motor	104
4.3.1	Hydraulic Motor Operating Modes	104
4.3.2	Controller Details	107
4.4	Closed-Loop Control	119
4.4.1	Types of Closed-Loop Control Systems	120
4.4.2	Proportional Closed-Loop Control Implementation	122
4.4.3	Proportional Gain Selection via Design of Experiments . . .	124
4.5	Hydraulic Accumulators Recharging Strategy	128
5	Performance Evaluation of CPR Architecture	133
5.1	Comparative Analysis of Fuel Economy - CPR vs LS	133
5.1.1	Dig and Dump Cycle Results	134
5.1.2	Air Grading Cycle Results	138
5.2	Analysis on Precision and Responsiveness of the CPR System . . .	140
5.2.1	Dig and Dump Cycle Results	140
5.2.2	Air Grading Cycle Results	144
6	Development of System Architecture and Control Logic for Com- mon Pressure Rail plus Electronic Flow Matching	148
6.1	Performance Analysis in Heavy-Duty Excavation Cycles	149
6.1.1	Heavy Duty Reference Work Cycle	150
6.1.2	Heavy Duty Work Cycle Results	153
6.2	Introduction to CPR plus EFM	161

6.2.1	Common Pressure Rail plus Electronic Flow Matching - Hydraulic Architecture	162
6.2.2	Common Pressure Rail plus Electronic Flow Matching - Fuel Consumption Results	163
6.3	Insights into Control of CPR+EFM	165
6.3.1	Control System Architecture	166
	Conclusions	169
7	Appendix A	171
8	Appendix B	174
	Bibliography	184

List of Tables

3.1	Index of pressure combination	39
3.2	Parameters for medium and high pressure accumulator settings . . .	42
4.1	Parameters used for each low-pass filter setting dedicated to force sensor signals	61
4.2	Window values of variation and discretization step of cutoff frequencies for low-pass filters	101
4.3	Optimal configurations of cutoff frequencies for low-pass filters for actuators	102
4.4	Hydrostatic machine operational modes based on pressure differential and rotational speed	107
4.5	Ranges and discretization steps $K_{p,i}$ for coarse DOE runs	125
4.6	Ranges and discretization steps $K_{p,i}$ for fine DOE runs	128
4.7	Optimal configurations of proportional gains for the closed-loop control for each utility	130
5.1	Load Sensing hydraulic system energy transfer and utilization - Dig and dump cycle	135
5.2	Common Pressure Rail hydraulic system energy transfer and utilization - Dig and dump cycle	136
5.3	Fuel consumption for different architectures - Dig and dump cycle .	137
5.4	Load Sensing hydraulic system energy transfer and utilization - Air grading	138
5.5	Common Pressure Rail hydraulic system energy transfer and utilization - Air grading	139
5.6	Fuel consumption for different architectures - Air grading cycle . . .	140
5.7	Actuators displacements maximum errors - Dig and dump cycle . .	145
5.8	Actuators displacements maximum errors - Air grading cycle	147
6.1	Settings of accumulators for the heavy-duty work cycle	156

6.2	Comparison of fuel consumption for heavy-duty work cycle - LS vs CPR_HP	156
6.3	Comparison of fuel consumption for dig and dump and air grading work cycle - LS vs CPR_HP	157
6.4	Actuators displacements maximum errors - Heavy duty cycle	161
6.5	Comparison of fuel consumption for dig and dump, air grading, and heavy duty work cycles - LS vs CPR+EFM	164

List of Figures

1.1	Hydraulic excavator constitution [4]	3
1.2	Crawler excavator [5]	4
1.3	Wheeled excavator [5]	4
1.4	Compact excavator [5]	5
1.5	General-purpose excavators - medium [5]	5
1.6	General-purpose excavators - large [5]	5
1.7	Layout of a typical hydraulic excavator [6]	6
1.8	Example of excavator cabs [7]	7
1.9	Hydraulic excavator lever control pattern [4]	7
1.10	Main Control Valve block [8]	7
1.11	Load quadrants experienced by a linear hydraulic actuator	8
1.12	Load quadrants experienced by a hydrostatic machine	8
2.1	Proposed classification of the working hydraulics for non-hybrid, valve-controlled mobile machines [9]	12
2.2	ISO scheme of a load-sensing circuit with precompensators for controlling two linear actuators [11].	14
2.3	ISO schematic of the load-sensing circuit with post-compensators for controlling two linear actuators [11].	15
2.4	Schematic representation of a hydraulic circuit implementing the Electronic Flow Matching strategy	17
2.5	Basic idea of Common-Pressure System [3].	20
2.6	A possible implementation of STEAM [3].	20
3.1	3D model of the Komatsu PC75R [12]	23
3.2	Traditional hydraulic excavator simplified AMESim model	24
3.3	Traditional hydraulic excavator simplified AMESim model without travelling motors	25
3.4	Volumetric efficiency of the fixed displacement pump	26
3.5	Mechanical efficiency of the fixed displacement pump	26
3.6	Volumetric efficiency of the variable displacement pump	26

3.7	Mechanical efficiency of the variable displacement pump	26
3.8	Representation of the excavator arm's geometry [11]	28
3.9	Excavator arm AMESim model	29
3.10	Soil submodel [15]	29
3.11	Turret AMESim submodel	30
3.12	Inertia submodel for equivalent inertia computation	31
3.13	Common Pressure Rail AMESim model	33
3.14	55 kW, 2.9 L 6-cylinder diesel ICE Map	34
3.15	Implementation of ICE using look-up table	35
3.16	Implementation of ICE using AMESim submodel	35
3.17	2D Fuel Consumption Map	35
3.18	3D Fuel Consumption Map	35
3.19	Flow generation unit AMESim model implementation	36
3.20	Volumetric efficiency of the 75 cc/rev variable displacement pump .	37
3.21	Hydraulic - mechanical efficiency of the 75 cc/rev variable displacement pump	37
3.22	Pressure levels of actuators in the Load Sensing system during the Dig and Dump cycle	38
3.23	Ideal distribution of forces generated by actuators function of the pressure combination	38
3.24	Forces generated by the actuator as a function of the chamber pressure combinations - Boom	39
3.25	Forces generated by the actuator as a function of the chamber pressure combinations - Arm	40
3.26	Forces generated by the actuator as a function of the chamber pressure combinations - Bucket	40
3.27	Medium and high pressure accumulators AMESim model implementation	41
3.28	High pressure accumulator parameter setting screen in AMESim . .	42
3.29	Migh pressure accumulator parameter setting screen in AMESim . .	42
3.30	Commencing the first phase of dig and dump: approaching the site for excavation and dumping	44
3.31	Executing the second phase of the dig and dump process: penetrating and lifting	44
3.32	Transitioning into the third phase of the dig and dump cycle: rotation and dumping	45
3.33	Concluding the dig and dump process: returning to the starting point	45
3.34	Boom actuator velocity profile during dig and dump cycle	46
3.35	Boom actuator displacement profile during dig and dump cycle . . .	46
3.36	Arm actuator velocity profile during dig and dump cycle	47
3.37	Arm actuator displacement profile during dig and dump cycle . . .	47

3.38	Bucket actuator velocity profile during dig and dump cycle	48
3.39	Bucket actuator displacement profile during dig and dump cycle	48
3.40	Turret motor velocity profile during dig and dump cycle	49
3.41	Turret motor displacement profile during dig and dump cycle	49
3.42	Commencing the first phase of air grading: approaching the site	50
3.43	Executing the second phase of the air grading process: cutting and filling	50
3.44	Concluding the air grading process: finishing pass	51
3.45	Boom actuator velocity profile during air grading cycle	51
3.46	Boom actuator displacement profile during air grading cycle	52
3.47	Arm actuator velocity profile during air grading cycle	52
3.48	Arm actuator displacement profile during air grading cycle	53
4.1	Illustration of a force sensor in the AMESim model	56
4.2	Boom digging force as measured by the Load Sensing model's force sensor	57
4.3	Arm digging force as measured by the Load Sensing model's force sensor	57
4.4	Bucket digging force as measured by the Load Sensing model's force sensor	58
4.5	Power Spectral Density (left) and Frequency Spectrum Analysis (right) of boom digging force measured by the Load Sensing model's sensor	58
4.6	Power Spectral Density (left) and Frequency Spectrum Analysis (right) of arm digging force measured by the Load Sensing model's sensor	59
4.7	Power Spectral Density (left) and Frequency Spectrum Analysis (right) of bucket digging force measured by the Load Sensing model's sensor	59
4.8	Magnitude-frequency characteristic of a low-pass filter	60
4.9	Magnitude-Normalized Frequency representation of the low-pass filter for the boom force sensor signal	62
4.10	Magnitude-Normalized Frequency representation of the low-pass filter for the arm force sensor signal	62
4.11	Magnitude-Normalized Frequency representation of the low-pass filter for the bucket force sensor signal	63
4.12	Comparison of boom force sensor signals before and after filtering	63
4.13	Comparison of arm force sensor signals before and after filtering	64
4.14	Comparison of bucket force sensor signals before and after filtering	64
4.15	Comparison of boom force sensor signals: FSA (top) and PSD (bottom) before (left) and after (right) filtering	65

4.16	Comparison of arm force sensor signals: FSA (top) and PSD (bottom) before (left) and after (right) filtering	65
4.17	Comparison of bucket force sensor signals: FSA (top) and PSD (bottom) before (left) and after (right) filtering	66
4.18	Simulink controller model for managing a single utility	67
4.19	Co-simulation: Simcenter AMESim as Master, Simulink as Slave (<i>SL2AMECosim</i>)	68
4.20	Co-simulation: Simcenter AMESim as Slave, Simulink as Master (<i>AME2SLCosim</i>)	68
4.21	Example of a Simulink model as it appears when imported into AMESim	68
4.22	System operating modes - linear actuator [3]	69
4.23	Region of operation of all nine modes - linear actuator [3]	70
4.24	System operating modes and controller setup - linear actuator . . .	71
4.25	Breaking down the Simulink controller model for the linear actuator: a detailed view of its components	72
4.26	Simulink controller model inputs - linear actuator	73
4.27	Controller's MATLAB function for outputs generation - linear actuator	74
4.28	AMESim model of a two-port two-position proportional valve . . .	80
4.29	Example of a linear actuator-proportional valve model implemented in the Common Pressure Rail architecture	82
4.30	Implementation of linear actuator and chocks submodels in AMESim	86
4.31	AMESim model of the simplified Common Pressure Rail architecture with a linear actuator, ideal pressure sources feeding the rails, and filtered force signals applied to both the actuator and as inputs to the controller.	89
4.32	Comparison between reference speed input to the controller and the actual speed generated by the actuator in the AMESim model of the simplified Common Pressure Rail architecture during a dig and dump cycle	90
4.33	Comparison between reference and the actual displacements in the AMESim model of the simplified Common Pressure Rail architecture during a dig and dump cycle	90
4.34	Near-final AMESim model of a Common Pressure Rail system with ideal pressure sources as the supply system	91
4.35	Unfiltered forces detected in the CPR AMESim model with ideal pressure sources as the supply system on the boom actuator during dig and dump cycle	92
4.36	Unfiltered forces detected in the CPR AMESim model with ideal pressure sources as the supply system on the arm actuator during dig and dump cycle	92

4.37	Unfiltered forces detected in the CPR AMESim model with ideal pressure sources as the supply system on the bucket actuator during dig and dump cycle	93
4.38	Comparison between reference and the actual velocity of the boom actuator in the CPR AMESim model with ideal pressure sources as the supply system during dig and dump cycle	93
4.39	Comparison between reference and the actual velocity of the arm actuator in the CPR AMESim model with ideal pressure sources as the supply system during dig and dump cycle	94
4.40	Comparison between reference and the actual velocity of the bucket actuator in the CPR AMESim model with ideal pressure sources as the supply system during dig and dump cycle	94
4.41	Dynamic response of an under-damped system: step input vs output	95
4.42	Evaluating forces exchanged between the boom actuator and the environment, with and without a handmade low-pass filter design, during the dig and dump cycle	96
4.43	Evaluating forces exchanged between the arm actuator and the environment, with and without a handmade low-pass filter design, during the dig and dump cycle	96
4.44	Evaluating forces exchanged between the bucket actuator and the environment, with and without a handmade low-pass filter design, during the dig and dump cycle	97
4.45	Comparison between reference and the actual velocity of the boom actuator in the CPR AMESim model during dig and dump cycle with the handmade low-pass filter design	97
4.46	Comparison between reference and the actual velocity of the arm actuator in the CPR AMESim model during dig and dump cycle with the handmade low-pass filter design	98
4.47	Comparison between reference and the actual velocity of the bucket actuator in the CPR AMESim model during dig and dump cycle with the handmade low-pass filter design	99
4.48	AMESim interface for DOE configuration	100
4.49	Sensitivity analysis of actuator velocity errors (ϵ) to filters cutoff frequencies	101
4.50	Boom actuator force signals at the input and output of new low-pass filters, with settings identified through DOE for the dig and dump excavation cycle	102
4.51	Arm actuator force signals at the input and output of new low-pass filters, with settings identified through DOE for the dig and dump excavation cycle	103

4.52	Bucket actuator force signals at the input and output of new low-pass filters, with settings identified through DOE for the dig and dump excavation cycle	103
4.53	Comparison between the reference and actual velocity of the boom actuator in the CPR AMESim model during the dig and dump cycle with DOE-optimized low-pass filter parameters	104
4.54	Comparison between the reference and actual velocity of the arm actuator in the CPR AMESim model during the dig and dump cycle with DOE-optimized low-pass filter parameters	105
4.55	Comparison between the reference and actual velocity of the bucket actuator in the CPR AMESim model during the dig and dump cycle with DOE-optimized low-pass filter parameters	106
4.56	System operating modes - swing	106
4.57	Region of operation for all nine modes - swing	107
4.58	Detailed view of the Simulink controller model components for the hydrostatic machine	108
4.59	Simulink controller model inputs - swing	109
4.60	Simulink controller model outputs - swing	110
4.61	Hydrostatic machine and 4-port 2-position proportional valve AMESim subsystem integration	116
4.62	Closed loop control system - System block diagram	120
4.63	Sensitivity analysis of boom actuator error (ϵ) to proportional gain $K_{p,boom}$, with K_p varied coarsely	126
4.64	Sensitivity analysis of arm actuator error (ϵ) to proportional gain $K_{p,arm}$, with K_p varied coarsely	126
4.65	Sensitivity analysis of bucket actuator error (ϵ) to proportional gain $K_{p,bucket}$, with K_p varied coarsely	127
4.66	Sensitivity analysis of turret motor error (ϵ) to proportional gain $K_{p,swing}$, with K_p varied coarsely	127
4.67	Sensitivity analysis of boom actuator error (ϵ) to proportional gain $K_{p,boom}$, with K_p varied finely	128
4.68	Sensitivity analysis of arm actuator error (ϵ) to proportional gain $K_{p,arm}$, with K_p varied finely	129
4.69	Sensitivity analysis of bucket actuator error (ϵ) to proportional gain $K_{p,bucket}$, with K_p varied finely	129
4.70	Finite State Machine submodel in AMESim	130
4.71	Signal on-off sent to the pump during a dig and dump cycle	131
4.72	Finite State Machine diagram for the recharging strategy of hydraulic accumulators	132

5.1	Operating points of the thermal engine during the dig and dump cycle - Common Pressure Rail architecture	137
5.2	Comparison of reference and actual velocities for boom actuator during Dig and Dump cycles	141
5.3	Comparison of reference and actual displacement for boom actuator during Dig and Dump cycles	141
5.4	Comparison of reference and actual velocities for arm actuator during Dig and Dump cycles	142
5.5	Comparison of reference and actual displacement for arm actuator during Dig and Dump cycles	142
5.6	Comparison of reference and actual velocities for bucket actuator during Dig and Dump cycles	143
5.7	Comparison of reference and actual displacement for bucket actuator during Dig and Dump cycles	143
5.8	Comparison of reference and actual velocities for turret hydrostatic machine during Dig and Dump cycles	144
5.9	Comparison of reference and actual displacement for turret hydrostatic machine during Dig and Dump cycles	144
5.10	Comparison of reference and actual Velocities for boom actuator during Air Grading cycles	145
5.11	Comparison of reference and actual displacement for boom actuator during Air Grading cycles	146
5.12	Comparison of reference and actual Velocities for arm actuator during Air Grading cycles	146
5.13	Comparison of reference and actual displacement for arm actuator during Air Grading cycles	147
6.1	Commencing the first phase of heavy duty cycle: approaching the site for excavation	150
6.2	Executing the second phase of the of heavy duty cycle: penetrating	151
6.3	Force exerted on the boom actuator during the heavy-duty work cycle	151
6.4	Force exerted on the arm actuator during the heavy-duty work cycle	152
6.5	Force exerted on the bucket actuator during the heavy-duty work cycle	152
6.6	Boom actuator velocity profile during heavy duty work cycle	153
6.7	Boom actuator displacement profile during heavy duty work cycle .	153
6.8	Arm actuator velocity profile during heavy duty work cycle	154
6.9	Arm actuator displacement profile during heavy duty work cycle . .	154
6.10	Bucket actuator velocity profile during heavy duty work cycle . . .	155
6.11	Bucket actuator displacement profile during heavy duty work cycle	155
6.12	Comparison of reference and actual velocities for boom actuator during Heavy Duty cycles - CPR in CPR_HP configuration	158

6.13	Comparison of reference and actual displacement for boom actuator during Heavy Duty cycles - CPR in CPR_HP configuration	158
6.14	Comparison of reference and actual velocities for arm actuator during Heavy Duty cycles - CPR in CPR_HP configuration	159
6.15	Comparison of reference and actual displacement for arm actuator during Heavy Duty cycles - CPR in CPR_HP configuration	159
6.16	Comparison of reference and actual velocities for bucket actuator during Heavy Duty cycles - CPR in CPR_HP configuration	160
6.17	Comparison of reference and actual displacement for bucket actuator during Heavy Duty cycles - CPR in CPR_HP configuration	160
6.18	Common Pressure Rail architecture featuring Electronic Flow Matching capability	162
6.19	Pump discharge pressure during heavy duty cycle - CPR plus EFM	165
6.20	Control signal for on-off valve at high-pressure accumulator - CPR plus EFM	165
6.21	Detailed view of the Simulink controller model for managing the CPR+EFM architecture	166
7.1	Adds-on to be installed in MATLAB	172
7.2	Simulink solver settings	172

List of Algorithms

1	On-off valves control logic algorithm - linear actuators - part 1 . . .	76
2	On-off valves control logic algorithm - linear actuators - part 2 . . .	78
3	Proportional valve control logic algorithm - linear actuators	84
4	Proportional valve control logic algorithm - linear actuators with chokes	88
5	On-off valves control logic algorithm - hydrostatic machine - part 1	113
6	On-off valves control logic algorithm - hydrostatic machine - part 2	115
7	Proportional valve control logic algorithm - hydrostatic machine . .	118

Introduction

Environmental awareness and stricter regulations are driving the demand for eco-friendly and fuel-efficient machinery, motivating researchers to develop energy-saving and efficiency-enhancing solutions. In this regard, numerous proposals have been made to improve the efficiency of fluid power systems in off-road vehicles with multiple actuators, primarily aiming to reduce throttling losses. These losses could be entirely eliminated if each actuator had a dedicated pump operated in displacement control. This approach would allow the removal of valves from the circuit, thus reducing throttling losses to zero, but would also be significantly more expensive than other alternatives.

Besides reducing throttling losses in the hydraulic circuit, another potential method to increase the efficiency of mobile machines is to recover the kinetic and potential energy from the swing motion and the lowering of the boom actuator. Currently, the conventional Load Sensing hydraulics system is widely used in mobile applications for its optimal balance between cost-effectiveness and fuel efficiency. Nevertheless, it has a total efficiency as low as 4% [1] and does not allow for the recovery of kinetic or mechanical energy. For these reasons, from an efficiency standpoint, it could be greatly surpassed by new system architectures, including hybrids, which are undoubtedly more efficient but also significantly more expensive.

Among the innovative solutions that have emerged from the wave of innovation since the second half of the twentieth century, one approach that has gained interest in recent years is based on the Common Pressure Rails (CPRs) concept. In these architectures, multiple actuators share common supply lines, maintained at different pressure levels. The hydraulic circuit is designed so that all actuator chambers can be connected to any of these supply lines. This simple but effective concept was first introduced by Lumkes and Andruch [2]. The only limitation of this solution was the inability to recover potential and kinetic energy.

This idea was further improved by the STEAM architecture, which added accumulators to at least two of these pressure rails. Making this modification enabled energy storage within the system and advanced secondary control strategies for the cylinders. The concept was presented by Vukovic, Sgro, and Murrenhoff [3], with an 18-ton prototype.

The focus of this thesis project, detailed in the subsequent pages, was the implementation and performance verification of the Common Pressure Rail system in terms of its capability to execute standard dig and dump cycles and air grading, along with a specially created cycle to test the system's limits, referred to as the heavy-duty work cycle. The starting point was a model of a 9-ton excavator with a hydraulic circuit based on the Load Sensing architecture, which was modified to convert the architecture to Common Pressure Rail.

Specifically, the entire thesis project centered on the controller of the Common Pressure Rail system developed in the Simulink environment. This controller, operating in co-simulation with the AMESim environment, generates all the signals for the various components of the Common Pressure Rail circuit, including on-off valve signals, proportional valve signals, pump flow signals, and the thermal engine throttle signal. These are evaluated in real-time based on signals from pressure, torque, flow, and force sensors in the circuit and the desired speeds set by the excavator operator via joystick commands.

The final project section will be dedicated to an architecture called Common Pressure Rail plus Electronic Flow Matching (CPR+EFM). This solution is engineered to leverage the advantages of both the Electronic Flow Matching strategy and Common Pressure Rail architecture.

Chapter 1

Hydraulic Excavator

1.1 Excavator Types, Sizes, and Purposes

Excavators are powerful construction machines featuring a boom, arm, and bucket collectively known as the front attachment. These components are connected to a cab mounted on a rotating superstructure, which sits atop an undercarriage equipped with either tracks or wheels (see Figure 1.1).

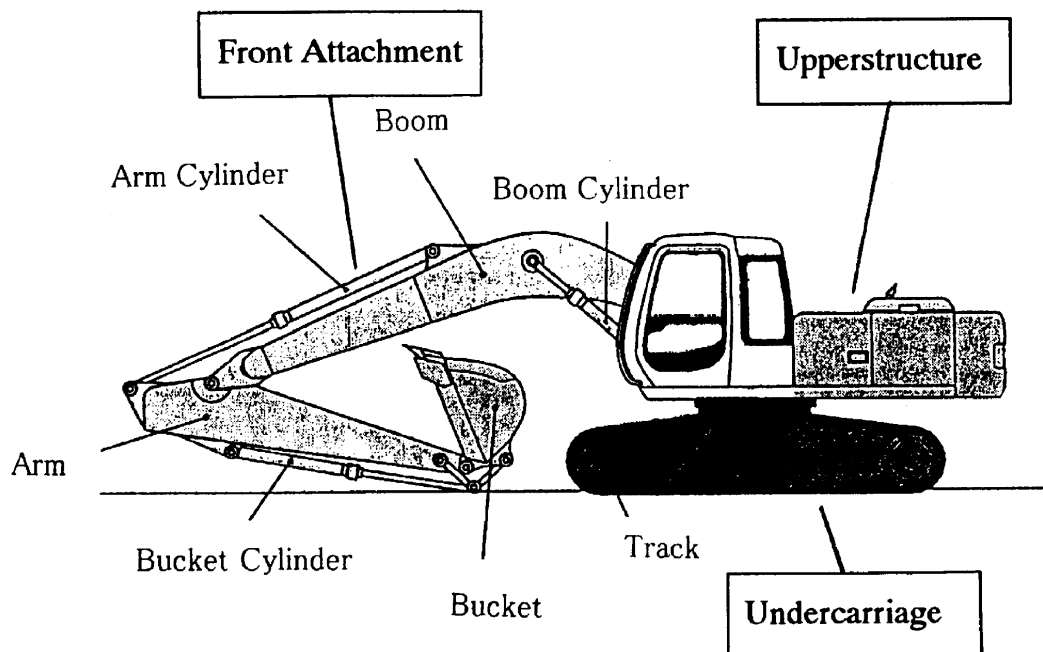


Figure 1.1: Hydraulic excavator constitution [4]

These machines are primarily used for digging, as well as a variety of lifting and carrying tasks across different applications. With the addition of specialized tools such as hydraulic breakers, cutters, shears, grapples, and couplers at the end of various boom and arm configurations, excavators can tackle an even broader range of jobs. They come in different sizes, each tailored to specific needs and goals, such as maximizing productivity, fuel efficiency, and versatility [5]. Each size serves a unique purpose, with some models being highly specialized for particular tasks.

1.1.1 Types of Excavators

Let's explore the primary types of excavators and their respective purposes:

- Crawler excavators: equipped with a bucket, boom, and arm, these versatile machines are ideal for digging, demolition, trenching, and lifting heavy objects (see Figure 1.2).
- Wheeled excavators: similar to crawler excavators but with wheels instead of tracks, these machines can travel directly on roads between job sites, offering greater mobility and reducing transportation time and costs (see Figure 1.3).



Figure 1.2: Crawler excavator [5]



Figure 1.3: Wheeled excavator [5]

1.1.2 Excavator Size and Purpose Classification

Having reviewed the main types of excavators, let's now look at the different sizes of excavators and their specific uses:

- Compact excavators: also called mini excavators, are ideal for small or tight areas. With minimal tail swing, they are easy to maneuver around buildings, making them perfect for precise digging and landscaping projects like digging holes for trees (see Figure 1.4).

- Mini excavators: weighing under five metric tons, compact excavators are easy to transport and ideal for soft terrain. They are perfect for smaller projects needing precision and minimal lifting.
- Midi excavators: typically weighing between five and ten metric tons, offer more power and capacity than mini excavators.
- General-purpose excavators - medium: weighing between ten and twenty-five metric tons, are the most common size. They are versatile, supporting various attachment tools and suitable for lifting or hauling large materials. Their tail swing can also pose challenges in confined areas. These excavators are typically used on most construction sites (see Figure 1.5).
- General-purpose excavators - large: they are robust machines designed for high-powered tasks and substantial hauling needs. They find frequent application in commercial construction and extensive demolition endeavors. While weighing over twenty-five metric tons, their transportation and storage can pose challenges. However, if your projects entail heavy lifting or significant demolition work, large excavators are the optimal choice (see Figure 1.6).



Figure 1.4: Compact excavator [5]



Figure 1.5: General-purpose excavators - medium [5]



Figure 1.6: General-purpose excavators - large [5]

1.2 Subsystems and Equipment Configuration

Having given a broad overview on excavators, let's delve deeper into their typical system layout, subsystems, and individual components that make up a state-of-the-art excavator (Figure 1.7).

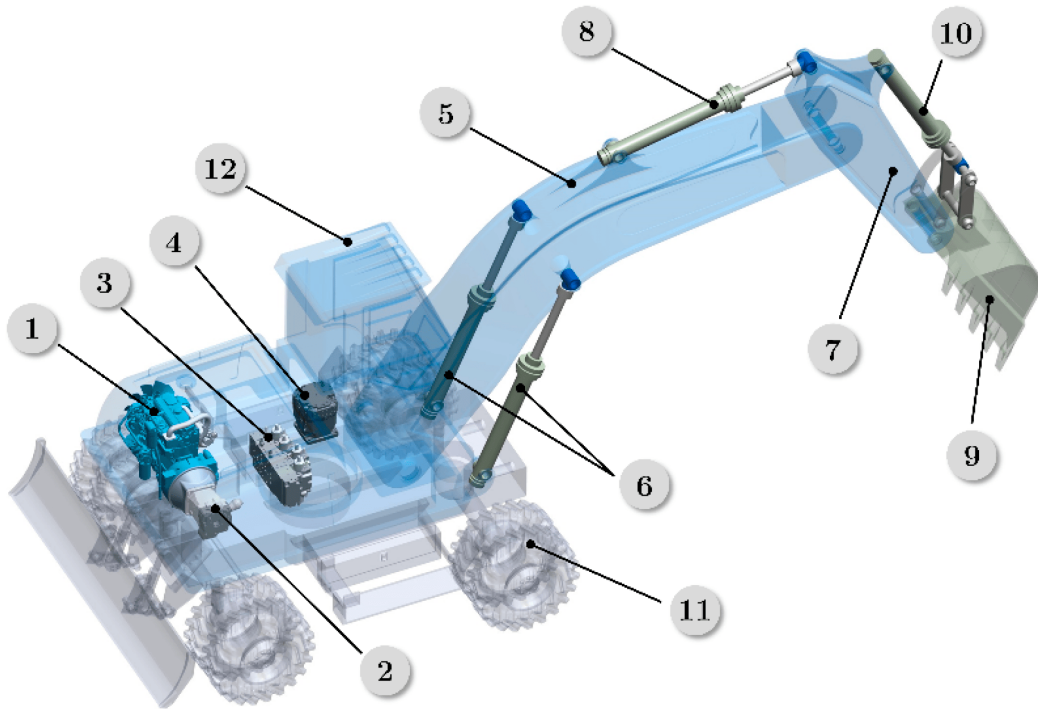


Figure 1.7: Layout of a typical hydraulic excavator [6]

An excavator typically comprises one or multiple hydraulic pumps (2), powered by a diesel engine (1), for supplying pressurized flow to the system. The operator, stationed in the cab (12)(see Figure 1.8), utilizes joysticks (see Figure 1.9) to manipulate a series of directional valves situated in a manifold block, commonly referred to as the main control valve (MCV) (3) (see Figure 1.10). These valves enable intuitive and precise control of the linear actuators governing the front attachment structure (boom (6), arm (8), bucket (10)), and the hydraulic motors for the upper structure rotation (4) and the vehicle motion (11).

1.2.1 Hydraulic System

The main objective of any mobile hydraulic system is to allow the operator to control all the machine's movements effortlessly and intuitively. The operator directs the desired actuator movements, while external forces determine the system pressure,



Figure 1.8: Example of excavator cabs [7]

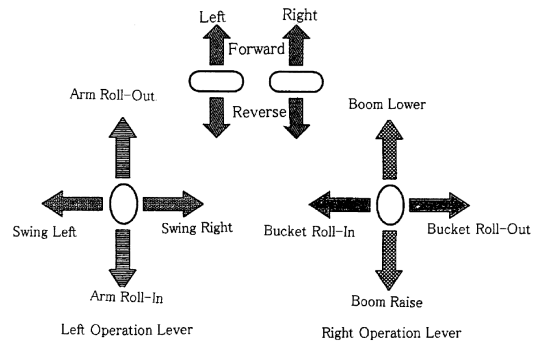


Figure 1.9: Hydraulic excavator lever control pattern [4]

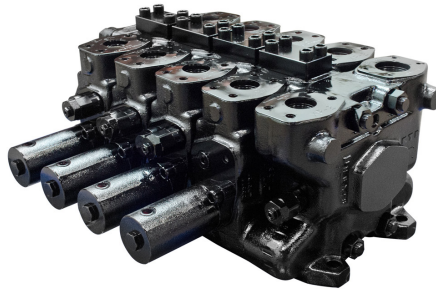


Figure 1.10: Main Control Valve block [8]

and the engine supplies the required power. With a simple joystick movement in the cab, the operator can open the valves connected to the actuators. This action allows the pump's flow to enter the actuator chamber, initiating movement once the circuit pressure rises enough to generate hydraulic force that overcomes the surrounding load.

The interaction between hydraulic actuators and the external environmental load is notably complex. Each actuator's force and velocity requirements, as well as the hydraulic motor's torque and rotational speed demands, are distinct and independent of each other. These factors are influenced by the environmental conditions interacting with the mobile hydraulic system and the operator's commands, respectively. Both the linear actuator and the hydraulic motor can operate under four different conditions, as illustrated in Figures 1.11 and 1.12. The x-axis represents the flow needed by each utility (Q_L), which can be seen as the

operator's input to the system. The y-axis represents the force or load pressure (p_L) experienced by the utility as a direct result of the surroundings.

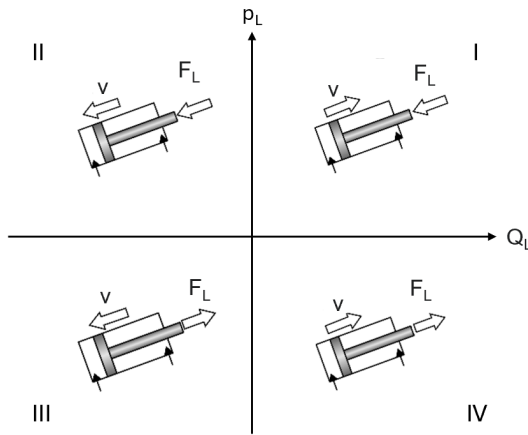


Figure 1.11: Load quadrants experienced by a linear hydraulic actuator

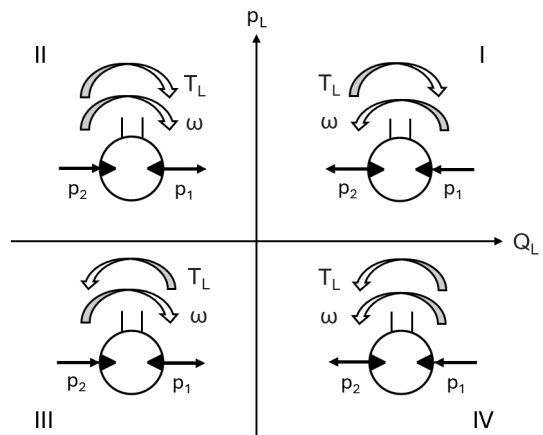


Figure 1.12: Load quadrants experienced by a hydrostatic machine

By making reference to the Figure 1.11 it is possible to make some considerations on the working conditions of the linear actuators. For linear actuators, the force acting on them is due to both the weight of the attached structure and the external forces encountered during digging and other operations. Inertial forces generated during acceleration play a less significant role. Depending on the movement, each actuator experiences either a resistive force opposing its motion (Quadrants I and III) or an assistive force aiding its motion (Quadrants II and IV). As a result, in Quadrants I and III, the actuator must be actively supplied with power, while in Quadrants II and IV, the actuators can actually supply power to the system.

Due to the kinematic arrangement and the significant weight of the implement structure, the boom cylinders almost exclusively operate in load Quadrants I and II. In contrast, the magnitude and direction of the load acting on the arm and bucket cylinders vary greatly, causing operation in all four quadrants.

By making reference to the Figure 1.12 it would be possible to make some considerations on the working conditions of the hydraulic motor. Both the motor driving the turret and the travel motors also experiences four-quadrant operation, in fact, depending on the rotational movements, the hydrostatic machine could encounter either a resistive torque opposing its motion (Quadrants I and III), working in motoring mode, or an assistive torque aiding its motion (Quadrants II and IV), working in pumping mode. Thus, in Quadrants I and III, the hydrostatic machine must be actively supplied with power, whereas in Quadrants II and IV, the hydrostatic machine operates as a pump and can supply power to the system.

Typically, the hydraulic motor functions within Quadrants I and III when, for instance, the turret is stationary and needs to be mobilized. In this scenario, following the pump sign convention, the torque (T_L) and the flow rate (Q_L) vectors point in opposite directions, necessitating the hydrostatic machine to operate in motoring mode. Conversely, when the hydraulic motor operates within Quadrants II and IV, such as when the turret is in motion and requires stopping, the torque (T_L) and the flow rate (Q_L) vectors align in the same direction. In this case, the hydrostatic machine functions in pumping mode.

Each point in the two planes of Figures 1.11 and 1.12 represents a state of quasi-stationary equilibrium, in which the pump flow rate is proportional to the operator's joystick displacement, the system pressure is determined by the load, and the engine torque and pump torque are equal.

Chapter 2

Principles, Classification, and Review of Valve-Controlled and Valve-Less Hydraulic Circuits

Hydraulic circuits are used in various industrial applications. These systems often perform complex operations, making their controllability, reliability, and interoperability essential for technological development. Over the years, various hydraulic architectures have been developed and implemented, classified into two main categories: valve-less and valve-controlled systems. The main characteristics of the mentioned classes are summarized in the following.

- Valve-controlled hydraulic circuits are systems in which the hydraulic valves play a pivotal role as control elements. Flow throttling primarily occurs in the main transmission lines, providing a precise method for achieving control functions. This configuration enables regulated fluid flow, allowing for meticulous adjustments in hydraulic machinery.
- Valve-less hydraulic circuits opt for solutions that exclude throttling valves from the primary transmission lines; the control elements in the valve-less systems are variable-flow hydraulic units. This approach eliminates the need for conventional valves, offering a different strategy for achieving control and maintaining the fluid dynamics within the system.

Both systems can implement an hybrid technology, thus incorporating an additional energy source beyond the machine's combustion engine. This supplementary energy source can be electric, hydraulic, or mechanical in nature. This integration of diverse energy forms contributes to improved overall performance and adaptability, making hybrids a compelling choice in certain applications.

Catering to specific requirements in various industrial and technological contexts, each of the above mentioned classes could be implemented, thus leading to advantages and disadvantages.

2.1 Valve-Controlled Hydraulic Systems

Hydraulic systems with valve control represent a well-established and frequently employed class of hydraulic circuits that have enjoyed popularity in the past due to their precise control and regulation capabilities. Within these systems, hydraulic valves assume a central role as primary control elements strategically positioned within the principal transmission lines.

A notable challenge associated with this solution arises during the valve control operation, where flow throttling occurs to attain the pressure requested by the end-users, leading to significant power losses within the system.

Broadly speaking, valve-controlled systems can be categorized into hybrid and non-hybrid systems based on the presence or absence of energy accumulator systems, which may be hydraulic, electrical, or mechanical.

To illustrate the subdivision of non-hybrid valve-controlled systems, a summary image has been attached for this purpose (see Figure 2.1).

A brief description of the main categories into which valve-controlled systems are divided is provided in the following text:

- Mechanical-hydraulic systems exclusively rely on pure mechanical-hydraulic regulations, excluding electronic involvement in system control. These systems are traditionally classified as open-center or closed-center types based on the design of proportional directional control valves (PDCVs), where the classification pertains to the nature of the connection established between the pump and reservoir when the valves are centered.
- Electro-hydraulic systems leverage advanced control strategies that were not feasible in the past, enabling more flexible machine setups and enhanced energy efficiency. Some electro-hydraulic architectures evolve from their mechanical-hydraulic counterparts, incorporating electronics at various levels (e.g., electronic joysticks whose electrical output signal depends not only on the lever position itself but also on other quantities measured by various transducers. Therefore, the output signal controlling the Proportional Directional Control Valves (PDCVs) is determined by a dedicated ECU).

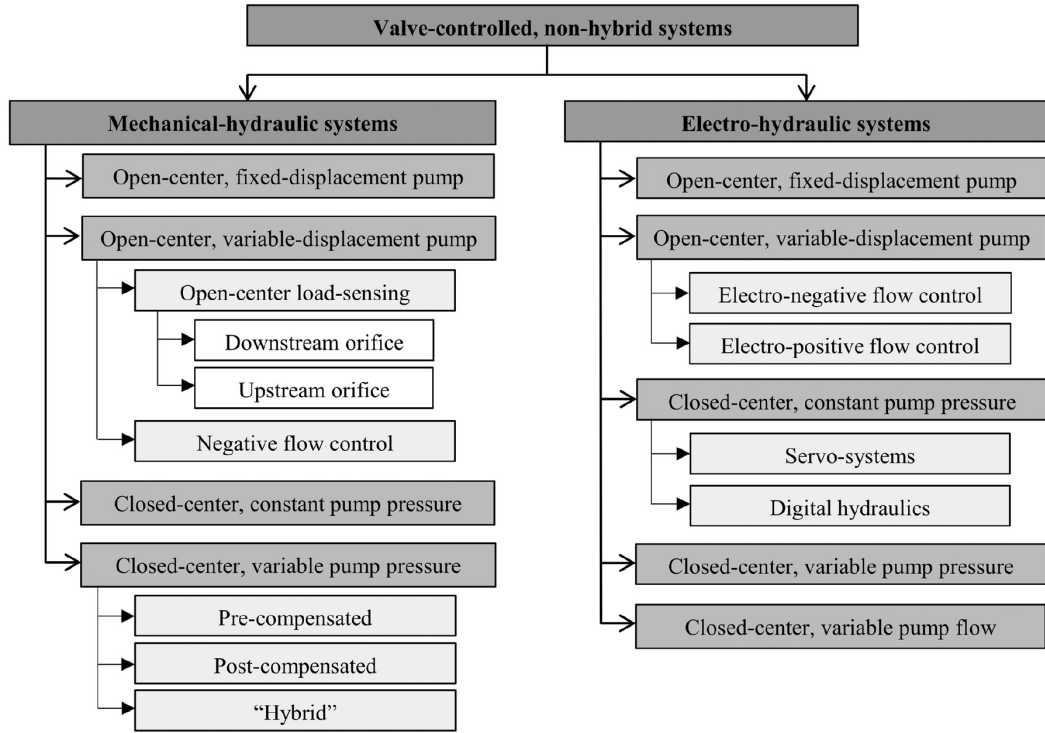


Figure 2.1: Proposed classification of the working hydraulics for non-hybrid, valve-controlled mobile machines [9]

These systems could be further classified as either open-center or closed-center, as shown in Figure 2.1, based on the design of the proportional directional control valves (PDCVs). The classification depends on the type of connection established between the pump and the reservoir when the valves are in the centered position.

The following section will delve into one of the most prevalent non-hybrid valve-controlled systems, known as Load Sensing, classified as a mechanical-hydraulic system with a closed-center variable pressure pump in Figure 2.1. This section will also discuss the non-hybrid valve-controlled Electronic Flow Matching, classified as an electro-hydraulic system with a closed-center variable pump flow in Figure 2.1. Specifically, for Load Sensing, a brief description of the pre-compensated and post-compensated Load Sensing systems will be provided. The pre-compensated architecture has served as the baseline for our analysis, characterizing the 9-ton excavator model, which has been used as a starting point and for comparative purposes throughout our performance and energy analysis. Meanwhile, the Electronic Flow Matching system has served as the baseline for the development of the Common Pressure Rail plus Electronic Flow Matching described later.

2.1.1 Non-hybrid - Load Sensing Hydraulic System

Load Sensing stands out as a prevalent method employed in mobile machinery for hydraulic power transmission [9] [10]. It has supplanted the traditional fixed-displacement pump systems, characterized by a constant flow provision to the system. The primary drawback of the fixed-displacement pump system lies in its propensity to release excessive flow to the tank via a pressure relief valve under lower load pressure conditions, resulting in substantial losses manifested in the form of heat across the valve. Consequently, in practical scenarios where loads fluctuate, particularly in mechanisms like excavators, the efficiency of this system diminishes.

The Load Sensing system comprises local pressure compensators (LCs) added to the closed-center proportional directional control valves (PDCVs). The choice of local pressure compensators prevents interaction between loads when multiple actuators are moved simultaneously. Additionally, the presence of local compensators allows for load controllability with pressure-independent speed characteristics.

The most commonly used LCs are configured in two ways:

- Pre-compensated systems: the LCs are located upstream of the main spools and are normally open (see Figure 2.2).
- Post-compensated systems: the LCs are located downstream of the main spools and are normally closed (see Figure 2.3).

Pre-compensated Load Sensing System As illustrated in Figure 2.2, there are local pressure compensators located upstream of the distributors. In the diagram, the distributor is depicted as 2-port valves for simplicity, but in real application, they are 4-port valves connected to both piston chambers. These compensators function as continuously adjustable valves (variable throttles), typically in an open state.

When the pressure between p_{L1} and p_{L2} is unequal, the higher pressure sets the global Load-Sensing pressure p_{LS} , as determined by the selector valve $VSEL$. Let's consider a specific case where the pressure generated by the load on actuator $L1$ is greater than that on load $L2$.

In this scenario, the compensators regulate and impose the respective pressures:

$$\begin{aligned} p_{m1} &= p_{LS} + s_c = p_{L1} + s_c; \\ p_{m2} &= p_{L2} + s_c; \end{aligned} \tag{2.1}$$

The flow rates directed towards the actuators are then described by the following equations:

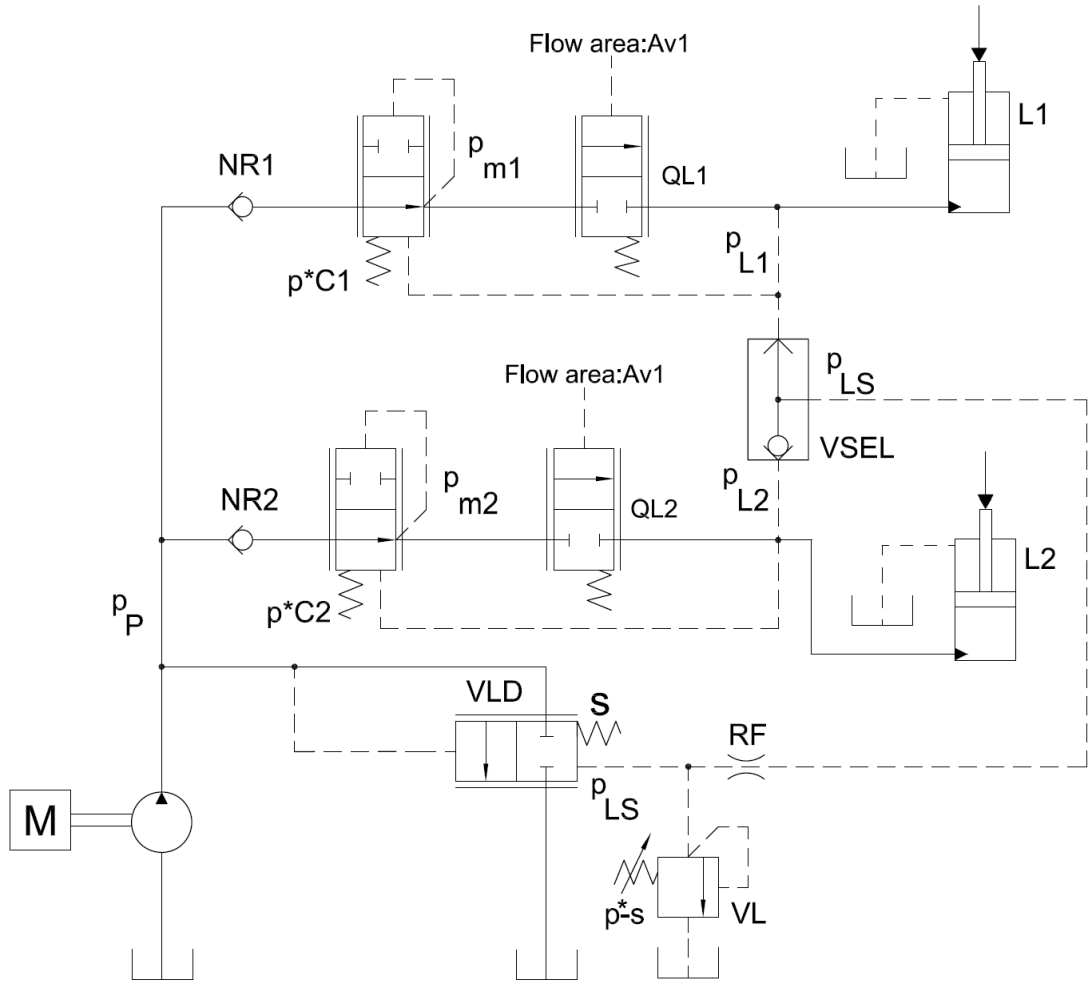


Figure 2.2: ISO scheme of a load-sensing circuit with precompensators for controlling two linear actuators [11].

$$\begin{aligned} Q_{L1} &= K_1 \cdot A_{v1} \cdot \sqrt{p_{m1} - p_{L1}}; \\ Q_{L2} &= K_2 \cdot A_{v2} \cdot \sqrt{p_{m2} - p_{L2}}; \end{aligned} \quad (2.2)$$

By combining the two sets of equations 2.1 and 2.2, the flow rates directed to the two actuators are determined by the following laws:

$$\begin{aligned} Q_{L1} &= K_1 \cdot A_{v1} \cdot \sqrt{s_c}; \\ Q_{L2} &= K_2 \cdot A_{v2} \cdot \sqrt{s_c}; \end{aligned} \quad (2.3)$$

Thus, the flow rates no longer depend on the pressures of the loads or the pump line pressure. This condition holds as long as the pump pressure p_P remains greater

than the pressures $p_{m,i}$.

This arrangement prevents interference between loads, ensuring that the flow rates to the actuators, and consequently their speeds, depend solely on the input given to the distributor valve, which is a function of the operator's input.

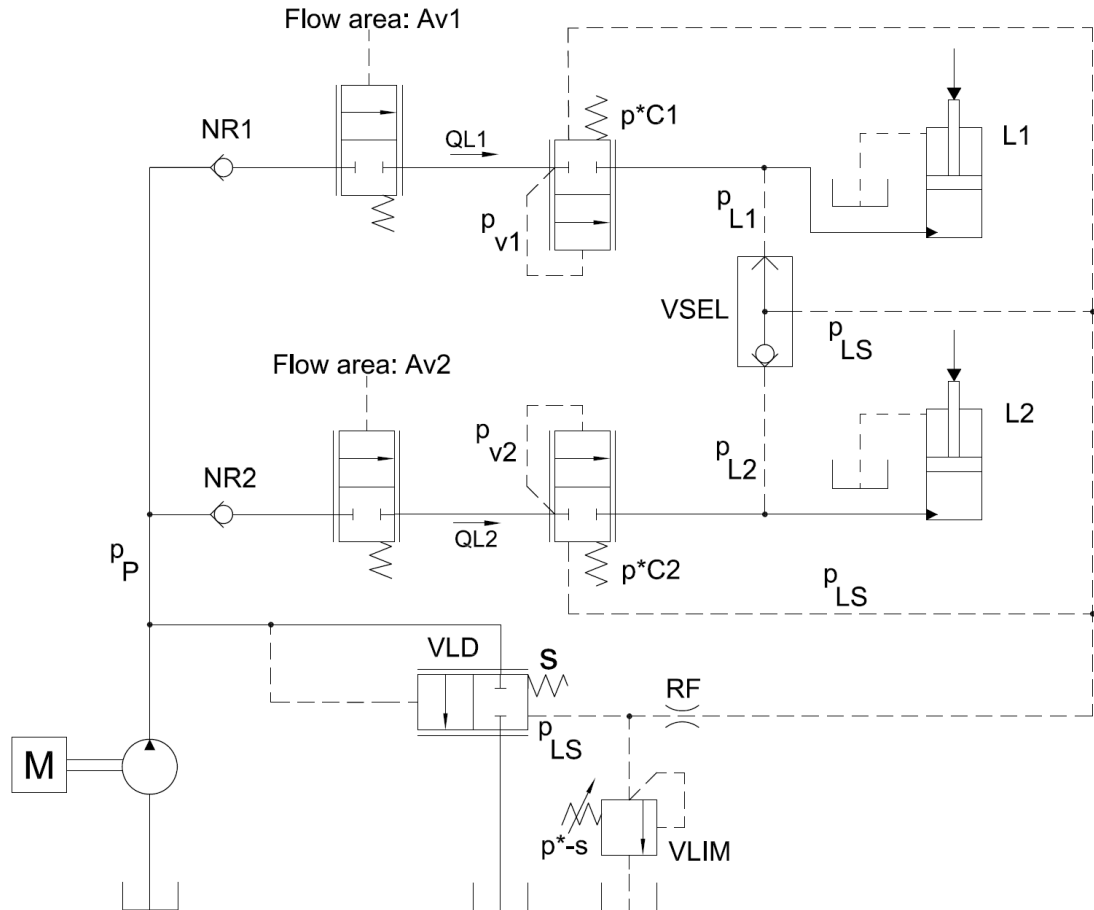


Figure 2.3: ISO schematic of the load-sensing circuit with post-compensators for controlling two linear actuators [11].

Post-compensated Load Sensing System Pre-compensated systems are highly effective under all working conditions until the flow saturation point is reached, i.e., when the flow demand from the actuators exceeds the maximum deliverable by the pump. This limitation is addressed by the introduction of the post-compensated Load-Sensing architecture (Figure 2.3).

In a post-compensated system, the pressure compensation valves are situated downstream of the main directional valves. Consequently, pressure compensation

occurs after the fluid has passed through the directional valve. These compensators operate as continuously variable throttles and are normally in a closed position. When one of the pressures between p_{L1} and p_{L2} predominates, it establishes the global Load-Sensing pressure p_{LS} , as determined by the selector valve $VSEL$. Let us assume that the pressure generated by the load on actuator $L1$ is greater than that generated by actuator $L2$.

In this scenario, during regulation by the compensators, the respective downstream pressures are imposed according to the following equations:

$$p_{v1} = p_{LS} + s_c = p_{L1} + s_c; \quad (2.4)$$

$$p_{v2} = p_{LS} + s_c = p_{L1} + s_c; \quad (2.5)$$

This implies:

$$p_{v1} = p_{v2} = p_v \quad (2.6)$$

As a result, the downstream pressures of all the distributors, modulated by the local compensators, are maintained equal and denoted as p_v , defined by the highest load.

The flow rates to the actuators are given by:

$$\begin{aligned} Q_{L1} &= K_1 \cdot A_{v1} \cdot \sqrt{p_P - p_{v1}}; \\ Q_{L2} &= K_2 \cdot A_{v2} \cdot \sqrt{p_P - p_{v2}}; \end{aligned} \quad (2.7)$$

Knowing that the pump pressure is a function of the Load-Sensing pressure, we have:

$$p_P = p_{LS} + s_p \quad (2.8)$$

By combining equations 2.6, 2.7, and 2.8, we can express the flow rate to the actuators as:

$$\begin{aligned} Q_{L1} &= K_1 \cdot A_{v1} \cdot \sqrt{s_p - s_c}; \\ Q_{L2} &= K_2 \cdot A_{v2} \cdot \sqrt{s_p - s_c}; \end{aligned} \quad (2.9)$$

Thus, in this case as well, the flow rate is independent of the load or the pump pressure, thereby preventing interference between the loads.

Generally speaking for both the LS architectures shown, while the LS technique effectively reduces excess flow to the system, its efficiency decreases in applications with multiple actuators, such as excavators with a single power source. In such cases, the LS system is efficient only for the actuator requiring maximum pressure, leading to inefficiencies and significant power losses for the other actuators with

lower pressure needs. The cumulative energy losses in this configuration can be substantial.

A potential solution is to group the actuators into two separate subcircuits based on their power demands, each fed by an LS pump.

2.1.2 Non-hybrid - Electronic Flow Matching System

The Electronic Flow Matching (EFM) strategy is based on flow control of the pump, rather than pressure control. This implies that the displacement of the pump is determined by the demand from the actuators, which is commanded by the operator through joystick inputs.

Figure 2.4 illustrates a hydraulic circuit where this strategy has been implemented.

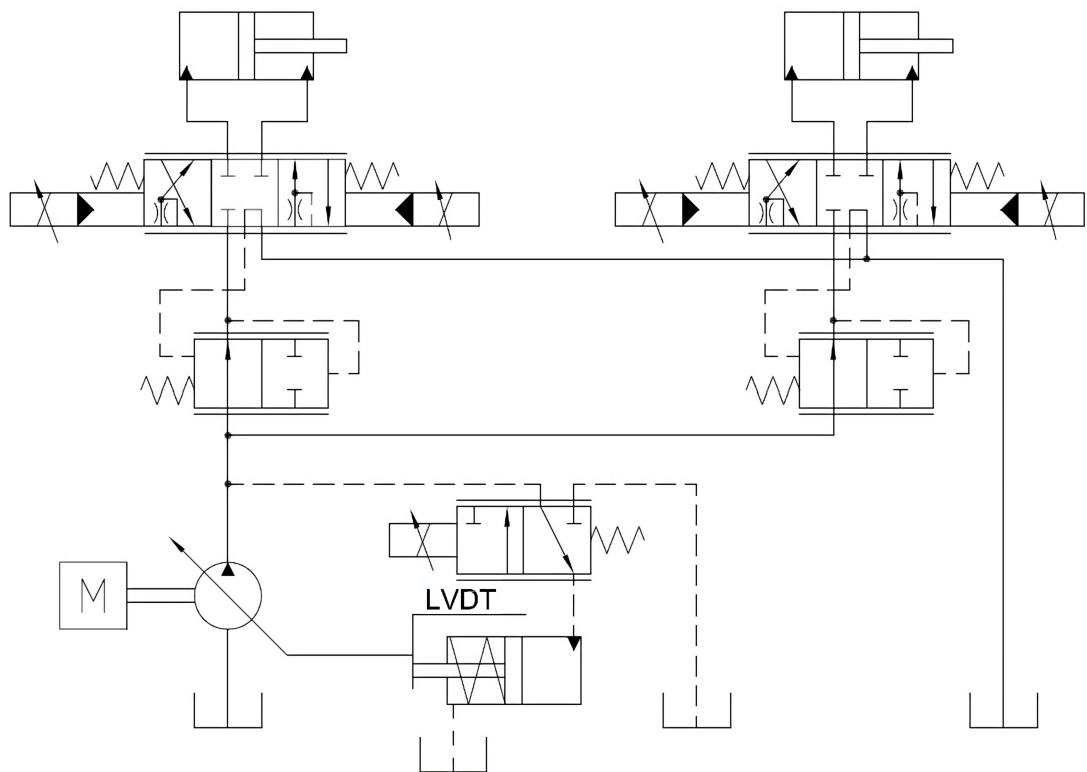


Figure 2.4: Schematic representation of a hydraulic circuit implementing the Electronic Flow Matching strategy

In the absence of a global Load-Sensing pressure line, which is present in the previously described circuits, this deficiency is compensated by the presence of a sensor measuring the angular position on the pump's swash plate to enable

electrical control of the pump (denoted as *LVDT* in Figure 2.4).

To determine the flow rate to be generated and thus the pump displacement, in the case of manually or hydraulically actuated distributors, position transducers are necessary to ascertain the degree of opening of each spool. Conversely, in the case of electrohydraulic actuation of the spools, the electrical signal sent to the spool can be utilized to determine its opening.

The EFM strategy offers significant advantages in terms of efficiency and responsiveness. By directly controlling the pump flow based on the operator's input, it reduces energy losses typically associated with pressure-based control systems. This method also enhances the precision of actuator movements, leading to improved overall system performance.

In conclusion, the adoption of Electronic Flow Matching represents a substantial advancement in hydraulic system design, leveraging modern control technologies to achieve superior performance and efficiency.

2.2 Valve-Less Hydraulic Systems

Valve-less systems, distinct from valve-controlled counterparts due to the absence of traditional valves for flow regulation, have several defining attributes that will be summarized in the following.

These systems often feature reduced complexity, with fewer moving parts compared to valve-reliant architectures, potentially reducing maintenance requirements and overall expenses. Additionally, their minimized mechanical components contribute to heightened reliability and operational uptime. Notably, valve-less systems mitigate pressure drops and energy inefficiencies commonly associated with traditional valve setups, thereby potentially enhancing efficiency in specific contexts. Furthermore, they exhibit improved dynamic response, enabling quicker reactions and superior performance.

Valve-less systems can operate either with flow control or pressure control mechanisms, each having distinct characteristics. In essence, the key difference lies in what aspect of the system is being controlled: flow or pressure. Flow-controlled systems manage the rate at which the fluid moves through the system, while pressure-controlled systems focus on maintaining a specific pressure level within the system. Depending on the application and requirements, one approach might be more suitable than the other.

Within the examined configurations, two primary approaches are predominantly employed in flow-controlled systems. The first involves displacement control utilizing a linear actuator in conjunction with a variable displacement pump, commonly referred to as a hydrostatic actuator (HA) in existing literature. Conversely, the second strategy revolves around regulating the velocity of a fixed displacement

pump, typically achieved through the regulation of the primary power source. Consequently, the principal architectures in this category are hybrid and encompass Electro-Hydrostatic Actuators (EHA) and Hybrid Hydraulic-Electric Architecture (HHEA).

On the other hand, pressure control might involve mechanisms that adjust or modulate the pressure based on preset parameters or feedback loops. Pressure-controlled systems might be advantageous in situations where maintaining a consistent pressure is critical, irrespective of fluctuations in flow rate. Among the various systems developed over the years, the Common Pressure Rail (CPR) architecture has demonstrated the most significant efficiency improvement compared to the Load Sensing system, achieving approximately a 50% increase. Moreover, the CPR architecture requires lower investment costs for adapting the existing hydraulic system of a modern excavator currently based on the Load Sensing architecture.

2.2.1 Steam - the Concept

The concept of a Common Pressure Rail, also known as a Multi-Pressure System, represents an innovative advancement in hydraulic systems aimed at enhancing energy efficiency and minimizing throttling losses. This approach facilitates the downsizing of both the pump and the diesel engine [6] [3]. In traditional LS systems, as previously mentioned, throttling losses arise when the supply pressure must align with the load pressure. This alignment necessitates a constant pressure differential between the pump and the actuator, leading to substantial power losses. These inefficiencies are further pronounced when multiple actuators with varying pressure requirements operate simultaneously.

In mobile hydraulic applications, the diesel engine serves as the primary power source, dimensioned to meet peak power demands in LS systems. The diesel engine provides mechanical power to the pump, which then delivers hydraulic power to the actuator. The fluctuating power needs of the actuator cause rapid changes in the diesel engine's output, thereby increasing fuel consumption and emissions. Notably, the diesel engine's efficiency peaks at only 40% at its optimal operating point. The main contributors to the overall efficiency reduction in the power transmission system are throttling and diesel engine losses, with minor losses occurring in other hydraulic components.

The common-pressure system aims to address these inefficiencies by introducing multiple pressure sources within the system. This method allows actuators to receive precise pressure levels matching their load requirements, thereby reducing throttling losses. Figure 2.5 illustrates the basic concept of the common-pressure system. Cylinder chambers connect to pressure sources through on/off valves, ensuring discrete pressure levels for actuators and minimizing pressure drops across valves.

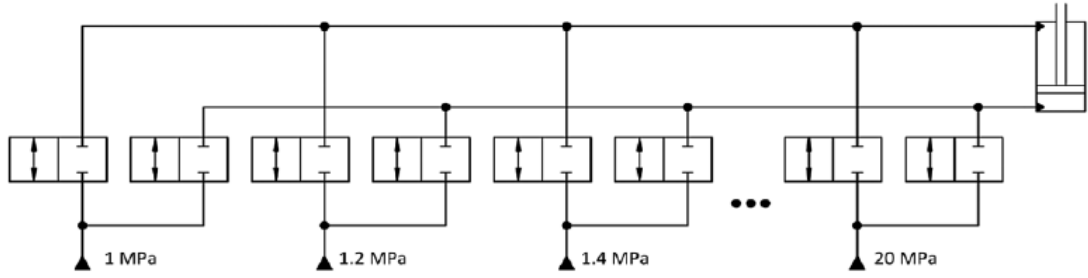


Figure 2.5: Basic idea of Common-Pressure System [3].

The STEAM system, essentially a hydraulic hybrid, utilizes two pressure rails (high pressure HP and medium pressure MP) along with a series of simple valves to mitigate the primary loss mechanisms found in current mobile hydraulic circuits. Figure 2.6 depicts one potential implementation of the STEAM system.

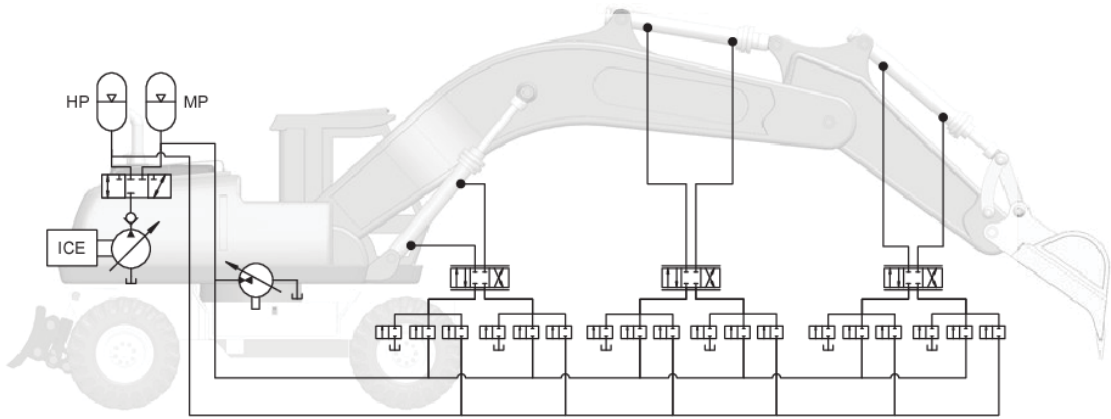


Figure 2.6: A possible implementation of STEAM [3].

These pressure rails and their accumulators manage peak power demands, facilitating more efficient engine operation at lower speeds, around 1200 rpm. To further reduce throttling losses when supplying flow to linear actuators, a series of switching valves allows both pressure rails and the tank line to be individually connected to both the piston and rod chambers of each cylinder. This arrangement generates a system of nine artificial supply pressures, which, depending on the current load pressure, can lower throttling losses and enable energy recovery.

A key advantage of this system is the enhanced efficiency of engine and pump operation. Since these components are solely responsible for charging the accumulators, they are decoupled from the immediate actuator power demands and can thus function in a digital mode. When the accumulator state of charge (SOC) drops,

the engine and pump operate at full capacity. Once the accumulators are fully charged, the engine and pump idle, avoiding part-load conditions and significantly reducing losses.

STEAM also addresses one of the main challenges in implementing boom potential energy recovery circuits. By connecting the boom piston chamber to a pressure rail, when lowering the actuator the accumulators are charged, and the stored energy can be utilized to power other actuators as needed. Additionally, the system can prevent pressure peaks at actuator endstops: in standard flow-impressed systems like load sensing, driving actuators to the end-stop during operations like digging often causes rapid supply pressure increases to the system's pressure relief setting, resulting in unnecessary pressure peaks and throttling losses. A constant pressure system avoids this issue by supplying pressure rather than flow to the actuator.

Chapter 3

Development of Simulation Models for Load Sensing and Common Pressure Rail Architectures

This chapter presents and analyzes the models of hydraulic excavators based on the Load Sensing and Common Pressure Rail architectures. Both models were developed using the AMESim simulation software. The Load Sensing excavator model was created using data from a commercially available Komatsu 9-ton excavator, specifically the PC75R [11]. In contrast, the Common Pressure Rail excavator model was developed using the same characteristics and technical specifications as the traditional excavator. However, the hydraulic system supplying the various actuators was modified, with its design optimized to meet the requirements of the excavator during the standard dig and dump work cycle.

3.1 Load Sensing-Based Excavator Model Layout

The 9-ton crawler excavator, a mid-size machine, is depicted as a 3D model in Figure 3.1.

The hydraulic circuit of the excavator utilized for all tests, developed using the AMESim environment, is illustrated in Figure 3.2. This model is derived from a doctoral thesis [11], with several simplifications and calibrations made to closely approximate the results of the detailed model.

This simplified hydraulic circuit was meticulously designed to meet the rigorous standards of hydraulic system modeling in engineering. It serves as a foundational



Figure 3.1: 3D model of the Komatsu PC75R [12]

tool for conducting comprehensive performance analyses, accurately capturing the dynamics and operational characteristics of the excavator's hydraulic system under various scenarios and load conditions. The adjustments made from the original thesis model were crucial for optimizing simulation efficiency while maintaining fidelity to real-world hydraulic behaviors and responses.

It is important to note that the diesel engine, which powers the commercial excavator, is not included in the AMESim model. In the actual commercial vehicle, this engine provides a maximum output of 55 kW and can reach a peak speed of 2300 rpm. However, in the AMESim model, the engine's role is simulated by an ideal prime mover to simplify the analysis and focus on the hydraulic circuit.

In the AMESim model, the ideal prime mover is connected to three hydraulic pumps: one with variable displacement and two with fixed displacements. The variable displacement pump and one fixed displacement pump supply hydraulic fluid to the boom, arm, and bucket actuators, while the other fixed displacement pump supplies fluid to the turret rotation motor and the travel motors for the left

and right tracks. Optional equipment is not included in this circuit.

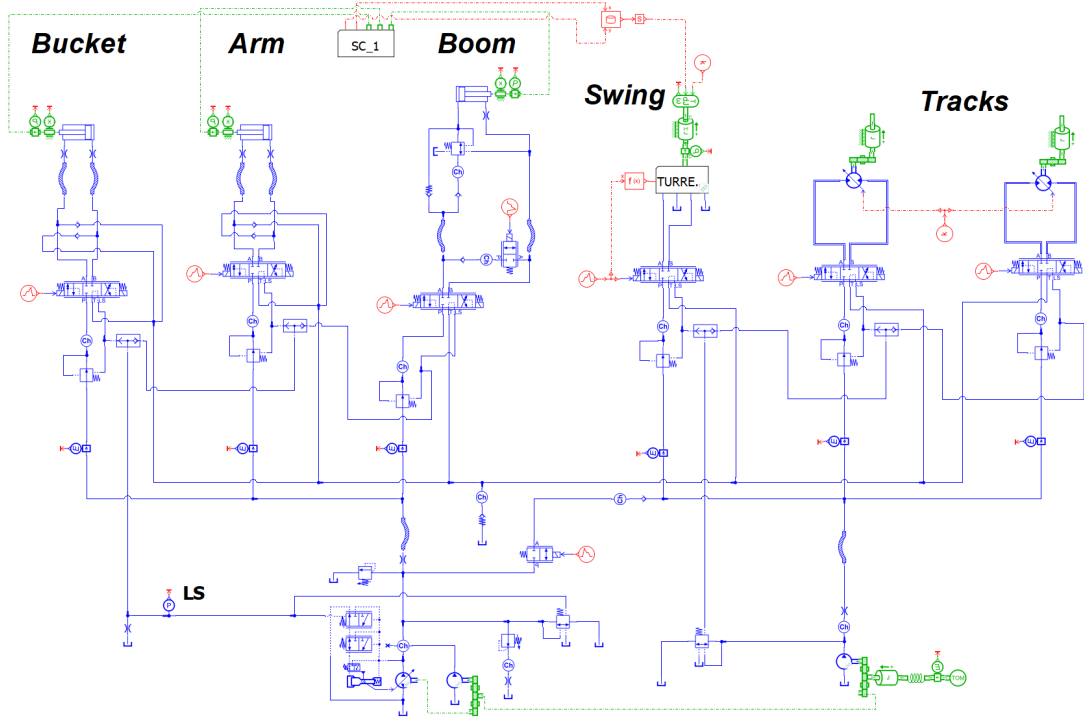


Figure 3.2: Traditional hydraulic excavator simplified AMESim model

Since all studies conducted on standard cycles are performed with the excavator at rest (thus the travel motors are inactive), a further simplification was made by removing the travel motors and all associated hydraulic circuits (see Figure 3.3). This final model was utilized for developing the Common Pressure Rail architecture-based model and served as a comparative model for studies on fuel economy and system losses.

3.1.1 Hydraulic Subsystems - Flow Generation Unit

This section provides detailed information about the hydraulic Load Sensing pre-compensated circuit subsystems. As previously mentioned, the reference hydraulic system model for the studies is powered by three pumps: a variable displacement piston pump of 65 cc/rev and a fixed displacement pump of 10.6 cc/rev jointly supplying the boom, arm, and bucket, and a fixed displacement gear pump of 27 cc/rev supplying the turret swing motor. In the commercial excavator, the two pumps supplying the linear actuators are replaced by a single variable displacement pump with a capacity of 75 cc/rev. This design choice stems from the fact that in the

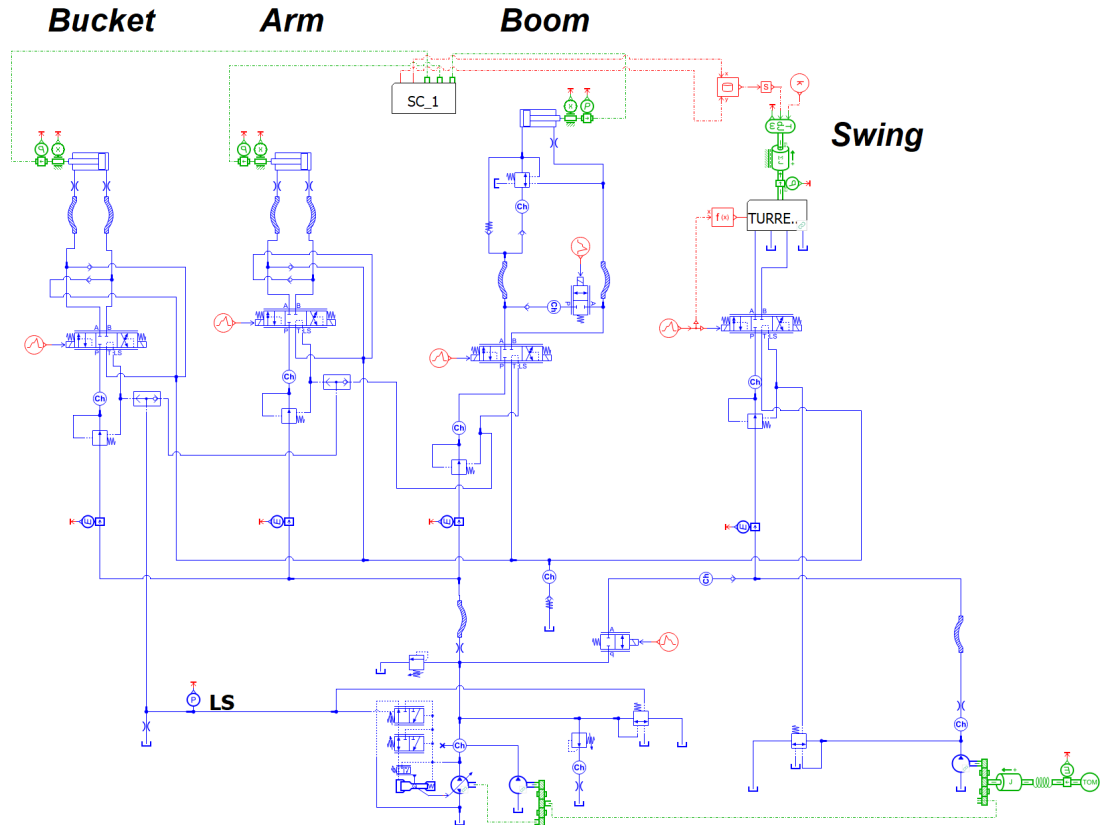


Figure 3.3: Traditional hydraulic excavator simplified AMESim model without travelling motors

commercial excavator, the 75 cc/rev pump, when set to its minimum displacement, delivers a flow rate of 10.6 cc/rev. However, the AMESim simulation environment does not support setting a minimum flow rate for a variable displacement pump. To address this limitation, the solution was to split the flow contributions between two pumps: a fixed displacement pump and a variable displacement pump. The fixed displacement pump consistently provides the minimum flow rate of 10.6 cc/rev, ensuring a baseline flow. Meanwhile, the variable displacement pump can adjust its displacement from zero up to its maximum value, supplying the additional variable flow rate as needed. This configuration replicates the behavior of the commercial excavator's hydraulic system within the constraints of the AMESim environment. The variable displacement pump is managed by a hydraulic piston actuator model. This model includes a torque limiter, which adjusts the pump's displacement to maintain a balanced product of flow rate and pressure difference at the pump ports, thus limiting the theoretical torque. Additionally, a pre-loaded spring is used to counteract the regulated pressure, ensuring that the system

remains minimally pressurized. Efficiency data for the pumps were integrated into the AMESim model based on information provided by customers. The volumetric and hydraulic-mechanical efficiencies of the fixed displacement pump that supplies the swing motor are shown respectively in in Figure 3.4 and 3.5. Meanwhile, Figure 3.6 and 3.7 illustrates the volumetric and hydraulic-mechanical efficiencies of both the variable displacement pump and the fixed displacement pump that supply the linear actuators. It is noteworthy that the efficiency maps for these last two pumps are identical.

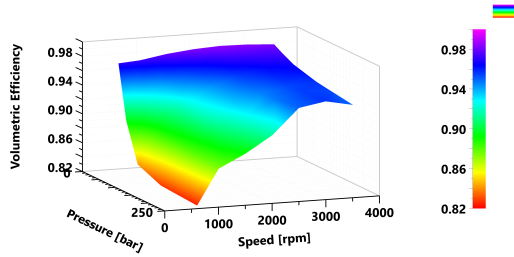


Figure 3.4: Volumetric efficiency of the fixed displacement pump

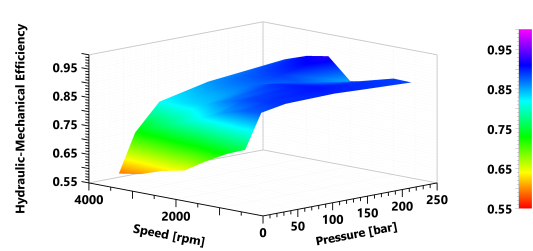


Figure 3.5: Mechanical efficiency of the fixed displacement pump

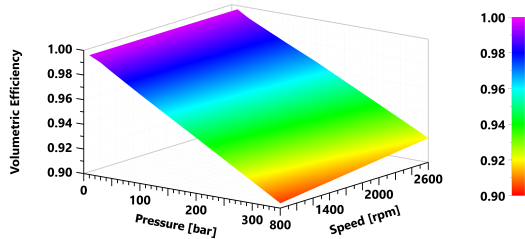


Figure 3.6: Volumetric efficiency of the variable displacement pump

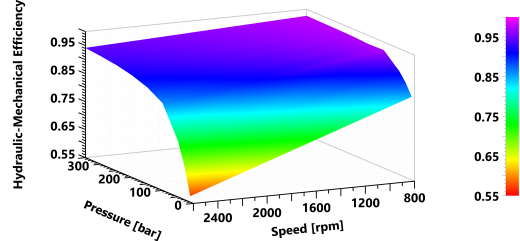


Figure 3.7: Mechanical efficiency of the variable displacement pump

To accurately replicate the real circuit's characteristics in terms of hydraulic losses, flow restrictors were utilized to account for pressure drops in the original excavator hydraulic circuit, ensuring a match in hydraulic losses between the commercial vehicle and the AMESim model. Flexible hoses were also included to account for volume variations due to pressure changes.

3.1.2 Hydraulic Subsystems - Actuators and Turret Motor Boom, Arm, and Bucket Actuators

Hydraulic Circuit The hydraulic system comprises four possible flow paths that connect the pump and the tank to the chambers of the two actuators. For each valve, specific flow rates (in L/min) and corresponding pressure drops (in bar) have been determined for the fully open path. These parameters are based on real components to yield meaningful insights into hydraulic losses, and they vary for each user. The proportional signal for valve opening is externally supplied by a current signal ranging from 0 to 1 mA, defining the connections of the ports within the blocks. The original model lacked control over the proportional valves' displacement signal, instead utilizing a fixed step-wise function to perform the dig and dump cycle.

It is crucial to highlight the presence of an over-center valve upstream of the boom actuator on the piston chamber side. This valve ensures the boom remains in a fixed position without safety concerns when no flow enters the actuator. Additionally, an on-off valve located upstream of the actuator on the rod chamber side can be opened to increase the lowering speed.

It is also noteworthy that an on-off valve is situated between the delivery lines of the three pumps. This valve allows the 27 cc/rev fixed displacement pump to connect with the variable displacement pump's delivery line, providing additional flow to the linear actuators, ensuring proper performance in terms of speed. This connection can effectively increase the flow rate only when the swing is activated along with the actuators; otherwise, the flow will be discharged by the relief valve connected to the fixed displacement pump's delivery line.

Kinematics and System-Environment Interaction The mechanics and kinematics of the actuator subsystem, along with the interaction between the excavator system and the environment, have been modeled using the Planar Mechanical Library of AMESim. This library facilitates the representation of rigid bodies and perfect joints with two or three degrees of freedom moving in a plane. It also allows the implementation of a soil model to compute the soil resistive force during digging operations and to calculate the volume and weight of the dug soil applied to the tool.

To construct the mechanical model of the excavator arm, the coordinates and dimensions of various components were defined using a CAD program. The 2D CAD model of the excavator arm is depicted in Figure 3.8.

The final AMESim implementation of the excavator arm is illustrated in Figure 3.9. This model is incorporated within the SC block of the AMESim excavator circuit shown in Figure 3.3.

Referring to the excavator arm model in Figure 3.9, several tags (1, 2, 3) can be

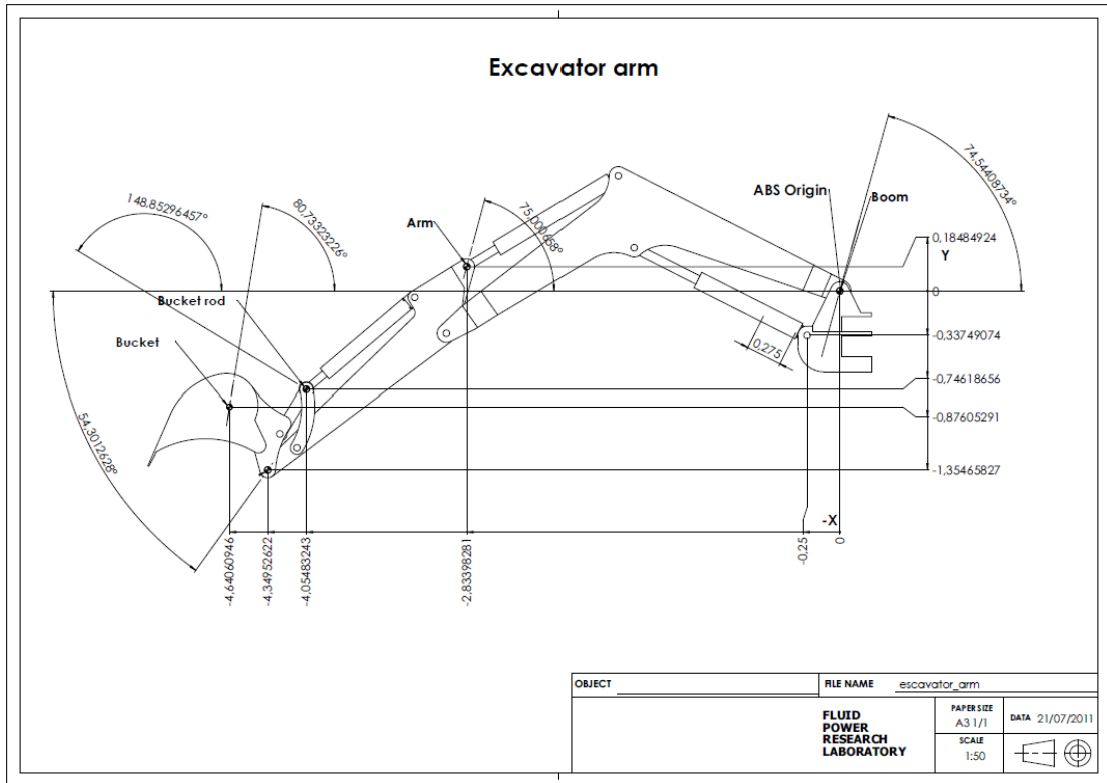


Figure 3.8: Representation of the excavator arm’s geometry [11]

identified that, outside the block containing the arm submodel, are connected to each actuator — specifically to the boom, arm, and bucket actuators (see Figure 3.3). These tags within the excavator arm model are connected to translational actuator components, which output the position, speed, and acceleration of the actuator based on the input force. Essentially, these tags enable the integration of the hydraulic and mechanical-kinetic aspects of the model.

Within the arm model, it is also pertinent to discuss the soil submodel, located at the bottom of Figure 3.9. A macro depiction of the soil submodel is provided in Figure 3.10. The theoretical foundation of this soil submodel is defined by Edward McKyes in "Soil Cutting and Tillage" (1985) [13] and extended to excavator digging by Howard N. Cannon in "Extended Earthmoving with an Autonomous Excavator" (1999) [14] [15]. The three signal ports (1, 2, and 3) represent the X, Y, and inclination of the soil, respectively, while the fourth port is a standard 2D port representing the tip of the tool blade. By inputting the coordinates and angle inclination of the soil, the submodel can output the torque and force in the X and Y directions, using the position, velocity, and acceleration of the tool blade’s tip obtained from port 4.

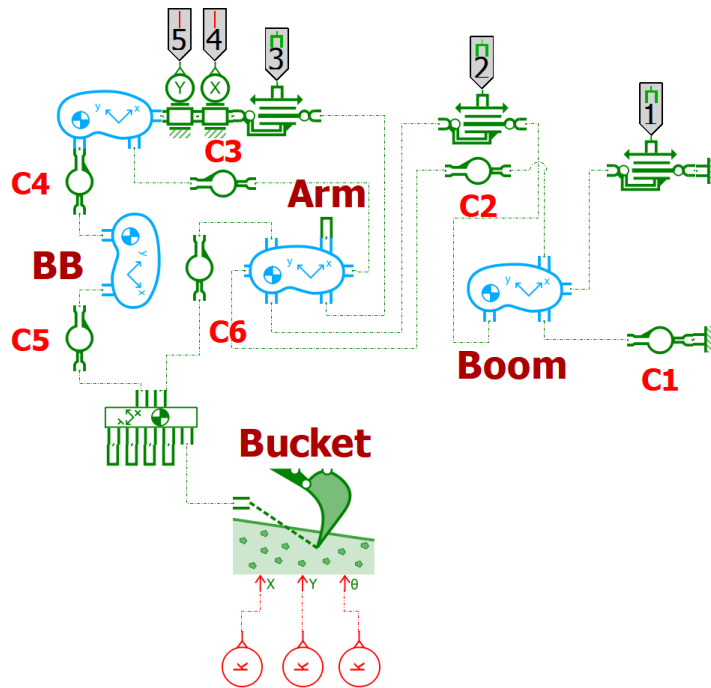


Figure 3.9: Excavator arm AMESim model

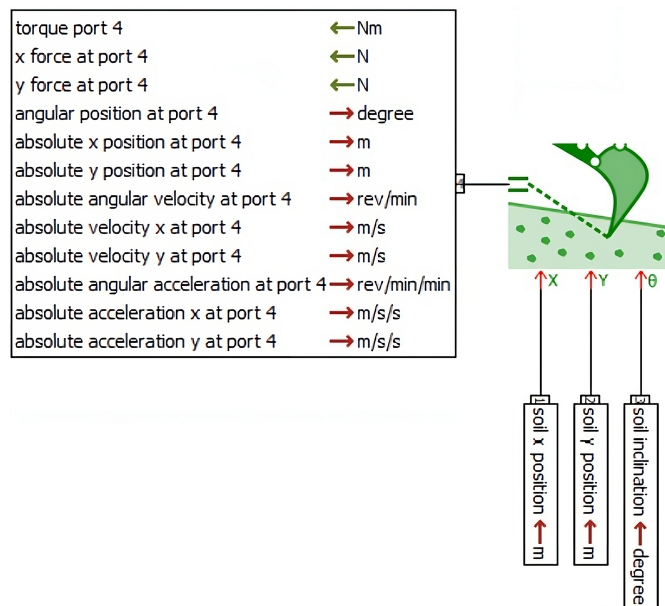


Figure 3.10: Soil submodel [15]

The excavator arm model also includes two additional tags, numbers 4 and 5, which provide the X and Y positions of the bucket element, respectively. These data are used to compute the variation of the moment of inertia. More details on this will be provided in Section 3.1.2.

Turret Hydraulic Motor

The turret rotation subsystem can be divided into hydraulic and mechanical components. The hydraulic circuit includes the hydraulic motor, parking brake lock and unlock valves, anti-cavitation valves, and a relief valve. The mechanical component includes a planetary gear system that links the hydraulic motor to the brake lock, transmitting power to the output shaft. Additionally, a torque multiplier connects the output shaft of the planetary gear system to the turret, enhancing torque with a gear ratio of 200.88. The entire excavator system is represented as an inertia block. The corresponding AMESim turret submodel is illustrated in Figure 3.11.

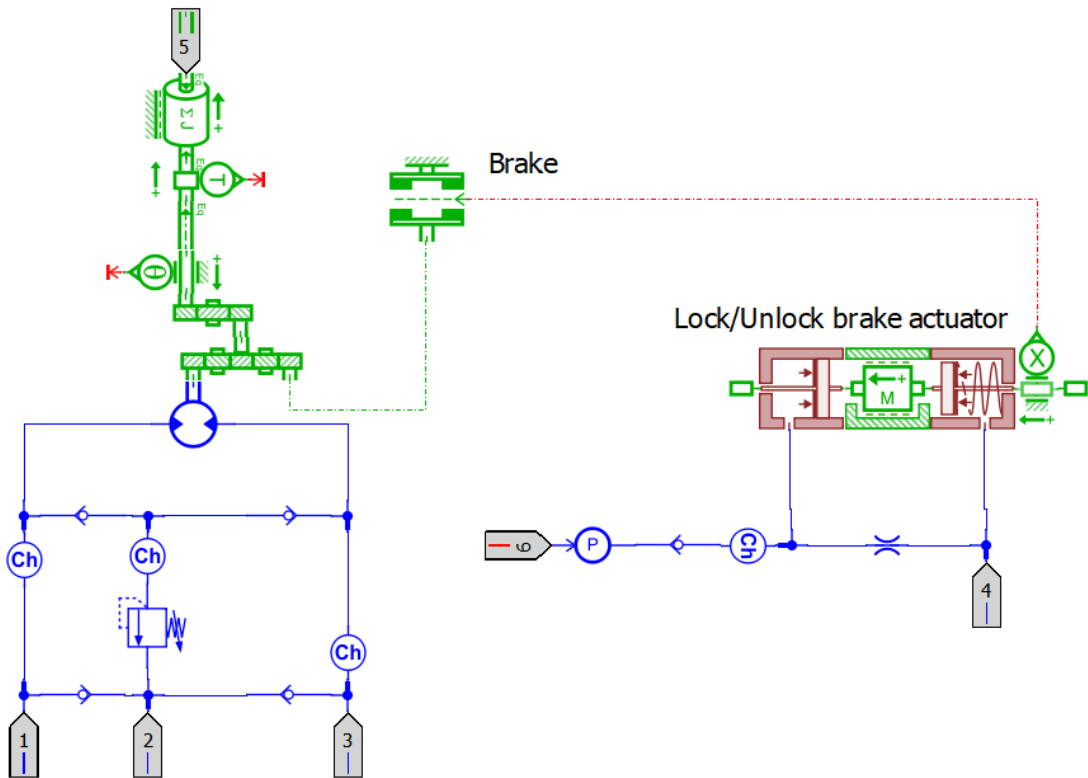


Figure 3.11: Turret AMESim submodel

The focus now shifts to the inertia block (Figure 3.12) and the calculation of

system acceleration and torque applied to the turret shaft. The inertia submodel computes the equivalent inertia by summing the inertias received at ports 1 and 2 with its own inertia.

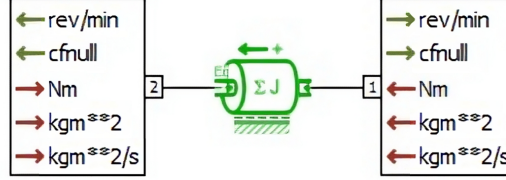


Figure 3.12: Inertia submodel for equivalent inertia computation

The system operates based on the following principle: the inertia block is initialized with the moment of inertia J of the entire excavator. The initial conditions for this moment of inertia J are set when the excavator's arm is fully extended, with all actuators retracted. As previously mentioned, the system calculates the equivalent inertia J_{eq} at the shaft by summing the inertia parameter J and the inertias received at ports 1 and 2 (J_1 and J_2).

$$J_{eq} = J_1 + J_2 + J \quad (3.1)$$

In this scenario, the parameter J is set to 15536 kgm^2 . The hydraulic machine and all mechanical elements connected to the shaft at port 1 are assumed to be ideal, meaning they have no mass, thus resulting in $J_1 = 0$. The inertia J_2 is a function of the excavator arm position. Since the value of the inertia J represents the maximum inertia of the excavator when the arm is fully extended, the values of J_2 are always less than zero as the arm is moved. Therefore, the equation for the equivalent inertia can be simplified to $J_{eq} = J + J_2$.

At this point, the rotary acceleration of the inertia is computed as follows:

$$accel = \frac{T_1 - T_2 - (\partial J_1 + \partial J_2) \times \omega_2}{J_{eq}} \quad (3.2)$$

In this equation:

- Torque T_1 is the output torque from the torque multiplier, originating from the hydraulic motor or the brake;
- Torque T_2 is the torque from the environment, which is generally 0. This is because when the turret rotation is operated by the swing motor or arrested by the brake, it encounters no obstacles during rotation. Therefore, there is no external force from the environment that could generate an opposing torque;

- The derivative of the hydraulic motor and brake's moment of inertia ∂J_1 is assumed to be 0, as these are considered ideal components with no mass;
- The derivative of the excavator's moment of inertia ∂J_2 is the torque that the motor or brake must counteract. This is calculated by interpolating the bucket's position (X and Y coordinates) obtained from the excavator arm submodel with a lookup table containing data derived from real excavator measurements.

Viscous friction or Coulomb friction can also be applied to the equivalent inertia submodel. In this case, a viscous friction coefficient of 340 Nm/rpm is imposed.

The rotary velocities ω_1 and ω_2 that are output at the ports are deduced from the acceleration:

$$\omega_2 = -\omega_1 = \int accel dt \quad (3.3)$$

3.2 Common Pressure Rail-Based Excavator Model Layout

The following section provides an analysis and description of the excavator model developed in the AMESim simulation environment, based on the Common Pressure Rail architecture (see Figure 3.13). As previously mentioned, the starting point for the hydraulic circuit design was the simplified model of the 9-ton Komatsu PC75R excavator. Specifically, the hydraulic circuit was modified by removing the tracks used for traction (see Figure 3.3), as vehicle movement was not required for the standard cycles chosen for the energy analysis. The excavator's characteristics, such as mass, actuators, and hydraulic motor for swing rotation, remained unchanged. The main modification was made to the power supply system for the various actuators.

3.2.1 Engine Subsystem

As with the excavator model based on the Load Sensing architecture, the internal combustion engine was replaced with an ideal prime mover to simplify the analysis process and focus on the hydraulic system. To obtain data on fuel consumption, a look-up table was implemented in the AMESim model. By providing the engine torque and engine speed as inputs, the table outputs the fuel flow rate through interpolation.

The data in the look-up table were extracted from experimental data on a 6-cylinder turbocharged diesel engine with a displacement of 2.9 liters. This engine has a maximum speed of 2900 rpm and a maximum power output of 55 kW. The

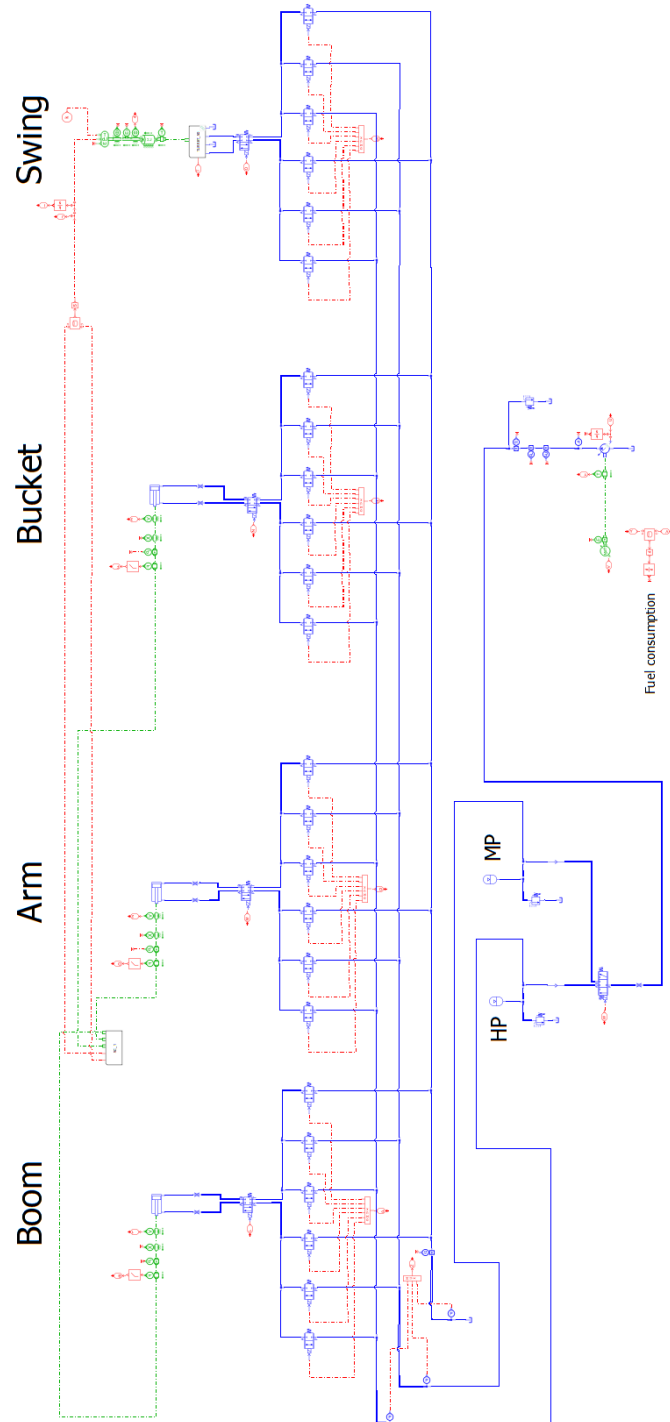


Figure 3.13: Common Pressure Rail AMESim model

engine map, containing the maximum torque for each rotational speed and the iso-efficiency curves, is shown in Figure 3.14.

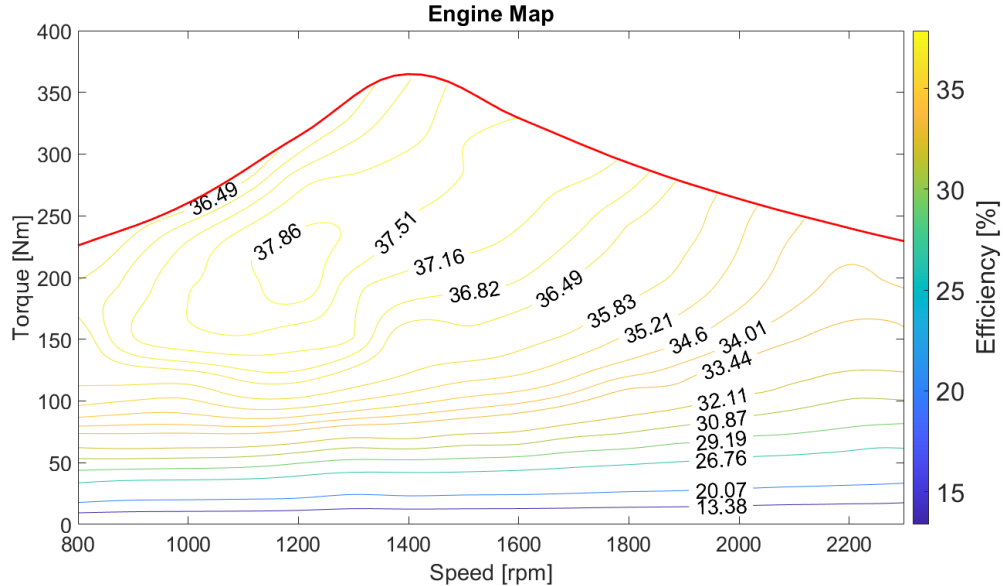


Figure 3.14: 55 kW, 2.9 L 6-cylinder diesel ICE Map

The decision to use a look-up table for obtaining fuel consumption data (see Figure 3.15), instead of utilizing the ICE model available in the AMESim library (see Figure 3.16), was made to reduce simulation times and improve result accuracy. The ICE model had issues with accurately calculating fuel consumption, especially at zero torque, where it failed to provide reliable data due to limitations in the model's algorithms.

The data included in the look-up table are presented in both 2D and 3D formats in Figure 3.17 and Figure 3.18, respectively.

3.2.2 Hydraulic Subsystems - Flow Generation Unit

This section offers comprehensive details regarding the subsystems of the hydraulic circuit, namely the flow generation unit consisting of a variable displacement pump, the energy storage unit comprising two accumulators, and the on-off and proportional valves facilitating access of the actuators' chambers to the various rails.

For which concern the flow generation unit, a variable displacement pump of 75 cc/rev was chosen (see Figure 3.19). This decision was made for several reasons: primarily, to meet the flow demand of actuators in the dig and dump standard operational cycle, where the pump needed to ensure the required average flow.

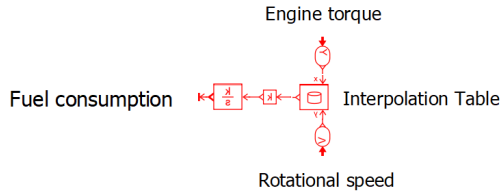


Figure 3.15: Implementation of ICE using look-up table

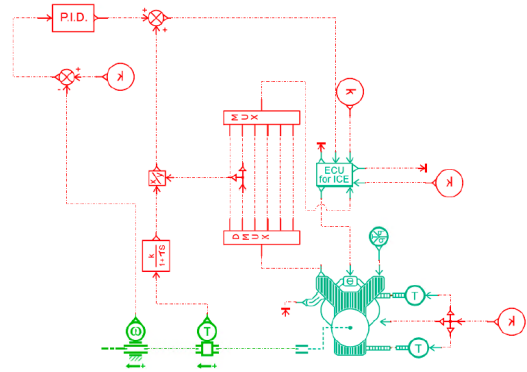


Figure 3.16: Implementation of ICE using AMESim submodel

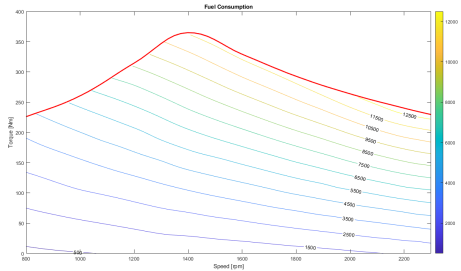


Figure 3.17: 2D Fuel Consumption Map

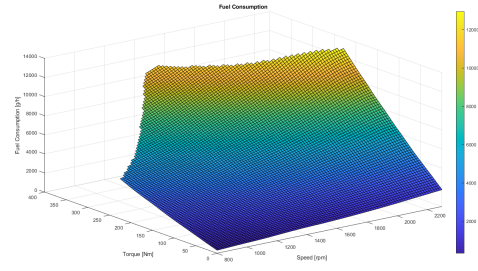


Figure 3.18: 3D Fuel Consumption Map

Furthermore, to optimize the thermal engine’s performance in terms of fuel consumption, the downspeeding strategy was implemented, involving reducing the engine’s rotational speed and maximizing applied torque. Therefore, setting the thermal engine’s rotational speed to approximately 1200 rpm, the choice of the 75 cc/rev pump size enabled meeting the average flow requirement of the actuators.

Another reason for selecting this pump pertains to the operating points of the thermal engine relative to the pump itself. With rail pressures set at 175 bar for high pressure and 85 bar for medium pressure, the 75 cc/rev pump was chosen to operate within the thermal engine’s peak efficiency zone during the high-pressure charging phase, which represents the most energy-intensive stage. During this phase, the pump generates a shaft torque of about 220 Nm. Given the downspeeding strategy and the 1200 rpm rotational speed, these torque values allowed operating within the thermal engine’s efficiency zone at approximately 38%.

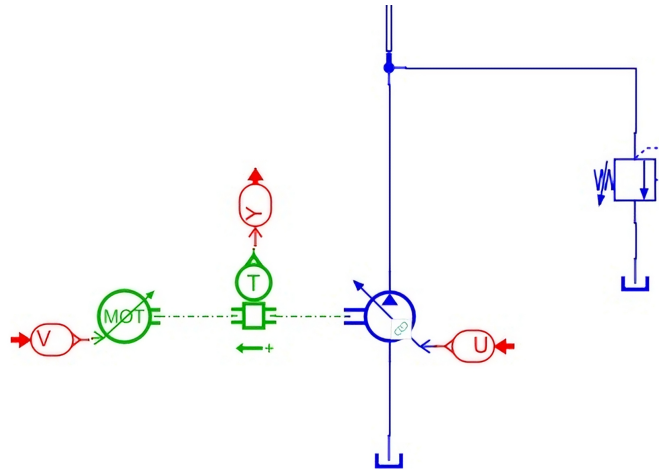


Figure 3.19: Flow generation unit AMESim model implementation

Lastly, the decision was also influenced by the availability of hydraulic-mechanical and volumetric efficiency data (see Figure 3.20 and 3.21 respectively) related to a 75 cc/rev variable displacement pump, similar to the one used in the Load Sensing system for linear actuator supply (see Figure 3.6 and 3.7). It is noteworthy that, unlike the Load Sensing system where the 75 cc/rev pump only supplied actuators in commercial vehicles, while the swing hydraulic motor was powered by another pump, in the Common Pressure Rail system, the flow generation unit only needs to ensure the average flows required by the utilities. Consequently, with a single 75 cc/rev pump, it was possible to meet the demands of both linear actuators and the turret hydraulic motor.

Regarding the decision on how to operate the pump, considering previous discussions and aiming to maximize its efficiency, the choice was made to always run the pump at maximum displacement (ensuring the engine operates at maximum torque and minimum speed), thus allowing for the use of a fixed displacement pump as well. The adoption of variable displacement is a feature that was later integrated into the Common Pressure Rail architecture plus Electronic Flow Matching. Further details on this topic will be provided in the related section.

In conclusion, as depicted in Figure 3.19, a relief valve set to 350 bar has been implemented for safety reasons.

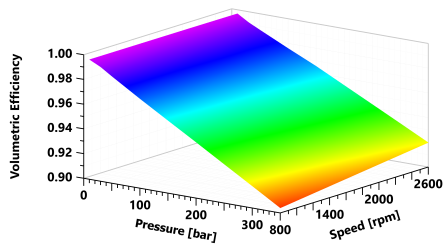


Figure 3.20: Volumetric efficiency of the 75 cc/rev variable displacement pump

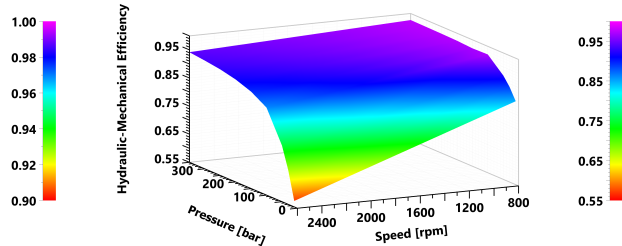


Figure 3.21: Hydraulic - mechanical efficiency of the 75 cc/rev variable displacement pump

3.2.3 Hydraulic Subsystems - Energy Storage Units and Pressure Levels

Let's now delve into the explanation of energy storage units and the process involved in determining pressure levels for medium and high-pressure lines.

Decision-Making Process for Pressure Levels

A crucial initial consideration in pressure level selection is determining the maximum system pressure required to fulfill operational tasks. Current machine standards indicate typical peak pressures range between 350 to 380 bar. Initial tests of the LS system for the dig and dump cycle consistently showed system pressures below 200 bar, with occasional peaks during swing drive acceleration. Pressures exceeding 200 bar occurred only when actuators reached their end-stroke and remained there. Figure 3.22 depicts the pressure profile observed during the dig and dump cycle of the Load Sensing system.

Excluding instances where actuators hit end-stops (causing sharp pressure spikes) from Figure 3.22, the maximum pressure peak required by actuators during the dig and dump cycle was approximately 170 bar. Therefore, setting the maximum pressure of the high-pressure (HP) rail at 175 bar ensures a safety margin.

The selection of medium pressure (MP) followed a different rationale. With the high-pressure value determined and the low-pressure (LP) line set at tank pressure, the medium-pressure value was chosen to achieve a linear distribution of forces generated by the actuators across the possible combinations of pressures that could be connected to the two chambers. Figure 3.23 illustrates the ideal force distribution based on pressure combinations, while Table 3.1 details pressure assignments for each combination index.

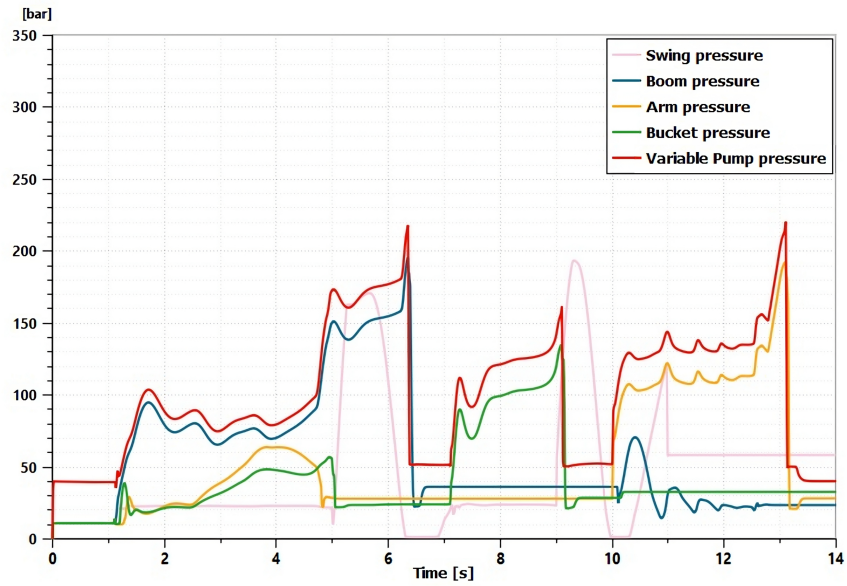


Figure 3.22: Pressure levels of actuators in the Load Sensing system during the Dig and Dump cycle

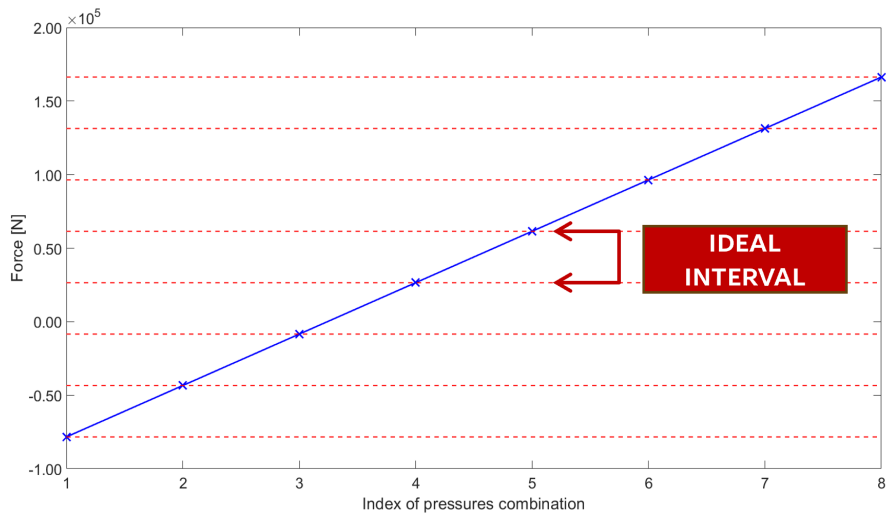


Figure 3.23: Ideal distribution of forces generated by actuators function of the pressure combination

To achieve uniform force distribution and maintain consistent ΔF intervals across pressure combinations, thereby minimizing proportional valve losses downstream of on-off valves, an optimal MP of 85 bar was chosen. This design focus primarily on the boom actuator, which exhibits the highest force requirements and flow rates

Combination Index	Small Chamber	Big Chamber
1	HP	LP
2	MP	LP
3	HP	MP
4	MP	MP
5	LP	MP
6	HP	HP
7	MP	HP
8	LP	HP

Table 3.1: Index of pressure combination

among the three actuators, ensures optimal force distribution as depicted in Figures 3.24, 3.25, and 3.26.

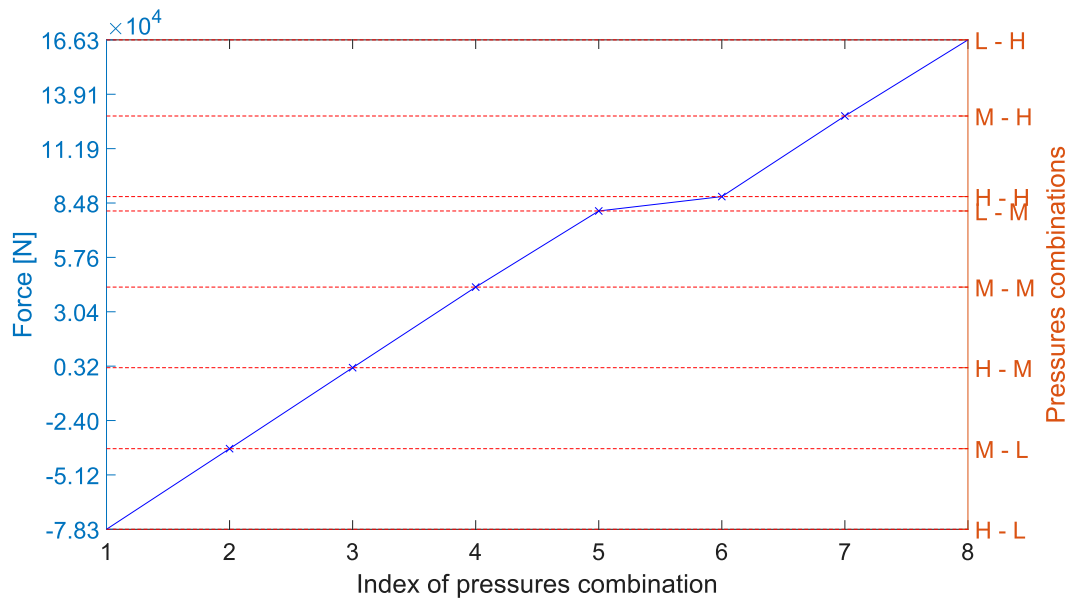


Figure 3.24: Forces generated by the actuator as a function of the chamber pressure combinations - Boom

Accumulator Design

When designing accumulators, two critical variables must be defined: the volume of the accumulators (V_0) and the pre-charge pressure (p_0). These parameters

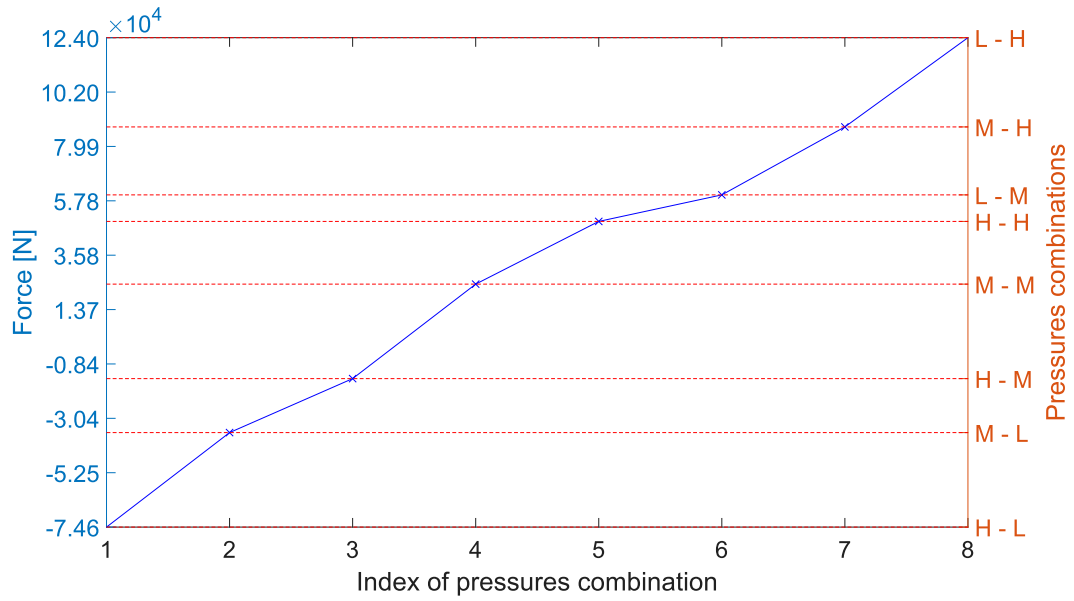


Figure 3.25: Forces generated by the actuator as a function of the chamber pressure combinations - Arm

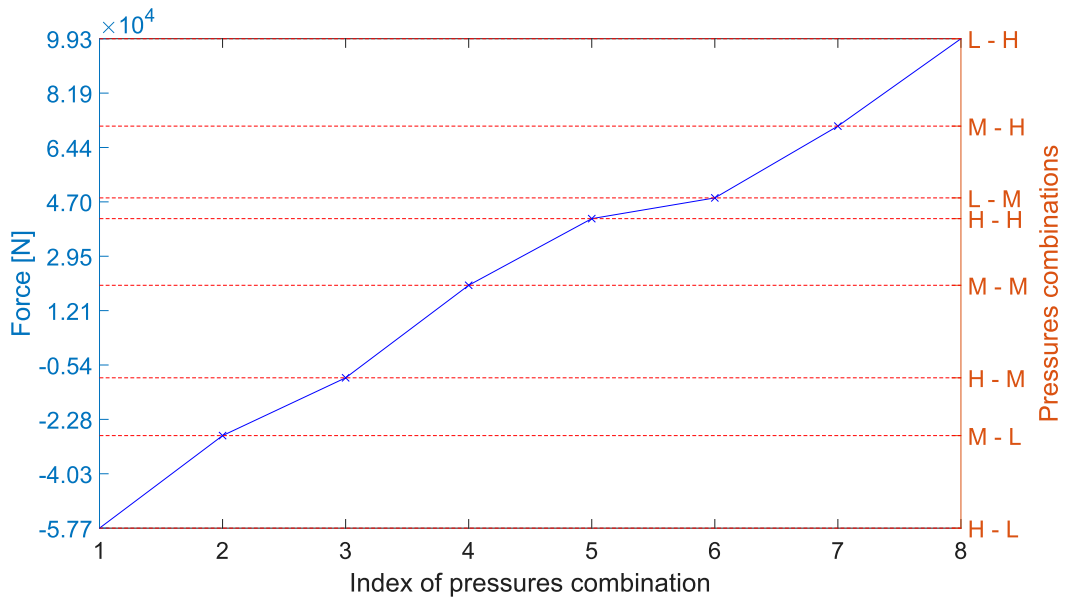


Figure 3.26: Forces generated by the actuator as a function of the chamber pressure combinations - Bucket

determine the stiffness of the bladder and the pressure variations as oil is released.

Figure 3.27 illustrates the implementation of accumulators in the AMESim Common Pressure Rail model. Figures 3.28 and 3.29 present the parameter setting screens in AMESim for high pressure and medium pressure accumulators, respectively. Referring to these figures, the third setting pertains to the thermal law used for the transformation, where the default adiabatic transformation was chosen with a polytropic index set to 1.4.

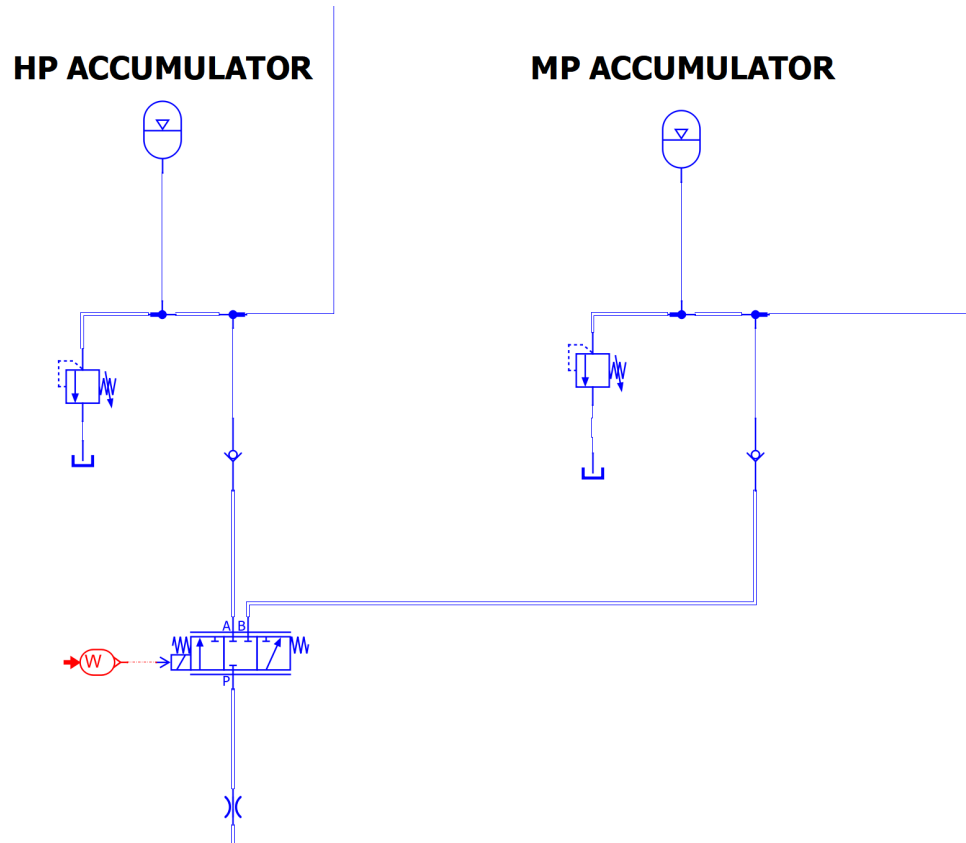
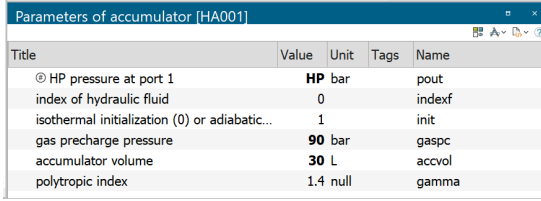


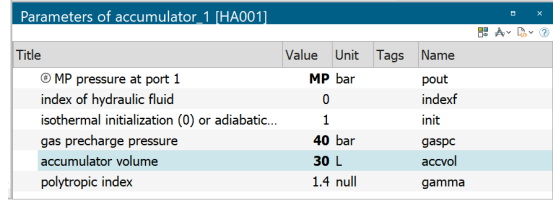
Figure 3.27: Medium and high pressure accumulators AMESim model implementation

Next, our focus shifts to the volume (V_0) and pre-charge pressure (p_0) of the accumulators. These parameters have been carefully selected to ensure adequate stiffness in the accumulators, which is crucial for maintaining stability within the controller and the overall system. By maintaining a consistent rail pressure, the behavior of the accumulators approaches that of ideal pressure sources. This, in turn, reduces the frequency of adjustments required by the controller, allowing it to concentrate on adapting pressure combinations for actuators based on external variables such as environmental conditions and the excavator system's interaction



Title	Value	Unit	Tags	Name
⊙ HP pressure at port 1	90	bar		pout
index of hydraulic fluid	0			indexf
isothermal initialization (0) or adiabatic...	1			init
gas precharge pressure	90	bar		gasp
accumulator volume	30	L		accvol
polytropic index	1.4	null		gamma

Figure 3.28: High pressure accumulator parameter setting screen in AMESim



Title	Value	Unit	Tags	Name
⊙ MP pressure at port 1	40	bar		pout
index of hydraulic fluid	0			indexf
isothermal initialization (0) or adiabatic...	1			init
gas precharge pressure	40	bar		gasp
accumulator volume	30	L		accvol
polytropic index	1.4	null		gamma

Figure 3.29: High pressure accumulator parameter setting screen in AMESim

with its surroundings. Consequently, this approach minimizes the need for adjustments due to internal system changes and simplifies the decision of which rail to connect the actuator chambers to at each moment in time (∂t).

The dig and dump work cycle served as a consistent reference throughout the iterative process of defining these variables. The chosen values of (V_0) and (p_0) for the accumulators are detailed in Table 3.2, which strike an optimal balance between stabilizing the system and minimizing the footprint of the accumulators on a 9-ton excavator.

Accumulator	Nominal volume [L]	Pre-charge pressure [bar]
High Pressure	30	90
Medium Pressure	30	40

Table 3.2: Parameters for medium and high pressure accumulator settings

3.3 Duty Cycles

Hydraulic excavators are versatile machines utilized for a wide range of tasks extending well beyond simple excavation and earthmoving. Consequently, engineers are confronted with the intricate challenge of designing these machines without precise knowledge of their future applications [3].

Field testing of excavators is widely recognized as the most comprehensive way to assess operational performance in real-world scenarios. However, due to the increasing pressure to shorten time-to-market, engineers have turned to software simulations as a leading method. These simulations enable rapid and reliable predictions of performance outcomes [16].

Regarding simulation analysis, numerous standardized tests have gained widespread acceptance for testing and validating the performance of excavator models. Examples of these standardized tests include the dig and dump test and the air grading test. Utilizing standardized tests for model evaluation offers several advantages, like comparability of results across different models, the reliability and consistency of the results obtained, and the reproducibility of the test conditions. Additionally, standardized tests ensure impartiality in the assessment of performance.

Typically, the duty cycle of an excavator refers to the sequence of operations it performs during a work cycle. This cycle includes phases such as digging, swinging, dumping, and returning to the dig site. Each phase within this duty cycle involves distinct mechanical and hydraulic actions, which collectively contribute to the overall efficiency and productivity of the excavator.

In the following sections, a detailed analysis will be conducted on the movements of actuators and the hydraulic swing motor that characterize each standardized test utilized for the evaluation of excavator model performance.

3.3.1 Dig and Dump

The standard process of dig and dump forms the core operational procedure for extracting materials from a site. Here is an outline of its steps, based on the case study used to evaluate the excavator model:

1. Approach to the site (see Figure 3.30): the excavator approaches the excavation point with its arm fully extended and actuators retracted.
2. Penetration and Lifting (see Figure 3.31): using its bucket, the excavator's arm penetrates into the material to be excavated; after gripping the material, the arm raises the bucket, combining arm extension and bucket lifting to secure the collected material.
3. Rotation and Dumping (see Figure 3.32): in this specific instance, the arm and bucket rotate 120° to position the material over the discharge point, ensuring precise direction to the desired location; once properly positioned, the material is discharged into the designated destination, such as a truck, by tilting the bucket to allow the material to flow freely out.
4. Return to starting point (see Figure 3.33): the excavator returns to the starting point to prepare for the next digging cycle. The arm fully extends, and the bucket returns to the initial position, ready for the next load.

This cycle may vary slightly in different literature depending on the excavator's specifications and site conditions but represents the general process for material handling during excavation operations.

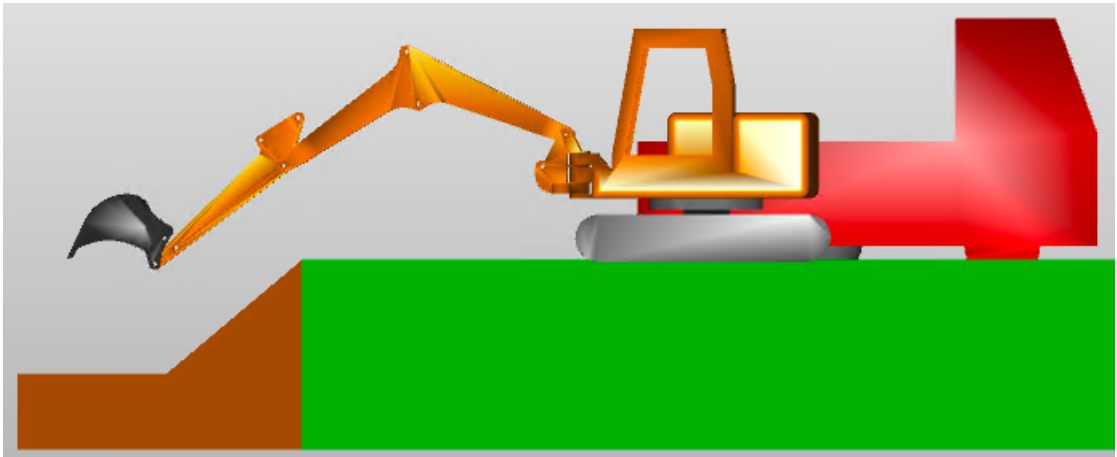


Figure 3.30: Commencing the first phase of dig and dump: approaching the site for excavation and dumping

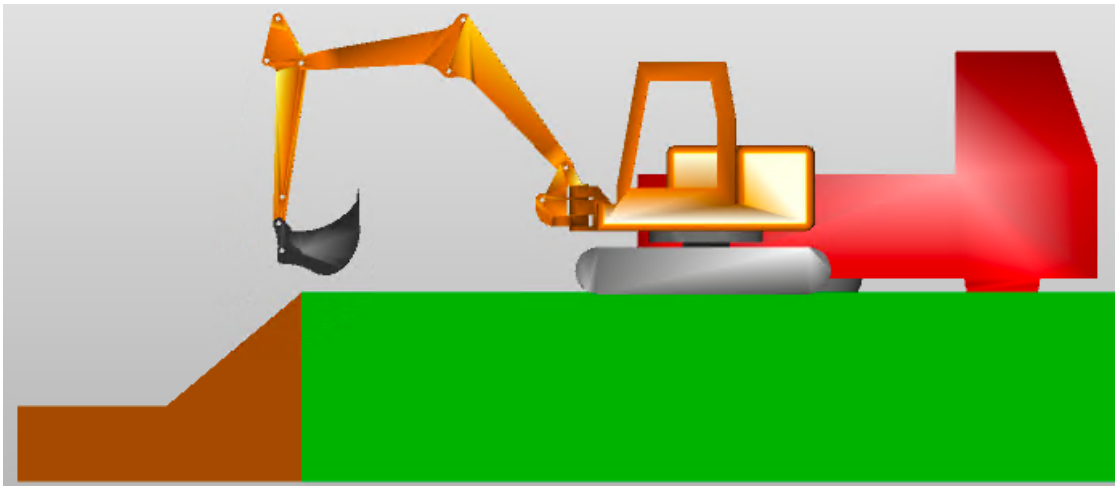


Figure 3.31: Executing the second phase of the dig and dump process: penetrating and lifting

For completeness, the reference velocities and displacements of each actuator during all phases of the cycle are also provided. Specifically, Figure 3.34 and Figure 3.35 show the velocity and displacement profiles of the boom actuator, respectively. Figures 3.36 and 3.37 display the velocity and displacement profiles of the arm actuator. Figure 3.38 and Figure 3.39 present the velocity and displacement profiles of the bucket actuator. Finally, Figure 3.40 and Figure 3.41 illustrate the velocity and displacement profiles of the turret motor.

It is important to note that the velocity profiles represent signals proportional to

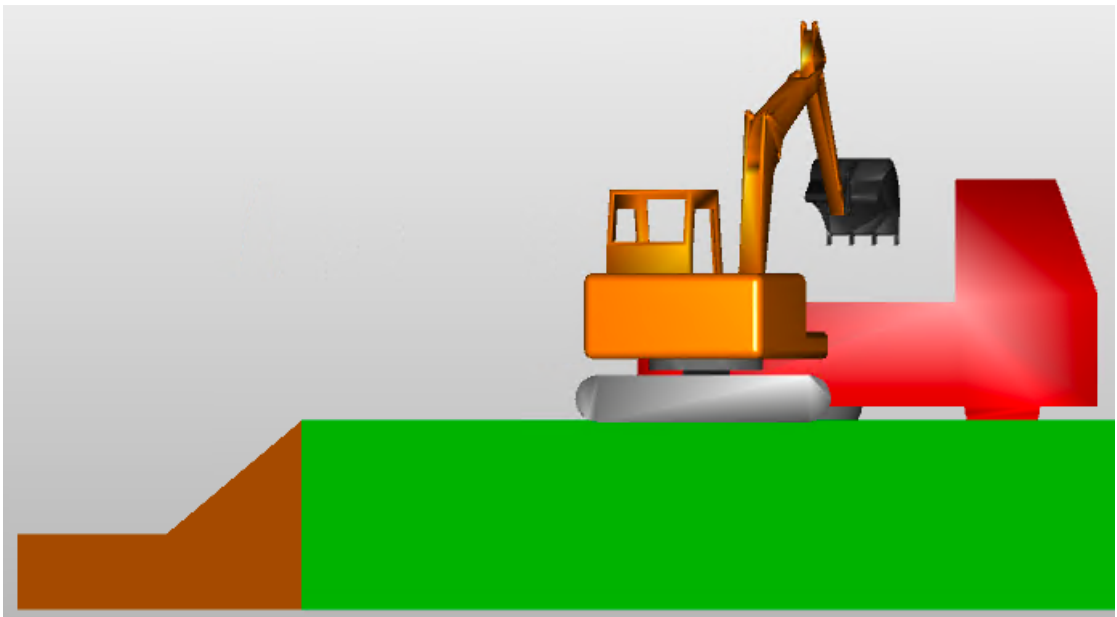


Figure 3.32: Transitioning into the third phase of the dig and dump cycle: rotation and dumping

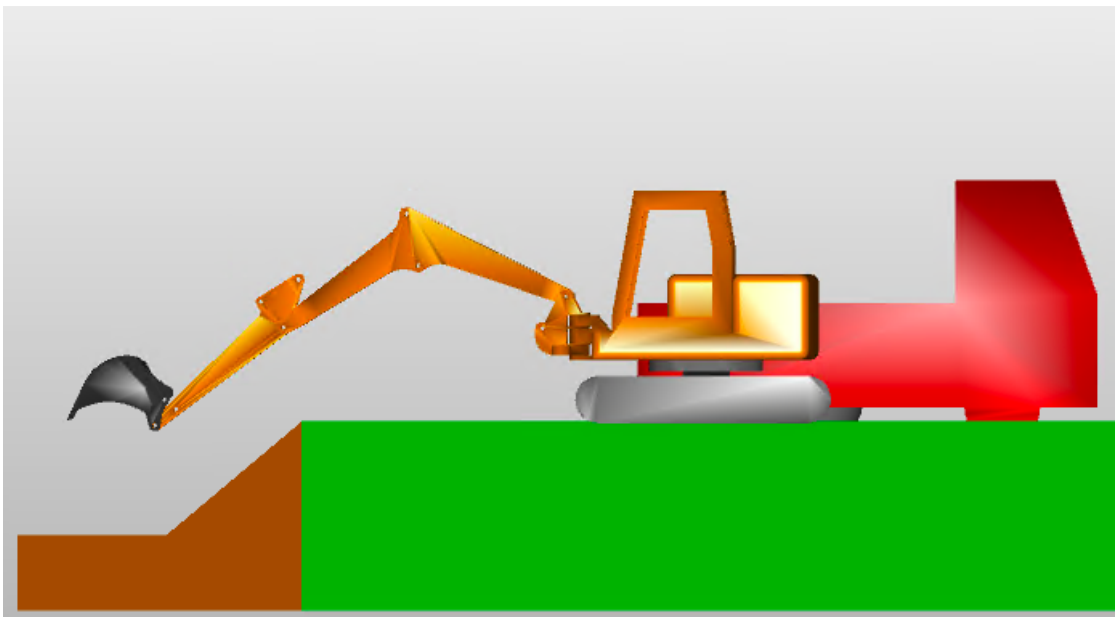


Figure 3.33: Concluding the dig and dump process: returning to the starting point

the joystick commands located in the excavator's cabin. These will be, as elaborated in subsequent sections, a fundamental input to the various control systems of the excavator model based on the Common Pressure Rail architecture.

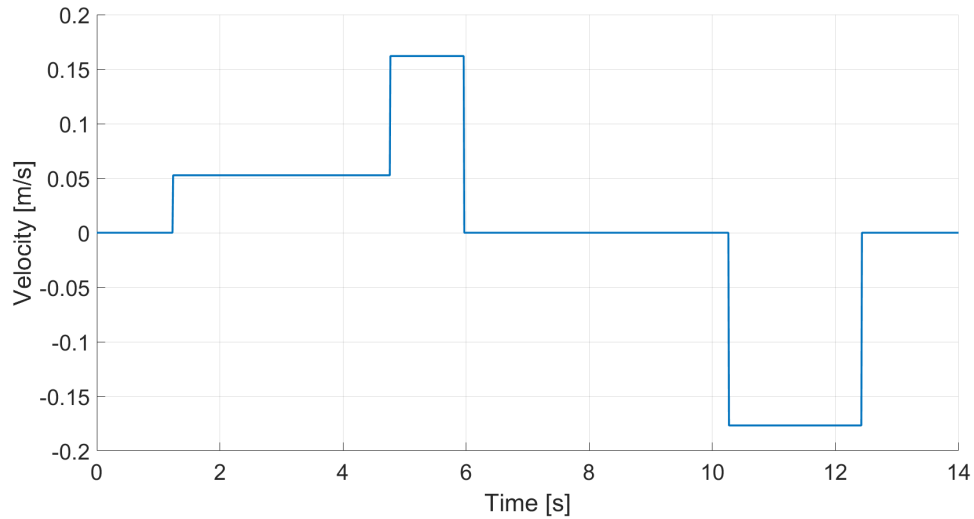


Figure 3.34: Boom actuator velocity profile during dig and dump cycle

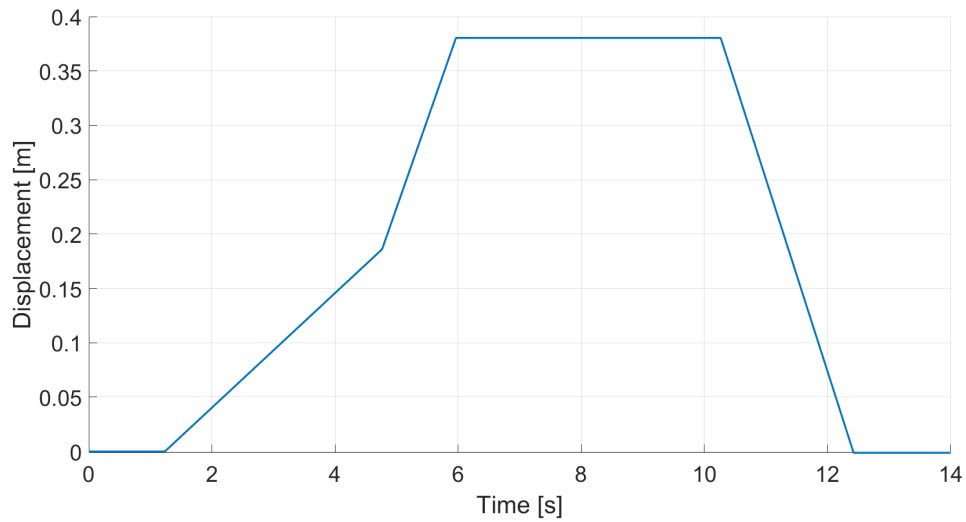


Figure 3.35: Boom actuator displacement profile during dig and dump cycle

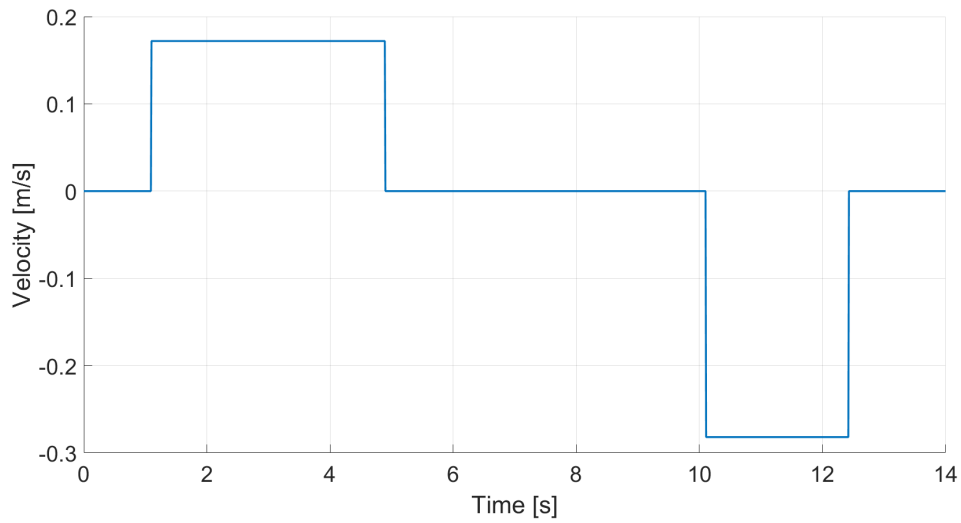


Figure 3.36: Arm actuator velocity profile during dig and dump cycle

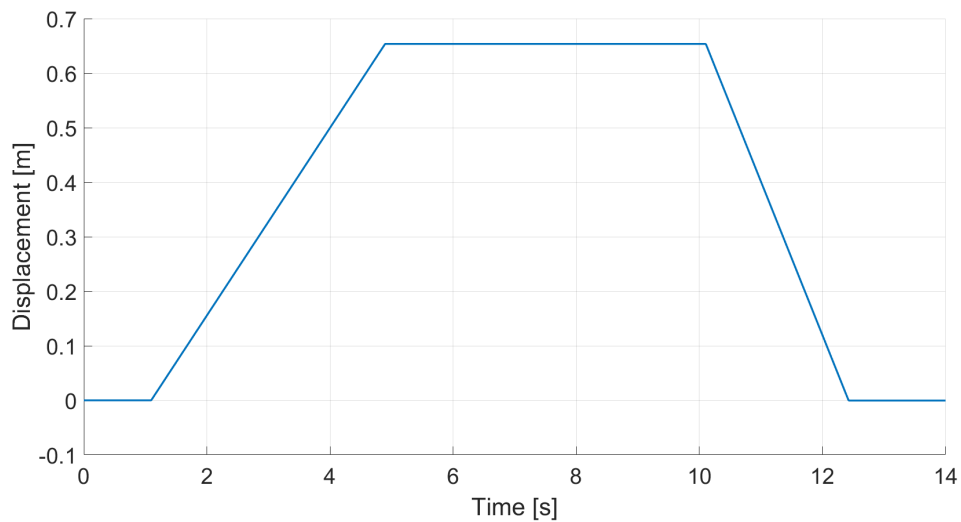


Figure 3.37: Arm actuator displacement profile during dig and dump cycle

3.3.2 Air Grading

The air grading or soil leveling standard cycle typically involves several key steps to achieve effective leveling of the ground. Here is an outline of its steps, based on the case study used to evaluate the excavator model:

1. Approach to the site (see Figure 3.42): the excavator approaches the site with its arm fully extended and actuators retracted. This positioning allows the

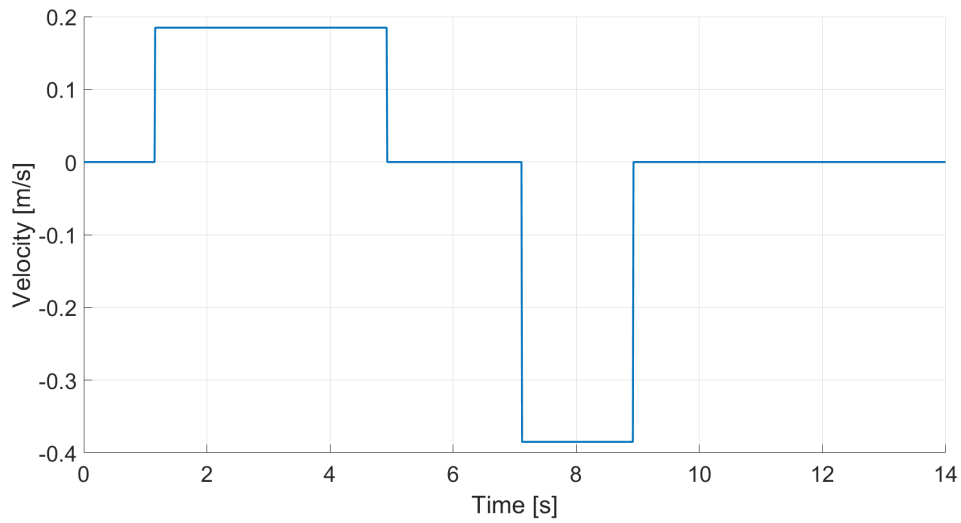


Figure 3.38: Bucket actuator velocity profile during dig and dump cycle

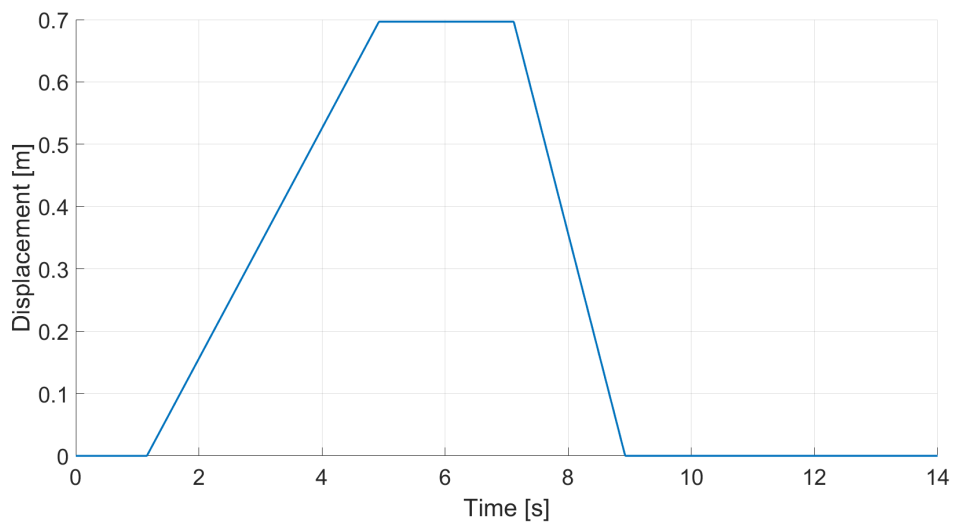


Figure 3.39: Bucket actuator displacement profile during dig and dump cycle

excavator to reach the work area efficiently.

2. Cutting and filling (see Figure 3.43): the excavator retracts its arm while using the bucket to cut into higher areas of soil and fill in lower areas. Throughout this process, the arm and boom actuators are adjusted to maintain a constant bucket height relative to the ground, ensuring effective leveling.
3. Finishing pass (see Figure 3.44): after leveling the area, the excavator extends

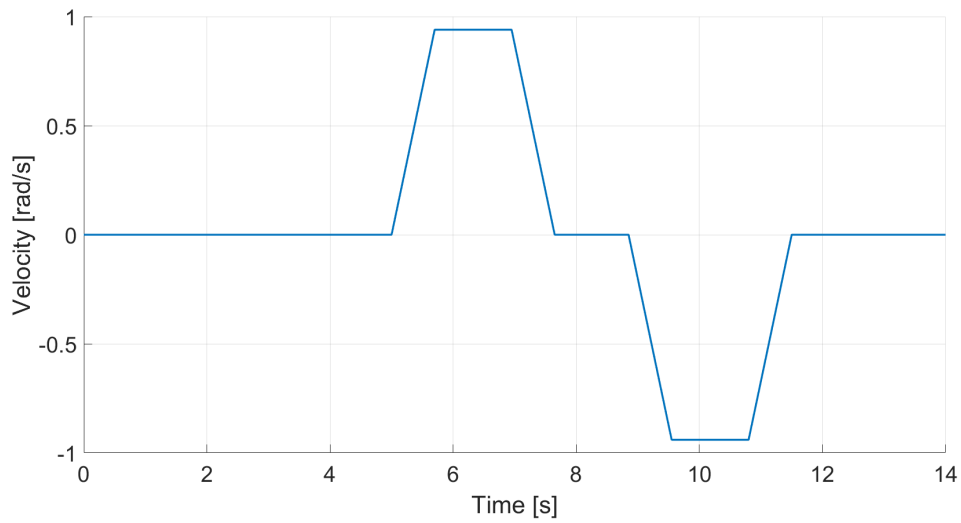


Figure 3.40: Turret motor velocity profile during dig and dump cycle

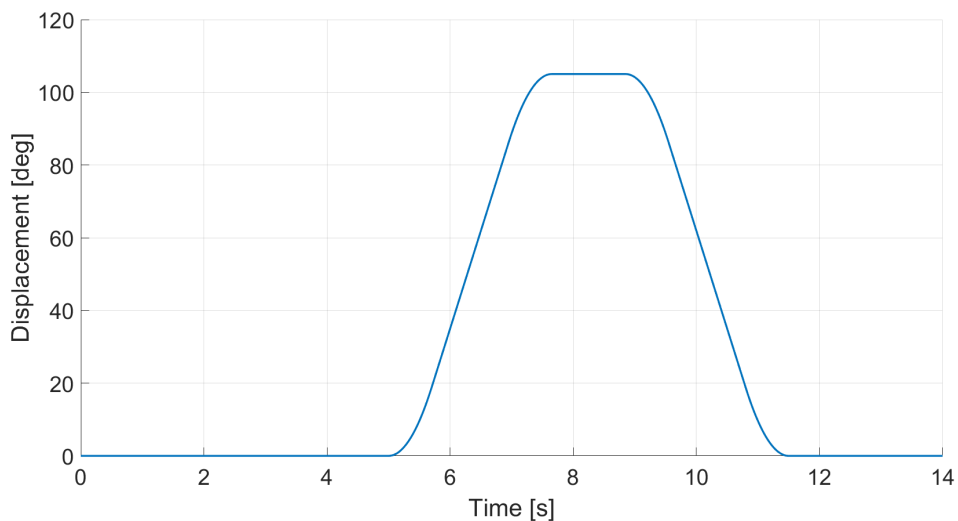


Figure 3.41: Turret motor displacement profile during dig and dump cycle

its arm to return the bucket to its original position. Similar to the cutting and filling phase, the arm's actuators are adjusted to keep the bucket height consistent as it moves away from the excavator cabin, ensuring a smooth and uniform finish to the leveled soil.

Each step in the air grading cycle is critical to achieving a well-prepared and even surface suitable for further construction or landscaping activities. The efficiency

and precision of the cycle depend heavily on the operator's skill and the capabilities of the excavator and its attachments.

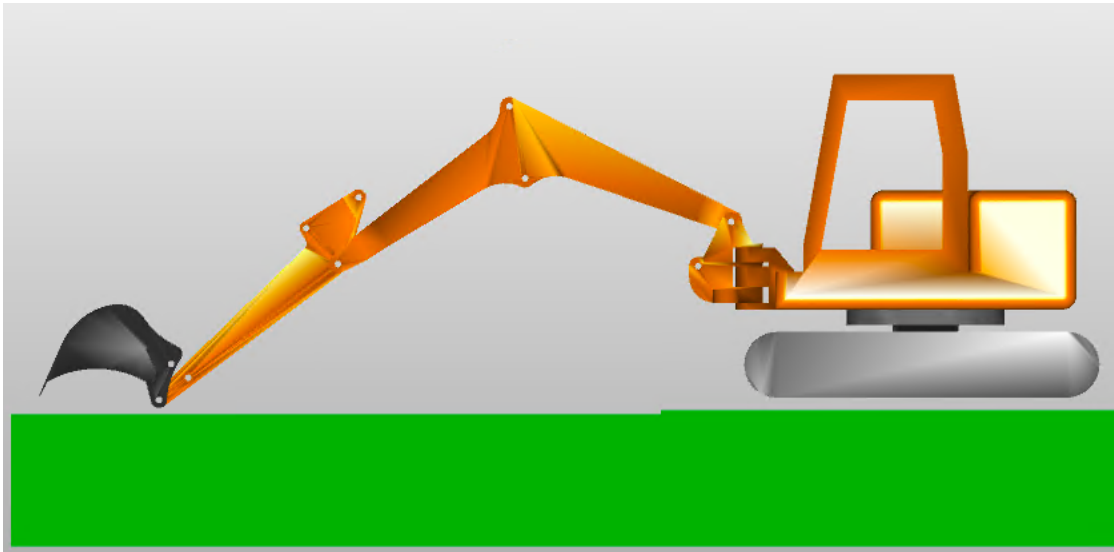


Figure 3.42: Commencing the first phase of air grading: approaching the site

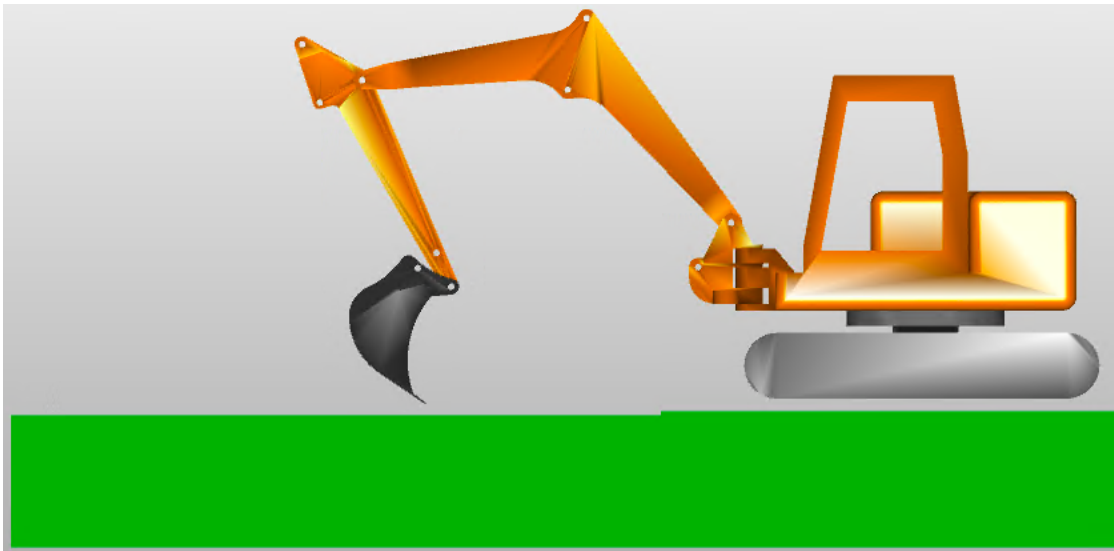


Figure 3.43: Executing the second phase of the air grading process: cutting and filling

Also for this cycle, for completeness, the reference velocities and displacements of each actuator during all phases of the cycle are also provided. Specifically, Figure

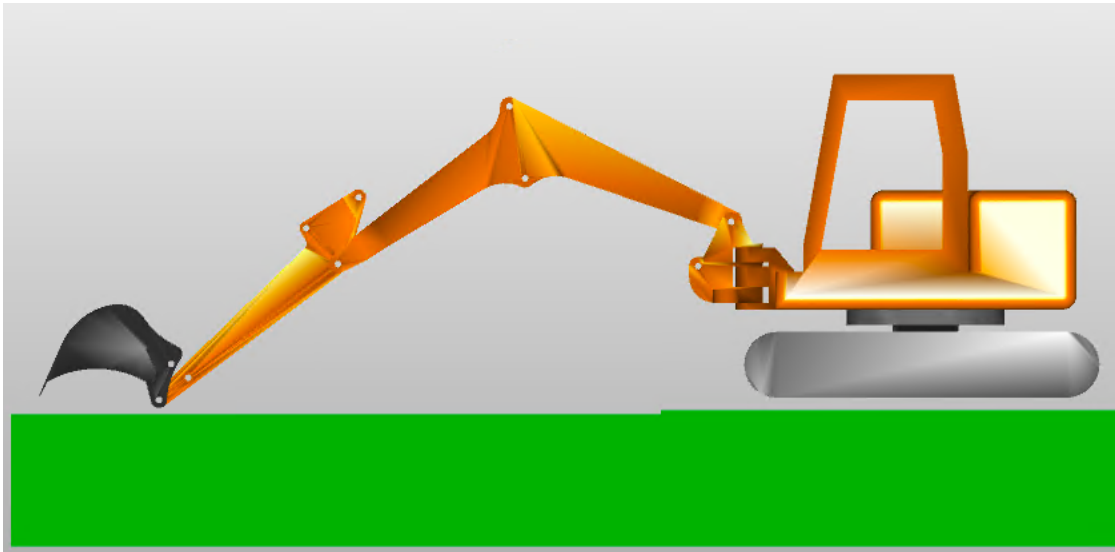


Figure 3.44: Concluding the air grading process: finishing pass

3.45 and Figure 3.46 show the velocity and displacement profiles of the boom actuator, respectively. Figures 3.47 and 3.48 display the velocity and displacement profiles of the arm actuator.

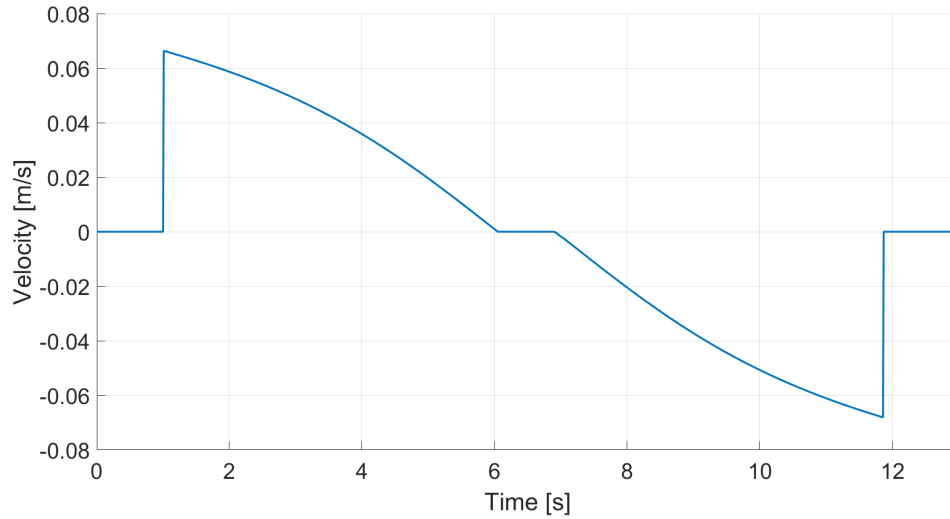


Figure 3.45: Boom actuator velocity profile during air grading cycle

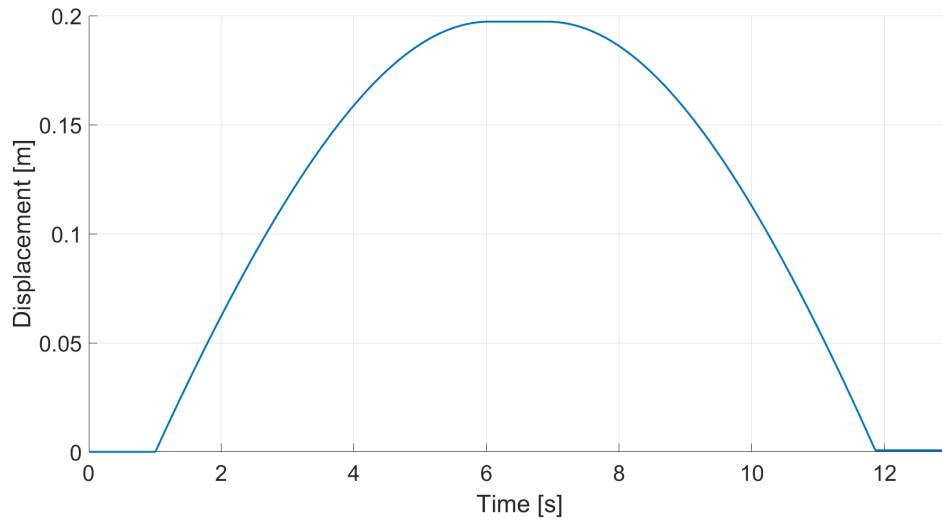


Figure 3.46: Boom actuator displacement profile during air grading cycle

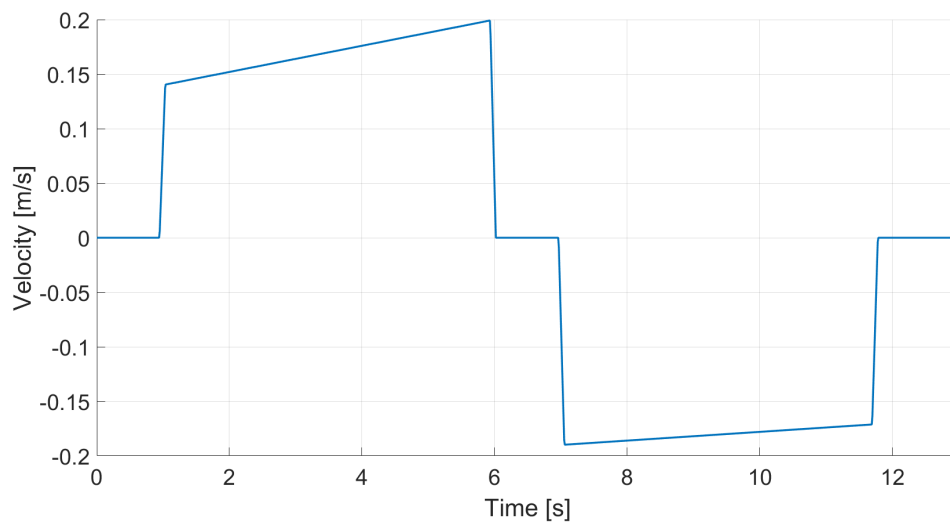


Figure 3.47: Arm actuator velocity profile during air grading cycle

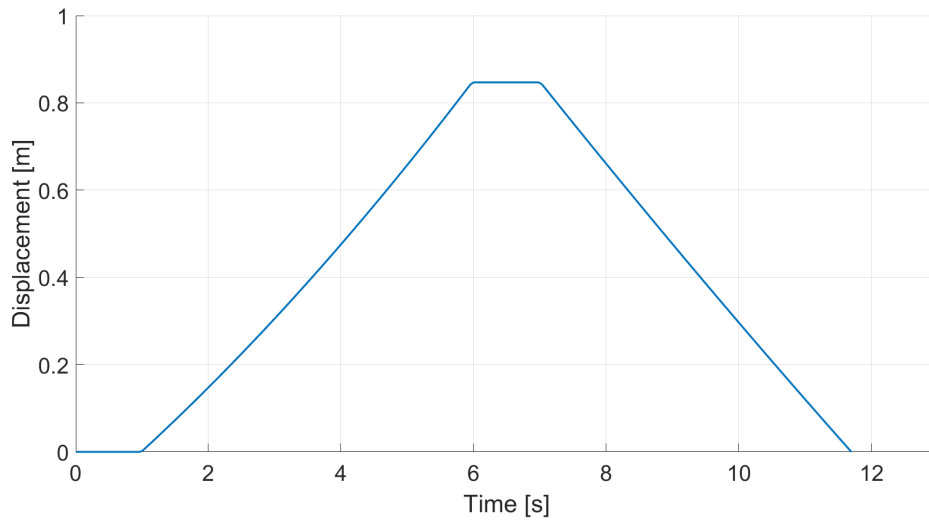


Figure 3.48: Arm actuator displacement profile during air grading cycle

Chapter 4

Development of Control Logic for Common Pressure Rail Architecture

This chapter focuses on the development of control logic for the Common Pressure Rail architecture. The primary objective is to enhance the performance and efficiency of hydraulic systems by implementing advanced control strategies. The discussion begins with an explanation of the significance of low-pass filters for sensor signals, emphasizing their role in noise reduction and signal integrity. A detailed analysis of force sensor signals within the AMESim model will be presented, along with the design considerations and implementation of the low-pass filters employed.

Subsequently, the chapter will delve into the algorithms developed and implemented in the Simulink environment for the control of the CPR architecture. These algorithms are critical for the precise management of the on-off valves of each actuator and the hydraulic motor. The control logic enables the actuators and the hydraulic motor chambers to access various pressure lines, thereby optimizing their performance. Furthermore, the chapter will cover the proportional valve control to ensure that the operator's requirements for actuator speed, as well as the force and torque demands generated by the system's interaction with the environment, are simultaneously met.

4.1 Actuator Force Signals - Power Spectral Density, Frequency Spectrum Analysis and Low-Pass Filter Design

As discussed in previous chapters, the starting point for developing the excavator model based on the Common Pressure Rail architecture was the Load Sensing excavator model, which is detailed in Section 3.1. An essential initial step in the development of the architecture was the analysis of the excavator model's interaction with its environment. This required extracting the forces generated during the interaction between the Load Sensing excavator model and the environment throughout the reference dig and dump cycle described in Section 3.3.1.

4.1.1 Characteristics of Actuator Forces in the Load Sensing Model

The information about physical environment could be translated by sensors into variations of electrical quantities, known as analog signals [17]. These signals, particularly those related to forces resulting from the interaction of actuators with the environment, are crucial inputs for the controller operating within the CPR architecture. They enable the controller to make informed decisions regarding the optimal pressures to apply to the actuator chambers.

An analog signal typically comprises dominant low-frequency components containing actionable information, alongside higher-frequency noise. Techniques such as power spectral density (PSD) and frequency spectrum analysis (FSA) are essential for precisely analyzing the frequency spectrum that encompasses these components. By utilizing the insights gained from PSD and FSA analyses, several low-pass filters have been designed and implemented to effectively attenuate high-frequency noise. This ensured a precise representation of the excavator's interaction dynamics with its environment, free from distortions.

Lets dig more in detail about the sensors implementation. They have been positioned at the actuators' outputs (see Figure 4.1) before the connection with the arm's mechanical model.

In practical excavator systems, these force sensors are often substituted with pressure sensors connected directly to each actuator chamber. This substitution facilitates the calculation of forces exerted by the excavator on its environment using fundamental hydraulic principles. The force exerted on the piston rod, for instance, can be calculated as a function of pressures in the piston and rod chambers, the respective cross-sectional areas, rod velocity, and viscous friction coefficient:

$$f_{rod} = p_1 \cdot A_1 - p_2 \cdot A_2 + v \cdot \text{viscous_friction_coefficient}, \quad (4.1)$$

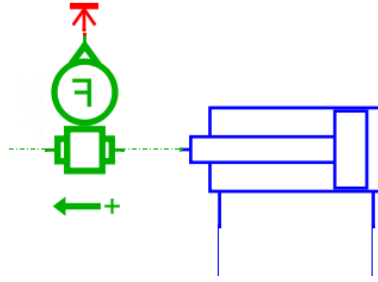


Figure 4.1: Illustration of a force sensor in the AMESim model

where:

- f_{rod} is the force applied to the piston rod,
- p_1 and p_2 are pressures in the actuator's piston and rod chambers respectively,
- A_1 and A_2 are the cross-sectional areas of the piston and rod chambers,
- v is the rod's velocity,
- `viscous_friction_coefficient` is the viscous friction coefficient, characteristic for each actuator.

While this relation could calculate force from the pressure transducers, implementation of the force sensor from AMESim's library was preferred for simplicity.

The force signals from the force sensors applied to the actuator's rod of the boom, arm, and bucket in the Load Sensing model are shown in Figures 4.2, 4.3, and 4.4, respectively.

To provide a comprehensive understanding of how these forces manifest in the frequency domain, Figures 4.5, 4.6, and 4.7 depict the power spectral density and frequency spectrum analysis for force signals from the boom, arm, and bucket actuators, respectively. These visual representations highlight the presence and distribution of noise components relative to the dominant signal frequencies.

4.1.2 Design of Low-Pass Filters

In the pursuit of developing the Common Pressure Rail model, it was imperative to ascertain the operational demands placed on the system. Central to this endeavor was the need to analyze the dynamics of a 9-ton excavator during its interactions with the environment. This involved extracting force data from the Load Sensing excavator model across its dig and dump cycle.

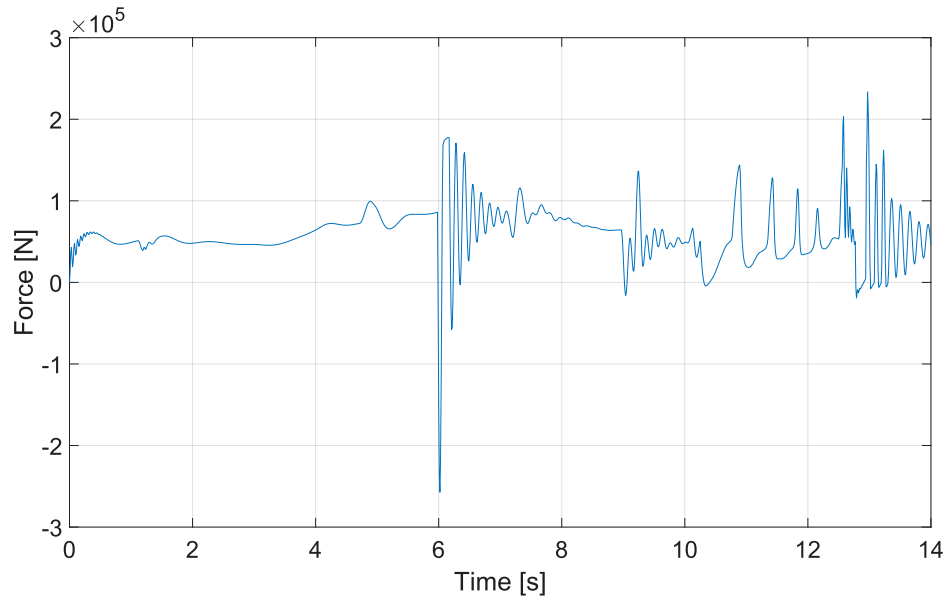


Figure 4.2: Boom digging force as measured by the Load Sensing model's force sensor

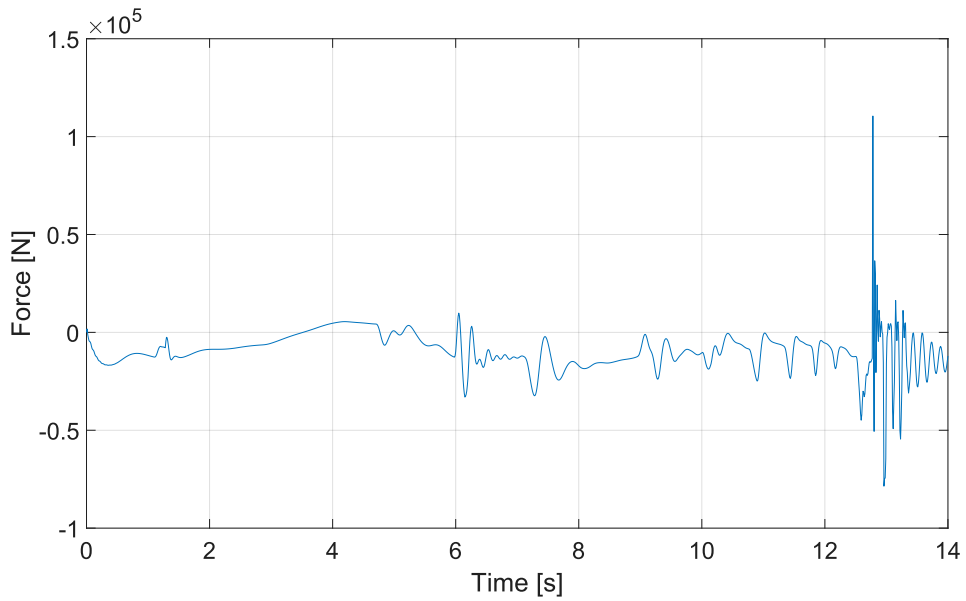


Figure 4.3: Arm digging force as measured by the Load Sensing model's force sensor

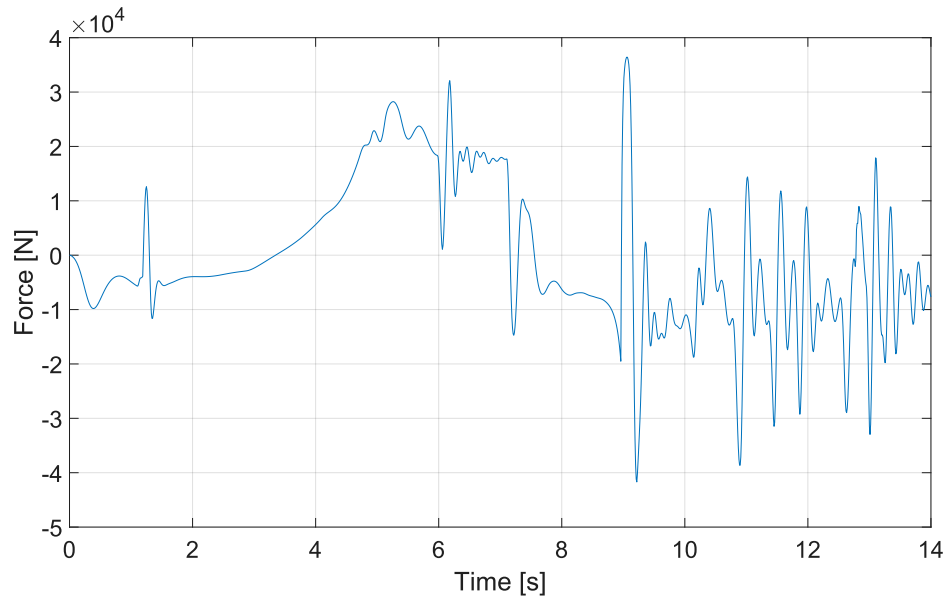


Figure 4.4: Bucket digging force as measured by the Load Sensing model's force sensor

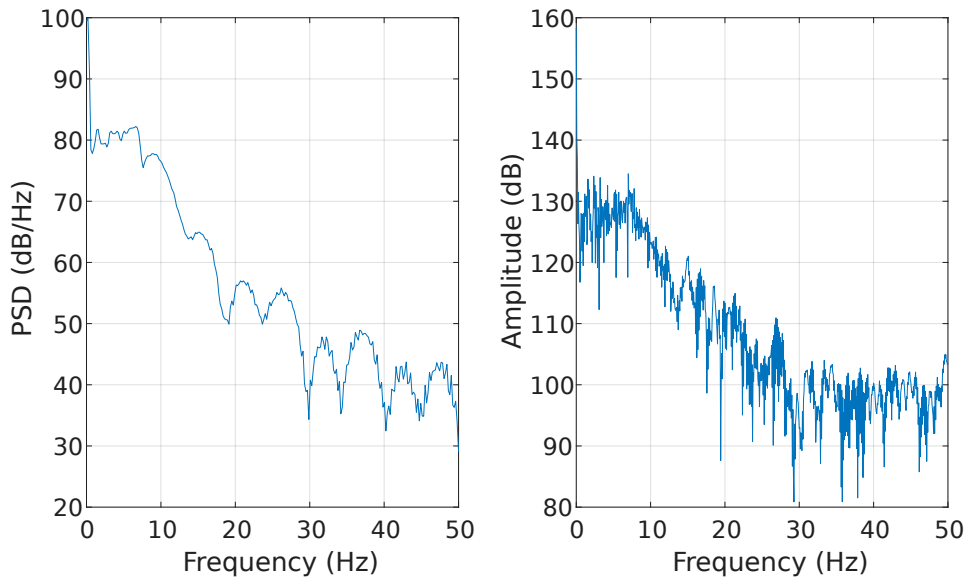


Figure 4.5: Power Spectral Density (left) and Frequency Spectrum Analysis (right) of boom digging force measured by the Load Sensing model's sensor

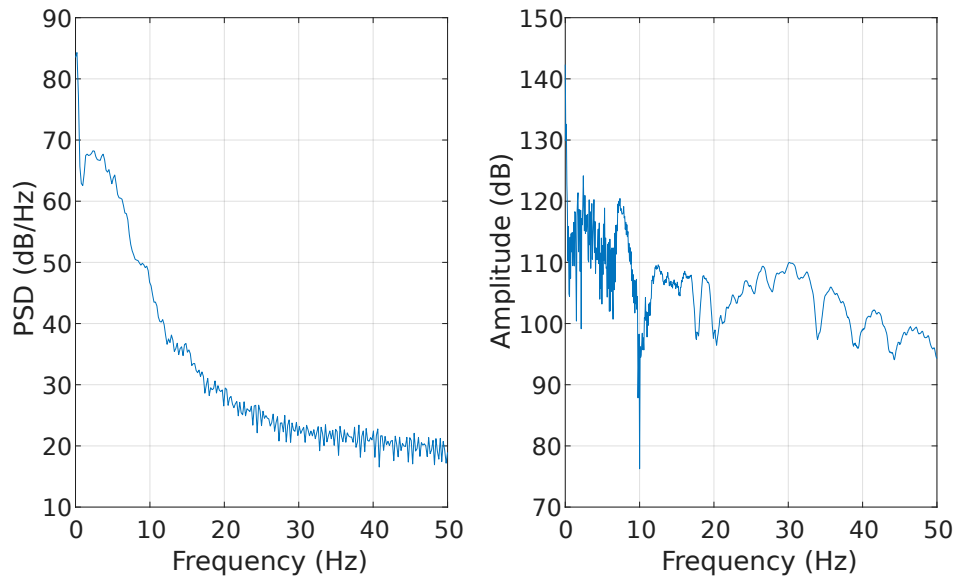


Figure 4.6: Power Spectral Density (left) and Frequency Spectrum Analysis (right) of arm digging force measured by the Load Sensing model's sensor

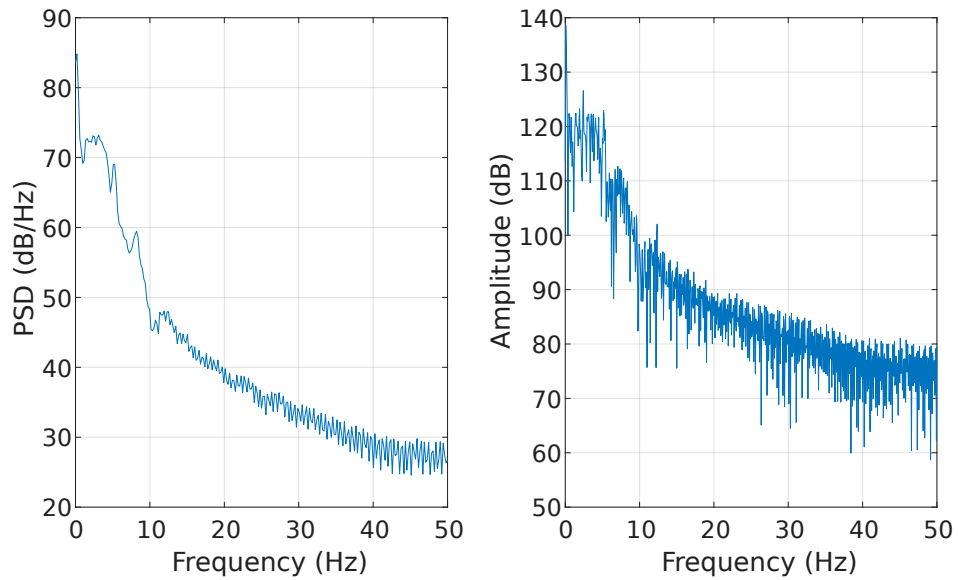


Figure 4.7: Power Spectral Density (left) and Frequency Spectrum Analysis (right) of bucket digging force measured by the Load Sensing model's sensor

The challenge arose from dimensioning the system to meet these varying force requirements derived directly from unprocessed sensor signals. Architecturally, this approach risked overestimating system capabilities. Conversely, from a control perspective, meeting such dynamic force demands without signal conditioning would have destabilized the system, rendering it overly sensitive to minor fluctuations.

To address these challenges, low-pass filters were meticulously designed and implemented using MATLAB. Their primary objective was to accurately characterize the forces applied to actuators during typical dig and dump operations within the CPR model. Once validated in MATLAB, the next step was to evaluate the feasibility of implementing these filters within the AMESim environment, ensuring stability in the input signals to the controller.

The design process of these filters involved iterative adjustments, utilizing the *filterDesigner* tool available in MATLAB. Various parameters such as cutoff frequencies (F_{pass} and F_{stop}), sample frequency (F_s), and ripple amplitudes in pass-band (A_{pass}) and stop-band (A_{stop}) were fine-tuned based on insights gathered from Power Spectral Density (PSD) and Frequency Spectrum Analysis (FSA).

Figure 4.8 illustrates the typical magnitude-frequency response of the designed low-pass filters. The design method employed was *Butterworth*, chosen for its optimal phase response and minimal group delay characteristics, crucial for maintaining signal integrity.

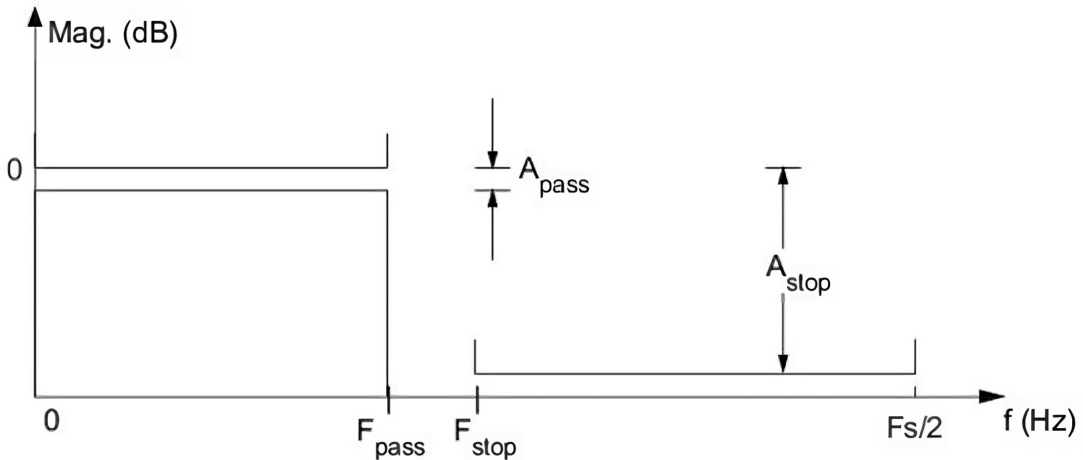


Figure 4.8: Magnitude-frequency characteristic of a low-pass filter

The parameters for each filter configuration are detailed in Table 4.1. These configurations were determined through a trial-and-error process, guided by the aforementioned PSD and FSA analyses, aimed at preserving essential low-frequency components critical for accurate system performance assessment.

Theoretically, it is known that an ideal cut-off frequency should be vertical. This is because, once the frequency beyond which the signal is affected by noise is identified, having a cut-off centered at this frequency allows for complete signal cleaning. As can be seen from the values in the table, particularly the pass-band frequency and stop-band frequency, the selection of these values aimed to approximate an ideal low-pass filter as closely as possible. This means achieving a filter with a steep slope in both the magnitude and phase response curves, indicating a high level of suppression. The delta between the pass-band frequency and stop-band frequency is 3 Hz for all filters, reflecting this effort.

	Sample frequency [F_s - Hz]	Pass-band frequency [F_{pass} - Hz]	Stop-band frequency [F_{stop} - Hz]	Amplitude pass-band [A_{pass} - dB]	Amplitude stop-band [A_{stop} - dB]
Boom	4800	2.0	2.3	25	28
Arm	4800	2.5	2.8	26	29
Bucket	4800	3.7	4.0	28	30

Table 4.1: Parameters used for each low-pass filter setting dedicated to force sensor signals

Figures 4.9, 4.10, and 4.11 depict the magnitude-normalized frequency representations of the filters applied to boom, arm, and bucket force sensor signals, respectively.

The efficacy of these filters was evaluated by applying them to force signals extracted from the Load Sensing AMESim model. Figures 4.12, 4.13, and 4.14 illustrate comparative plots of these signals before and after filtering.

Subsequently, an analysis of the filtered signals compared to their original counterparts was conducted in terms of PSD and FSA (Figures 4.15, 4.16, and 4.17), revealing the successful reduction of signal noise while preserving critical low-frequency components.

Referring to Figures 4.12, 4.13, and 4.14, it is evident that the filtered signals have effectively eliminated all oscillations present in the original signals. This achievement underscores the successful reduction of signal noise, enabling the identification of force trends applied to the boom, arm, and bucket actuators during the dig and dump cycle. Consequently, this insight has clarified the operational performance requirements for the CPR architecture.

In the pursuit of identifying parameters for low-pass filters to be applied within the Common Pressure Rail model on AMESim for the purpose of attenuating force sensor signals fed into the controller, the task appears achievable at face value. However, the practical reality involves greater complexity and intricacy. While low-pass filters indeed reduce or eliminate signal noise when properly designed,

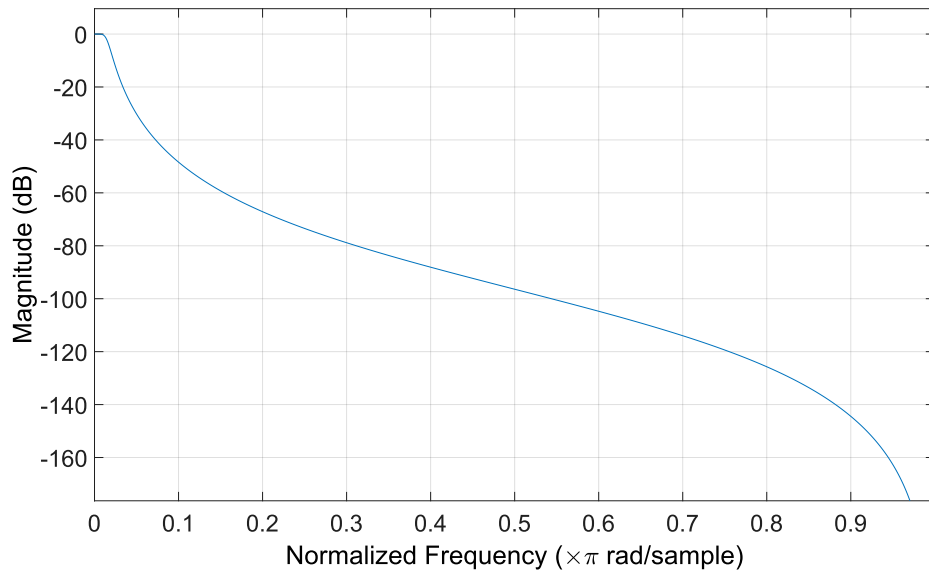


Figure 4.9: Magnitude-Normalized Frequency representation of the low-pass filter for the boom force sensor signal

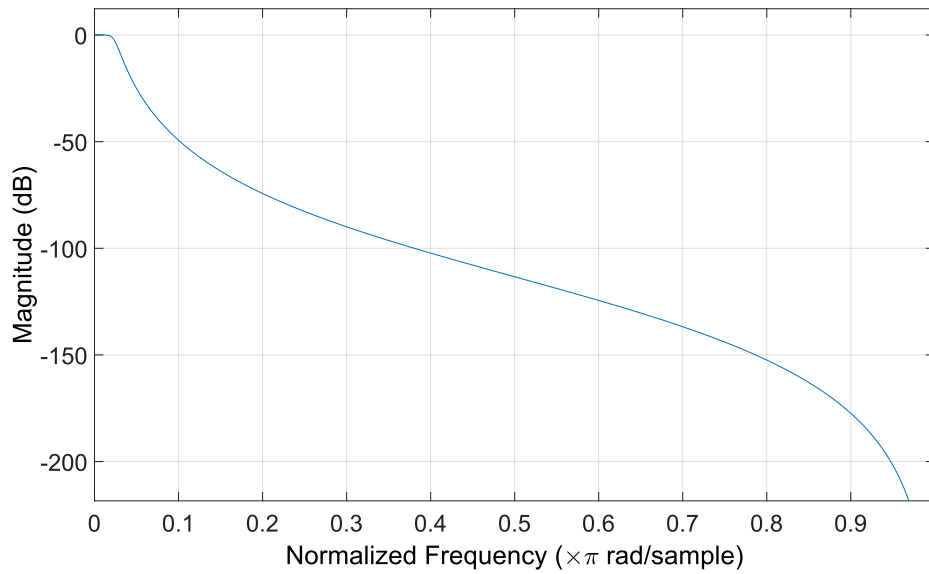


Figure 4.10: Magnitude-Normalized Frequency representation of the low-pass filter for the arm force sensor signal

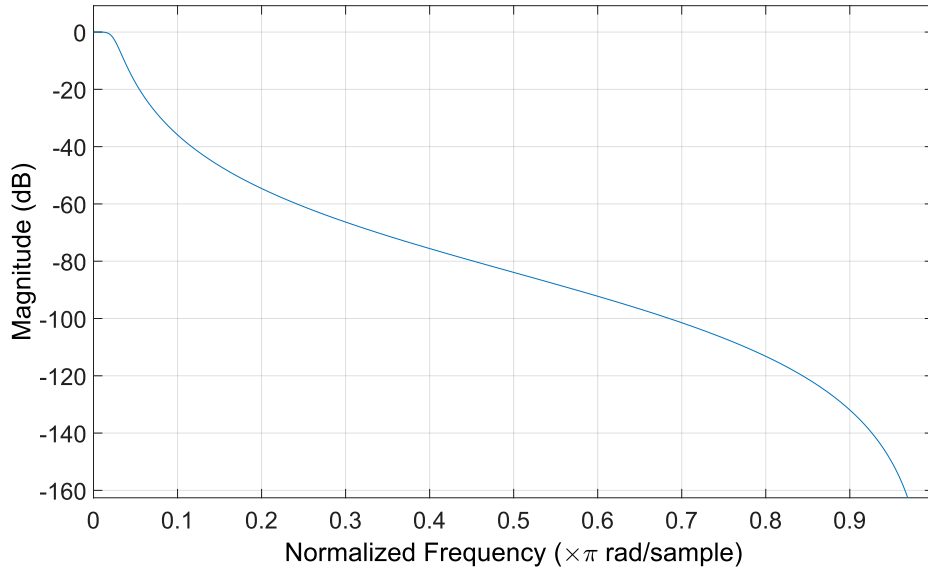


Figure 4.11: Magnitude-Normalized Frequency representation of the low-pass filter for the bucket force sensor signal

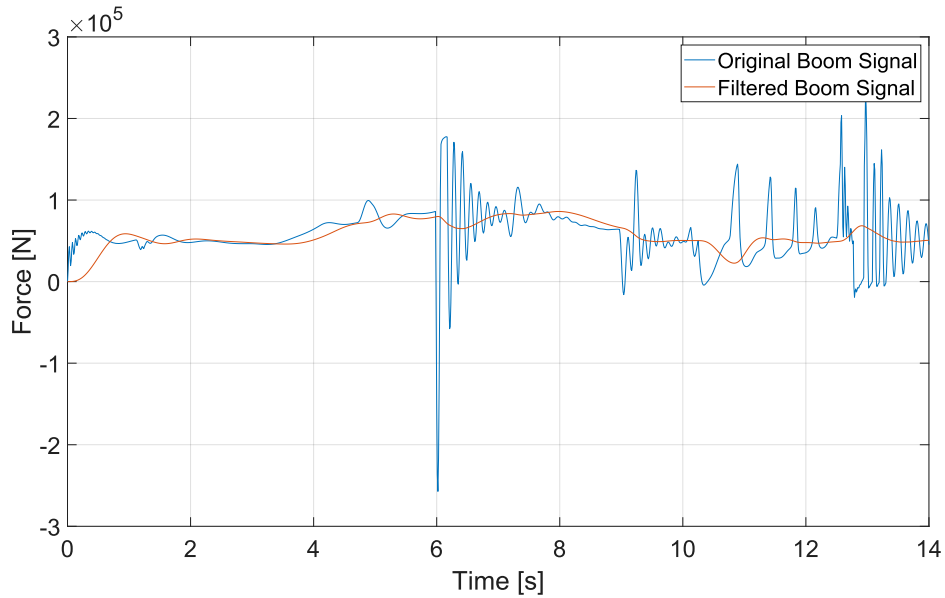


Figure 4.12: Comparison of boom force sensor signals before and after filtering

their implementation introduces output delays due to their inherent characteristic of attenuating high-frequency components. This delay directly results from the

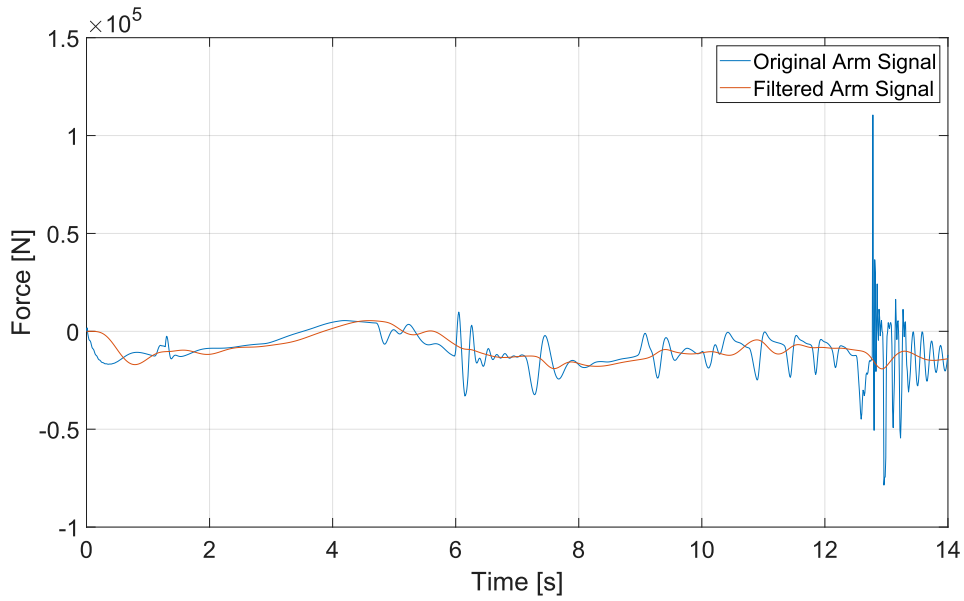


Figure 4.13: Comparison of arm force sensor signals before and after filtering

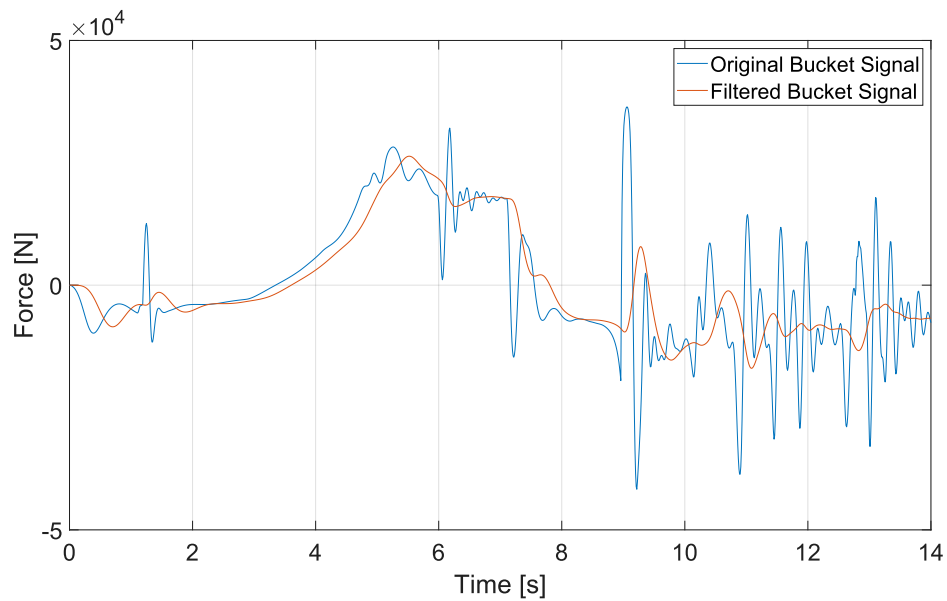


Figure 4.14: Comparison of bucket force sensor signals before and after filtering

time required for high-frequency signals to be dampened or attenuated by the filter. Examining comparative signal images before and after filtering, particularly in Figure 4.14 where the phenomenon may be more pronounced, reveals a shift of

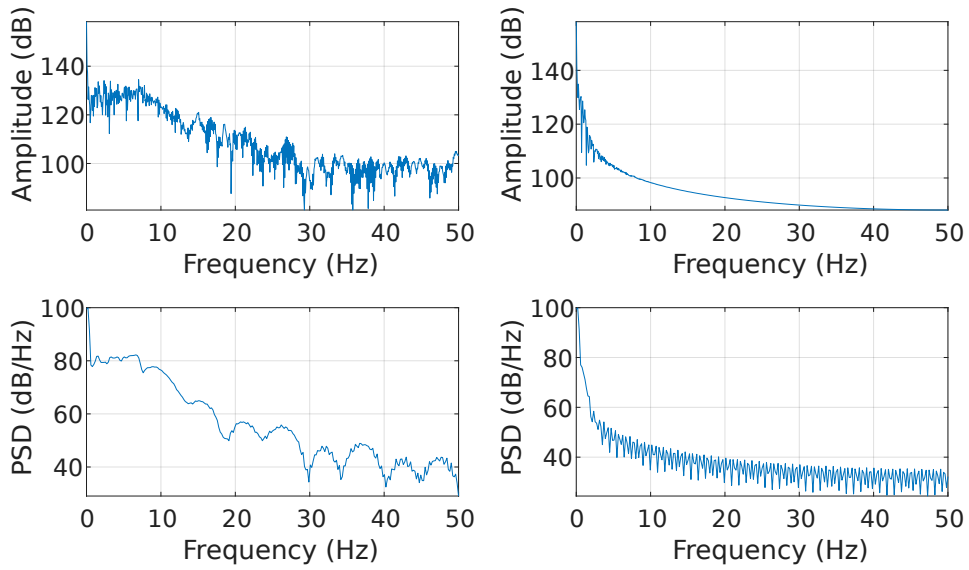


Figure 4.15: Comparison of boom force sensor signals: FSA (top) and PSD (bottom) before (left) and after (right) filtering

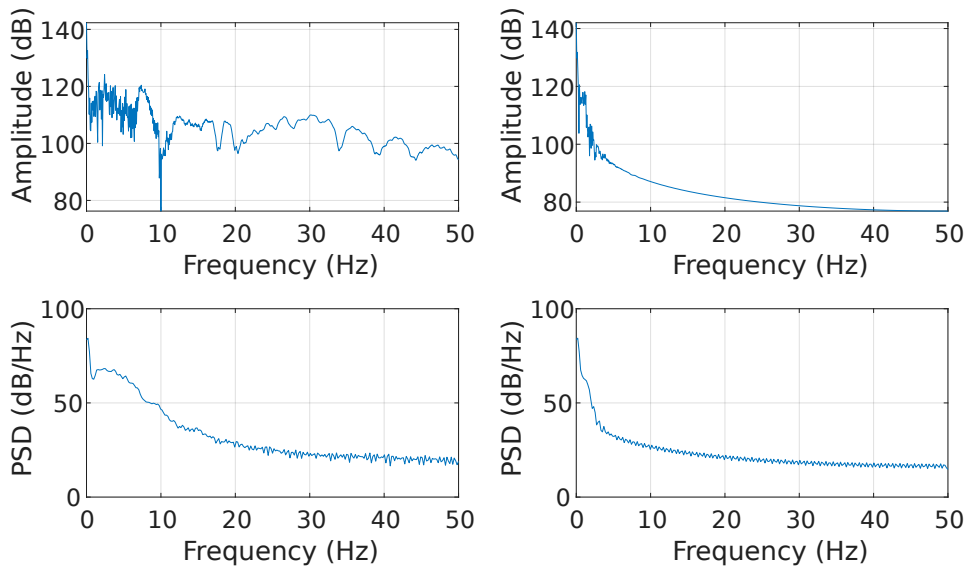


Figure 4.16: Comparison of arm force sensor signals: FSA (top) and PSD (bottom) before (left) and after (right) filtering

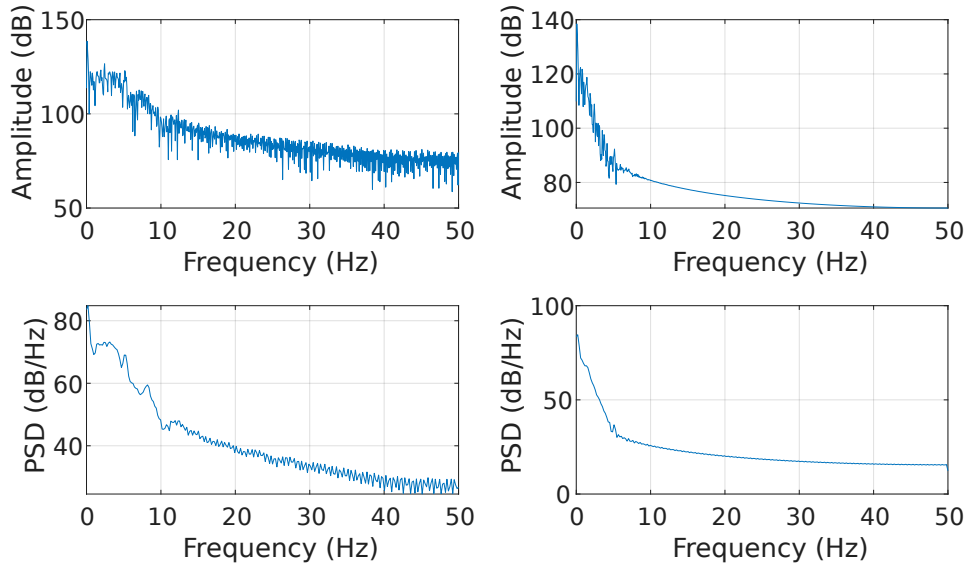


Figure 4.17: Comparison of bucket force sensor signals: FSA (top) and PSD (bottom) before (left) and after (right) filtering

approximately 0.3 seconds on the x-axis between the original and filtered signal graphs. This delay affects any low-pass filter and is more pronounced with higher suppression factors applied to the filter.

Therefore, in terms of controller stability, greater signal suppression enhances stability by ensuring a more consistent and stable input for the decision-making process of the controller. However, increased suppression also correlates with increased input signal delay, thereby causing delayed controller outputs and hindering the system's responsiveness to environmental stimuli. In such scenarios, the system may fail to promptly respond to changes in its surroundings. Thus, the challenge lies in striking a balance between maximizing signal noise reduction and minimizing the delay introduced by the filter application. This balance represents a compromise between system stability and responsiveness.

4.2 Insights into Control of Linear Actuators

The discussion now turns to the controller, which constitutes the cornerstone of this thesis. The controller has two primary tasks: the first is the selection of the pressure lines to be connected to the chambers of the actuators and the hydraulic motor of the turret; this selection is made not only based on the forces and torques applied to the utilities resulting from their interaction with the environment but also on the

required movement speeds. The term "selection of pressure lines" involves actuating on-off valves placed on the pressure rails, allowing the chambers of each utility to access the appropriate pressure line. The second task assigned to the controller is the modulation of the proportional valve located upstream of each utility so that its movement in terms of speed corresponds to the signal provided by the operator via joystick. An example of the Simulink model used for managing a single utility is shown in Figure 4.18. More detail about it will be provided in the dedicated section.

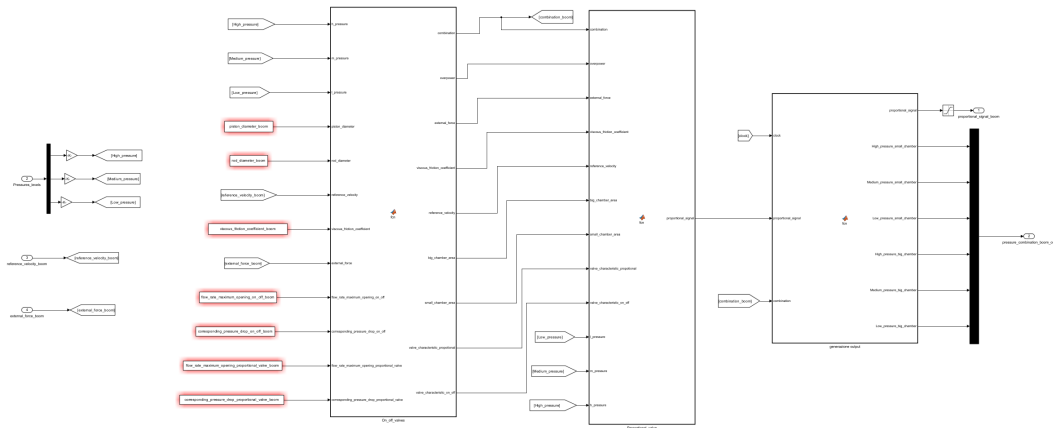


Figure 4.18: Simulink controller model for managing a single utility

The following discussion explains how the controller operates with the hydraulic model. Developed in the Simulink environment, the controller is executed in AMESim through co-simulation, where solvers from both software packages perform the simulation together. The interfaces between Simcenter AMESim and Simulink allow for simulations that combine models from both platforms. There are two main options for integration: importing the Simcenter AMESim model into Simulink (see Figure 4.20) or importing the Simulink model into Simcenter AMESim (see Figure 4.19). This work chose the latter—importing the Simulink model into AMESim—because the primary objective was to test and develop the Simcenter AMESim CPR model. In this setup, Simcenter AMESim operates as the Master and Simulink as the Slave. Figure 4.19 and 4.20 shows how the two software packages could function in co-simulation.

Once the controller model is created in Simulink, a MATLAB command ("*SL2AMECosim*") can be used to generate a library. This library can then be imported into AMESim, where it is treated as a "black box" with all the inputs and outputs defined in Simulink connected to it (see Figure 4.21). Running the simulation enables information exchange between the AMESim model and the

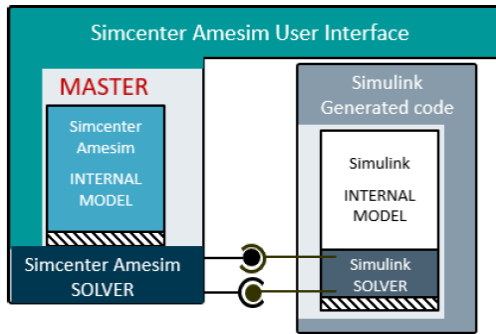


Figure 4.19: Co-simulation: Simcenter AMESim as Master, Simulink as Slave (*SL2AMECosim*)

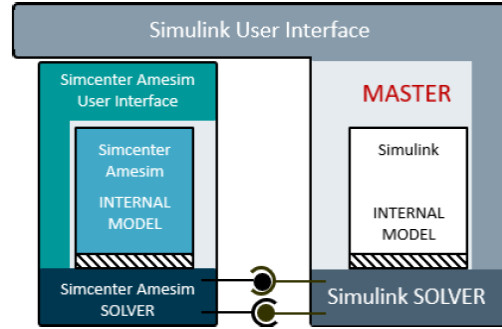


Figure 4.20: Co-simulation: Simcenter AMESim as Slave, Simulink as Master (*AME2SLCosim*)

Simulink model via the input/output interface of the black box. Further information on performing co-simulation, the required packages, and compatible software versions can be found in Appendix 7.

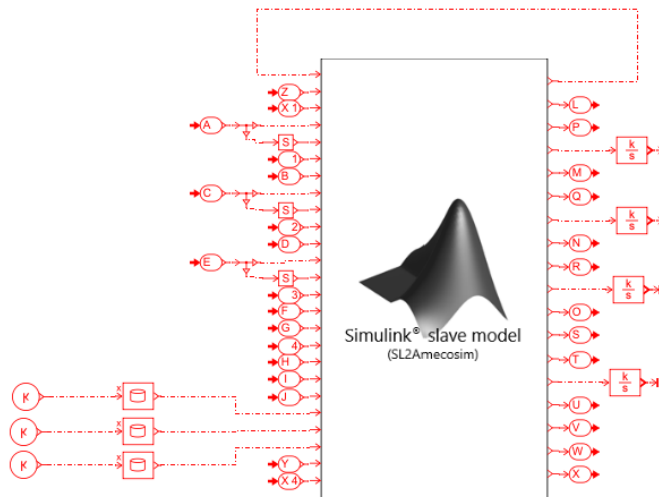


Figure 4.21: Example of a Simulink model as it appears when imported into AMESim

4.2.1 Linear Actuator Operating Modes

The operating modes of a linear actuator pertain to the various configurations in which the actuator can be connected to the three system pressure levels: high pressure (HP), medium pressure (MP), and tank pressure (TP). As illustrated in Figure 4.22, the use of switching valves enables each cylinder chamber to connect to all three pressure levels, resulting in a total of nine distinct operating modes.

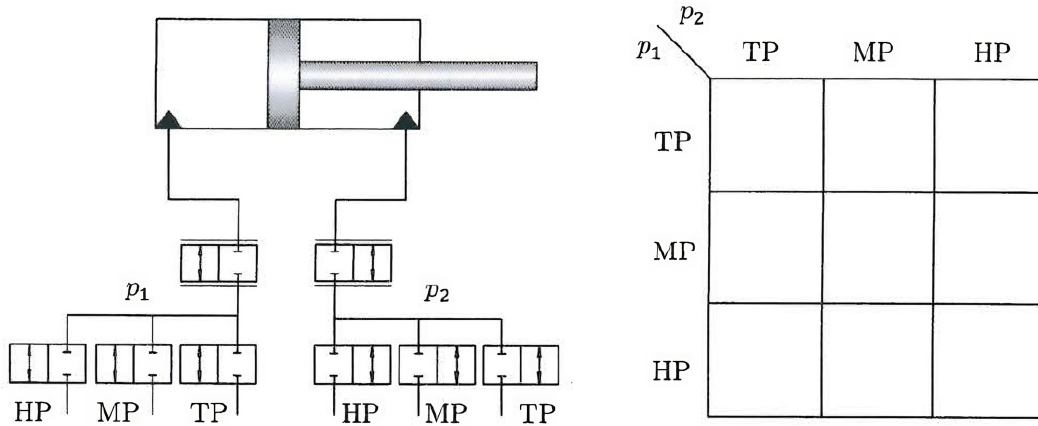


Figure 4.22: System operating modes - linear actuator [3]

Each operating mode is defined by a specific region in the load pressure/flow plane (p_L/Q_L). Figure 4.23 schematically represents all nine operating modes. The naming convention specifies the pressure level connected to the piston side first, followed by the pressure level connected to the rod side. For instance, MP/HP indicates medium pressure on the piston side and high pressure on the rod side. The relative positions of these modes are influenced by the HP, MP, and TP pressure levels, as well as the piston area ratio α .

The strategy for positioning these lines to facilitate efficient operation with minimal throttling is discussed in detail in Section 3.2.3. Lines passing through Quadrants I and III are utilized to actively supply power to the actuator. Conversely, lines passing through Quadrants II and IV facilitate energy recovery from the actuator, thereby contributing to energy conservation and promoting efficient system operation. This approach involves storing excess energy in accumulators when available.

To clarify the selection of the operating mode, consider the following examples (see Figure 4.23): in the right-hand plane, the most efficient operating mode is the one with the line directly above the current operating point, such as HP/HP for OP1. In the left-hand plane, the most efficient mode is defined by the line directly below the current operating point, such as MP/MP for OP2. The objective

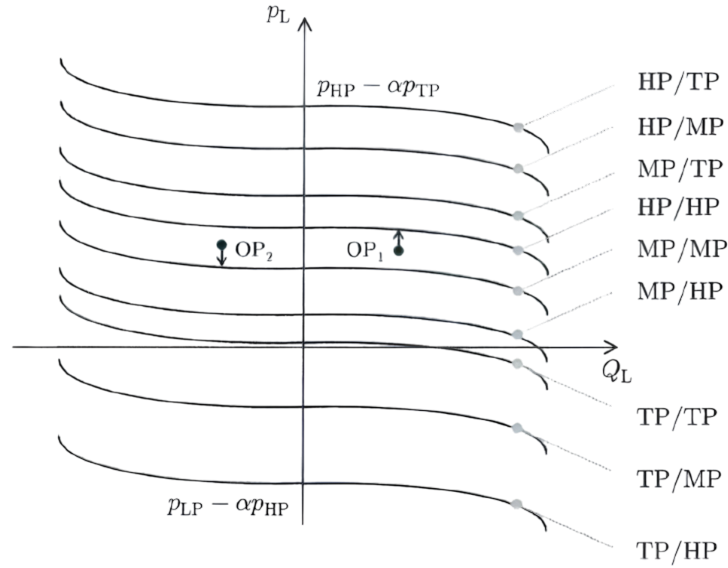


Figure 4.23: Region of operation of all nine modes - linear actuator [3]

with valve actuation and proportional valve modulation is to match the actuator's operating point both in terms of p_L (i.e., the pressure difference between the two chambers) and Q_L (i.e., the flow rate difference between the two chambers).

If the system is in the right-hand plane of the load pressure/flow plane, choosing the operating mode just above the operating point allows bridging the gap on the y-axis between the operating mode line and the ordinate of the operating point (represented as the vector between OP1 and the HP/HP operating mode line) through proportional valve modulation. The proportional valve ensures the adequate flow rate for the desired velocities and the appropriate ΔP between the two chambers to match the force applied to and generated by the actuator. By modulating the proportional valve, the pressure downstream on the supply side will be lower, and on the return side, higher. This modulation reduces the force generated by the actuator, bridging the Δp_L between the operating mode and the working point. The closer the operating point is to the operating mode line, the lesser the modulation of the proportional valve required, thus minimizing hydraulic losses.

Conversely, in the left-hand plane, the chosen operating mode should be just below the operating point. For OP2, the mode just below is MP/MP. Medium pressure is connected to the supply side of the proportional valve, linked to the small chamber, and medium pressure to the return side, linked to the large chamber. Proportional valve modulation increases the pressure difference p_L to match the required force. So selecting the appropriate pressure level requires knowledge of

the actuator's current load pressure and load flow.

Figure 4.24 shows a setup used in our Common Pressure Rail model, featuring a force sensor, electric joysticks, and a controller to select the required mode and activate the corresponding switching valves. However, in real excavator applications, this setup is typically replaced by two pressure transducers connected to each actuator chamber, eliminating the need for a force sensor. The proportional valves must also be regulated to maintain the desired actuator velocity. As load pressure and joystick inputs vary, the controller identifies the operating point within the plane and switches modes to minimize throttling.

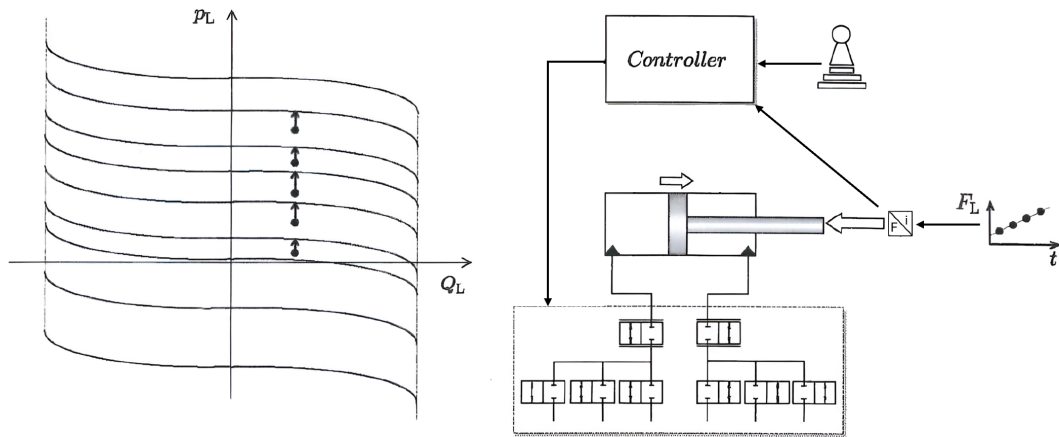


Figure 4.24: System operating modes and controller setup - linear actuator

One significant concern during the development phase was the impact of mode switching on actuator performance and operator comfort. Ideally, the operator should not notice any transition between modes. The influence of mode switching on actuator motion is crucial for the technology's industrial application. Given that these valves do not operate instantaneously, interruptions in the fluid flow path can occur, leading to fluctuations in actuator speed and vibrations within the mechanical system. In our thesis research, this issue has been addressed by opting not to model the dynamic behavior of on-off valves during their opening process, deferring this aspect to future development. The transfer function representing all the valves used in the model is defined as:

$$G(s) = K \quad (4.2)$$

where K is a constant, generally set to 1. These systems introduce no delays in their response to input.

4.2.2 Controller Details

This section provides a detailed analysis of the Simulink model of the controller, using the example of a single utility for reference (see Figure 4.25). The discussion commences with the input-output interface, corresponding to elements 1 and 5. Subsequently, the parameters essential for the correct functioning of the model, denoted as element 2, will be examined.

Following this, the section will delve into the algorithm responsible for the actuation of the on-off valves, represented by element 3. Finally, the analysis will address the algorithm for calculating the modulation of the proportional valve, corresponding to element 4. This comprehensive examination aims to provide a thorough understanding of each component and their interactions within the controller model.

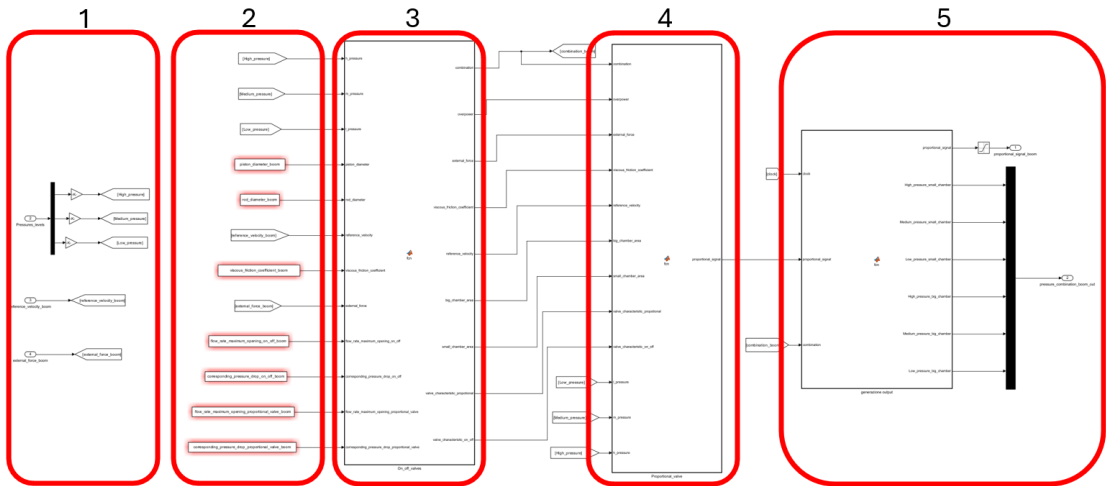


Figure 4.25: Breaking down the Simulink controller model for the linear actuator: a detailed view of its components

Controller Input-Output Requests

After explaining the co-simulation process between the Simcenter AMESim and Simulink environments, it is essential to identify the input-output (I/O) interface facilitating communication between the two models. The interaction between controllers and the systems they manage is fundamentally mediated through a series of input-output (I/O) requests (see figure 4.26).

To function properly, the controller requires three main input variables: the pressure signals from each line, which include high pressure (HP), medium pressure (MP), and low pressure (LP), the force applied to the actuator from its interaction

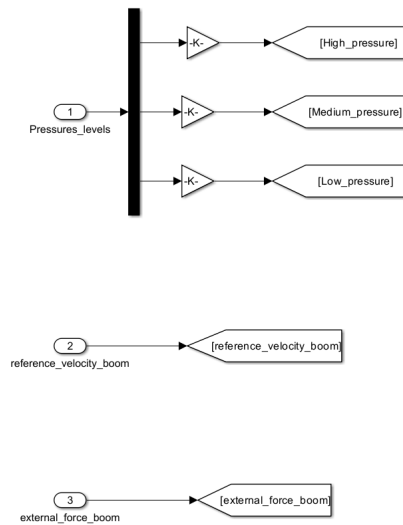


Figure 4.26: Simulink controller model inputs - linear actuator

with the environment and the reference velocity at which the actuator should move. These input variables are crucial for the following reasons:

1. Pressure signals: the values of the pressure signals from the various rails are necessary because of their variability over time. Since the system does not have ideal pressure sources but rather accumulators with finite volumes, the outflow rate from the accumulators affects the pressure. Specifically, as the flow rate exiting the accumulators increases, the pressure tends to decrease. The stiffness of the accumulator affects the rate of pressure change; the stiffer the accumulator, the less the pressure varies from fully charged to fully discharged. However, pressure variation is inevitable. Therefore, to make informed decisions about the operational mode, it is crucial to be aware of the pressure states in the system at any given time. This allows for understanding where the various operating mode curves are positioned on the load pressure/flow rate graph.
2. Force applied to the actuator: the force applied to the actuator is essential for the controller to define one of the coordinates of the actuator's operating point, specifically the y-axis on the load pressure/flow rate graph. This input is pivotal for determining the actuator's current state and ensuring it operates within the desired parameters.
3. Reference velocity: the reference velocity at which the actuator should move is directly proportional to the second coordinate of the actuator's operating

point, which corresponds to the required flow rate to achieve the desired movement speed. These signals are proportional to the joystick commands given by the operator. Without this input, the controller would not know the necessary flow rate to provide to the actuator's chamber.

Regarding the output (see Figure 4.27), the Simulink model of the controller sends two variables to the AMESim model: the proportional valve opening value and the opening value of each on-off valve. For the proportional valve, since the hydraulic valves used in the AMESim model have a parameter called valve rated current, where maximum opening corresponds to 1 mA, all output values range between 0 and 1. Specifically, the signal for the proportional valve is an analog signal ranging from 0 to 1, while the signals sent to each on-off valve are digital signals, either 0 or 1.

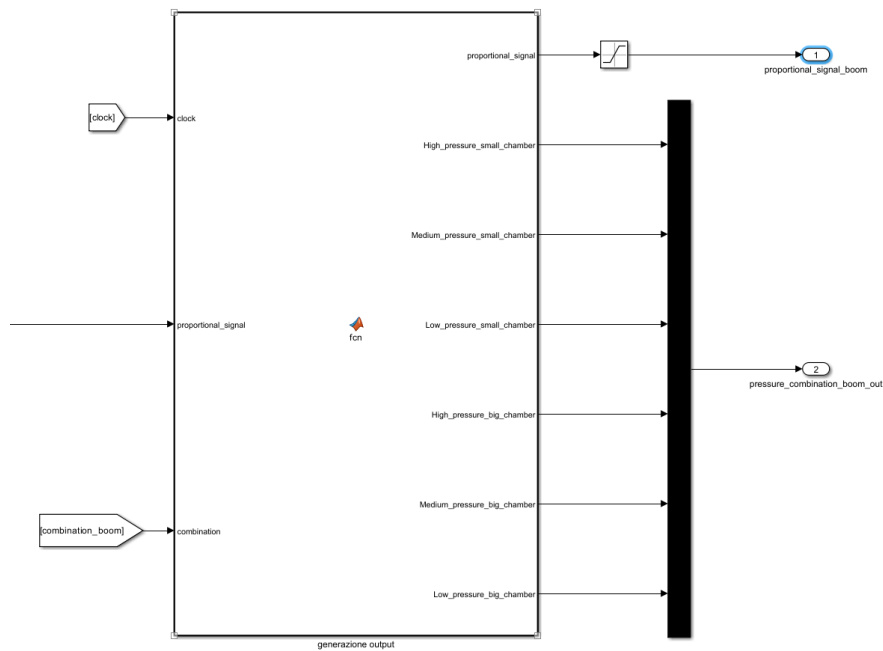


Figure 4.27: Controller's MATLAB function for outputs generation - linear actuator

Furthermore, both the input values of rail pressures and the output signals sent to each on-off valve appear as a single input or output because they are properly multiplexed and demultiplexed during the transition between the two models, reducing the number of required input/output ports.

Controller Parameter Requests

To maximize the modularity of the controller model, all MATLAB functions that calculate the combinations of pressures to be applied to the actuator and the modulation value of the proportional valve have been made parametric. The model requires input parameters including geometric data of the actuator, such as piston diameter (*piston_diameter*), actuator diameter (*actuator_diameter*), and viscous friction coefficient of the actuator (*viscous_friction_coefficient*), as well as data of the valves. For the CPR model in AMESim, as discussed in previous sections, the valves were sized by setting the maximum flow rate of each valve at maximum opening and determining the corresponding pressure drop. Consequently, the input parameters required by the controller include these values for both the on-off valves (assumed to be equal for all valves) and the proportional valve.

Let's delve into the specific purposes of each parameter:

- Geometric data of actuators: these parameters are necessary to calculate the annular area of the actuator on the rod side (A_{piston}) and on the piston side (A_{rod}) using the following equations:

$$\begin{aligned} A_{piston} &= \frac{\pi \times (\text{piston_diameter}^2)}{4} \\ A_{rod} &= \frac{\pi \times (\text{piston_diameter}^2 - \text{actuator_diameter}^2)}{4} \end{aligned} \quad (4.3)$$

- Viscous friction coefficient of actuator: this coefficient is essential for calculating the force generated by the actuator based on the pressures connected to its two chambers, using the formula:

$$f_{rod} = p_1 \times A_{piston} - p_2 \times A_{rod} - \text{velocity} \times \text{viscous_friction_coefficient} \quad (4.4)$$

- Maximum flow rate and corresponding pressure drop of valves: these parameters are necessary to define the valve characteristic. The relationship between the pressure drop across the valve and the flow rate passing through it is governed by the formula:

$$\frac{Q}{\sqrt{\Delta P}} = c_q \times A \times \sqrt{\frac{2}{\rho}} \quad (4.5)$$

where c_q is the flow coefficient, A is the valve orifice area and ρ is the fluid density. In ideal fluid conditions, c_q and ρ are constants, making $\frac{Q}{\sqrt{\Delta P}}$ directly proportional to the valve orifice area A . However, because fluid density ρ

changes with pressure due to the bulk modulus K , which is specific to each hydraulic oil, a typical bulk modulus value used in simulations is approximately 10000 bar, approximating a characteristic of hydraulic oil. The bulk modulus relates the change in pressure to the change in density according to the equation:

$$K = \rho \times \frac{\partial p}{\partial \rho} \quad (4.6)$$

Given that pressure variations in our simulations were not significant, density variations were neglected, and c_q was considered constant. Under these assumption the term $\frac{Q}{\sqrt{\Delta P}}$ is only proportional to the valve orifice area A . Choosing to define the valve in terms of maximum flow rate and corresponding pressure drop rather than valve area was for convenience.

On-Off Valves Controller Algorithm

The analysis of the algorithm developed for the control of the on-off valves of each actuator is now presented. This algorithm, implemented in a MATLAB function of Simulink (element 3 in Figure 4.25), is essentially a straightforward translation into code of what was explained in Section 4.2.1.

Below is a detailed explanation of how the algorithm operates, accompanied by the code (see Algorithms 1 and 2). The description starts with the initial code segment (see Algorithm 1) where all necessary variables are thoroughly defined.

Algorithm 1 On-off valves control logic algorithm - linear actuators - part 1

- 1: $A_{piston} \leftarrow \pi \times \left(\frac{piston_diameter}{2}\right)^2$;
 - 2: $A_{rod} \leftarrow \pi \times \left(\frac{piston_diameter}{2}\right)^2 - \left(\frac{rod_diameter}{2}\right)^2$;
 - 3: $matrix \leftarrow [LP, MP, HP]$;
 - 4: $valve_char_on_off \leftarrow \frac{flow_rate_max_on_off}{\sqrt{pressure_drop_on_off}}$;
 - 5: $valve_char_prop \leftarrow \frac{flow_rate_max_prop}{\sqrt{pressure_drop_prop}}$;
 - 6: $combination \leftarrow [0,0]$
-

1. Calculation of areas (see Algorithm 1 - lines 1 \rightarrow 2);
2. Initialization of matrix (see Algorithm 1 - line 3): a matrix is initialized with three rail pressure values: LP (Low Pressure), MP (Medium Pressure), and

HP (High Pressure). These values are received as input from three pressure sensors located on the AMESim model rails.

3. Valve characteristics definition (see Algorithm 1 - lines 4 → 5): the characteristics of the on-off valves (`valve_char_on_off`) and the proportional valve (`valve_char_prop`) are determined using the maximum flow rate and the corresponding pressure drop taken in input in full spool opening position.
4. Initialization MATLAB function's output (see Algorithm 1 - line 6): the variable `combination` is a vector initialized with the value `[0,0]`, serving as the initial output placeholder within the MATLAB function. It will store the indices of the on-off valves that need activation for optimal operational mode control. Specifically, the first element of the vector denotes the index of the on-off valve to activate on the small chamber side, while the second element denotes the index for the big chamber side.

Let us consider an example to ensure a better understanding of the variable's meaning and its possible content. Suppose that, at the end of the algorithm's execution, for a given operating point, the optimal operating mode is determined to be (HP connected to the actuator's small chamber and LP connected to the big chamber). In this case, the algorithm will output the vector `combination` containing the values `[3,1]`. These values correspond to the indices of the matrix `matrix`.

The description proceeds to the core section of the code (see Algorithm 2), where it is evaluated the operating mode to select.

5. Reference velocity check (see Algorithm 2 - line 1 → 22): if the `reference_velocity` is non-zero, calculations commence. A zero velocity indicates that no joystick in the cabin is being operated, thus necessitating no movement from the actuator. In this scenario, the actuator position remains fixed. This condition is ensured by the closure and sealing of the on-off valves, as specified by the entries in the `combination` vector, which will be set to `[0,0]`.
6. Optimal pressure combination search:
 - A variable representing the minimum force difference `force_diff_min` is initialized with an infinite value. This stored value will be updated during each iteration only if the evaluated force difference `force_diff` is less than the current stored value (see Algorithm 2, lines 2 → 21).
 - Two nested loops iterate through all potential pressure combinations. This procedure generates all feasible operational modes for identifying the one that best aligns with the working point (see Algorithm 2 - line 3 → 20).

Algorithm 2 On-off valves control logic algorithm - linear actuators - part 2

```
1: if reference_velocity  $\neq$  0 then
2:   force_diff_min  $\leftarrow$   $\infty$ ;
3:   for  $k = 1 : \text{length}(\text{matrix})$  do
4:     for  $j = 1 : \text{length}(\text{matrix})$  do
5:       if  $k \neq 1$  or  $j \neq 1$  then
6:         if reference_velocity > 0 then
7:            $p_{\text{piston}} \leftarrow \text{matrix}(k) - \text{on\_off\_p\_drop} - \text{prop\_p\_drop}$ ;
8:            $p_{\text{rod}} \leftarrow \text{matrix}(j) + \text{on\_off\_p\_drop} + \text{prop\_p\_drop}$ ;
9:            $\text{force\_diff} \leftarrow f_{\text{rod}} - \text{external\_force}$ ;
10:        else if reference_velocity < 0 then
11:           $p_{\text{piston}} \leftarrow \text{matrix}(k) + \text{on\_off\_p\_drop} + \text{prop\_p\_drop}$ ;
12:           $p_{\text{rod}} \leftarrow \text{matrix}(j) - \text{on\_off\_p\_drop} - \text{prop\_p\_drop}$ ;
13:           $\text{force\_diff} \leftarrow -f_{\text{rod}} + \text{external\_force}$ ;
14:        end if
15:        if  $\text{force\_diff} > 0$  and  $\text{force\_diff} < \text{force\_diff\_min}$  then
16:           $\text{force\_diff\_min} \leftarrow \text{force\_diff}$ ;
17:           $\text{combination} \leftarrow [j, k]$ ;
18:        end if
19:      end if
20:    end for
21:  end for
22: end if
```

- To avoid cavitation issues in the circuit together with useless calculations, the LP/LP operational mode is excluded from consideration (see Algorithm 2 - line 5 \rightarrow 19).
- Determine the quadrant of the load pressure/flow rate graph: Quadrants I and IV where *reference_velocity* is greater than zero, requiring the operational mode above the working point, and Quadrants II and III where *reference_velocity* is less than zero, requiring the operational

mode below the working point (see Algorithm 2 - line 6 \rightarrow 14).

- Determination of the upstream pressures of the actuators (see Algorithm 2, lines 7-8 and 11-12): based on the known pressures upstream of the on-off valves stored in matrix `matrix` and knowing the flow rate magnitude and direction as a function of the reference velocity, it becomes possible to assess the pressure drops occurring through both the on-off valves and the fully open proportional valve as a function of the valve characteristics `valve_char_on_off` and `valve_char_prop`.

$$on_off_p_drop_i = \frac{Q_i}{valve_char_on_off} = \frac{v_{ref} \cdot A_i}{valve_char_on_off}$$

$$prop_p_drop_i = \frac{Q_i}{valve_char_on_off} = \frac{v_{ref} \cdot A_i}{valve_char_on_off}$$

Where A_i could be either the piston side chamber area or the rod side one. Consequently, the pressures at the actuators' piston and rod side inlets can be determined, thus allowing the evaluation of the force equilibrium at the actuator.

$$p_{pis} = \begin{cases} matrix(k) - on_off_p_drop - prop_p_drop, & \text{if reference_velocity} > 0; \\ matrix(k) + on_off_p_drop + prop_p_drop, & \text{if reference_velocity} < 0; \end{cases}$$

$$p_{rod} = \begin{cases} matrix(j) + on_off_p_drop + prop_p_drop, & \text{if reference_velocity} > 0; \\ matrix(j) - on_off_p_drop - prop_p_drop, & \text{if reference_velocity} < 0; \end{cases}$$

- Determine the difference in force caused by the pressure combination in the two chambers and compare it to the sum of the external force and the viscous friction force generated by the piston moving at velocity v (see Algorithm 2 - line 9 and line 13). If the actuator's operating point lies to the right on the load pressure/flow rate graph, then the rod force generated with the proportional valve fully open must exceed the external force. Conversely, if it lies to the left on the graph, it must be less than the external force. Therefore, by setting up the following equations, the variable `force_diff` will be greater than 0 for all operating modes that satisfy this condition.

$$force_diff = \begin{cases} f_{rod} - external_force, & \text{if reference_velocity} > 0; \\ -f_{rod} + external_force, & \text{if reference_velocity} < 0. \end{cases}$$

- Update the optimal combination (see Algorithm 2 - line 15 → 18): in each iteration of the nested `for loop`, ensure the force difference (`force_diff`) is positive and, if so, verify it is the smallest among all analyzed iterations. By the end of the loop, `force_diff_min` holds the smallest difference among all operational modes relative to the actuator’s working point, while `combination` contains the corresponding indices of the pressures to be connected to the two actuator chambers.

Proportional Valve Controller Algorithm

The final component of the linear actuator controller, focusing on the modulation of the proportional valve, is now examined. The algorithm developed for this purpose has been implemented as a MATLAB function, depicted as element 4 in Figure 4.25.

As previously outlined, the on-off valve controller is instrumental in selecting the optimal operational mode for the actuator’s working point. This selection process significantly minimizes the throttling effect on the proportional valve. Consequently, the proportional valve serves two pivotal functions in this control system.

Firstly, the proportional valve compensates for the discrepancy between the virtual load pressure (p_L) generated by the on-off valve pressures and the p_L required by the operating point. This compensation is crucial for ensuring that the gap Δy in the load pressure/flow rate plane converges to zero.

Secondly, the proportional valve regulates the actuator’s speed in response to commands received from the operator via joystick inputs.

The subsequent paragraph will elucidate the mechanisms and methodologies through which these objectives are effectively realized.

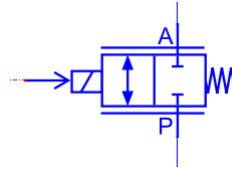


Figure 4.28: AMESim model of a two-port two-position proportional valve

Referring to a two-port, two-position valve (see Figure 4.28), the relationship between the pressure differential across the valve ($P_P - P_A$), the fluid flow rate through the valve (Q), and the characteristics of both the valve (orifice area A) and the fluid (density ρ and fluid coefficient c_q) for a turbulent fluid is given by:

$$\frac{Q}{\sqrt{P_P - P_A}} = c_q \cdot A \cdot \sqrt{\frac{2}{\rho}} \quad (4.7)$$

Under the assumptions made in section 4.2.2, this relation can be approximated as:

$$\frac{Q}{\sqrt{\Delta P}} = \text{valve_characteristic} \approx \text{constant} \quad (4.8)$$

Referring to equation 4.7, the orifice area A represents the effective flow area, distinct from the nominal design area of the valve. For a proportional valve, the modulation phase involves varying the orifice opening to achieve the desired outcome (analog operation). In AMESim, the effective area is calculated using a linear law:

$$A_{effective} = x \cdot A_{nominal} \quad (4.9)$$

Thus, the effective flow area is proportional to the nominal valve area, with a variable x ranging from 0 to 1:

$$0 \leq x \leq 1 \quad \rightarrow \quad 0 \leq A_{effective} \leq A_{nominal} \quad (4.10)$$

By linking equations 4.7, 4.8 and 4.9 it would be possible to write:

$$\begin{aligned} \frac{Q}{P_P - P_A} &= c_q \cdot A_{effective} \cdot \sqrt{\frac{2}{\rho}} \\ &= c_q \cdot x \cdot A_{nominal} \cdot \sqrt{\frac{2}{\rho}} \\ &= x \cdot \text{valve_characteristic} \end{aligned} \quad (4.11)$$

Figure 4.29 illustrates the implementation of the linear actuator-proportional valve subsystem within the AMESim CPR model. The decision to use a four-port, two-position proportional valve instead of two two-port, two-position valves simplifies the control logic and aligns the system closer to a commercially viable model, avoiding overestimation of fuel economy benefits.

For the four-port, two-position proportional valve, the physical relations describing the valve behaviour are given by equation 4.11 for both the P-A and T-B paths:

$$\begin{cases} \frac{v \cdot A_{piston}}{P_T - P_B} = c_q \cdot A_{effective} \cdot \sqrt{\frac{2}{\rho}} \\ \frac{v \cdot A_{rod}}{P_A - P_P} = c_q \cdot A_{effective} \cdot \sqrt{\frac{2}{\rho}} \end{cases} \quad (4.12)$$

By assuming constant nominal orifice areas for both paths and ideal fluid conditions, with constants ρ and c_q , the system of equations simplifies to:

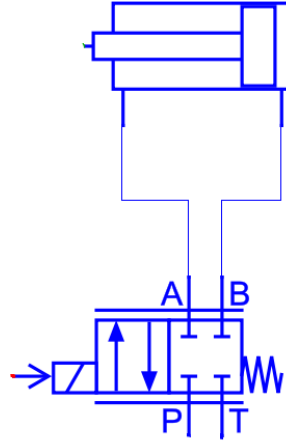


Figure 4.29: Example of a linear actuator-proportional valve model implemented in the Common Pressure Rail architecture

$$\begin{cases} \frac{v \cdot A_{piston}}{P_T - P_B} = x \cdot \text{valve_characteristic} \\ \frac{v \cdot A_{rod}}{P_A - P_P} = x \cdot \text{valve_characteristic} \end{cases} \quad (4.13)$$

The goal of the proportional valve algorithm is to determine the value of x in the system of equations 4.13, ensuring the actuator meets the flow rate and load pressure requirements.

In the system of equations 4.13, the variables P_A , P_B , and x are unknowns. P_A and P_B are defined according to the actuator load, while x represents the modulation value of the proportional valve, ensuring alignment with both pressure and speed requirements.

Given this scenario, the system 4.13 is underdetermined, described by two equations with three unknowns. However, one of the controller inputs is the external force applied to the actuator, which must equal the force generated by the actuator f_{rod} :

$$F_{external} = f_{rod} \quad (4.14)$$

Combining equations 4.14 and 4.4 yields:

$$P_B \cdot A_{piston} - P_A \cdot A_{rod} = F_{external} + v \cdot \text{viscous_friction} \quad (4.15)$$

Adding this equation to the system 4.13:

$$\begin{cases} \frac{v \cdot A_{piston}}{P_T - P_B} = x \cdot \text{valve_characteristic} \\ \frac{v \cdot A_{rod}}{P_A - P_P} = x \cdot \text{valve_characteristic} \\ P_B \cdot A_{piston} - P_A \cdot A_{rod} = F_{external} + v \cdot \text{viscous_friction} \end{cases} \quad (4.16)$$

This results in a fully-defined system of three equations with three unknowns. The algorithm's primary function is to resolve this system of equations, outputting the value of x .

Now that the entire theoretical aspect regarding the algorithm for calculating proportional valve modulation has been addressed, it would be possible to proceed to the developed algorithm where all the considerations have been translated into code (see Algorithm 3).

1. Initialize the pressure matrix vector (**matrix**) with pressure values sourced from the interface between Simulink and AMESim models, representing the pressures within the rails (see Algorithm 3 - line 1).
2. Initialization MATLAB function's output (see Algorithm 3 - line 2): the variable **proportional_signal** is a float variable initialized with the value 0, serving as the initial output placeholder, storing the modulation value for the proportional valve, which ranges from 0 (fully closed) to 1 (fully open).
3. Reference velocity check and load pressure/flow rate graph quadrant determination (see Algorithm 3 - lines 3 and 11): when the **reference_velocity** is non-zero, the system initiates the necessary calculations. Conversely, the **proportional_signal** output reverts to zero, signifying that the valve is fully closed, thus contributing to the sealing process.
4. Calculate the pressures at the ports P and T of the proportional valve (see Algorithm 3 - lines 4 \rightarrow 5 and lines 23 \rightarrow 13): in the theoretical section, when the operational principle of the algorithm was described, it was mentioned that the pressures at the P_P and P_T ports of the proportional valve must be known to have a completely defined system of equations. To this end, it is possible to calculate these pressures based on two known data points. The first is the pressure values of the rails connected to the two chambers. This value is passed as an index of the matrix **matrix** via the input from the on-off valve combination calculation function (**combination[j,k]**). The second data point is the fluid flow rate passing through the on-off valves, from which the downstream pressure drop across the on-off valves can be evaluated.
5. Resolution of the system of equations for evaluating the **proportional_signal** to be output by the Simulink function (see Algorithm 3 - lines 6 \rightarrow 10 and 14

Algorithm 3 Proportional valve control logic algorithm - linear actuators

```
1: matrix = [LP, MP, HP];
2: proportional_signal = 0;
3: if reference_velocity > 0 then
4:    $p_P = \text{matrix}(\text{combination}(1,1)) - \text{on\_off\_valve\_p\_drop}$ ;
5:    $p_T = \text{matrix}(\text{combination}(1,2)) + \text{on\_off\_valve\_p\_drop}$ ;
6:   syms proportional_signal,  $p_{piston}$ ,  $p_{rod}$ 
7:    $eq1 \leftarrow |Q_{piston}| / \sqrt{p_T - p_{piston}} = \text{proportional\_signal} \times \text{valve\_char\_prop}$ ;
8:    $eq2 \leftarrow |Q_{rod}| / \sqrt{p_{rod} - p_P} = \text{proportional\_signal} \times \text{valve\_char\_prop}$ ;
9:    $eq3 \leftarrow f_{rod} - \text{external\_force} = 0$ ;
10:  [proportional_signal,  $p_{piston}$ ,  $p_{rod}$ ]  $\leftarrow$  solve([eq1, eq2, eq3]);
11: else if reference_velocity < 0 then
12:    $p_P = \text{matrix}(\text{combination}(1,1)) + \text{on\_off\_valve\_press\_drop}$ ;
13:    $p_T = \text{matrix}(\text{combination}(1,2)) - \text{on\_off\_valve\_press\_drop}$ ;
14:   syms proportional_signal,  $p_{piston}$ ,  $p_{rod}$ 
15:    $eq1 \leftarrow |Q_{piston}| / \sqrt{p_{piston} - p_T} = \text{proportional\_signal} \times \text{valve\_char\_prop}$ ;
16:    $eq2 \leftarrow |Q_{rod}| / \sqrt{p_P - p_{rod}} = \text{proportional\_signal} \times \text{valve\_char\_prop}$ ;
17:    $eq3 \leftarrow f_{rod} - \text{external\_force} = 0$ ;
18:  [proportional_signal,  $p_{piston}$ ,  $p_{rod}$ ]  $\leftarrow$  solve([eq1, eq2, eq3]);
19: end if
```

\rightarrow 18); the unknown variables in the system are defined as symbolic scalar variables using the `syms` command.

Once the value of proportional valve modulation ensuring the required force generation and actuator speed has been calculated, this value is outputted by the Simulink model and applied within the same timestep as data acquisition to the AMESim model.

4.2.3 Implementation and Analysis of Chokes Integration in the Simulink Model

Prior analysis has been conducted on a relatively idealized system configuration. The dimensions and characteristics of the on-off valves have been selected to represent those that could feasibly be implemented in a distributor installed on a 9-ton excavator utilizing a Common Pressure Rail architecture. However, it must be noted that the baseline excavator model, as well as the comparative model for fuel economy and hydraulic losses, is based on an AMESim model employing a Load Sensing architecture, as discussed in Section 3. This latter model incorporates several hydraulic chokes to achieve fuel consumption and hydraulic losses that are comparable to a real-world Load Sensing excavator. These dissipative elements were added to enhance the model's realism.

The integration of these dissipative elements into the Common Pressure Rail model in AMESim could have been straightforwardly achieved by modifying the on-off valves such that the orifice area when the valve is fully open is smaller than that calculated for a potential application of the architecture. The decision-making algorithms for both the operating mode of the on-off valves and the modulation of the proportional valve are designed to be modular, with the characteristics of the on-off valves provided as input parameters to the controller. Thus, should smaller or larger valves be utilized, the controller's evaluations could be adjusted simply by inputting the new valve data as parameters, obviating the need for any algorithmic modifications.

In the interest of maintaining modularity and ensuring an unbiased comparison between the AMESim Load Sensing model and the developed Common Pressure Rail model, it was decided to retain the previously evaluated on-off valves and incorporate the same hydraulic chokes present in the LS circuit. Figure 4.30 illustrates a macro example of the linear actuator subsystem, including the hydraulic chokes and proportional valve arrangement in the AMESim models. The chokes are integrated into all linear actuators within the model. As depicted in the figure, the chokes are installed on both the supply and return lines, situated downstream of the proportional valve and before the actuator chambers on both sides of each linear actuator. This placement renders the algorithms presented in Sections 4.2.2 and 4.2.2 unusable.

Both algorithms rely on two information sources: one upstream of the on-off valves and one downstream of the actuators. Specifically, the first source comprises pressure transducers positioned on the rails, informing the controller of the state of the supply system. The second source includes force sensors on the piston rods, providing data on the interaction between the system and the environment. The excavator subsystem state, encompassing everything between these two information sources, is calculated within the controller. The controller, informed by input

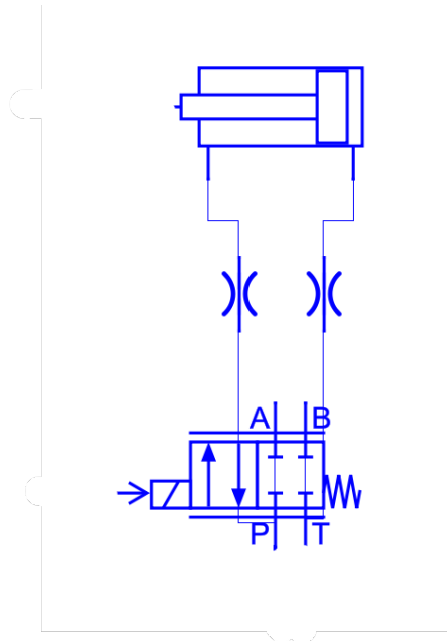


Figure 4.30: Implementation of linear actuator and chocks submodels in AMESim

parameters regarding the various circuit components, determines the pressure and flow rate at the input and output of each circuit element. The introduction of new elements such as hydraulic chokes into the subsystem, without accurately modifying the algorithm to account for their presence, would result in erroneous outputs that do not consider the presence of these elements.

Therefore, the following section details the modifications made to various parts of the two algorithms to account for the presence of these additional elements. To avoid redundancy, only the updated sections of the algorithms integrating hydraulic chokes at the code level are included, excluding the complete versions.

In the context of hydraulic systems, a choke refers to a flow restriction device, often a type of orifice or valve, that is used to control the flow rate and pressure within the system while creating a deliberate pressure drop and dissipating energy. In the AMESim environment, it is possible to define the characteristics of such an element similarly to valves by setting the orifice area or specifying the maximum flow rate that can pass through it and the pressure drop it must generate at the passage of the maximum flow rate. In this case, as with all valves, the orifices have been characterized using the latter methodology. Based on this and the assumptions made in Section 4.2.2, a choke characteristic can be defined as:

$$\begin{aligned}
 choke_characteristic &= c_q \cdot A \cdot \sqrt{\frac{2 \cdot \Delta P}{\rho}} \\
 &= \frac{maximum_flow}{corresponding_pressure_drop} \\
 &\approx constant
 \end{aligned} \tag{4.17}$$

The variables *maximum_flow* and *corresponding_pressure_drop* have been defined in the CPR model to match those characterizing the chokes present in the LS model circuit.

Starting from this, the next step is to incorporate these into the on-off valve decision-making algorithm. For the on-off valve algorithm, the necessary modifications include defining the variables *choke_characteristic* for both the supply-side and return-side chokes based on the new input parameters provided to the controller, such as *maximum_flow* and *corresponding_pressure_drop* for each choke. Regarding the decision-making process, the presence of chokes alters the pressure that each actuator will actually have in the big chamber and the small chamber depending on the operational mode. Therefore, when calculating the pressures p_{piston} and p_{rod} for each operational mode to compute the rod force f_{rod} , it is essential to account for the pressure drops that will occur across the chokes when a certain flow rate proportional to the reference velocity is required:

$$p_{pis} = \begin{cases} matrix(k) - on_off_p_drop - prop_p_drop - choke_p_drop, & \text{if } v_{ref} > 0; \\ matrix(k) + on_off_p_drop + prop_p_drop + choke_p_drop, & \text{if } v_{ref} < 0; \end{cases}$$

$$p_{rod} = \begin{cases} matrix(j) + on_off_p_drop + prop_p_drop + choke_p_drop, & \text{if } v_{ref} > 0; \\ matrix(j) - on_off_p_drop - prop_p_drop - choke_p_drop, & \text{if } v_{ref} < 0; \end{cases}$$

$$choke_p_drop_i = \frac{Q_i}{choke_characteristic} = \frac{v_{ref} \cdot A_i}{choke_characteristic}$$

Where A_i could be either the piston side chamber area or the rod side one.

Concerning the algorithm for the proportional valve modulation decision-making, the task is more complex. As previously mentioned, the controller must evaluate at each time step what happens in terms of pressures and flow rates throughout the subsystem it is controlling. Initially, the algorithm for the proportional valve relied on three known data points: the pressures at the P and T ports of the proportional valve and the applied force on the actuator. From these three pieces of information, a system of three equations 4.16 was constructed, enabling the evaluation of the pressures at ports A and B and the valve displacement necessary to generate them. This allowed evaluation of the subsystem pressures at any point.

In the subsystem discussed in this paragraph, however, the components now include not only the linear actuator and proportional valve but also two hydraulic chokes. Therefore, the algorithm's development aimed to generate a set of equations that, upon resolution, would provide the pressure values throughout the subsystem. This includes pressures A and B downstream of the proportional valve as well as the pressures downstream of the chokes. In this context, a set of five equations in five unknowns was formulated (see Algorithm 4), relating the known flow rate as a function of the reference velocity with the characteristics of the proportional valve and linear chokes.

Algorithm 4 Proportional valve control logic algorithm - linear actuators with chokes

```

if reference_velocity > 0 then
    syms prop_signal, ppiston, prod, pA, pB
    eq1 ← Qpiston/√pT - pB = prop_signal × valve_char_prop;
    eq2 ← Qpiston/√pB - ppiston = prop_signal × choke_char_piston;
    eq3 ← Qrod/√pprod - pA = choke_char_rod;
    eq4 ← Qrod/√pA - pP = prop_signal × valve_char_prop;
    eq5 ← frod - external_force = 0;
    [prop_signal, ppiston, prod, pA, pB] ← solve([eq1, eq2, eq3, eq4, eq5]);
else if reference_velocity < 0 then

```

The case of negative reference velocity is left to the reader to explore further.

```

end if

```

By solving this system of equations, the algorithm determines the proportional valve displacement that matches the operational pressures and meets the speed requirements despite the presence of hydraulic chokes.

4.2.4 Implementation of Low-Pass Filter for Actuator Control

In the section dedicated to the design of low-pass filters (Section 4.1.2), it was discussed how, although such filters can effectively reduce signal noise, their implementation inevitably introduces delays in the output.

The development of the algorithms implemented in the Simulink model of the controller, along with the testing phase of these algorithms, was conducted considering a simplified model of a Common Pressure Rail architecture in AMESim (see Figure 4.31) with a single linear actuator. Ideal pressure sources supplied the rails, and the filtered force signals, generated using low-pass filters, were utilized as inputs for both the controller and the actuators. These filters, discussed in Section 4.1.2, were designed based on the force sensor signals connected to the linear actuators in the AMESim model of the excavator based on the Load Sensing architecture. The objective in designing these filters, as previously mentioned, was to obtain force signals that accurately reflect the relevant trends and magnitudes for the digging and dumping work cycle, capturing the interactions between the excavator system and the surrounding environment.

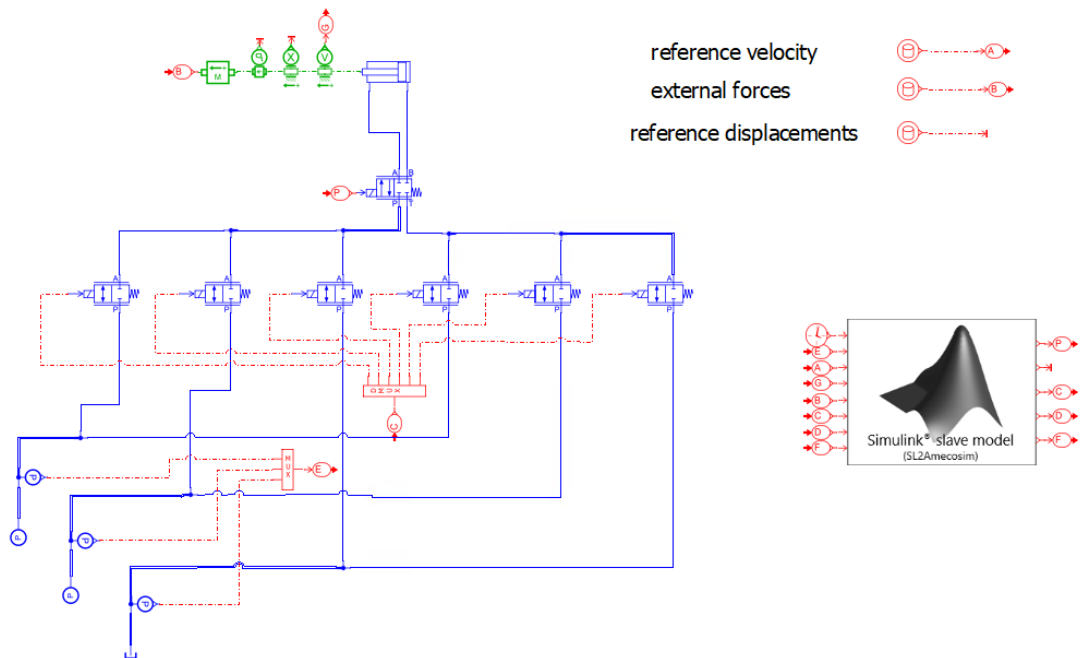


Figure 4.31: AMESim model of the simplified Common Pressure Rail architecture with a linear actuator, ideal pressure sources feeding the rails, and filtered force signals applied to both the actuator and as inputs to the controller.

Considering this highly simplified model, the final results obtained upon the completion of the controller development were highly satisfactory, with errors in terms of actuator speed and displacement remaining below 1%. Figures 4.32 and 4.33 illustrate the results obtained with the simplified CPR model and the previously described Simulink controller model, in terms of speed and displacement of the boom actuator, respectively.

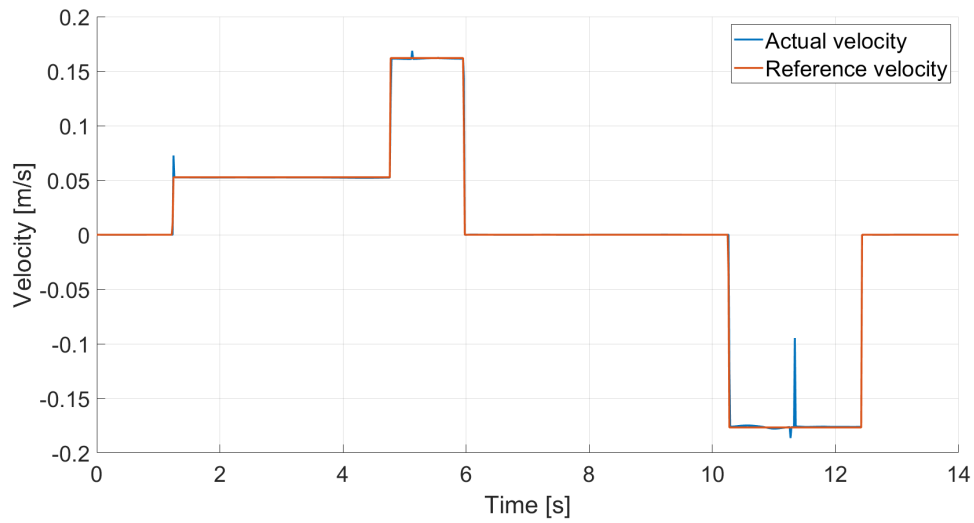


Figure 4.32: Comparison between reference speed input to the controller and the actual speed generated by the actuator in the AMESim model of the simplified Common Pressure Rail architecture during a dig and dump cycle

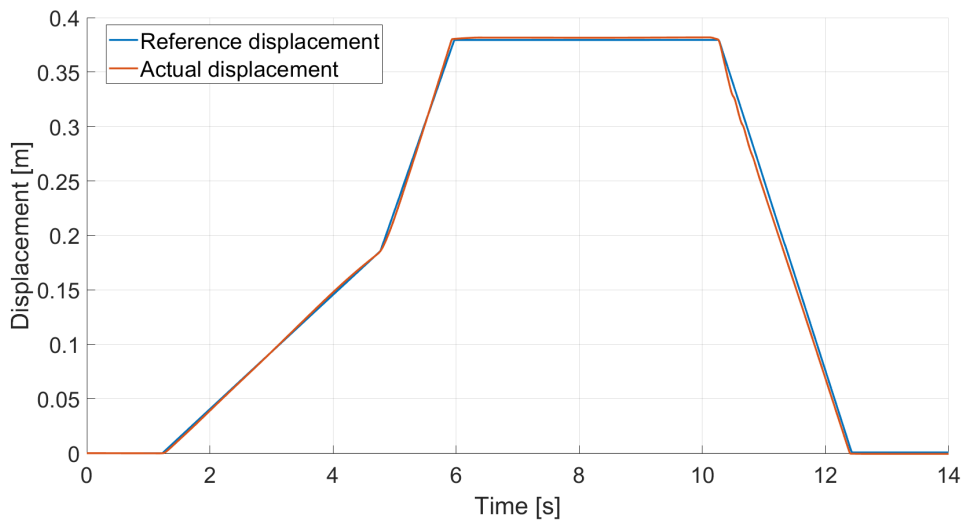


Figure 4.33: Comparison between reference and the actual displacements in the AMESim model of the simplified Common Pressure Rail architecture during a dig and dump cycle

The collected data clearly demonstrate the algorithm's capability to manage the entire architecture, ensuring optimal performance even under the most critical operational conditions. This success highlights the robustness and effectiveness of

the system in promptly responding to diverse requirements that may arise during a standard work cycle.

However, as the model complexity increased, the results obtained were not equally positive. The implementation of the mechanics and kinematics of the actuator subsystem, along with the interaction between the excavator system and the environment using the Planar Mechanical Library in AMESim, led to stability issues. The forces resulting from the interaction between the excavator system and the environment were not characterized by a frequency spectrum with only low-frequency components, but were affected by significant noise contributions, as shown in Section 4.1.2. Providing unfiltered input values to the Simulink controller meant basing the controller's decision-making process on misleading data that were not effectively meaningful for the actuator. Some tests were conducted using a more complex AMESim CPR model than the one described in Figure 4.31, where all three linear actuators were connected to the pressure rails, and the Planar Mechanical Library was implemented for simulating the actuator-soil interaction (see Figure 4.34).

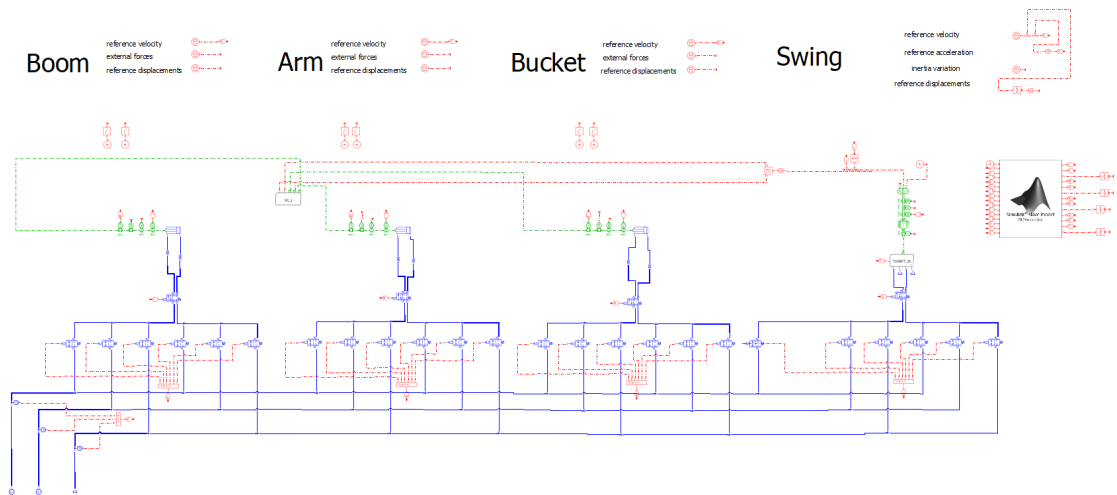


Figure 4.34: Near-final AMESim model of a Common Pressure Rail system with ideal pressure sources as the supply system

In the considered model, the forces detected by sensors positioned on each actuator are not subjected to any filtering operation before being sent to the controller (Figures 4.35, 4.36, and 4.37 for the boom, arm, and bucket, respectively). The velocities of the actuators in response to these forces are depicted in Figures 4.38, 4.39, and 4.40 for the boom, arm, and bucket, respectively.

As evident from the forces and velocity graphs, the system exhibits high-magnitude and high-frequency stable under-damped oscillations. This phenomenon

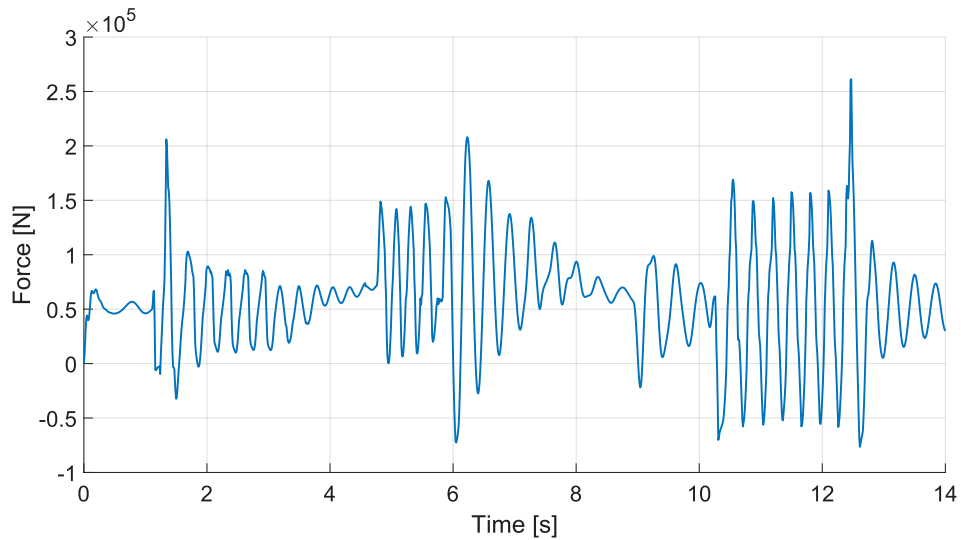


Figure 4.35: Unfiltered forces detected in the CPR AMESim model with ideal pressure sources as the supply system on the boom actuator during dig and dump cycle

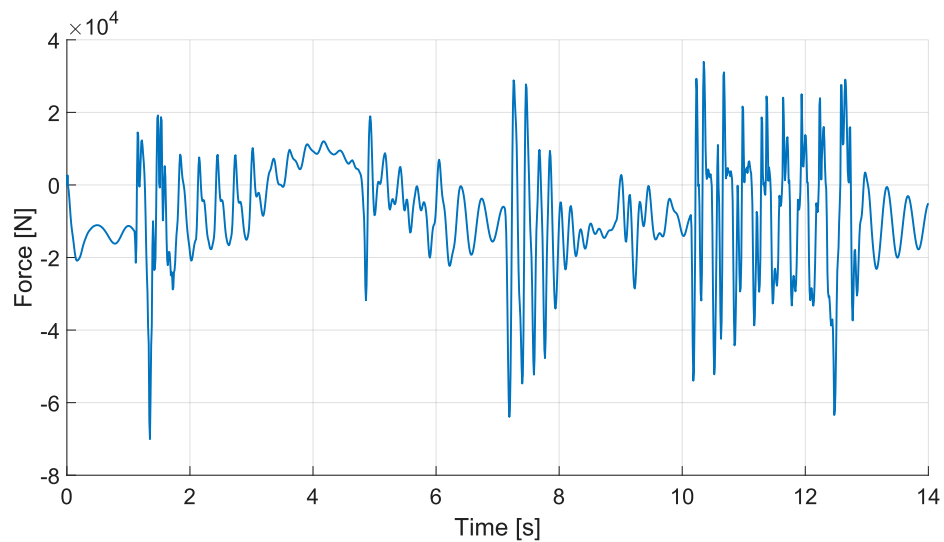


Figure 4.36: Unfiltered forces detected in the CPR AMESim model with ideal pressure sources as the supply system on the arm actuator during dig and dump cycle

is caused by the nature of the excavator system, as configured in generating the results shown in Figures 4.35, 4.36, and 4.37 for forces, and in Figures 4.38, 4.39, and 4.40 for velocities. This system can be described as under-damped, characterized

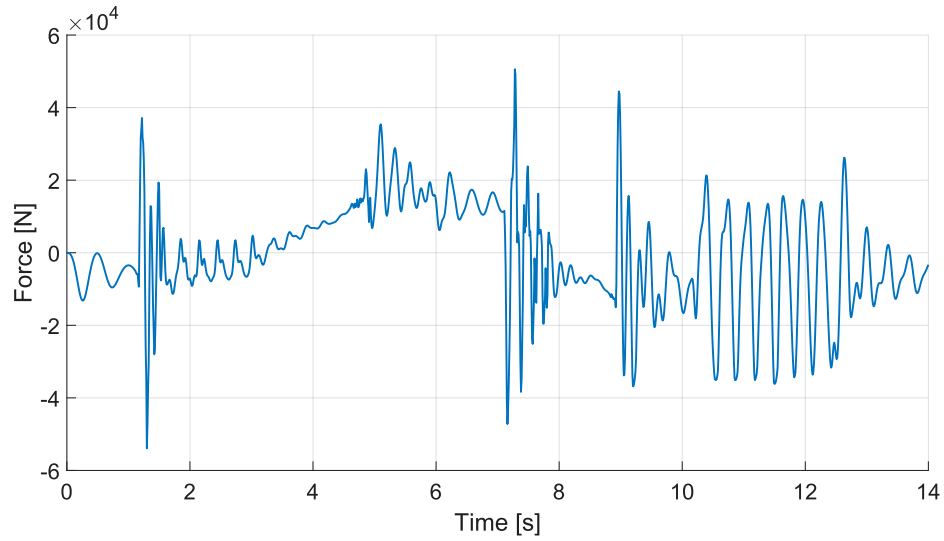


Figure 4.37: Unfiltered forces detected in the CPR AMESim model with ideal pressure sources as the supply system on the bucket actuator during dig and dump cycle

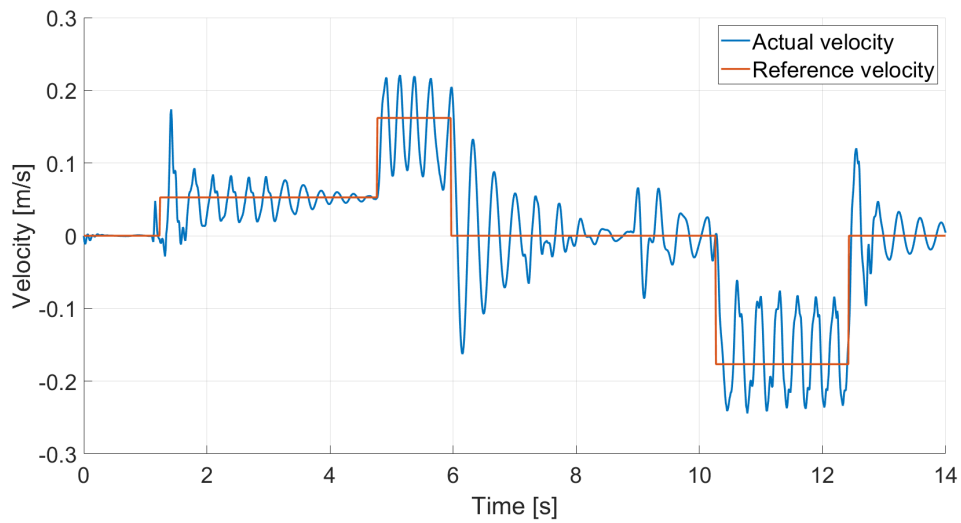


Figure 4.38: Comparison between reference and the actual velocity of the boom actuator in the CPR AMESim model with ideal pressure sources as the supply system during dig and dump cycle

by the transfer function reported in the equation 4.18.

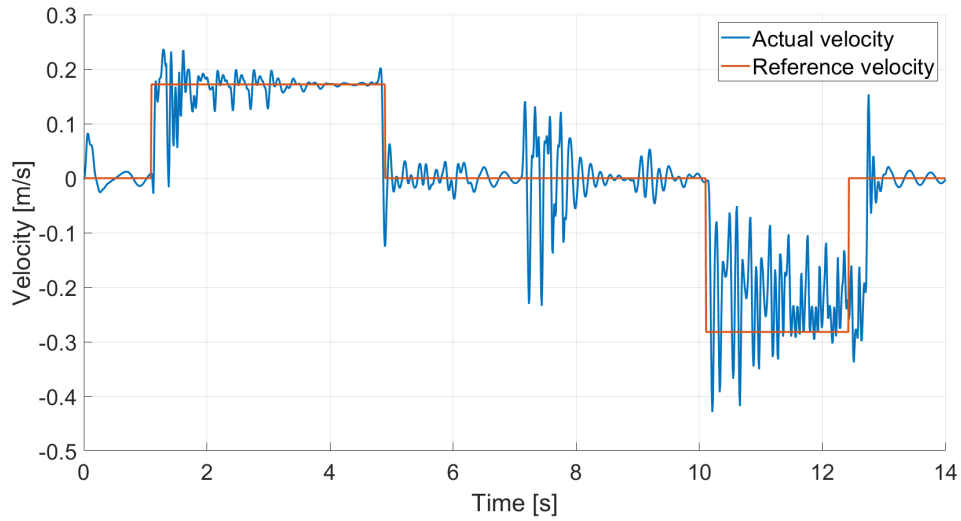


Figure 4.39: Comparison between reference and the actual velocity of the arm actuator in the CPR AMESim model with ideal pressure sources as the supply system during dig and dump cycle

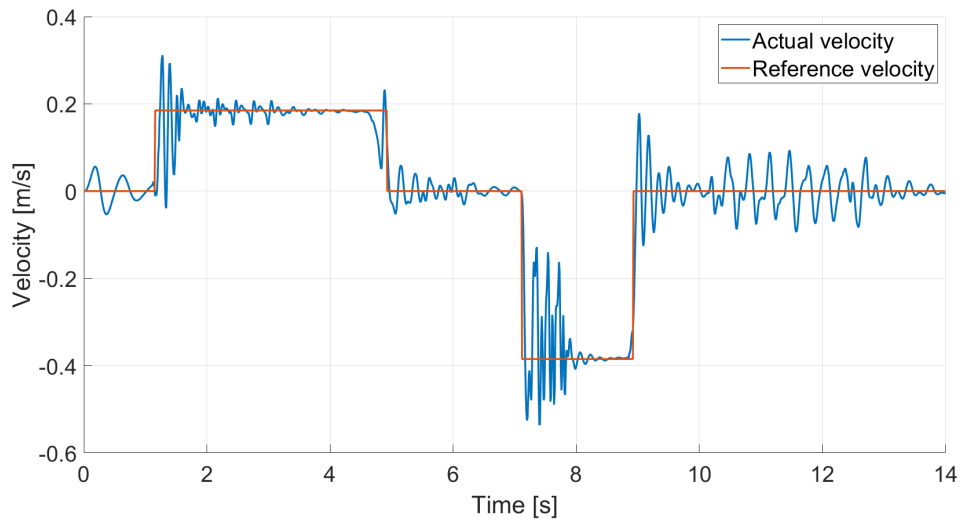


Figure 4.40: Comparison between reference and the actual velocity of the bucket actuator in the CPR AMESim model with ideal pressure sources as the supply system during dig and dump cycle

$$G(s) = \frac{\omega_0^2}{s^2 + 2\zeta\omega_0s + \omega_0^2} \quad (4.18)$$

where ω_0 represents the natural frequency of the system and ζ denotes the damping coefficient. The issue with the current configuration is that ζ is less than 1, indicating underdamped behavior characterized by oscillations that decay exponentially over time. Figure 4.41 illustrates the response of such a system to a step input. In the chosen setup, the only source of damping is the non-ideal fluid effects; however, due to the limited fluid volumes in the circuit, this damping coefficient is minimized.

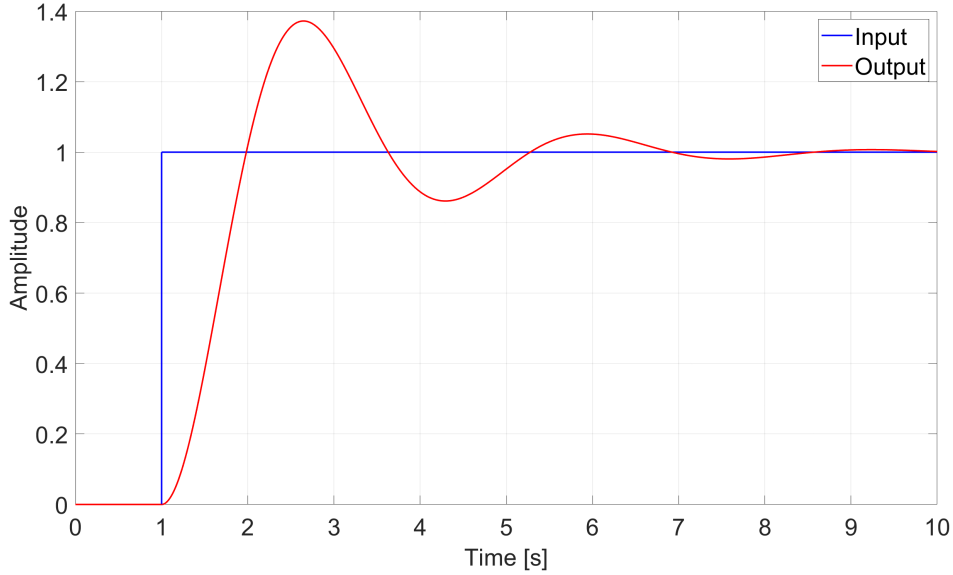


Figure 4.41: Dynamic response of an under-damped system: step input vs output

This type of system response is evident in the velocity graphs of the three actuators, as shown in Figures 4.38, 4.39, and 4.40. During the extension phase, the velocities exhibit initial oscillations following a step input, which gradually diminish in magnitude. The introduction of fluid volumes into the circuit is, however, not sufficient to significantly increase the damping coefficient, as the forces involved are of very high magnitude.

To address this issue and increase the damping ratio, a straightforward solution was implemented: low-pass filters developed in Section 4.1.2 were applied to each actuator's force signals before entering the controller. This approach aimed to ensure a reliable, stable, and robust decision-making process. Figures 4.42, 4.43, and 4.44 depict the force signals of each actuator before and after the application of the filter. Additionally, Figures 4.45, 4.46, and 4.47 illustrate the velocities of the actuators.

The clear improvement over the previously described case study is now evident. However, the achieved results have been somewhat unsatisfactory, as all three

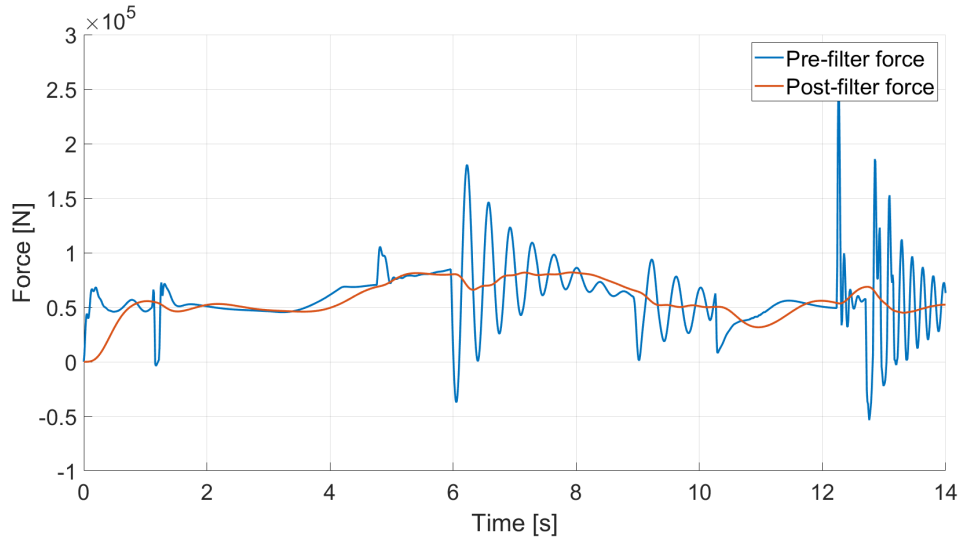


Figure 4.42: Evaluating forces exchanged between the boom actuator and the environment, with and without a handmade low-pass filter design, during the dig and dump cycle

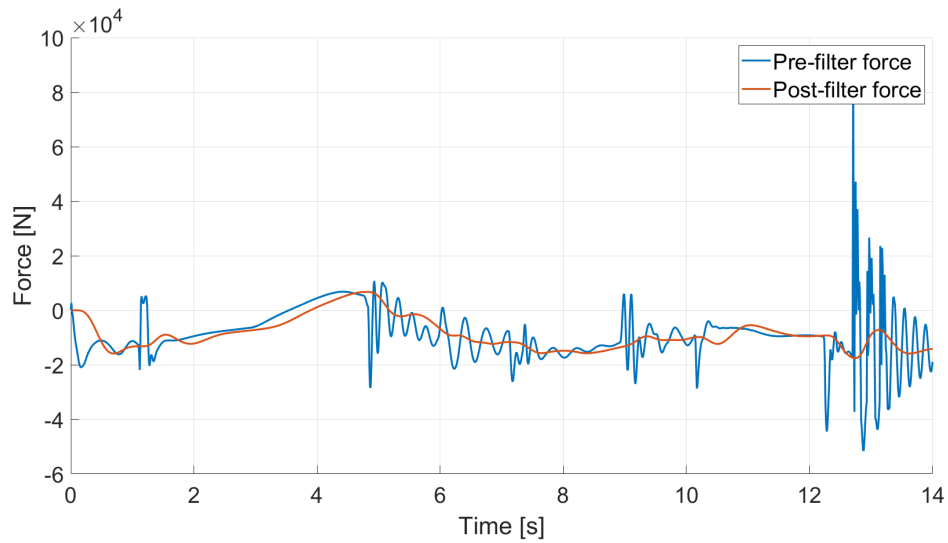


Figure 4.43: Evaluating forces exchanged between the arm actuator and the environment, with and without a handmade low-pass filter design, during the dig and dump cycle

velocity graphs show that the actuators' velocity trends do not properly follow the reference curves. Specifically, the actual actuator velocity curves often lag below the reference curve during the extension phase and exceed it during the retraction

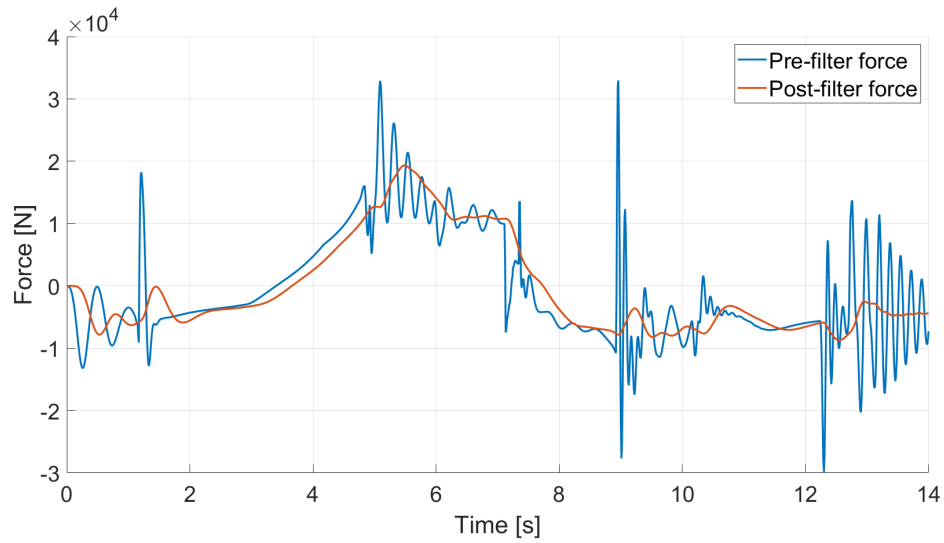


Figure 4.44: Evaluating forces exchanged between the bucket actuator and the environment, with and without a handmade low-pass filter design, during the dig and dump cycle

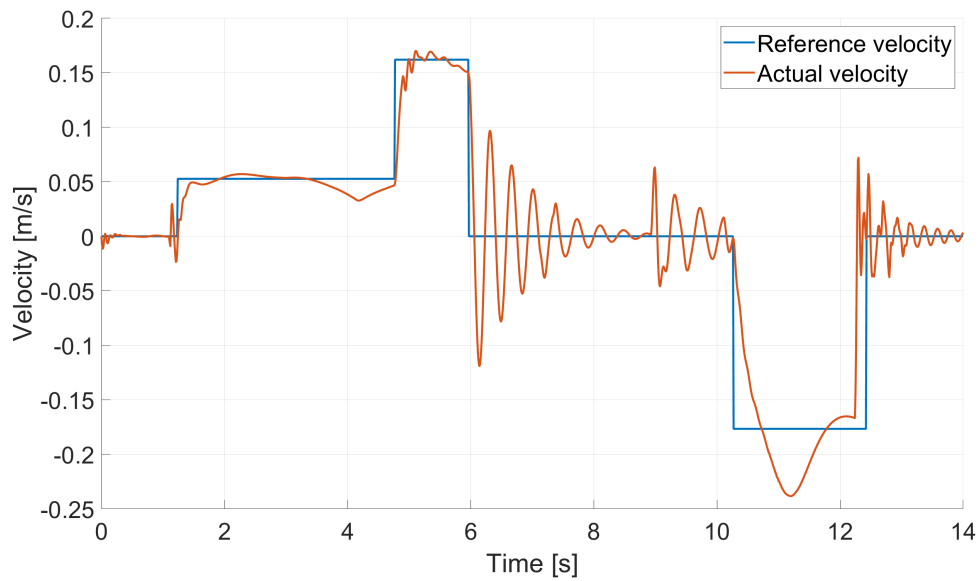


Figure 4.45: Comparison between reference and the actual velocity of the boom actuator in the CPR AMESim model during dig and dump cycle with the handmade low-pass filter design

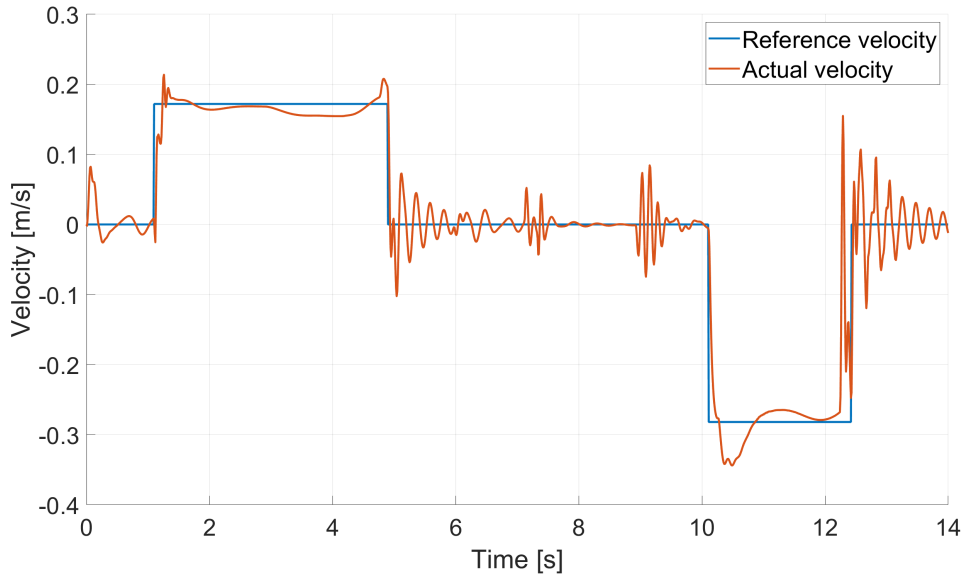


Figure 4.46: Comparison between reference and the actual velocity of the arm actuator in the CPR AMESim model during dig and dump cycle with the handmade low-pass filter design

phase. This discrepancy can be observed by examining the force graphs in Figures 4.42, 4.43, and 4.44. These graphs show how the filtered output curves are shifted along the x-axis by several milliseconds.

As highlighted in Section 4.1.2, increased signal suppression enhances controller stability, ensuring a more consistent and stable input for the controller’s decision-making process. However, heightened suppression also introduces input signal delays. Given the trend of force signals, which increase during the actuators’ extension phase and decrease during their retraction phase, an x-axis shift causes the controller to underestimate the demand during extension and overestimate it during retraction. This condition leads to delays in the controller’s response and compromises the system’s ability to promptly react to environmental stimuli.

Optimizing Low-Pass Filter Cut-off Frequencies for Actuator Control: A Design of Experiments Approach

In response to the observed limitations of the previously employed low-pass filters, an optimal method was sought to adjust their cutoff frequencies. The primary objective was to minimize velocity errors encountered in the system’s three actuators. An approach based on Design of Experiments (DOE), a statistical method, was adopted to systematically explore how variations in cutoff frequencies influence

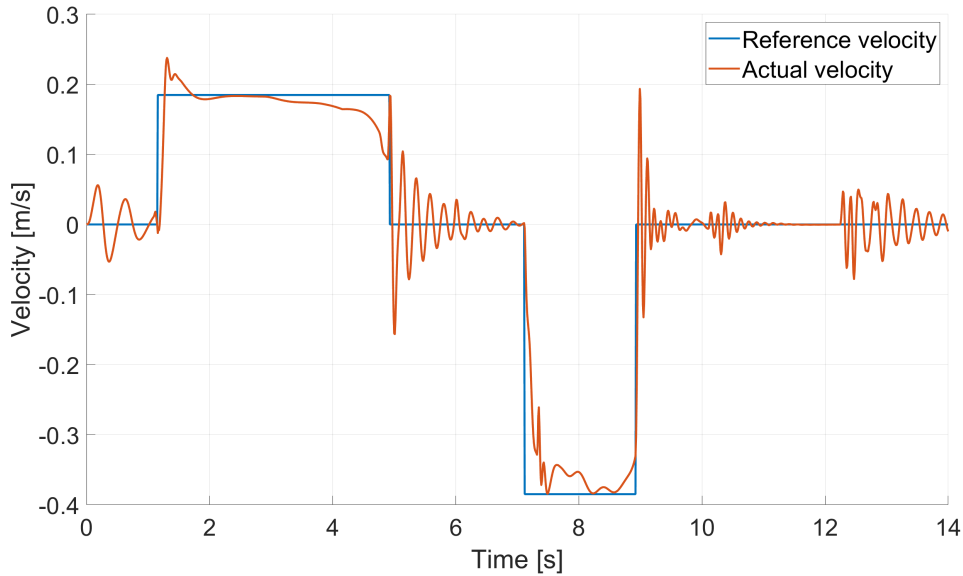


Figure 4.47: Comparison between reference and the actual velocity of the bucket actuator in the CPR AMESim model during dig and dump cycle with the handmade low-pass filter design

actuator performance. This method facilitated a more efficient and optimized design process, identifying optimal filter configurations to enhance overall system operation.

The DOE was implemented directly within the AMESim simulation environment, using the cutoff frequencies of the three low-pass filters as design variables. It is crucial to note that a filter's specification extends beyond its cutoff frequency alone; the filter order plays a critical role in its characterization. Following a series of experiments, first-order filters were selected for all actuators due to their balanced performance in terms of frequency response slope, selectivity, phase response accuracy, and implementation complexity. Consequently, the variables considered in the DOE were exclusively the cutoff frequencies.

AMESim provides various techniques for configuring the DOE, including full combination, unidirectional, and user-defined setups (see Figure 4.48).

In the research, the full combination technique was chosen. This decision was guided by the mechanical configuration of the excavator under study, where the arm subsystems are interconnected through ideal revolute joints. Consequently, vibrations generated by one actuator propagate to other components, making it crucial to assess the mutual influence of low-pass filter cutoff frequencies on all three actuators to optimize overall system performance. This approach allowed for a detailed and systematic analysis of the design variables' effects, enhancing

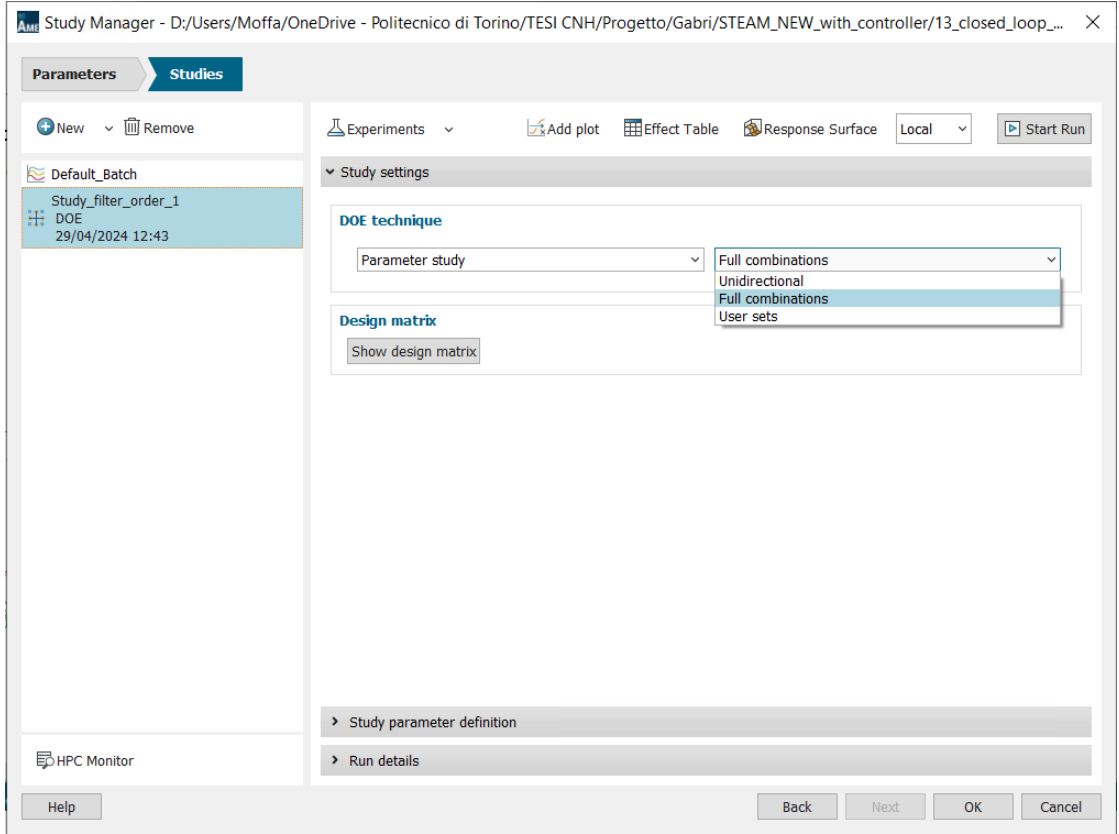


Figure 4.48: AMESim interface for DOE configuration

understanding and optimization of the actuator control system within the specific context of the studied excavator.

Regarding the DOE objective, the goal was to minimize the root mean square (rms) of the velocity errors between the reference velocity input to the controller and the velocity actually generated by the three actuators, based on the low-pass filter cutoff frequencies:

$$\text{Minimize } \sqrt{\sum_{i=1}^3 \epsilon_i^2} \quad (4.19)$$

where:

- ϵ_i represents the velocity error of actuator i , defined as $\epsilon_i = v_{ref} - v_{actual}$
- ϵ_i depends on the cutoff frequencies of the low-pass filters $f_{c,boom}$, $f_{c,arm}$, $f_{c,bucket}$

Thus, the objective is formulated as:

$$\text{Minimize } \sqrt{\sum_{i=1}^3 \epsilon_i^2(f_{c,\text{boom}}, f_{c,\text{arm}}, f_{c,\text{bucket}})}$$

To determine the range values for the three variables, the power spectral density graphs and frequency spectrum analysis presented in Section 4.1.2 were considered. These data defined a suitable domain to explore all possible combinations without generating physically unrealizable scenarios. Table 4.2 shows the range values along with their discretization steps.

Variable	Range of Variation	Discretization Step
$f_{c,\text{boom}}$	From 1 Hz to 3 Hz	0.1 Hz
$f_{c,\text{arm}}$	From 1 Hz to 3 Hz	0.1 Hz
$f_{c,\text{bucket}}$	From 1 Hz to 3 Hz	0.1 Hz

Table 4.2: Window values of variation and discretization step of cutoff frequencies for low-pass filters

Based on the ranges of variation for the three variables, the DOE explored a total of 9261 cases. Figure 4.49 illustrates the plot of ϵ as a function of combination i .

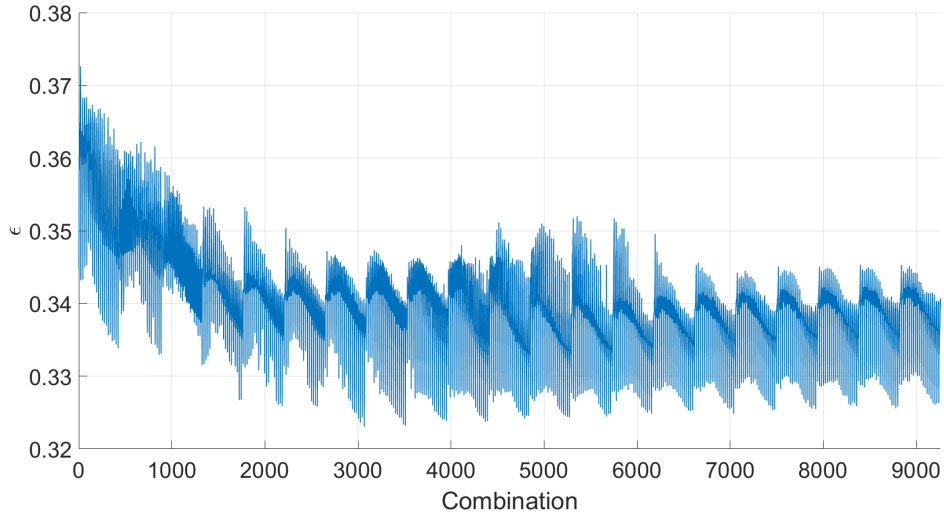


Figure 4.49: Sensitivity analysis of actuator velocity errors (ϵ) to filters cutoff frequencies

Among all configurations tested, those that achieved the best results for the defined objective are presented in Table 4.3.

Actuator	f_c [Hz]	Filter Order
Boom	1.1	1
Arm	3.0	1
Bucket	1.6	1

Table 4.3: Optimal configurations of cutoff frequencies for low-pass filters for actuators

The force signals measured before and after the filters during the dig and dump excavation cycle, configured with the optimal characteristics identified through DOE, are shown in Figures 4.50, 4.51, and 4.52 for the boom, arm, and bucket actuators, respectively.

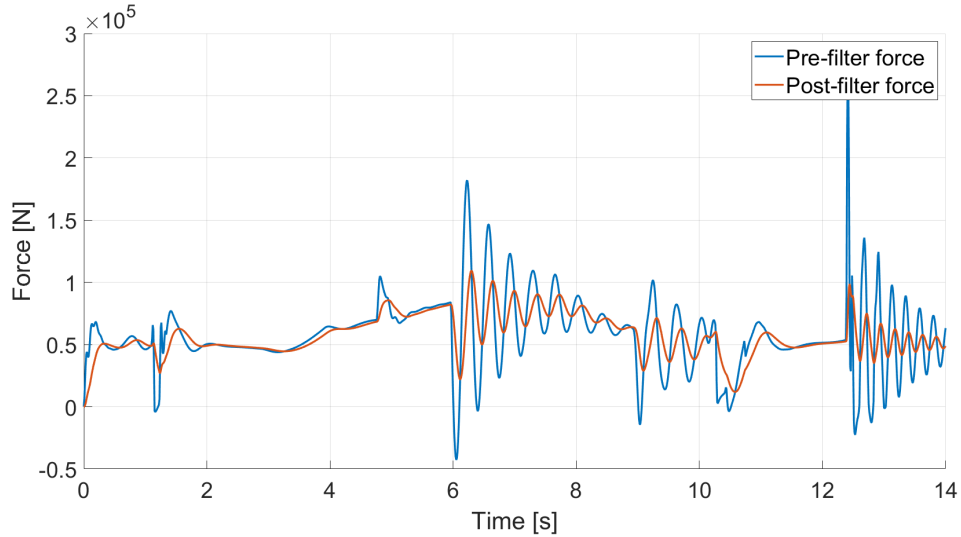


Figure 4.50: Boom actuator force signals at the input and output of new low-pass filters, with settings identified through DOE for the dig and dump excavation cycle

It can be observed that the spikes present in the graph are prevalent only when the actuators are stationary, meaning when the input velocities are zero. During the motion of the actuators, the forces exhibit linear variations or acceptable oscillations. This indicates effective suppression of interference in the input signal. Furthermore, the delay introduced by applying these filters is nearly negligible, allowing for a responsive and stable controller response to stimuli, ideal conditions for achieving a robust and reliable system. The velocity results of the actuators under open-loop control are illustrated in Figure 4.53, 4.54 and 4.55 for the boom, arm, and bucket actuators, respectively.

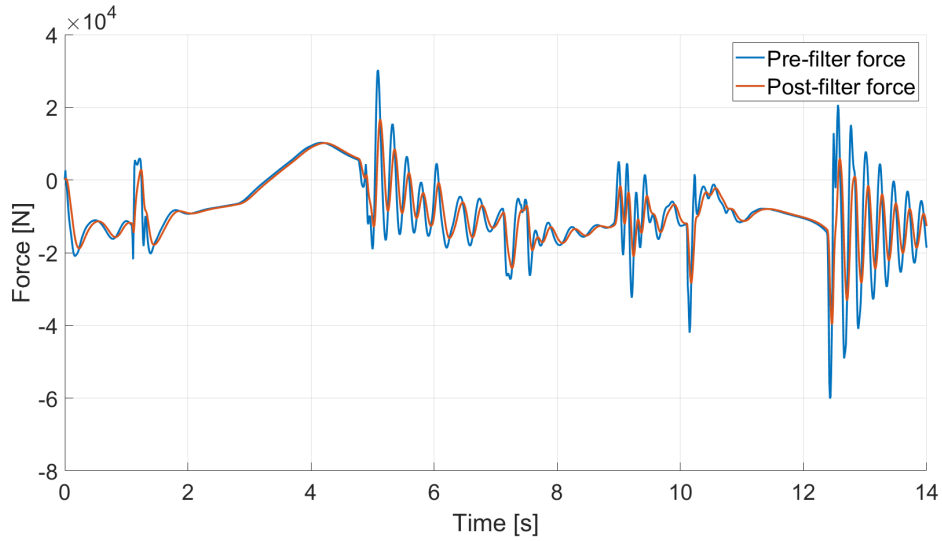


Figure 4.51: Arm actuator force signals at the input and output of new low-pass filters, with settings identified through DOE for the dig and dump excavation cycle

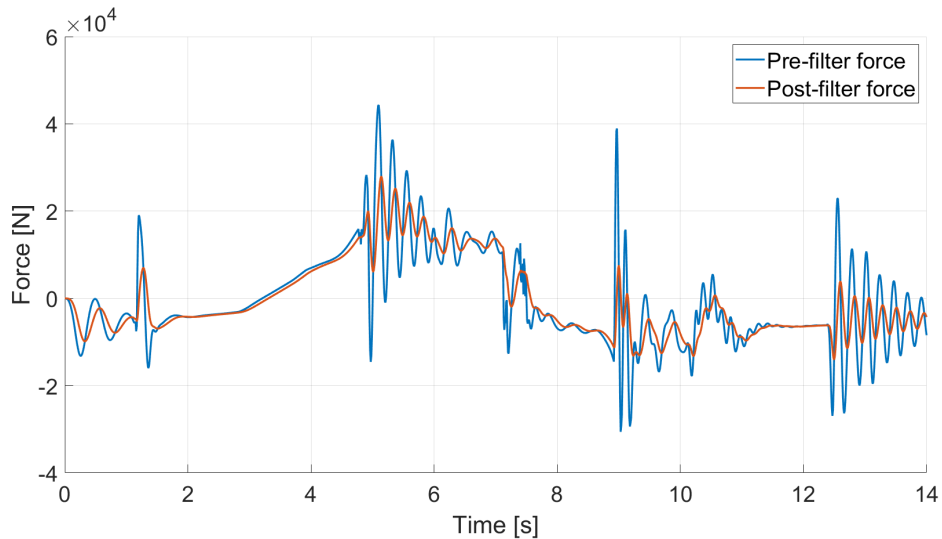


Figure 4.52: Bucket actuator force signals at the input and output of new low-pass filters, with settings identified through DOE for the dig and dump excavation cycle

The results clearly demonstrate a marked improvement in open-loop performance compared to previous approaches, thereby confirming the effectiveness of optimizing cutoff frequencies using DOE.

In conclusion, the DOE-based approach not only facilitated a thorough understanding of the design variables' effects but also enabled a more efficient and precise

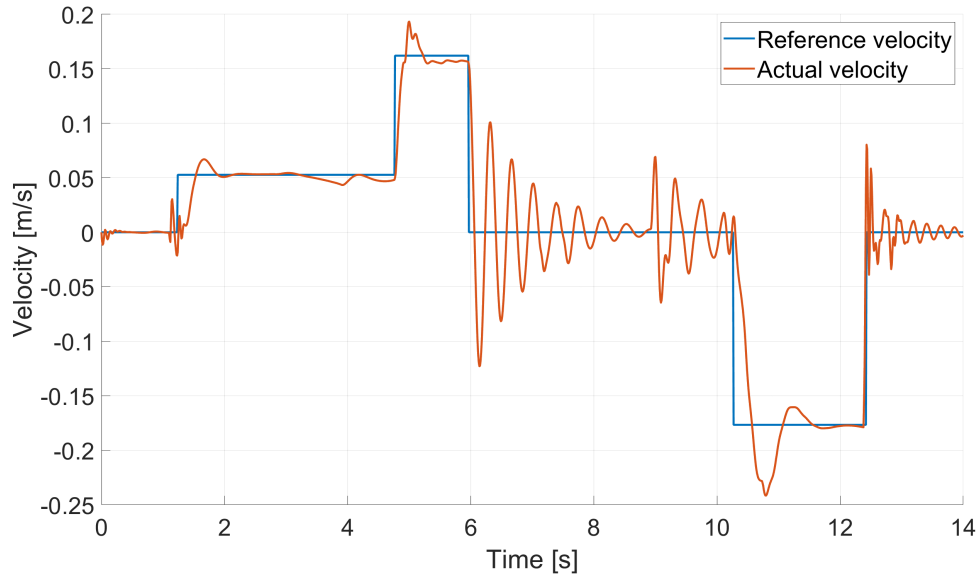


Figure 4.53: Comparison between the reference and actual velocity of the boom actuator in the CPR AMESim model during the dig and dump cycle with DOE-optimized low-pass filter parameters

design of the actuator control system. This study underscores the crucial role of DOE in optimizing the performance of complex systems, leading to significant enhancements in dynamic response and operational reliability of the actuators.

4.3 Insights into Control of the Hydraulic Motor

The discussion now moves towards the examination of the Simulink controller model part that handles the actuation of the turret hydraulic motor.

As mentioned in Section 4.2, this controller part has two primary roles. The first is to select the pressure lines to connect to the two ports of the hydraulic motor. The second is to determine the modulation of the proportional valve upstream of the hydraulic motor. Both tasks have to be performed according to the torque applied to the hydraulic motor shaft and the required movement speeds as dictated by the operator via the joystick.

4.3.1 Hydraulic Motor Operating Modes

The operating modes of a hydraulic motor, similar to those described for the linear actuator, pertain to the various configurations in which the hydraulic motor can be

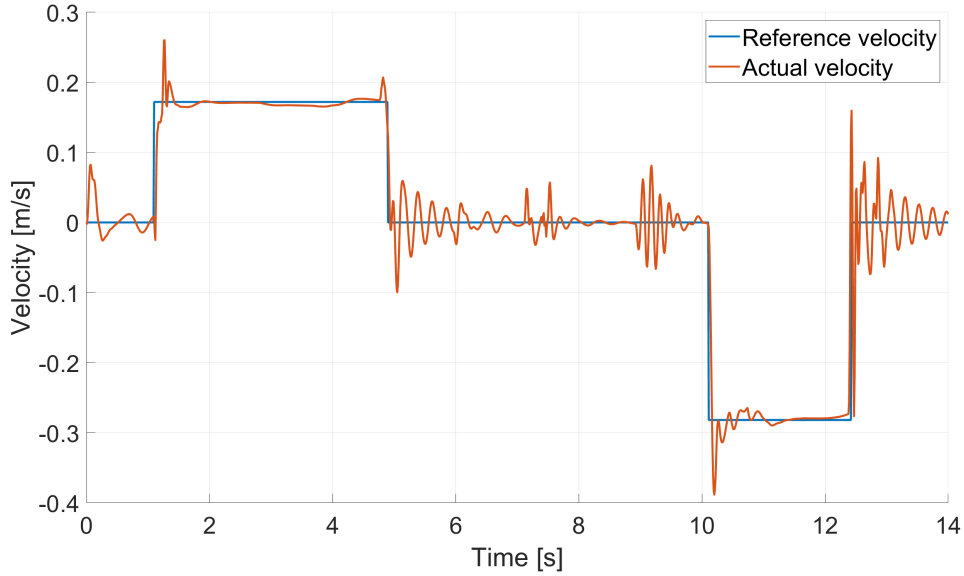


Figure 4.54: Comparison between the reference and actual velocity of the arm actuator in the CPR AMESim model during the dig and dump cycle with DOE-optimized low-pass filter parameters

connected to the three system pressure levels: high pressure (HP), medium pressure (MP), and tank pressure (LP). As illustrated in Figure 4.56, the use of switching valves enables each motor port (A and B) to connect to all three pressure levels, resulting in a total of nine distinct operating modes, as for the linear actuators.

Each operating mode is defined by a specific region in the load pressure/flow plane (p_L/Q_L). In the right half-plane, only operating points below the operating mode lines can be supplied with sufficient pressure, whereas in the left half-plane, only points above the operating mode lines are feasible.

Figure 4.57 schematically represents all nine operating modes. The naming convention specifies the pressure level connected to port A, followed by the pressure level connected to port B. The relative positions of these modes are influenced by the HP, MP, and LP pressure levels.

Briefly mentioning the physics and equations related to the hydraulic motor, it would be possible to write:

$$\begin{cases} T_{th} = V \cdot \partial p \\ q_{th} = V \cdot \omega \end{cases} \quad (4.20)$$

Considering an ideal motor, the torque generated at the shaft T_{th} is directly proportional to the motor displacement V and the pressure drop across the two

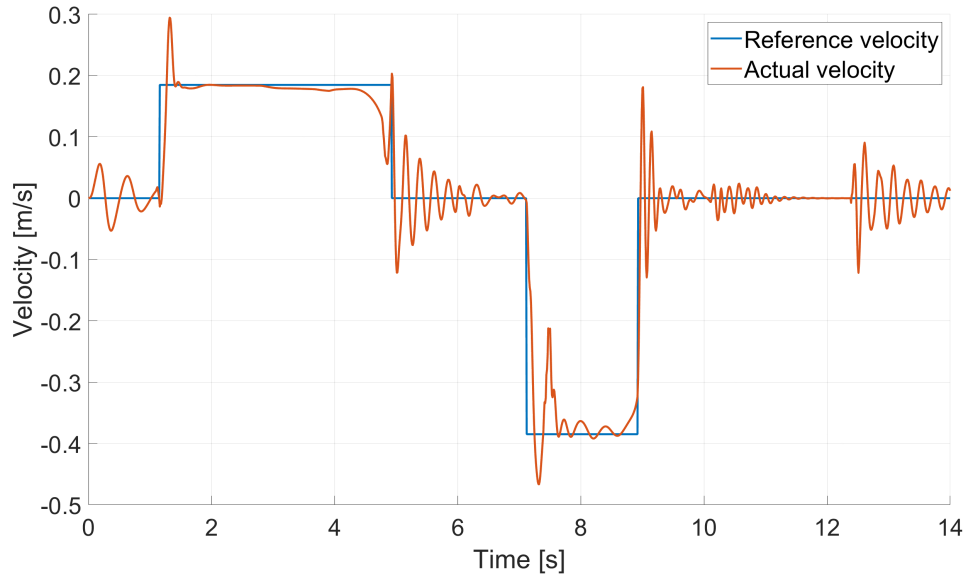


Figure 4.55: Comparison between the reference and actual velocity of the bucket actuator in the CPR AMESim model during the dig and dump cycle with DOE-optimized low-pass filter parameters

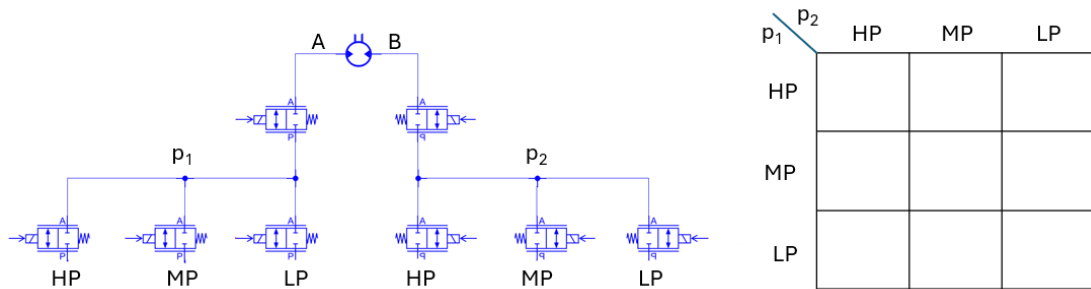


Figure 4.56: System operating modes - swing

ports. The rotational speed ω of the shaft instead, results to be directly proportional to the theoretical flow rate q_{th} passing through the motor and inversely proportional to the displacement.

Given that the hydraulic motor operates in all four quadrants of the load pressure/flow rate plane during tests, it is more appropriate to refer to it as a hydrostatic machine. The lines that pass through Quadrants I and III are used to actively supply power to the hydrostatic machine. This indicates that net positive power has been generated, and the hydrostatic machine behaves as a hydraulic motor. Conversely, lines passing through Quadrants II and IV enable kinetic energy

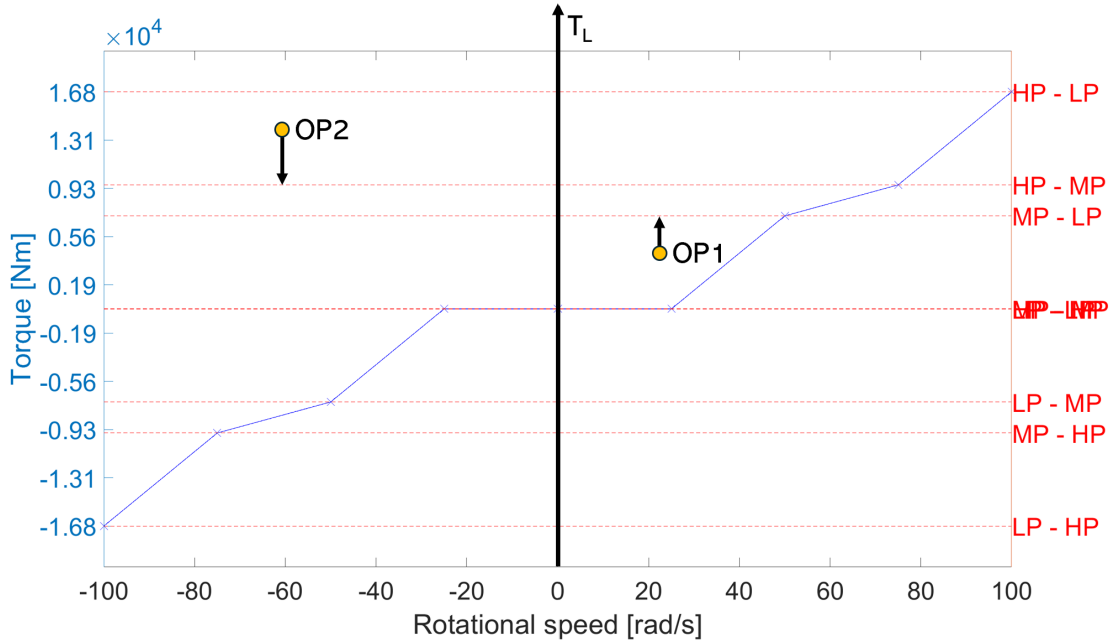


Figure 4.57: Region of operation for all nine modes - swing

recovery; this configuration allows net negative power, and the hydrostatic machine behaves as a hydraulic pump (see Table 4.4). The generated pressurized fluid can be fed back into the system, contributing to energy conservation and efficient system operation by storing excess energy in accumulators when available.

Inputs	$\omega > 0$	$\omega < 0$
$\partial p > 0$	Pumping mode	Motoring mode
$\partial p < 0$	Motoring mode	Pumping mode

Table 4.4: Hydrostatic machine operational modes based on pressure differential and rotational speed

4.3.2 Controller Details

This section presents a comprehensive analysis of the Simulink model of the swing motion controller (see Figure 4.58). The discussion begins with the input-output interface, corresponding to elements 1 and 5, followed by an examination of the parameters essential for the model's correct functioning, denoted as element 2.

Next, the section explores the algorithm responsible for actuating the on-off valves, represented by element 3. Finally, the analysis addresses the algorithm for

calculating the modulation of the proportional valve, which is located upstream of the linear actuator and corresponds to element 4. This thorough examination aims to provide a detailed understanding of each component and their interactions within the controller model.

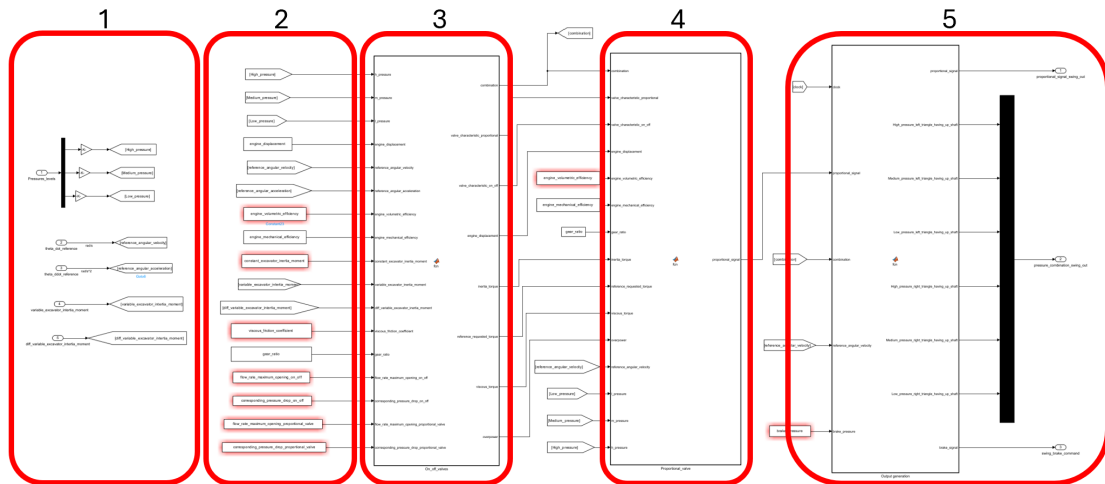


Figure 4.58: Detailed view of the Simulink controller model components for the hydrostatic machine

Controller input-output requests

Regarding the input-output (I/O) aspect of the swing motion controller, it requires partially different information compared to the hydraulic actuator controller model (see Figure 4.59).

To function correctly, the controller requires five main input variables. The purpose of each is detailed below:

1. Pressure signals from each rail: as discussed in section 4.2.2, rail pressures change over time. To make informed decisions about the operational mode based on the operating point of the hydrostatic machine, it is crucial to know the system's pressure states at any given time.
2. Reference velocity: this is the velocity at which the hydrostatic machine should move, directly proportional to the flow rate passing through the machine. The reference velocity signals are proportional to the joystick commands given by the operator.
3. Reference acceleration: this command is generated by the operator's variation in velocity while controlling the swing motion through the joystick. This

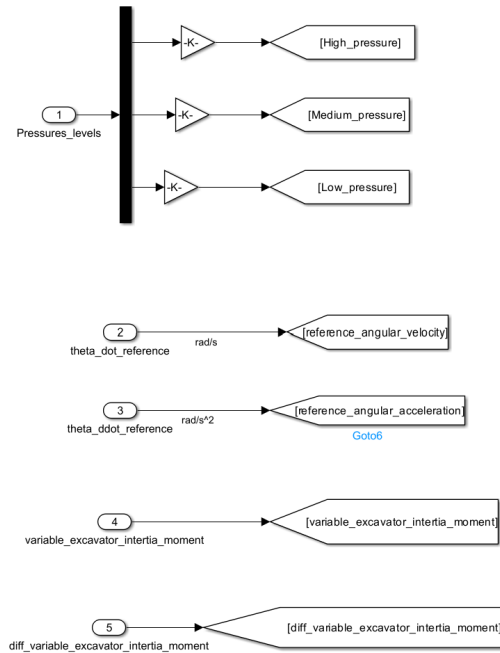


Figure 4.59: Simulink controller model inputs - swing

parameter is needed to calculate the reference requested torque, equal to the product of acceleration and the equivalent inertia of the excavator.

4. Variable excavator inertia moment: this is the variation in the excavator's inertia caused by changes in the arm position. This parameter is necessary for calculating the equivalent inertia of the excavator.
5. Derivative of the variable excavator inertia moment: the derivative of the inertia moment variation ∂J is required to calculate the torque applied to the shaft, as described in the Section 3.1.2.

These inputs are indispensable for the controller's accurate and efficient operation, enabling it to make informed decisions and control the system effectively.

For the outputs (see Figure 4.60), the Simulink model of the controller sends three variables to the AMESim model: the proportional valve opening value, the opening value of each on-off valve, and the pressure signal to be applied to the parking brake. Regarding the latter, as explained in the Section 3.1.2, in stationary conditions where the hydrostatic machine is not moving, a hydraulically actuated brake is implemented to maintain position when the reference velocity is zero.

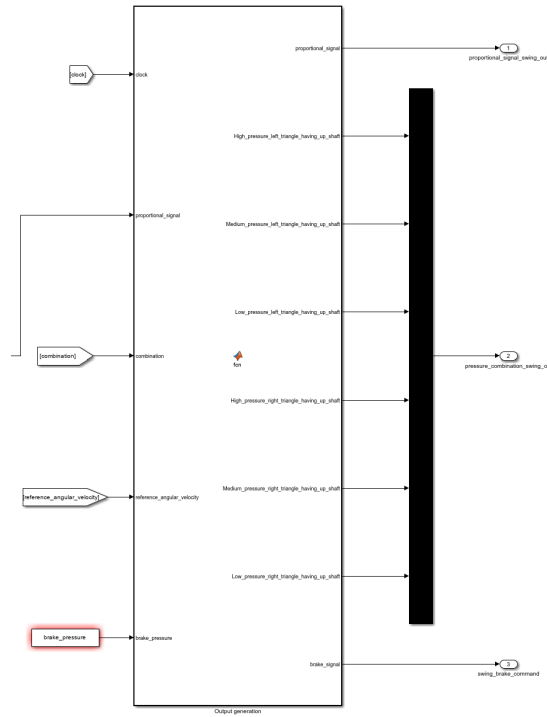


Figure 4.60: Simulink controller model outputs - swing

Controller parameter requests

To maximize the modularity of the controller model for possible further applications, such as the hydraulic motors of the excavator's tracks, all MATLAB functions have been made parametric. The model requires input parameters including data about the hydrostatic machine, such as engine displacement and engine efficiencies, both volumetric and hydraulic-mechanical. Additionally, it requires data about the inertia block, such as the maximum excavator inertia and the friction coefficient.

Let's delve into the specific purposes of each parameter:

- Characteristics of the hydrostatic machine: these parameters are necessary to calculate the torque and rotational speed that could be generated, based on the flow rate passing through the machine and the pressure drop across the two ports.

$$\begin{aligned}
 T_{effective} &= V \cdot \Delta p \cdot \eta_{hym} \\
 Q_{effective} &= \frac{V \cdot \omega}{\eta_{vol}}
 \end{aligned}
 \tag{4.21}$$

- Inertia block data: the AMESim CPR model uses the inertia block to describe the excavator as a mass. To fully define it, the moment of inertia J must be

set to the maximum excavator inertia (*constant_excavator_inertia*) corresponding to a full extended arm condition. This parameter is essential for the Simulink controller model to evaluate the equivalent excavator inertia.

$$J_{eq} = J + J_2 \quad (4.22)$$

Additionally, the inertia block considers viscous friction phenomena, set by the parameter *viscous_friction_coefficient*. The controller needs to account for these phenomena to ensure accurate responses based on the required inputs.

- Torque multiplier gear ratio: as described in the AMESim model's turret block (Section 3.1.2), a torque multiplier is placed at the planetary gear output before the inertia block. This multiplier ensures adequate torque generation despite using a smaller hydraulic machine due to space constraints. To determine the necessary torque and speed at the primary shaft of the torque multiplier, which the hydraulic machine must generate, the gear ratio of this multiplier is required.

On - off valves control algorithm

The analysis of the algorithm developed for controlling the on-off valves in the turret motion is presented here. This algorithm is implemented within a MATLAB function in Simulink and operates on the same principles as the algorithm designed for the on-off valve controller of linear actuators.

At each simulation time step, the algorithm evaluates the position of the operating point required by the hydrostatic machine and its relative coordinates in terms of load pressure and flow rate. Based on this position, the algorithm determines the optimal operational mode that allows the execution of the requested inputs in terms of torque generation and movement speed, aiming to minimize discrepancies in load pressure.

If the operating point is situated on the left-hand side of the load pressure/flow rate plane, the controller selects the operational mode below the operating point. Conversely, if the operating point is on the right-hand side of the plane, the controller chooses the operational mode above the operating point. This adaptive selection ensures efficient control of the system across varying operational conditions.

Below is a detailed explanation of how the algorithm operates, accompanied by the code (see Algorithms 5, 6).

The description starts with the initial code segment (see Algorithm 5) where all necessary variables are thoroughly defined.

1. Initialization of matrix (see Algorithm 5 - line 1): a matrix `matrix` is initialized with the three rail pressure values, namely LP (Low Pressure), MP (Medium

Pressure), and HP (High Pressure). These values are identical to those received by the linear actuator function.

2. Valve characteristics definition (see Algorithm 5, lines 2 → 3): it involves determining the characteristics of both the on-off valves (`valve_char_on_off`) and the proportional valve (`valve_char_prop`) in fully open spool position.
3. Equivalent inertia calculation (see Algorithm 5, line 4): it is performed by summing the maximum inertia, which is provided as an input parameter to the controller, and the variation in inertia generated by the change in position of the excavator's arm.
4. Torque evaluation (see Algorithm 5, lines 5 → 7): previous sections 3.1.2 have addressed the calculation of torques applied to the shaft of the torque multiplier. It was demonstrated how the inertia block implemented in AMESim computes the turret's acceleration according to the following simplified equation:

$$accel = \frac{T_1 - \partial J_2 \times \omega_2}{J_{eq}} \quad (4.23)$$

By incorporating the contribution of friction, the output torque from the torque multiplier can be expressed as follows:

$$T_1 = J_{eq} \times accel + (\partial J_2 + \mu) \times \omega_2. \quad (4.24)$$

5. Initialization MATLAB function's output (see Algorithm 5, line 8): the variable `combination` is a vector initialized with the value `[0,0]`, serving as the initial output placeholder within the MATLAB function. It will store the indices of the on-off valves that need activation for optimal operational mode control. Specifically, the first element of the vector denotes the index of the on-off valve to activate on the port B of the hydrostatic machine, while the second element denotes the index for the port A.

The description continues with the core part of the code (see Algorithm 6) where it is evaluated the minimum torque difference between all operating modes and the required torque characterising the operating point.

6. Reference velocity check (see Algorithm 6, lines 1 → 22): if the variable `omega_ref` differs from 0, calculations commence. This condition implies that the operator is actuating the joystick in the cabin.
7. Optimal pressure combination search:

Algorithm 5 On-off valves control logic algorithm - hydrostatic machine - part 1

- 1: $matrix \leftarrow [LP, MP, HP];$
 - 2: $valve_char_on_off \leftarrow \frac{flow_rate_max_on_off}{\sqrt{pressure_drop_on_off}};$
 - 3: $valve_char_prop \leftarrow \frac{flow_rate_max_prop}{\sqrt{pressure_drop_prop}};$
 - 4: $J_{eq} \leftarrow J + J_2;$
 - 5: $T_J \leftarrow \partial J_2 \times \dot{\omega}_{ref};$
 - 6: $T_{acc} \leftarrow J_{eq} \times \dot{\omega}_{ref};$
 - 7: $T_\mu \leftarrow \mu \times \omega_{ref};$
 - 8: $combination \leftarrow [0,0];$
-

- A variable representing the minimum torque difference, T_{min} , is initialized with an infinite value. This stored value will be updated during each iteration only if the evaluated torque difference, T_{diff} , is less than the current stored value (see Algorithm 6, lines 2 \rightarrow 33).
- Two nested loops iterate through all potential pressure combinations. This procedure generates all feasible operational modes for identifying the one that best aligns with the working point (see Algorithm 6 - line 3 \rightarrow 32).
- To avoid unnecessary calculations, iterations are skipped where there is no Δp between the two hydraulic machine ports (see Algorithm 6 - line 5 \rightarrow 30).
- Determine the pressures at port A and port B of the hydrostatic machine based on the pressures upstream of the on-off valves stored in matrix **matrix**, and the reference velocity's direction and magnitude, which determine the direction and magnitude of the flow rate vector. Assuming full opening of both the on-off valves and the proportional valve, evaluate the pressure drop across each (**on_off_p_drop** and **prop_p_drop**). This assessment facilitates torque equilibrium at the machine level (see Algorithm 6 - lines 7 \rightarrow 8 and 11 \rightarrow 12).
- Determine the difference in torque (Δy on the p_L/Q_L plane) between the load pressure of the operating mode and that of the operating point. The torque of the operating mode generated at the secondary shaft of the torque multiplier is given by:

$$T_{op_mode} = V \times (p_B - p_A) \times \eta_{hym} \times \tau$$

while the torque characterizing the y -coordinate of the operating point is given by the sum of all torque contributions T_i :

$$T_{req} = T_{acc} + T_J + T_\mu$$

Therefore, given that the objective is to identify the operational mode closest to the operating point and that the difference between the ordinates should be positive for the algorithm's purposes, the set up of the system of equations will be as follows:

$$T_{diff} = \begin{cases} T_{op_mode} - T_{req}, & \text{if OP is in Quadrant I and IV;} \\ T_{req} - T_{op_mode}, & \text{if OP is in Quadrant II and III;} \end{cases}$$

Thanks to this setup, the variable `T_diff` will always be greater than 0 for all operational modes that meet the requirements of the operating point. By selecting the smallest difference, it would be possible to ensure that the operational mode generating this specific `T_diff` is the one closest to the operating point (see Algorithm 6, lines 9 and 13).

- Update the optimal combination (see Algorithm 6 - line 20 → 23): in each iteration of the nested `for` loop, ensure the torque difference (`T_diff`) is positive and, if so, verify it is the smallest among all analyzed iterations. By the end of the loop, `T_min` holds the smallest difference among all operational modes relative to the machine's working point, while `combination` contains the corresponding pressures indices to be connected to the two ports.

In conclusion, this section illustrates the efficacy of the controller and algorithm developed within MATLAB. Through these tools, the capability to activate optimal combinations of on-off valves has been established, facilitating operational modes closely aligned with the desired operating point in both motoring and pumping phases.

Proportional valve controller algorithm

The final component of the hydrostatic machine controller concerns the modulation of the proportional valve, which will now be examined. The algorithm developed for this purpose has been implemented as a MATLAB function, depicted as element 4 in Figure 4.58.

For all details regarding the assumptions made for the implementation of the algorithm, both for the fluid and the specific proportional valves used, as well as the physics equations that describe them and how they are implemented in the AMESim environment in the CPR model, refer to Section 4.2.2.

Algorithm 6 On-off valves control logic algorithm - hydrostatic machine - part 2

```

1: if  $\omega_{ref} \neq 0$  then
2:    $T_{min} \leftarrow \infty$ ;
3:   for  $j = 1 : \text{length}(matrix)$  do
4:     for  $k = 1 : \text{length}(matrix)$  do
5:       if  $k \neq j$  then
6:         if  $\omega_{ref} > 0$  then
7:            $p_B \leftarrow matrix(k) - on\_off\_drop - prop\_drop$ ;
8:            $p_A \leftarrow matrix(j) + on\_off\_drop + prop\_drop$ ;
9:            $T_{diff} \leftarrow V \times (p_B - p_A) \times \eta_{hym} \times \tau - T_{acc} - T_J - T_{\mu}$ ;
10:        else if  $\omega_{ref} < 0$  then
11:           $p_B \leftarrow matrix(k) + on\_off\_drop + prop\_drop$ ;
12:           $p_A \leftarrow matrix(j) - on\_off\_drop - prop\_drop$ ;
13:           $T_{diff} \leftarrow V \times (p_A - p_B) \times \eta_{hym} \times \tau + T_{acc} + T_J + T_{\mu}$ ;
14:        end if
15:        if  $T_{diff} > 0$  and  $T_{diff} < T_{min}$  then
16:           $T_{min} \leftarrow T_{diff}$ ;
17:           $combination \leftarrow [k, j]$ ;
18:        end if
19:      end if
20:    end for
21:  end for
22: end if

```

The next step is to construct the system of equations necessary to define the modulation of the 4-port, 2-position proportional valve (see Figure 4.61), ensuring that the operating point conditions in terms of torque and rotational speed are matched.

Referring to equation 4.11, it is shown that for a path of the 4-port, 2-position proportional valve, such as between port P and port A, the equation that links the flow rate through the orifice with the pressure drop between the two ports, the nominal area of the orifice, the fractional spool position, and the characteristics of

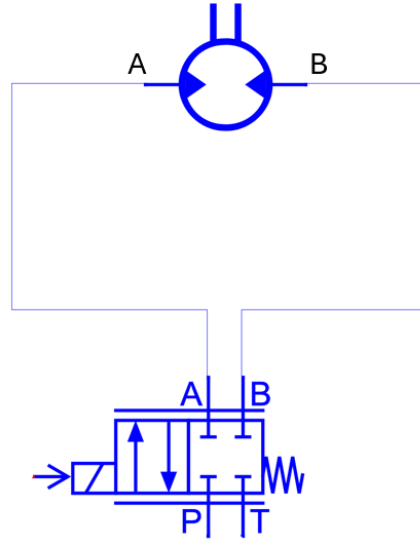


Figure 4.61: Hydrostatic machine and 4-port 2-position proportional valve AMESim subsystem integration

the fluid is the following:

$$\frac{Q}{P_P - P_A} = c_q \cdot A_{effective} \cdot \sqrt{\frac{2}{\rho}} \quad (4.25)$$

which, for the assumptions made in Section 4.2.2, can be simplified to:

$$\frac{Q}{P_P - P_A} = x \cdot \text{valve_characteristic} \quad (4.26)$$

For the hydrostatic machine under consideration, the equation that relates the flow rate passing through the machine with its geometric characteristics and the rotational speed of the shaft is:

$$Q = \frac{V \cdot \omega}{\eta_{vol}} \quad (4.27)$$

Considering that the operator, via joystick, imposes a reference speed ω_{ref} that must be maintained at the output of the torque multiplier connected to the hydrostatic machine shaft, and that this torque multiplier is characterized by a gear ratio τ , the previous equation becomes:

$$Q = \frac{V \cdot \omega_{ref} \cdot \tau}{\eta_{vol}} \quad (4.28)$$

By combining equations 4.28 and 4.26, it follows that between port P and port A of the proportional valve:

$$\frac{V \cdot \omega_{ref} \cdot \tau}{\eta_{vol} \cdot (P_P - P_A)} = x \cdot \text{valve_characteristic} \quad (4.29)$$

Describing the system of equations for both possible paths of the proportional valve P-A and T-B:

$$\begin{cases} \frac{V \times \omega_{ref} \times \tau}{\eta_{vol}(P_P - P_A)} = x \cdot \text{valve_characteristic} \\ \frac{V \times \omega_{ref} \times \tau}{\eta_{vol}(P_B - P_T)} = x \cdot \text{valve_characteristic} \end{cases} \quad (4.30)$$

The goal of the proportional valve algorithm is to determine the value of x in the system of equations 4.30, ensuring the hydrostatic machine meets the flow rate and load pressure requirements.

In the system of equations 4.30, the variables P_A , P_B , and x are unknowns. P_A and P_B are defined according to the required torque, and x represents the modulation value of the proportional valve, ensuring alignment with both pressure and rotational speed requirements.

Given this scenario, the system 4.30 is underdetermined, described by two equations with three unknowns. However, from what has been shown in the on-off valve control algorithm, four of the controller inputs could be utilized for evaluating the torque applied at the torque multiplier secondary shaft:

$$T_{ext} = T_{acc} + T_J + T_\mu \quad (4.31)$$

Obviously, this torque must be that generated by the hydraulic machine which, considering the torque multiplier, becomes:

$$T_{gen} = \frac{T_{ext}}{\tau} \quad (4.32)$$

where the generated torque is given by:

$$T_{gen} = V \cdot \Delta p \cdot \eta_{hym} \quad (4.33)$$

By combining equations 4.31, 4.32, and 4.33, it yields:

$$V \cdot (P_B - P_A) \cdot \eta_{hym} \cdot \tau = T_{acc} + T_J + T_\mu \quad (4.34)$$

Adding this equation to the previously underdetermined system, we have:

$$\begin{cases} \frac{V \times \omega_{ref} \times \tau}{\eta_{vol}(P_P - P_A)} = x \cdot \text{valve_characteristic} \\ \frac{V \times \omega_{ref} \times \tau}{\eta_{vol}(P_B - P_T)} = x \cdot \text{valve_characteristic} \\ V \cdot (P_B - P_A) \cdot \eta_{hym} \cdot \tau = T_{acc} + T_J + T_\mu \end{cases} \quad (4.35)$$

which results in a system of 3 equations in 3 unknowns that is fully defined. The algorithm's primary function is to resolve this system of equations, outputting the value of x .

With the entire theoretical aspect covered, it is now possible to proceed to the analysis of the algorithm where all the considerations have been translated into code (see Algorithm 7).

Algorithm 7 Proportional valve control logic algorithm - hydrostatic machine

```

1:  $matrix \leftarrow [LP, MP, HP]$ 
2:  $prop\_signal \leftarrow 0$ 
3: if  $\omega_{ref} > 0$  then
4:    $p_T \leftarrow matrix(combination(1,1)) - on\_off\_valve\_p\_drop$ 
5:    $p_P \leftarrow matrix(combination(1,2)) + on\_off\_valve\_p\_drop$ 
6:   syms  $prop\_signal, p_A, p_B$ 
7:    $eq1 \leftarrow \frac{V\omega_{ref}\tau}{\eta_{vol}\sqrt{p_A-p_P}} = prop\_signal \cdot valve\_char\_prop$ 
8:    $eq2 \leftarrow \frac{V\omega_{ref}\tau}{\eta_{vol}\sqrt{p_T-p_B}} = prop\_signal \cdot valve\_char\_prop$ 
9:    $eq3 \leftarrow V \cdot (P_B - P_A) \cdot \eta_{hym} \cdot \tau - T_{acc} - T_J - T_\mu = 0$ 
10:   $[prop\_signal, p_A, p_B] \leftarrow solve([eq1, eq2, eq3])$ 
11: else if  $\omega_{ref} < 0$  then
12:    $p_T \leftarrow matrix(combination(1,1)) + on\_off\_valve\_p\_drop$ 
13:    $p_P \leftarrow matrix(combination(1,2)) - on\_off\_valve\_p\_drop$ 
14:   syms  $prop\_signal, p_A, p_B$ 
15:    $eq1 \leftarrow \frac{V|\omega_{ref}|\tau}{\eta_{vol}\sqrt{p_P-p_A}} = prop\_signal \times valve\_char\_prop$ 
16:    $eq2 \leftarrow \frac{V|\omega_{ref}|\tau}{\eta_{vol}\sqrt{p_B-p_T}} = prop\_signal \times valve\_char\_prop$ 
17:    $eq3 \leftarrow V \cdot (P_A - P_B) \cdot \eta_{hym} \cdot \tau + T_{acc} + T_J + T_\mu = 0$ 
18:    $[prop\_signal, p_A, p_B] \leftarrow solve([eq1, eq2, eq3])$ 
19: end if

```

1. Initialize the pressure matrix vector (`matrix`) with pressure values within the AMESim CPR model rails (see Algorithm 7 - line 1).
2. Initialization MATLAB function's output (see Algorithm 7 - line 2): the variable `prop_signal` is a float variable initialized with the value 0, storing the modulation value for the proportional valve, which ranges from 0 to 1. If the reference velocity is 0, it indicates that no commands are provided by the operator, and the algorithm returns the value 0 as output.
3. Reference velocity check and load pressure/flow rate graph quadrant determination (see Algorithm 7 - lines 3 and 19): when the `reference_velocity` is non-zero, the system initiates the necessary calculations.
4. Calculate the pressures at the ports P and T of the proportional valve (see Algorithm 7 - lines 4 \rightarrow 5 and lines 12 \rightarrow 13): as function of the flow rate direction and on-off valve activated, the pressures at port P_P and P_T are evaluated.
5. Solving the system of equations to determine the value of `prop_signal` that the Simulink function should output (see Algorithm 7, lines 6 \rightarrow 10 and 14 \rightarrow 18).

After calculating the proportional valve modulation necessary to achieve the desired torque and rotational speed, the Simulink model outputs this value, which is then transmitted to the AMESim model.

4.4 Closed-Loop Control of Linear Actuators and Hydrostatic Machine

The analysis of the linear actuators and the hydrostatic machine of the turret has shown that the open-loop control results are satisfactory in terms of speed and displacement. However, a notable error persists between the input signal given to the controller and the actual response observed at the utility. This discrepancy is primarily attributed to the assumptions made during the execution of control algorithms for the on-off valves and the proportional valve, along with the introduction of low-pass filters.

One of the key assumptions involves treating the fluid as an ideal substance, where the fluid coefficient c_q and the fluid density ρ are considered invariant with respect to pressure changes. This simplification leads the controller to generate outputs that do not accurately reflect the real conditions within the circuit. Consequently, the controller's predictions do not align with the actual behavior of the fluid under varying pressure conditions, thereby contributing to the observed error.

Additionally, the implementation of low-pass filters, despite their meticulous design, introduces delays in the controller's response. These filters also cause a mismatch between the working point calculated by the controller and the actual working point of the utility.

The coexistence of these issues results in open-loop control outcomes that, while commendable, are still affected by error. To address these shortcomings and enhance the performance of the system, the most effective solution is the implementation of a closed-loop control system.

Closed-loop control systems (see Figure 4.62) offer the advantage of continuous feedback, allowing for real-time adjustments that compensate for any deviations between the desired and actual system behavior. By incorporating feedback mechanisms, closed-loop control can correct the errors introduced by the aforementioned assumptions and filtering delays, ensuring a higher degree of accuracy and reliability in the control of the linear actuators and the hydrostatic machine of the turret. This approach not only mitigates the impact of ideal fluid assumptions and filter-induced mismatches but also optimizes the overall system performance.

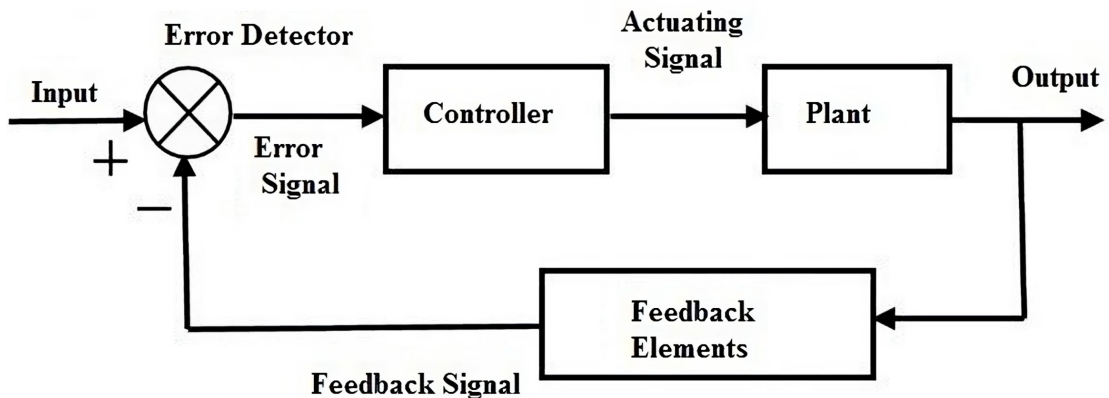


Figure 4.62: Closed loop control system - System block diagram

4.4.1 Types of Closed-Loop Control Systems

There are several types of closed-loop control systems that can be employed to improve the performance of the excavator control system. The most common types are Proportional (P), Proportional-Derivative (PD), Proportional-Integral (PI), and Proportional-Integral-Derivative (PID) control systems [18].

Proportional Control (P)

Proportional control is the simplest form of closed-loop control. The control signal $u(t)$ is proportional to the error signal $e(t)$, which is the difference between the desired setpoint and the actual output.

$$u(t) = K_p \cdot e(t)$$

where:

- $u(t)$ is the control signal.
- K_p is the proportional gain.
- $e(t)$ is the error signal.

Proportional-Derivative Control (PD)

PD control combines proportional control with a derivative term, which helps anticipate future errors based on the rate of change of the error.

$$u(t) = K_p \cdot e(t) + K_d \frac{de(t)}{dt}$$

where:

- K_d is the derivative gain.
- The derivative term anticipates future errors based on the rate of change of the error.

Proportional-Integral Control (PI)

PI control improves upon proportional control by adding an integral term, which helps eliminate steady-state error.

$$u(t) = K_p \cdot e(t) + K_i \int_0^t e(\tau) d\tau$$

where:

- K_i is the integral gain.
- The integral term accounts for the accumulation of past errors.

Proportional-Integral-Derivative Control (PID)

PID control is the most advanced strategy. It combines proportional, integral, and derivative terms to provide a balanced control approach.

$$u(t) = K_p \cdot e(t) + K_i \int_0^t e(\tau) d\tau + K_d \frac{de(t)}{dt}$$

Each of these control strategies offers different advantages and is suited to different types of systems and control objectives.

- Proportional control is simple and effective for systems where the error needs to be minimized proportionally.
- PD control provides a quick response to changing error conditions by combining proportional control with a predictive aspect from the derivative term.
- PI control is useful for eliminating steady-state error and is beneficial in systems where constant deviation from the setpoint is unacceptable.
- PID control is versatile and provides the best overall control by addressing present, past, and future errors, making it suitable for complex and dynamic systems.

The selection of the appropriate control strategy and the tuning of the gains (K_p , K_i , and K_d) are crucial for achieving optimal performance in the closed-loop control of the linear actuators and the hydrostatic machine of the turret.

4.4.2 Proportional Closed-Loop Control Implementation

Given the type of error observed in the results, the choice was made to implement a simple proportional control. In this setup, the error signal $e(t)$ is defined as the difference between the reference velocity of the utility and the actual velocity.

The closed-loop control was implemented in the Simulink controller model, where it was necessary to introduce new inputs to the controller: the actual velocities of the three linear actuators and the hydraulic motor of the turret. These velocities were obtained using velocity sensors placed on each actuator and the motor.

The resulting error signal is then multiplied by the proportional gain and added to the controller's open-loop prediction. Specifically, this error, as implemented in the closed-loop control, is added to the value calculated by the controller for the opening of the spool position valve of the proportional valves.

This implies that the closed-loop control does not influence the decision-making process regarding the selection of the operational mode for the utility's operating point. Instead, it solely modulates the proportional valve to achieve a fine matching

between the actual operating point of the utility and the operating point predicted by the controller based on the inputs.

In mathematical terms, the control signal $u(t)$ representing the modulation of the proportional valve in the closed-loop system can be expressed as:

$$u(t) = K_p \cdot e(t) + u_{open-loop}(t)$$

where:

- $u(t)$ is the final control signal corresponding to the opening of the spool position proportional valve.
- K_p is the proportional gain.
- $e(t)$ is the error signal, defined as the difference between the reference velocity and the actual velocity.
- $u_{open-loop}(t)$ is the control signal calculated by the open-loop controller.

The implementation of this closed-loop control strategy aims to refine the control of the proportional valve opening, thereby ensuring a closer alignment between the predicted and actual operating points of the utility. This refinement improves the overall system performance without altering the primary operational mode selection process.

The selection of the proportional gain K_p in the closed-loop control system significantly impacts system performance. Choosing an appropriate K_p is crucial as it directly influences the stability, responsiveness, and accuracy of the closed-loop control. There are two critical scenarios to consider:

- When K_p is too large: the control system becomes overly sensitive to small errors, leading to excessive oscillations or instability. This can cause the actuators to overshoot or undershoot their target positions or velocities, resulting in erratic behavior and potentially damaging mechanical components due to abrupt changes in control commands.
- When K_p is too small: the control system may be sluggish and slow to respond to deviations from the desired operating conditions. This results in prolonged settling times and poor transient response, affecting the overall performance and efficiency of the system. The utility may not achieve desired velocities or positions quickly enough, impacting productivity and operational effectiveness.

To determine the optimal K_p , a systematic approach such as Design of Experiments (DOE) was employed, with the objective to strike a balance where K_p is sufficiently large to ensure prompt response to disturbances while avoiding

instability, yet not so large as to induce excessive oscillations or overshoot. This fine-tuning process was critical for optimizing the closed-loop control performance of each utility subsystem and ensuring reliable operation under varying operating conditions.

4.4.3 Proportional Gain Selection via Design of Experiments

For the selection of the proportional gains K_p characteristic for each utility, a Design of Experiments (DOE) approach was utilized.

A DOE was generated for each utility where the variable was the proportional gain of the closed-loop control. In previous sections, it has been discussed how the mechanical configuration of the excavator system and the arrangement of the various subsystems (boom, arm, bucket, and turret) cause interactions where changes in one subsystem cascade to affect all others. Ideally, it would be evaluated the influence of each proportional gain on all other subsystems. However, due to the extensive range of variable windows and the number of variables to be analyzed simultaneously, this was not feasible.

Instead, a DOE was created for each utility with the sole variable being the K_p of the i -th subsystem. As this variable changed, the values imposed on the other utilities on the command for the proportional valve opening spool position were those calculated in open-loop by the controller.

The process for each utility's DOE was as follows:

- Define the range and discretization: establish the range of K_p values and discretize it into manageable increments for testing each subsystem.
- Generate experiments: create a set of experiments where only the K_p of the target subsystem varies, while other K_p parameters are kept constantly to zero.
- Run simulations: perform simulations for each experiment and collect data on system performance.
- Analyze results: evaluate the impact of varying K_p on the subsystem's performance, ensuring the closed-loop control meets desired specifications.

This method allowed for the systematic tuning of K_p for each utility, ensuring that each subsystem's performance was optimized individually. The trade-off in this approach was the assumption that interactions between subsystems, while present, could be managed through the predefined open-loop values, simplifying the overall tuning process.

Regarding the DOE objective, the goal was to minimize the root mean square (rms) of the velocity error between the reference velocity input to the controller and the velocity actually generated by the i -th utility, based on the closed loop proportional gains:

$$\text{Minimize } \sqrt{\sum_{i=1} \epsilon_i^2} \quad (4.36)$$

where:

- ϵ_i represents the velocity error of utility i , defined as $\epsilon_i = v_{ref} - v_{actual}$,
- ϵ_i depends on the i -th proportional gain of the subsystems.

Thus, the objective is formulated as:

$$\text{Minimize } \sqrt{\sum_{i=1} \epsilon_i^2(f_{K_{p_i}})}$$

To determine the range of values for each variable, a wide range of values was assumed initially due to the lack of knowledge about their optimal values. For this reason, for each K_p , a Design of Experiments was first conducted with coarse discretization, followed by another with fine discretization. Table 4.5 shows the settings for each DOE of every proportional gain in the initial coarse run.

Variable	Range of Variation	Discretization Step
$K_{p,boom}$	From 0 to 10	0.5
$K_{p,arm}$	From 0 to 10	0.5
$K_{p,bucket}$	From 0 to 10	0.5
$K_{p,turret}$	From 0 to 10	0.5

Table 4.5: Ranges and discretization steps $K_{p,i}$ for coarse DOE runs

While Table 4.5 outlines the ranges and discretization steps for $K_{p,i}$ in the coarse DOE runs, Figures 4.63, 4.64, 4.65, and 4.66 illustrate the sensitivity analyses conducted for each DOE. These figures depict the response of the boom, arm, bucket, and turret motor subsystems, respectively, to variations in their proportional gains.

Once the error trends with respect to $K_{p,i}$ values were identified, new variation ranges were defined for each variable, with a finer discretization parameter (see Table 4.6):

It is noteworthy that no fine tuning was performed for the turret motor since the K_p values obtained from the initial coarse DOE application were already deemed

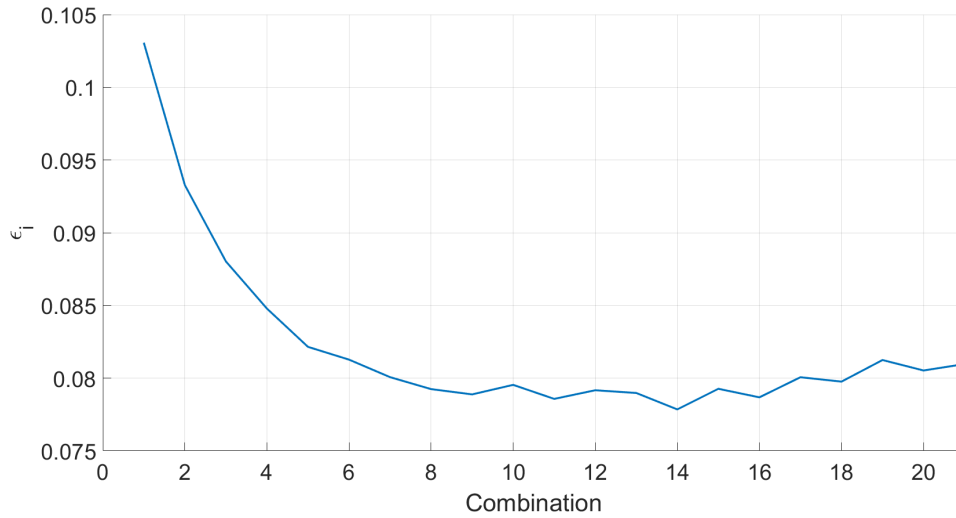


Figure 4.63: Sensitivity analysis of boom actuator error (ϵ) to proportional gain $K_{p,boom}$, with K_p varied coarsely

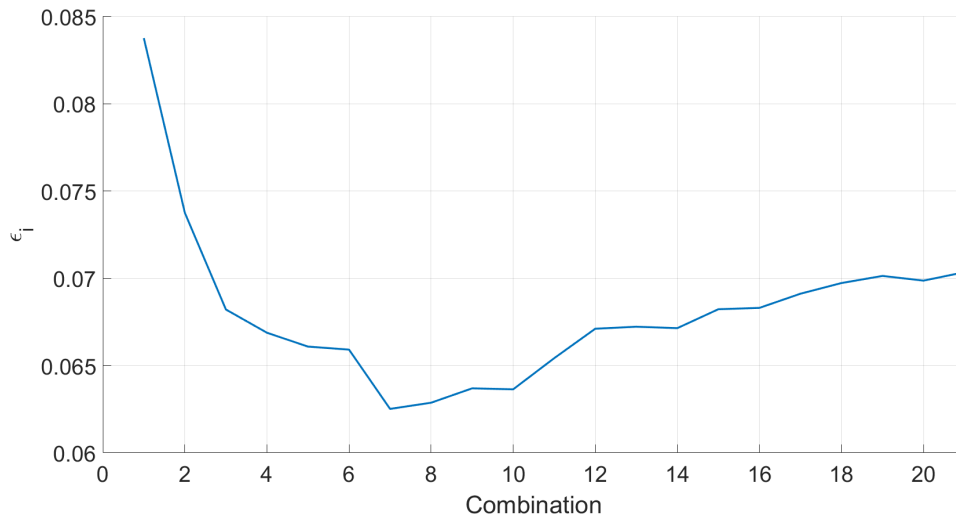


Figure 4.64: Sensitivity analysis of arm actuator error (ϵ) to proportional gain $K_{p,arm}$, with K_p varied coarsely

satisfactory. Figures 4.67, 4.68, and 4.69 depict the sensitivity analyses for the three actuators conducted with finer discretization.

Among all configurations tested, those achieving the best results according to the objectives defined in the Design of Experiments (DOE) are summarized in Table 4.7.

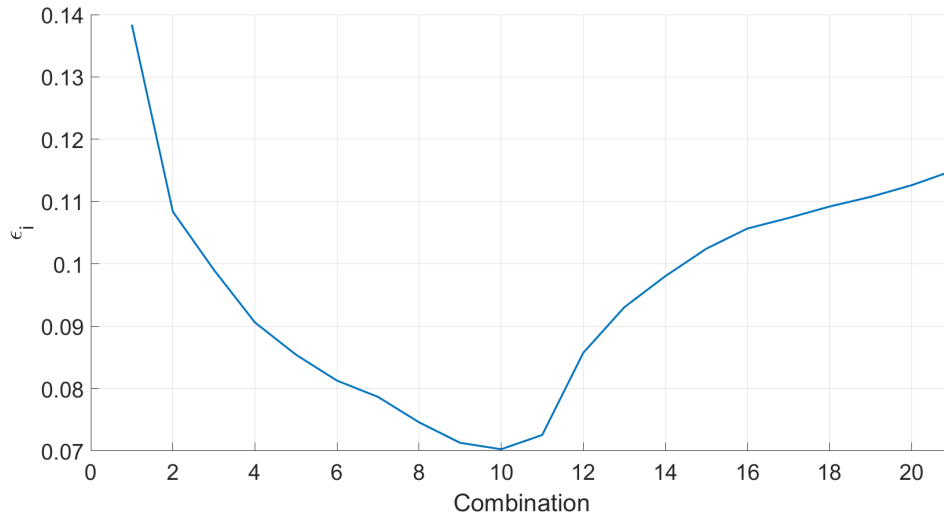


Figure 4.65: Sensitivity analysis of bucket actuator error (ϵ) to proportional gain $K_{p,bucket}$, with K_p varied coarsely

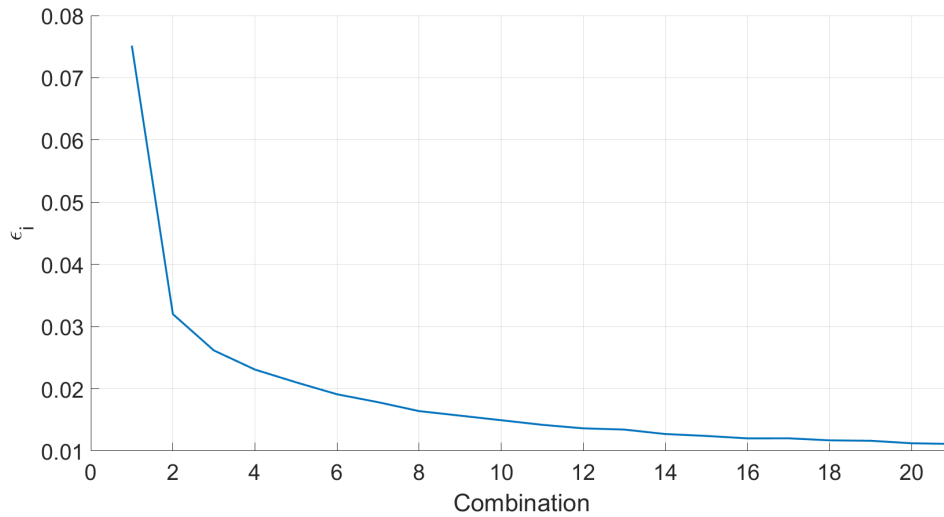


Figure 4.66: Sensitivity analysis of turret motor error (ϵ) to proportional gain $K_{p,swing}$, with K_p varied coarsely

The refinement of K_p ranges through sensitivity analyses with finer discretization highlighted optimal values that significantly minimized actuator errors across the excavator subsystems. The final configurations in Table 4.7 underscore the effectiveness of this approach in enhancing control performance while maintaining system stability.

Variable	Range of Variation	Discretization Step
$K_{p,boom}$	From 10 to 20	0.1
$K_{p,arm}$	From 3 to 6	0.1
$K_{p,bucket}$	From 3 to 5.5	0.1

Table 4.6: Ranges and discretization steps $K_{p,i}$ for fine DOE runs

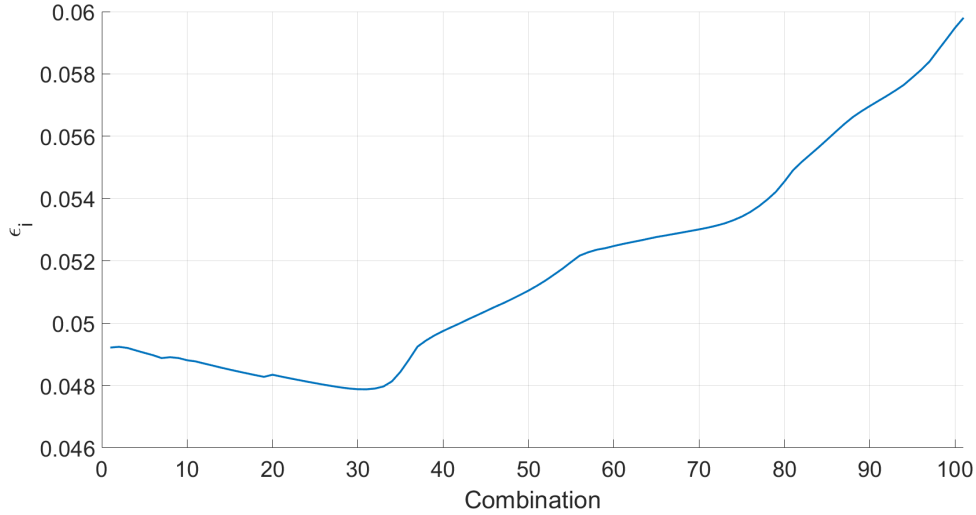


Figure 4.67: Sensitivity analysis of boom actuator error (ϵ) to proportional gain $K_{p,boom}$, with K_p varied finely

The detailed results concerning velocity and displacement errors will be comprehensively presented in the results chapter, providing a comprehensive assessment of the closed-loop control’s performance across all subsystems.

4.5 Hydraulic Accumulators Recharging Strategy

The accumulator charging controller cycles determine the timing and selection of which accumulator is charged by the pump [3]. This decision-making process is crucial to maintaining system stability and efficiency.

As previously discussed in section 3.2.3, the design choices regarding the accumulators, including the nominal volume and pre-charge pressure parameters, significantly influence the stiffness of the accumulator. The objective in selecting these parameters was to achieve pressure values that remain as stable as possible during testing. This stability is essential for approximating ideal pressure sources,

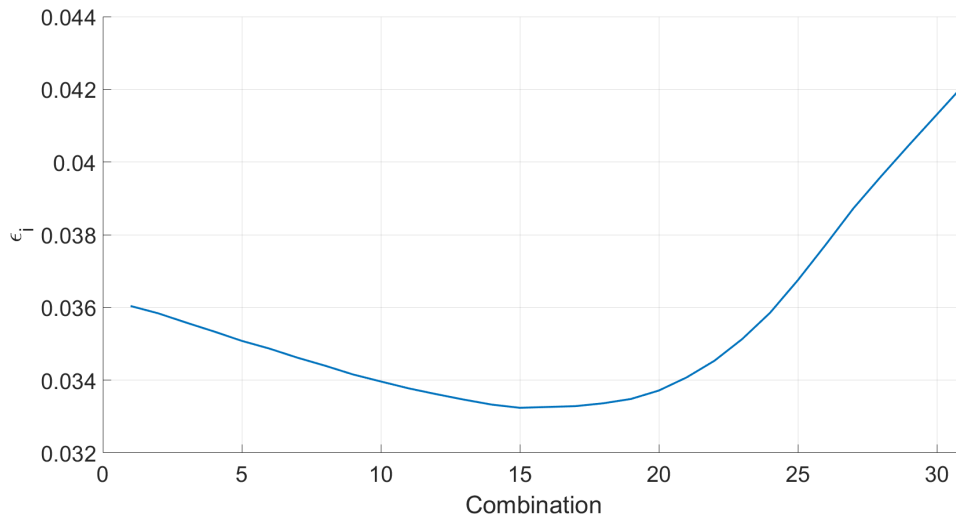


Figure 4.68: Sensitivity analysis of arm actuator error (ϵ) to proportional gain $K_{p,arm}$, with K_p varied finely

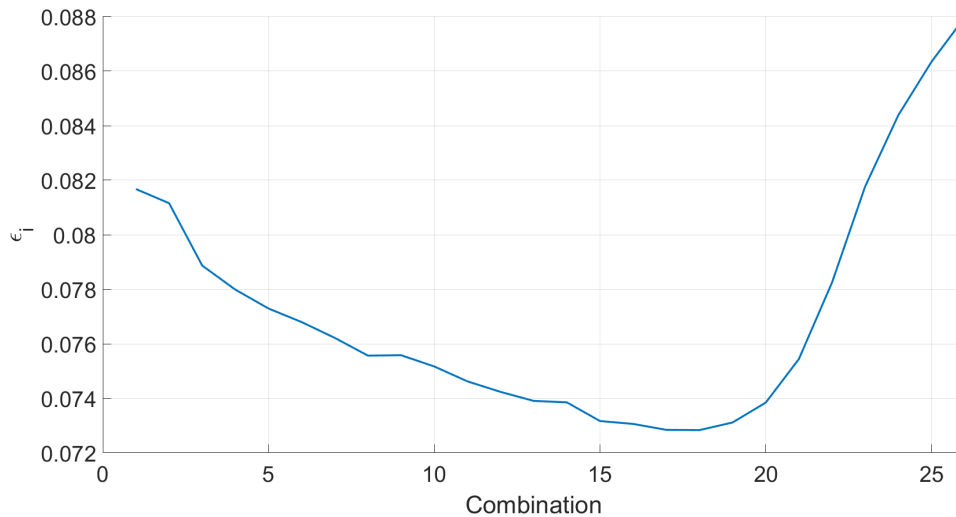


Figure 4.69: Sensitivity analysis of bucket actuator error (ϵ) to proportional gain $K_{p,bucket}$, with K_p varied finely

thereby enhancing the stability of both the controller and the overall system.

Beyond the aforementioned parameters, it is even more critical to implement an effective recharging strategy to achieve this goal. To this end, a tailored control strategy has been developed and implemented using a finite state machine in AMESim (Figure 4.70).

Actuator	Boom	Arm	Bucket	Turret
$K_{p,i}$	13.0	4.0	4.7	6.0

Table 4.7: Optimal configurations of proportional gains for the closed-loop control for each utility

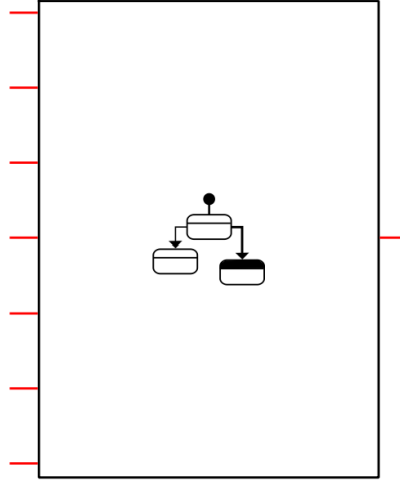


Figure 4.70: Finite State Machine submodel in AMESim

The recharging strategy relies on two concurrently implemented logics. The first logic is based on the pressure values of the high-pressure (HP) and medium-pressure (MP) rails, denoted as p_{HP} and p_{MP} . Threshold values are defined for both high and medium pressure: $p_{HP,max}$, $p_{HP,min}$, $p_{MP,max}$, and $p_{MP,min}$. When the pressure in an accumulator falls below the lower limit, the pump is activated to restore the pressure to the upper limit, at which point it stops. In this scenario, priority is given to high pressure.

The second logic is based on the flow rates exiting the accumulators. While the first strategy is straightforward, it has several limitations. Firstly, given that high pressure takes precedence over medium pressure, the HP pressure level must always be above its lower pressure threshold before the MP accumulator can be charged [3]. Secondly, the pump size was chosen based on the average flow rates required by the dig and dump cycle. The issue arises if, for instance, the HP accumulator reaches its lower threshold limit and activates the pump, but simultaneously there is a peak flow rate demand. The pump is not sized to handle peak flow rates, leading to a critical drop in rail pressure.

To address these issues, flow rate sensors were installed at the outlets of the

accumulators. If the flow rate exceeds a threshold limit, the pump activates regardless of the accumulator's pressure state. This combined action of the two logics ensures that the pump is almost always active, with pressure fluctuations not exceeding 15 bar during peak flow demands, such as when both the hydraulic motor and boom actuator are simultaneously engaged. Figure 4.71 illustrates the activation and deactivation of the hydraulic flow generation unit specifically during a dig and dump cycle. Integrating the signal over a 14-second period shows that the pump remains active for 9 seconds.

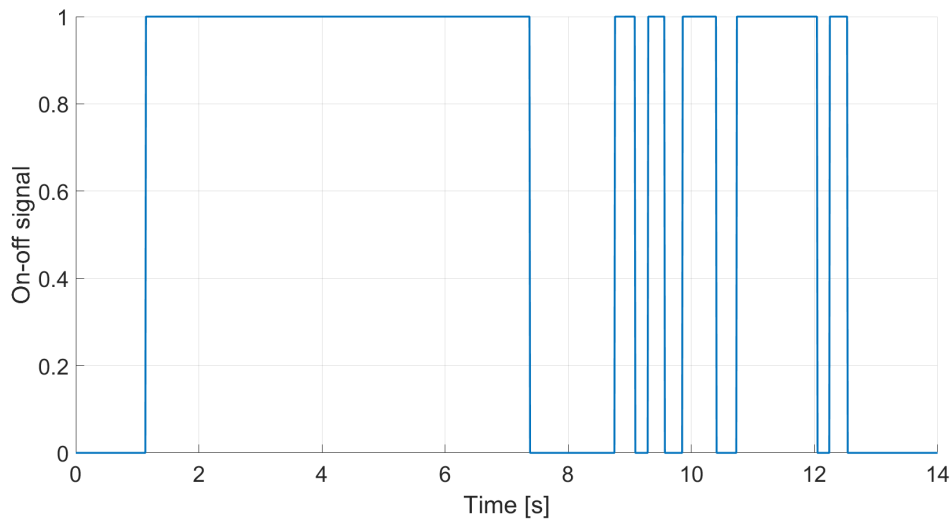


Figure 4.71: Signal on-off sent to the pump during a dig and dump cycle

The finite state machine consists of three states (see Figure 4.72):

- Standby: this state is active when no flow rate is required by the utilities and accumulator pressures are within the acceptable range.
- Charge MP: the system enters Charge MP if the utilities require flow rate from the medium-pressure accumulator or if its pressure falls outside the defined threshold limits.
- Charge HP: the system enters Charge HP if the utilities require flow rate from the high-pressure accumulator or if its pressure falls outside the defined threshold limits. Charge HP state always has priority over Charge MP.

This comprehensive control logic and recharging strategy ensure the efficient and stable operation of the hydraulic system, maintaining optimal performance even under varying operational demands.

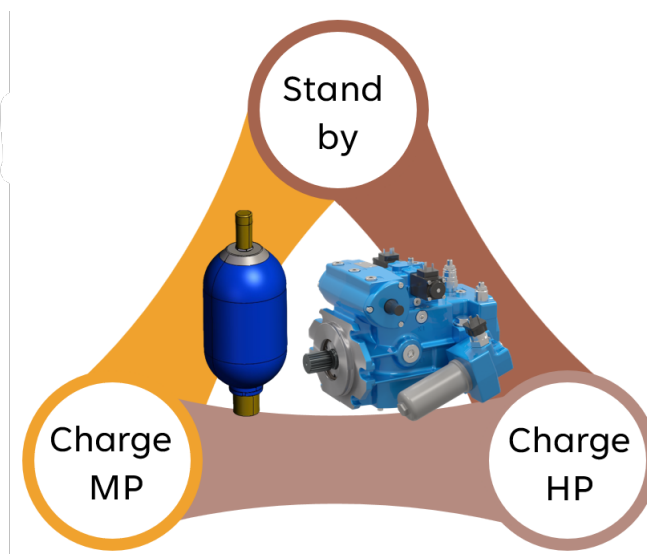


Figure 4.72: Finite State Machine diagram for the recharging strategy of hydraulic accumulators

Chapter 5

Performance Evaluation of Common Pressure Rail Architecture

This chapter presents the findings of the research conducted on the application of the Common Pressure Rail architecture to a hydraulic excavator. The primary objective of this study was to evaluate the performance improvements in terms of fuel economy compared to the traditional Load Sensing architecture. Additionally, this chapter will delve into the results pertaining to displacement and velocity errors, achieved through the implementation of the Simulink-based controller model specifically designed to manage the on-off valves and proportional valve of each linear actuator, as well as the hydrostatic machine of the turret.

Through detailed analysis and discussion, this chapter aims to underscore the advantages of the CPR architecture, not only in terms of fuel economy but also in enhancing the overall precision and operational capabilities of hydraulic excavators. The implications of these findings for future developments in hydraulic system design and control strategies will also be considered.

5.1 Comparative Analysis of Fuel Economy Between CPR and LS Architectures

This section provides a detailed examination of the fuel economy achieved by implementing the Common Pressure Rail architecture compared to the traditional Load Sensing architecture. By analyzing fuel consumption data across various operational conditions, the superior efficiency of the CPR system will be highlighted, demonstrating its potential for significant cost savings and environmental benefits.

Firstly, the settings employed for the internal combustion engine, pumps, control system, and accumulators in both systems will be detailed for each reference cycle performed, in order to ensure a comprehensive analysis. Following this, the actual results will be presented and discussed.

5.1.1 Dig and Dump Cycle Results

This section presents the operating conditions of the main components within the CPR and LS architectures, focusing on the dig and dump cycle.

Load Sensing Architecture Setup

In the LS AMESim model, the following operating parameters were utilized:

- Internal Combustion Engine (ICE) maintained a constant speed of 2300 rpm;
- Fluid generation unit comprised of two pumps with displacements of 75 cc/rev and 27 cc/rev, respectively;
- To control the excavator system for performing the reference standard cycle, the main control valves was managed using open-loop control

Common Pressure Rail Architecture Setup

Conversely, the CPR AMESim model has been operated under the following conditions:

- The ICE speed was maintained at approximately 1200 rpm;
- A single variable displacement pump with a maximum displacement of 75 cc/rev was employed. This pump operated at maximum displacement throughout the cycle to facilitate downspeeding operations, thereby maximizing torque while reducing rotational speed to achieve the desired flow rate;
- Two accumulators were utilized:
 - High-Pressure (HP) accumulator: 30 L capacity, set at 175 bar with a pre-charge of 90 bar;
 - Medium-Pressure (MP) accumulator: Also 30 L capacity, set at 85 bar with a pre-charge of 40 bar;
- The control logic for the CPR architecture was implemented using the closed-loop control approach described in Section 4.4.

These distinct configurations were employed to investigate and compare the fuel economy performance between the CPR and LS architectures during the dig and dump cycles. The differences in operational parameters such as engine speed, pump configurations, and control logic are crucial factors influencing overall efficiency and effectiveness in hydraulic systems.

Fuel Consumption Results

Once evaluated the working conditions of the 2 models lets now pass to effectively analyse the fuel consumption performance of two hydraulic system architectures during the dig and dump cycle. The comparison aims to identify differences in fuel economy and pinpoint areas of energy inefficiencies and losses within each system.

Table 5.1 outlines the energy transfer and utilization characteristics of the LS system.

Component/System	Energy Use [%]	Energy Use [kJ]
Fuel energy	100	1147.7
ICE out energy	30.77	353.2
Thermodynamic and auxiliary components losses	69.23	754.5
Pump out energy	21.37	245.3
Pump losses	9.40	107.9
MCV out energy	7.09	81.4
MCV losses	14.28	163.9
Actuator net energy	5.89	67.6
Actuator friction losses	4.61	52.9
Recoverable energy	3.41	39.1

Table 5.1: Load Sensing hydraulic system energy transfer and utilization - Dig and dump cycle

Referring to Table 5.1, it is evident that the greatest percentage losses in the energy flow path, from fuel to net energy at the actuator, are concentrated in two principal elements.

The first major source of loss is attributable to the thermal engine and the associated thermodynamic and auxiliary component losses. The inherently low efficiency of thermal engines is a well-documented phenomenon. Furthermore, the efficiency impact is exacerbated by the engine's operating points during the work cycle. The requirement to maintain the thermal engine at a constant rotational speed of 2300 rpm, with torque varying from several hundred Nm to approximately 220 Nm (corresponding to maximum power), significantly detracts from the achievable maximum efficiency of the thermal engine (see Figure 3.14). This factor represents a crucial area for potential improvement in system efficiency.

The second major source of inefficiency is linked to the Load Sensing architecture. It is well-known that LS systems suffer from substantial hydraulic inefficiencies, particularly within the Main Control Valve (MCV). These inefficiencies are primarily due to throttling losses caused by local compensators and proportional valves. As illustrated in Table 5.1, the hydraulic energy downstream of the proportional valves (MCV out energy) is less than half of the energy supplied by the pumps, indicating significant energy losses due to throttling.

Finally, it is important to mention the recoverable energy aspect, which refers to the additional energy that can be recuperated from the environment in the presence of dragged loads. This represents a further opportunity to enhance overall system efficiency.

In contrast Table 5.1 summarizes the energy transfer and usage characteristics in the CPR system.

Component/System	Energy Use (%)	Energy Use (kJ)
Fuel energy	100	528.8
ICE out	36.12	191.5
Thermodynamic and auxiliary components losses	63.88	337.3
Pump out	31.36	165.8
Pump losses	4.76	25.7
Accumulator out energy	29.04	153.6
Hydraulic system losses	2.32	12.2
On-off valves out energy	25.64	135.6
On-off valves losses	3.40	18.0
Proportional valves out energy	12.75	67.4
Proportional valves losses	12.89	68.2
Actuator net energy	11.50	60.8
Actuator friction losses	9.50	50.2
Recoverable energy	8.25	43.6

Table 5.2: Common Pressure Rail hydraulic system energy transfer and utilization - Dig and dump cycle

The CPR architecture was developed to address the two primary deficiencies of traditional Load Sensing systems. By decoupling the energy supplied by the power system from the energy required by the actuators, the CPR architecture could allow for the implementation of advanced strategies to enhance thermal engine efficiency. One such strategy is downspeeding, which exploits the engine's most efficient operating regions by positioning the operating points at low speed and high torque. In Figure 5.1 the operating points of the thermal engine during the dig and dump cycle are shown. This adjustment increases the output energy efficiency of the thermal engine from 30.77% in the traditional system to 36.12% in the CPR system.

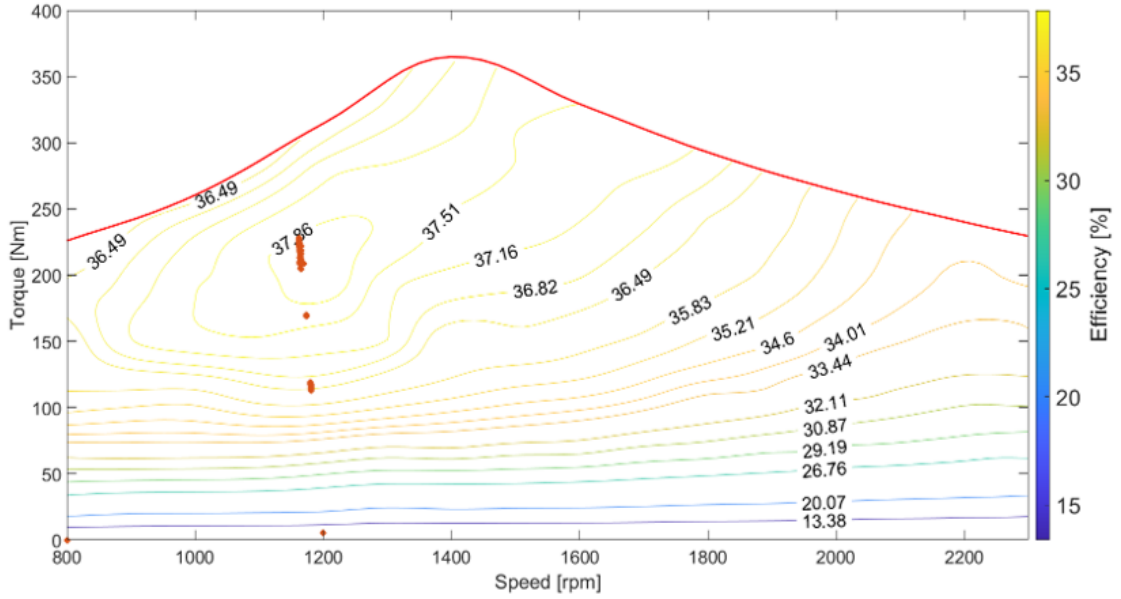


Figure 5.1: Operating points of the thermal engine during the dig and dump cycle - Common Pressure Rail architecture

Regarding the other critical aspect affecting the efficiency of Load Sensing systems—the valve group losses—the CPR system demonstrates a significant improvement. The efficiency of the valve group in the CPR system is approximately double that of the traditional LS system.

In conclusion, the energy flow analysis reveals that the CPR architecture enables the execution of the same cycle as the traditional LS system using 528.8 kJ instead of 1147.7 kJ, which is nearly half. The fuel consumption values for each architecture are presented in Table 5.3.

An important note regarding the CPR system’s fuel consumption: the values reported in the table include the energy surplus or deficit in the two accumulators at the end of the cycle compared to the initial conditions. If the accumulators complete the cycle with a net energy surplus, this energy can be utilized in the subsequent cycle.

Architecture	Energy Consumption	Fuel Consumption
	[kJ]	[g]
Traditional LS	1147.7	25.59
CPR	528.8	11.79

Table 5.3: Fuel consumption for different architectures - Dig and dump cycle

5.1.2 Air Grading Cycle Results

In order to implement the air grading cycle effectively, it was decided to maintain uniform operating conditions as those employed in the dig and dump cycle for both architectural configurations analyzed (refer to section 5.1.1).

Similarly, a comprehensive study of energy distribution within the systems was conducted for the current cycle. Comparing energy utilization across two distinct cycles enhances the significance of our findings, enabling broader assessments to determine whether the observed benefits are specific to particular scenarios or have broader applicability. Consistency in methodology and terminology was maintained throughout the energy flow analysis to facilitate clear and direct comparisons.

Fuel Consumption Results

The data related to the LS system are presented in the Table 5.4.

Component/System	Energy Use (%)	Energy Use (kJ)
Fuel energy	100.0	757.6
ICE out energy	27.0	204.3
Thermodynamic and auxiliary components losses	73.0	553.3
Pump out energy	18.6	141.2
Pump losses	8.3	63.1
MCV out energy	2.4	18.5
MCV losses	5.9	44.6
Actuator net energy	2.1	15.9
Actuator friction losses	2.2	16.9
Recoverable energy	1.9	14.3

Table 5.4: Load Sensing hydraulic system energy transfer and utilization - Air grading

Observing the data in Table 5.4, the performance characteristics of the LS architecture, as highlighted previously in the context of the dig and dump cycle, are reaffirmed. Primarily, the inefficiency of the internal combustion engine is notable, attributed to its operation at maximum speed with reduced torques. As a result, 73% of the total supplied energy is dissipated through thermodynamic losses and auxiliary components. Furthermore, the substantial impact of proportional valve throttling losses is reiterated, aligning closely with previous observations.

Conversely, the CPR architecture's pertinent findings are presented in Table 5.5.

For the CPR architecture as well, the energy flow data pertaining to the air grading cycle are consistent with the observations from the dig and dump cycle (see Table 5.5). Specifically, although the thermal engine efficiency is diminished compared to the previous cycle due to operation at lower torques and less efficient

Component/System	Energy Use (%)	Energy Use (kJ)
Fuel energy	100.0	277.2
ICE out energy	32.8	90.9
Thermodynamic and auxiliary components losses	67.2	186.3
Pump out energy	28.4	78.6
Pump losses	4.4	12.3
Accumulators out energy	27.3	75.8
Hydraulic system losses	1.0	2.9
On-Off valves out energy	24.9	69.1
On-Off valves losses	2.4	6.7
Proportional valves out energy	7.1	19.6
Proportional valves losses	17.9	49.5
Actuators net energy	5.7	15.9
Actuators friction losses	6.3	17.5
Recoverable energy	5.0	13.8

Table 5.5: Common Pressure Rail hydraulic system energy transfer and utilization - Air grading

regions of the engine map, due to the fact that it utilized only the medium pressure rail, it still maintains a more advantage over the LS architecture. Moreover, hydraulic losses associated with the on-off valve block and accumulators show reduced impact in this scenario, while losses attributed to proportional valves become more prominent. In this context, the primary benefit of the CPR architecture, which minimizes throttling by choosing the appropriate operating mode according to the utility's operating point, is less pronounced because the actuator pressure requirements exhibit minimal variation. Consequently, the system remains in a consistent operational mode, adjusting pressure delivery to demand through throttling.

Furthermore, it is noted that recoverable energy percentages in this cycle are lower compared to those observed in the dig and dump cycle. This observation is logical considering the absence of significant dynamic loads as in the dig and dump cycle, and additionally, kinetic energy recovery from turret movement, which contributed to recoverable energy in the previous cycle, is absent due to the stationary position of the turret in this cycle.

Despite the CPR architecture not reaching its full potential in optimizing efficiency for the leveling cycle due to the inherent characteristics of the cycle, it still exhibits superior efficiency compared to the LS system. This superiority is validated by the fuel consumption values reported in Table 5.6.

Architecture	Energy Consumption [kJ]	Fuel Consumption [g]
Traditional LS	757.6	17.58
CPR	277.2	6.18

Table 5.6: Fuel consumption for different architectures - Air grading cycle

5.2 Analysis on Precision and Responsiveness of Common Pressure Rail System

This section focuses on evaluating the precision and responsiveness of the Common Pressure Rail system. Using the Simulink model of the controller described in Chapter 4, the study assesses displacement and velocity errors of the actuators and the hydrostatic machine of the turret. The benchmarks employed to demonstrate these performances are based on standard excavation operations such as dig and dump cycles and air grading activities.

5.2.1 Dig and Dump Cycle Results

In the context of dig and dump cycles, the CPR system's performance is scrutinized by analyzing the alignment between the reference and actual velocities, as well as the reference and actual displacements. The dig phase involves the excavation of material, which requires precise control over the actuator displacement to ensure efficient and effective digging operations. Similarly, the dump phase necessitates controlled and responsive actuator movements to accurately deposit the material at the designated location.

The performance evaluation of the actuators during the dig and dump cycle is comprehensively illustrated in Figures 5.2, 5.3, 5.4, 5.5, 5.6, 5.7, 5.8, and 5.9.

These figures provide a comparative analysis of the reference and actual velocities for the boom, arm, bucket actuators, and the turret hydrostatic machine during the dig and dump cycles. The data illustrate the system's ability to closely follow the reference velocity, indicating a high level of responsiveness and precision in the control mechanism. The minor deviations observed are within acceptable limits, demonstrating the system's robustness in handling real-time excavation tasks.

Furthermore, a noticeable increment in performance has been achieved in these results with closed-loop control compared to the open-loop control results provided in Section 4.2.4. This improvement highlights the effectiveness of the closed-loop control strategy in enhancing system accuracy and reliability.

To provide a comprehensive overview of the system's performance, Table 5.7

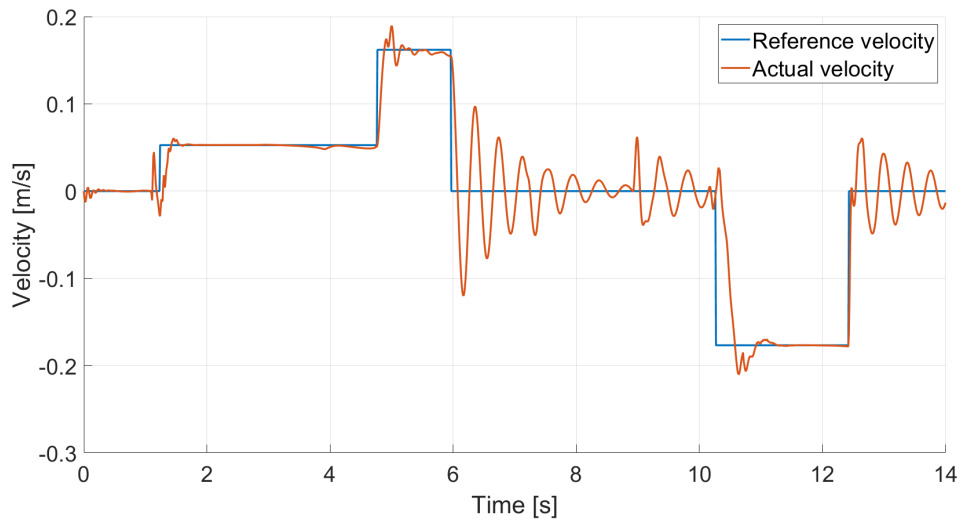


Figure 5.2: Comparison of reference and actual velocities for boom actuator during Dig and Dump cycles

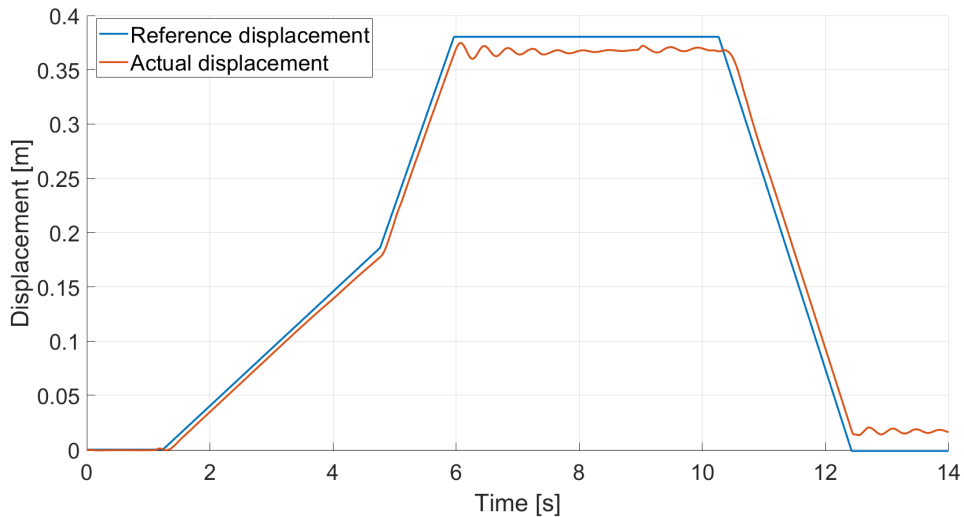


Figure 5.3: Comparison of reference and actual displacement for boom actuator during Dig and Dump cycles

summarizes the maximum errors in terms of percentage displacement that the actuators were supposed to achieve based on the operator's joystick input versus the actual displacement performed. This detailed analysis of the maximum errors offers critical insights into the performance limitations and areas for potential improvement in the control system.

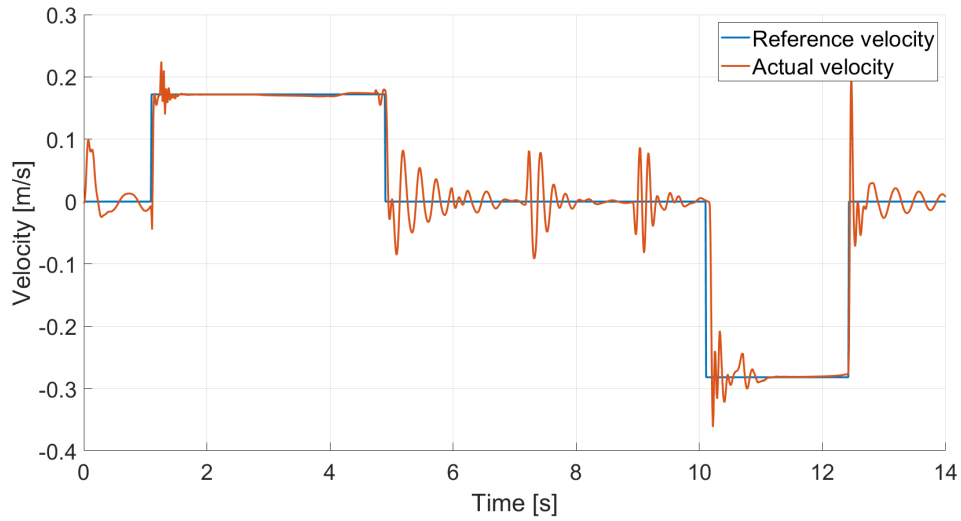


Figure 5.4: Comparison of reference and actual velocities for arm actuator during Dig and Dump cycles

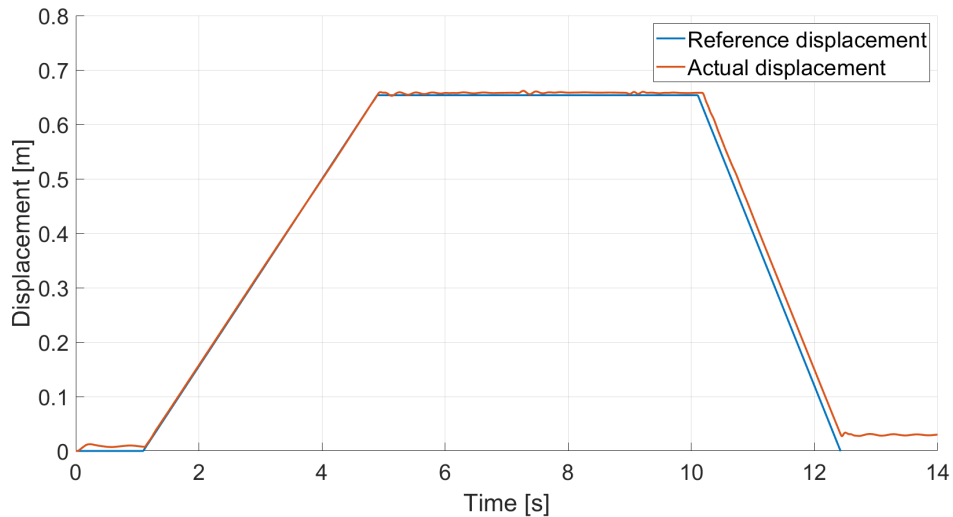


Figure 5.5: Comparison of reference and actual displacement for arm actuator during Dig and Dump cycles

It is observed that the overall performance achieved is very positive, with the maximum percentage error recorded on the boom actuator. Here, a percentage error of 6.18% corresponds to an actual error of approximately 2.5 cm, which is a more than acceptable margin. The best results, however, were achieved on the turret, as anticipated in Section 4.4, where the error is solely due to the phases in

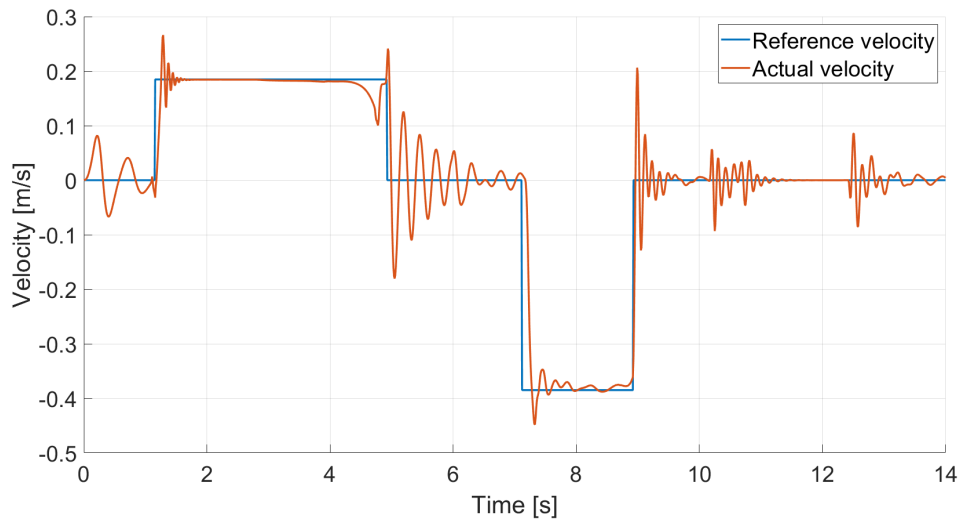


Figure 5.6: Comparison of reference and actual velocities for bucket actuator during Dig and Dump cycles

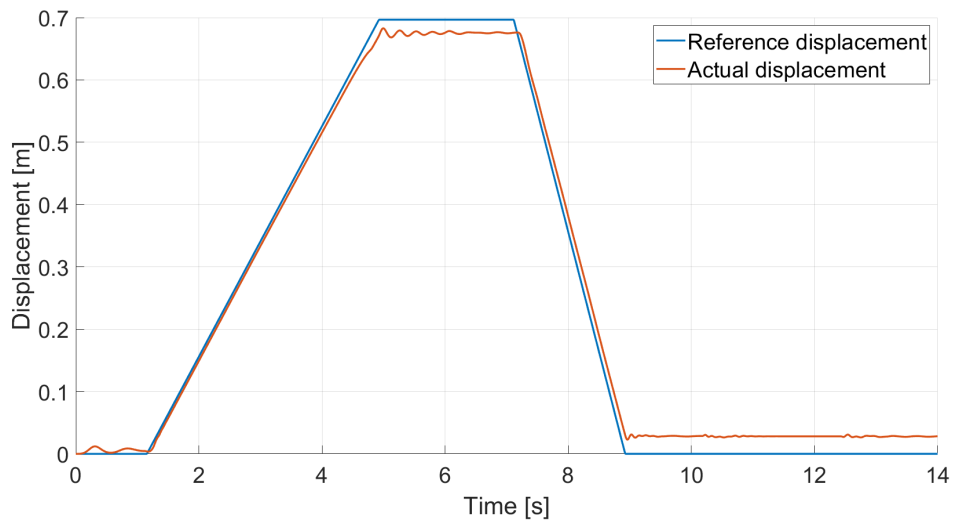


Figure 5.7: Comparison of reference and actual displacement for bucket actuator during Dig and Dump cycles

which the system is stopped, generated by the oscillations of the system itself.

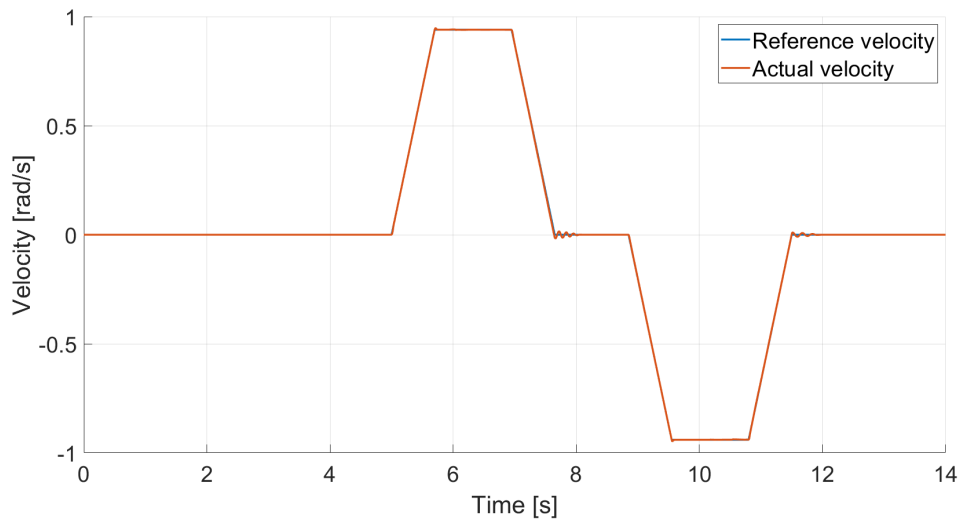


Figure 5.8: Comparison of reference and actual velocities for turret hydrostatic machine during Dig and Dump cycles

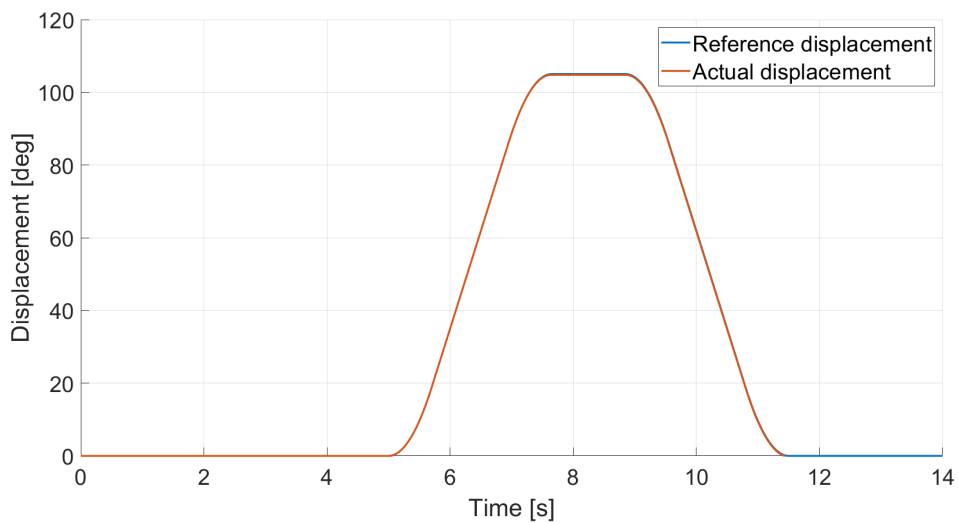


Figure 5.9: Comparison of reference and actual displacement for turret hydrostatic machine during Dig and Dump cycles

5.2.2 Air Grading Cycle Results

The performance of the CPR system is also assessed for air grading activities by examining the alignment between the reference and actual velocities, as well as between the reference and actual displacements, following a methodology similar to

Actuator	Maximum Error [%]
Boom	6.18
Arm	5.27
Bucket	4.49
Turret	0.21

Table 5.7: Actuators displacements maximum errors - Dig and dump cycle

that employed for dig and dump cycles. Air grading involves precise adjustments in actuator movements to achieve a smooth and level surface, necessitating high precision and responsiveness from the control system.

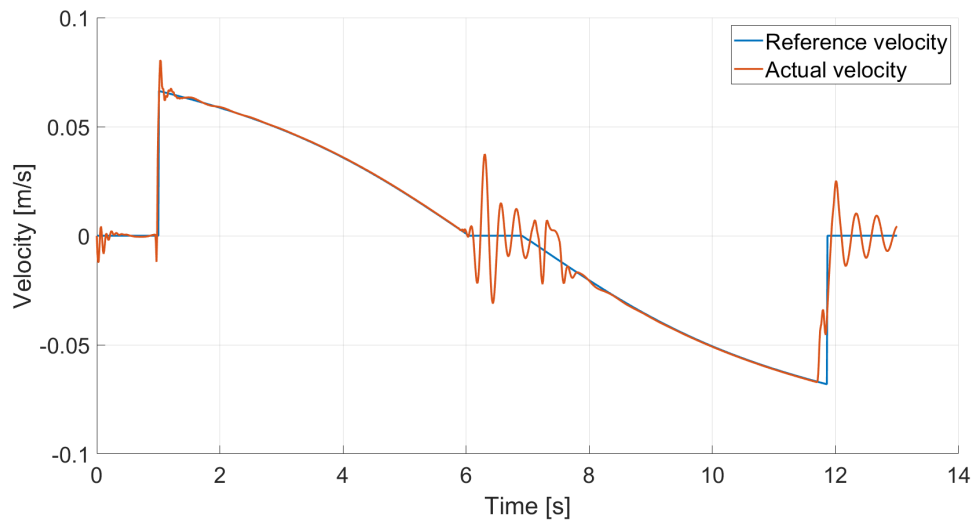


Figure 5.10: Comparison of reference and actual Velocities for boom actuator during Air Grading cycles

The performance evaluation of the actuators during the air grading cycle are comprehensively illustrated in Figures 5.10, 5.11 and 5.12, 5.13.

These figures provide a comparative analysis of the reference and actual velocities for the boom and arm during the air grading cycle. For what observed in the previous section, also in this case it is possible to denote the system's ability to closely follow the reference velocity.

In Table 5.8 they have been summarized also the maximum errors in terms of percentage displacement that the actuators were supposed to achieve, function of the operator's input.

In this study, the maximum error observed was approximately 5%, occurring in

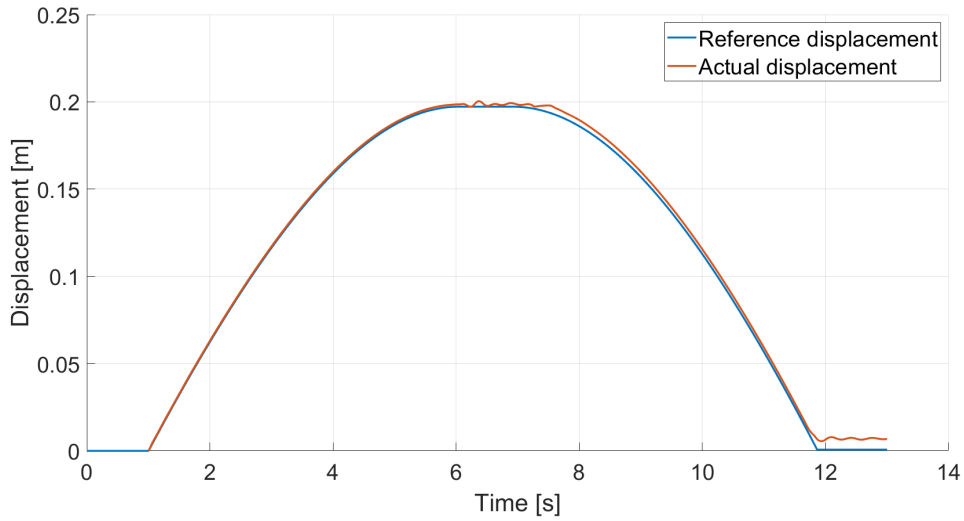


Figure 5.11: Comparison of reference and actual displacement for boom actuator during Air Grading cycles

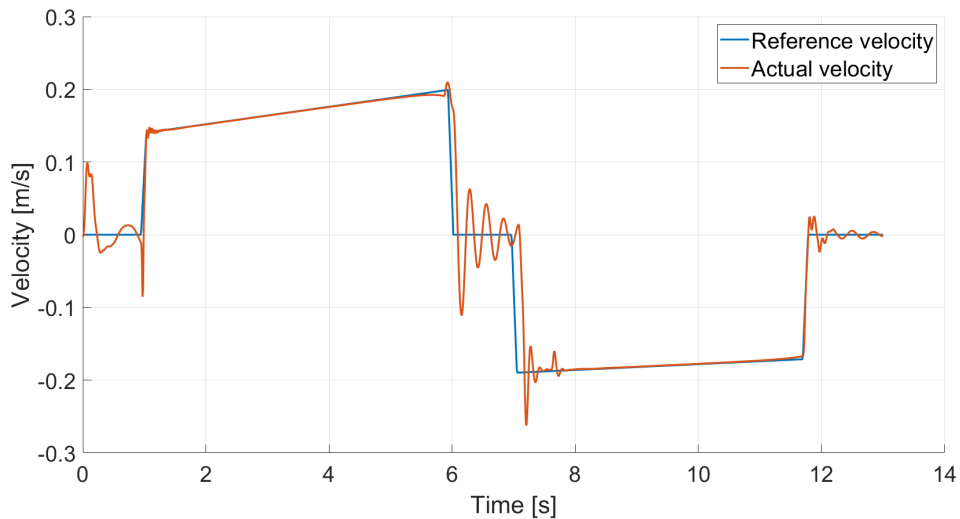


Figure 5.12: Comparison of reference and actual Velocities for arm actuator during Air Grading cycles

the arm actuator and corresponding to an error magnitude of around 4.5 cm.

Overall, the results demonstrate that the system exhibits stability, responsiveness, and accuracy. However, there is considerable scope for enhancement. The parameters utilized in the closed-loop control system were not optimally tuned; notably, the proportional coefficients were derived through a Design of Experiments

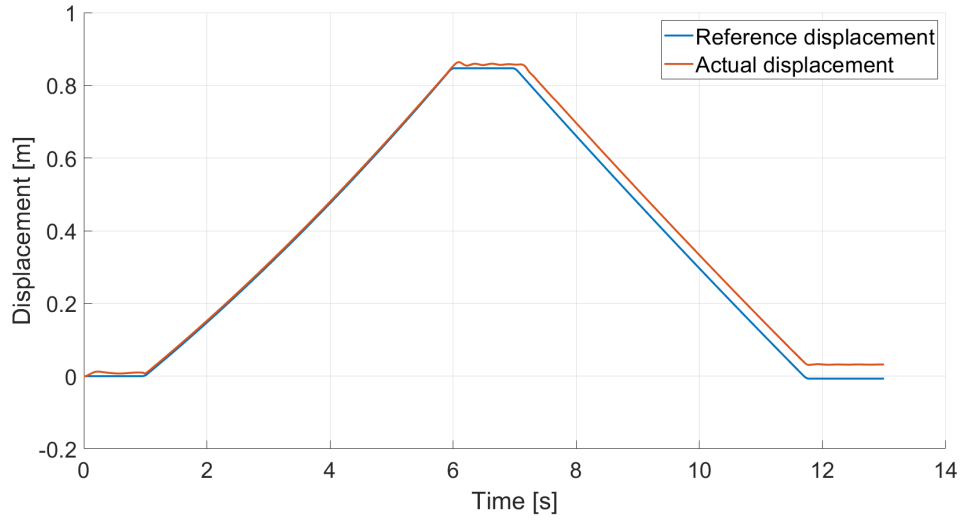


Figure 5.13: Comparison of reference and actual displacement for arm actuator during Air Grading cycles

Actuator	Maximum Error [%]
Boom	0.69
Arm	5.27

Table 5.8: Actuators displacements maximum errors - Air grading cycle

(DOE) approach. Nonetheless, the interaction effects between parameters affecting different actuators were not thoroughly considered, as discussed in section 4.4. This oversight likely undermined the system’s controllability.

Moreover, the proportional corrective coefficients for each actuator were determined based on the assumption of ideal pressure sources as flow generation unit. When these coefficients were applied to a comprehensive CPR architecture, where the flow generation unit comprised a hydraulic pump and accumulators, the results were inevitably affected by these real-world conditions.

To improve performance, it is crucial to revisit and refine these parameters. Additionally, implementing more advanced closed-loop strategies, such as Proportional-Derivative (PD) control, could yield even more favorable outcomes.

Chapter 6

Development of System Architecture and Control Logic for Common Pressure Rail plus Electronic Flow Matching

This chapter focuses on the development of system architecture and control logic for the Common Pressure Rail with Electronic Flow Matching. Thus far, the study has highlighted the significant benefits derived from implementing the CPR architecture on a 9-ton hydraulic excavator across various excavation cycles, including dig and dump and air grading. These benefits primarily manifest in notable fuel economy improvements compared to traditional Load Sensing architectures, while maintaining robust operational performance and precise cycle execution.

An important finding from the analysis, outlined in Section 3.2.3, indicates that the operational pressures of the system consistently remain significantly below the standard maximum thresholds expected for equipment of this size. Conventionally, a 9-ton excavator is capable of peak pressures ranging between 300 to 320 bar. Currently configured, the system's maximum generable pressure is constrained by the high-pressure rail, limited to 175 bar under current settings. Although sufficient for standard dig and dump or air grading cycles, these pressures may prove inadequate under more demanding conditions, such as encountering rocks or challenging substrates during excavation.

The subsequent sections will simulate and analyze a critical heavy-duty excavation cycle scenario to evaluate the CPR architecture's performance under extreme

operational conditions as outlined.

Following this evaluation, proposed enhancements to the STEAM architecture will be presented, integrating necessary hydraulic modifications alongside comprehensive control strategies. These developments encompass the entire system management—from the thermal engine to hydraulic pumps, and further to the on-off and proportional valve controls of each hydraulic actuator.

6.1 Performance Analysis of Common Pressure Rail Architecture in Heavy-Duty Excavation Cycles

This section focuses on simulating the challenging conditions under which excavators operate in real-world scenarios. As previously mentioned, the heavy-duty work cycle is designed to replicate these demanding environments.

For the Load Sensing architecture, executing heavier work cycles presents minimal challenges due to its innate capability for flow-pressure regulation. This allows the LS system to dynamically adjust flow rates to accommodate varying load demands, all while ensuring compliance with the mechanical and safety limits of the system.

Conversely, as discussed earlier, the Common Pressure Rail system's maximum actuator pressure p_L is determined by the HP/LP operational mode, currently set to a maximum of 175 bar based on previous tests. A proposed solution involves dynamically adjusting the rail pressure to accommodate specific load demands, such as replenishing the accumulator when encountering obstacles that exceed the current pressure capabilities. However, this approach is hindered by responsiveness issues. The time required to increase the accumulator's pressure from P_1 to a higher P_2 depends on several factors including the pressure differential (ΔP), accumulator volume, and pump size. The pump size was selected based on average flow rate requirements for typical dig and dump cycles, while the accumulator volume was chosen to maintain overall system stability, encompassing both the flow generation unit and distributor components.

Therefore, achieving higher rail pressures necessitates additional time, compromising the system's ability to respond promptly. Moreover, aside from responsiveness, the considerable fuel consumption required to elevate accumulator pressure further poses operational challenges.

The chapter proceeds with an analysis of the designed excavation cycle aimed at evaluating the operational limits of the CPR system.

6.1.1 Heavy Duty Reference Work Cycle

The heavy-duty work cycle, designed to assess the excavator's capabilities under demanding conditions, consists of the following phases:

1. **Approaching the excavation site** (see Figure 6.1): the excavator moves towards the designated excavation area with its arm fully extended and the actuators in a retracted position.
2. **Penetration** (see Figure 6.2): the excavator's arm, equipped with a bucket, penetrates the material to be excavated. During this phase, the arm encounters an obstruction within the ground. Overcoming this obstacle necessitates the hydraulic system to operate at maximum pressure levels, approximately 290 bar.

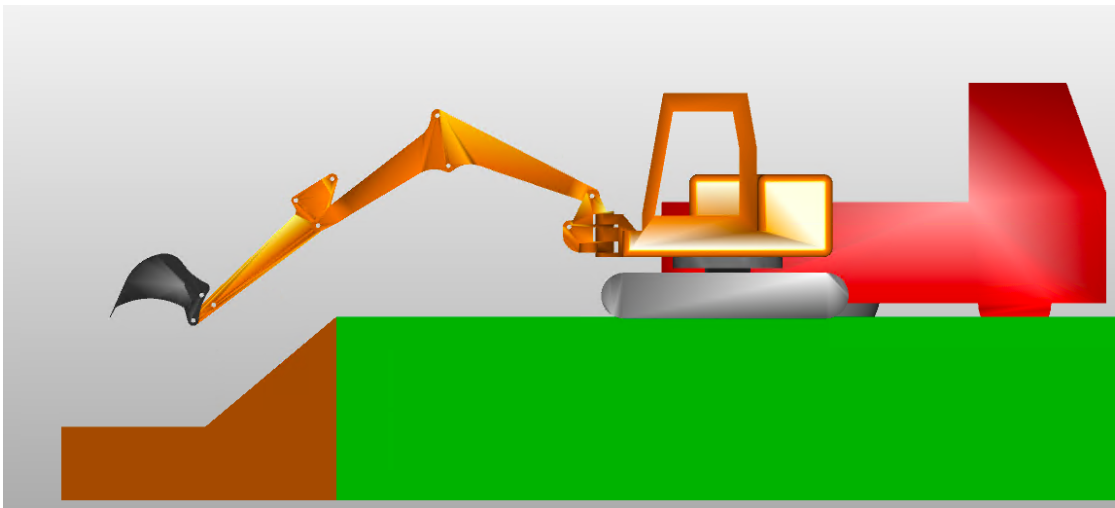


Figure 6.1: Commencing the first phase of heavy duty cycle: approaching the site for excavation

To achieve the desired pressures within the hydraulic circuit, the forces applied to the actuators were generated based on the specific characteristics of each actuator. It is well-established that the force produced by an actuator is proportional to the pressures within its chambers and the corresponding areas. By utilizing the geometric properties of the actuators, it has been possible to determine the necessary force magnitude required to attain the desired maximum pressure in the circuit. Figures 6.3, 6.4, and 6.5 display the input signals directed to the actuators and to the controller for regulating the architecture.

As illustrated in the figures showing the forces, the generated signal follows a specific pattern. From the cycle start time to second 3.6, the force values

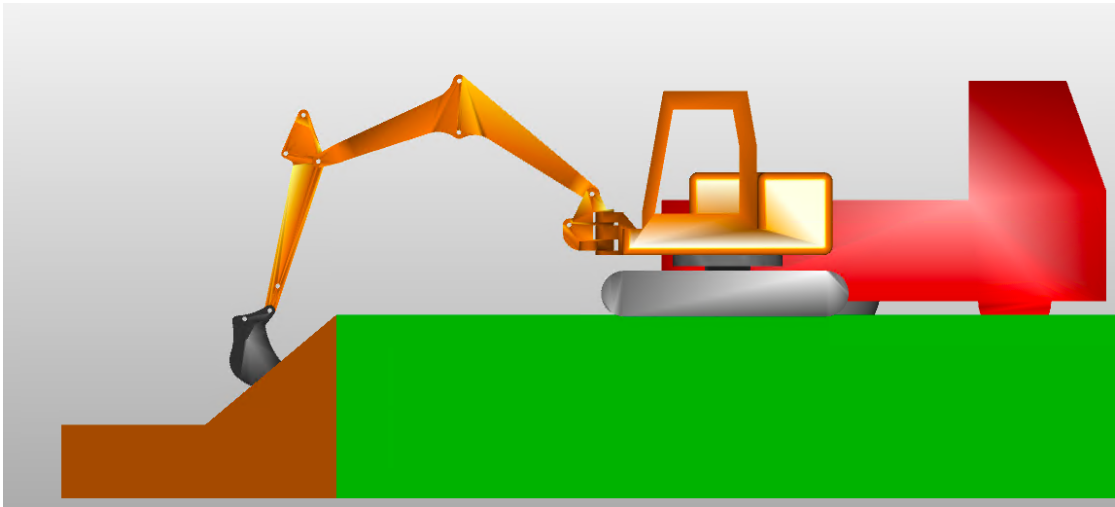


Figure 6.2: Executing the second phase of the of heavy duty cycle: penetrating

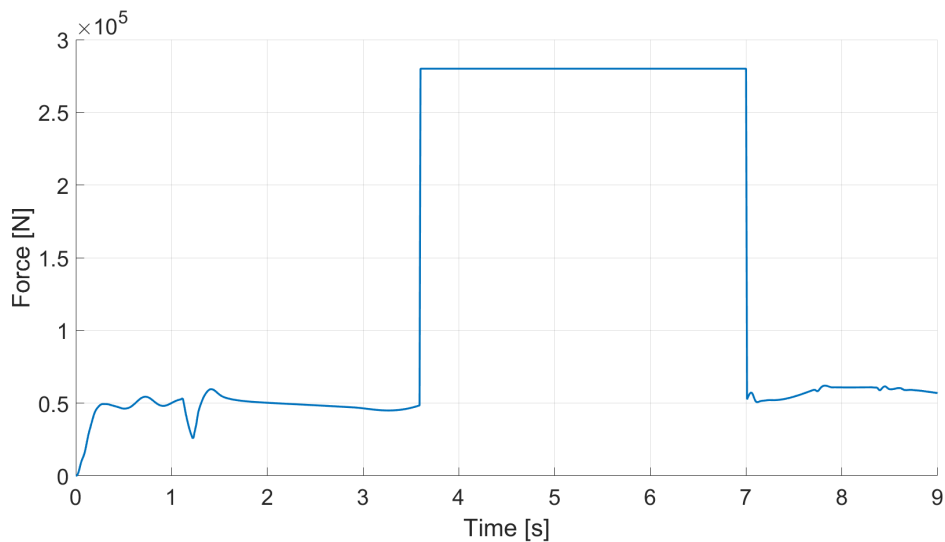


Figure 6.3: Force exerted on the boom actuator during the heavy-duty work cycle

correspond to those observed during the dig and dump cycle. At second 3.6, a step change is introduced, with its magnitude determined by the characteristics of the actuator as previously explained. This step signifies the encounter with an obstacle. Subsequently, from second 7.0 until the end of the cycle, the force returns to values identical to those of the dig and dump cycle.

The reference velocity commands input to the controller for each actuator during the cycle, along with their corresponding displacements, are depicted in Figures

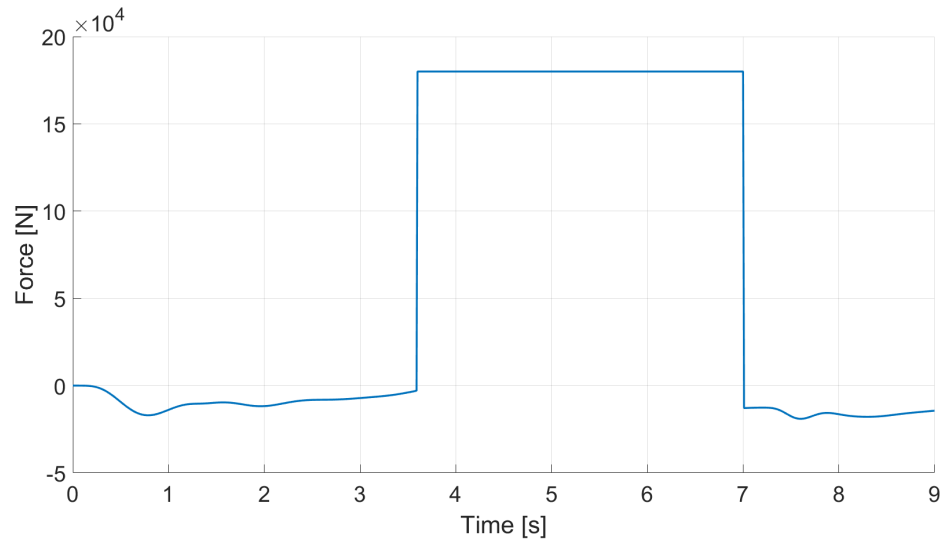


Figure 6.4: Force exerted on the arm actuator during the heavy-duty work cycle

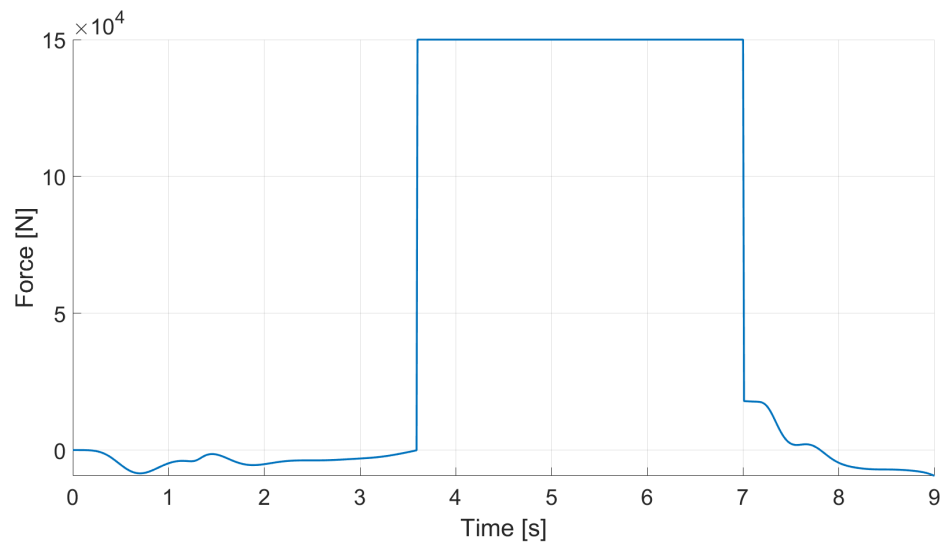


Figure 6.5: Force exerted on the bucket actuator during the heavy-duty work cycle

6.6 and 6.7 for the boom actuator, Figures 6.8 and 6.9 for the arm actuator, and Figures 6.10 and 6.11 for the bucket actuator.

From the velocity profiles in Figures 6.6, 6.8, and 6.10, it can be observed that at the same timestep where the force signals exhibit a step indicating the encounter with an obstacle, the velocity commands also undergo a corresponding step reduction. This simulation mirrors real-world scenarios encountered by excavators in

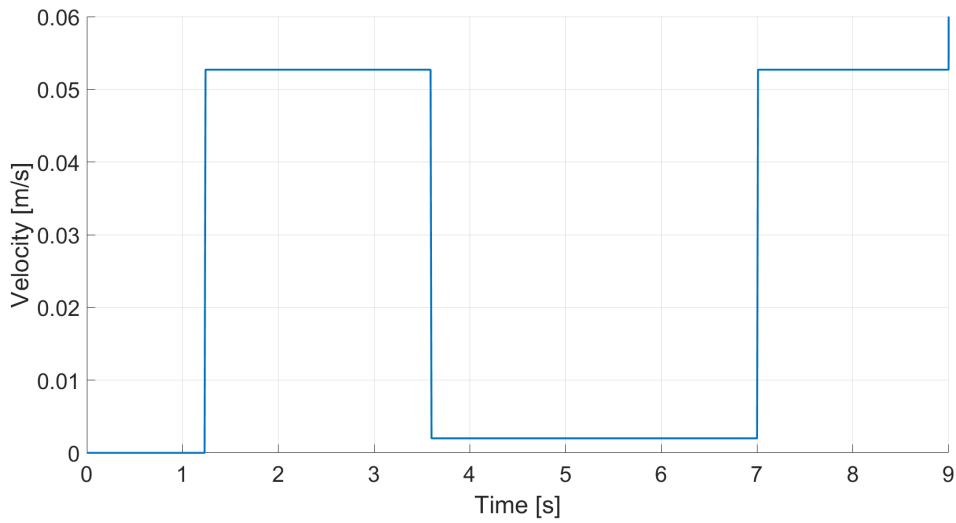


Figure 6.6: Boom actuator velocity profile during heavy duty work cycle

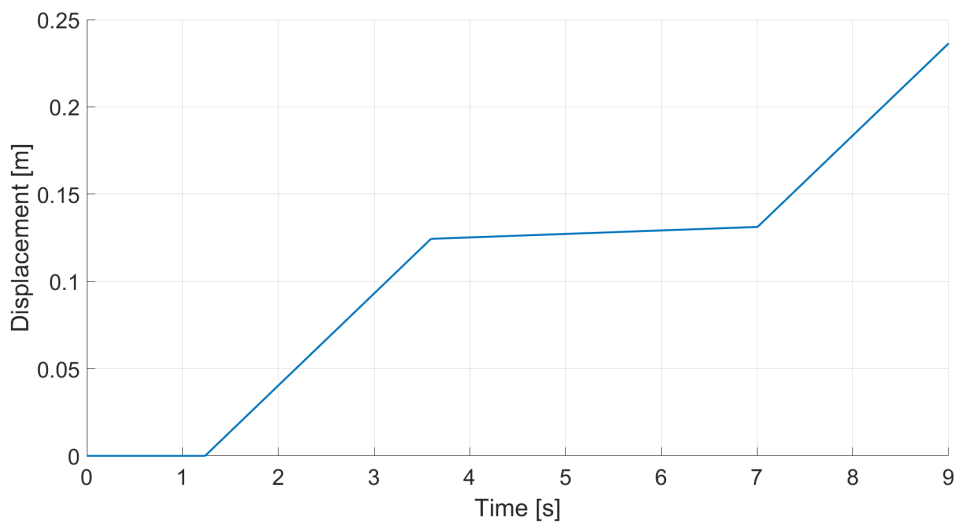


Figure 6.7: Boom actuator displacement profile during heavy duty work cycle

such situations.

6.1.2 Heavy Duty Work Cycle Results

As described previously in Section 6.1.1, the cycle outlined cannot be conducted using the Common Pressure Rail architecture with the parameter settings applied to all other reference cycles. Therefore, new operational parameters regarding the

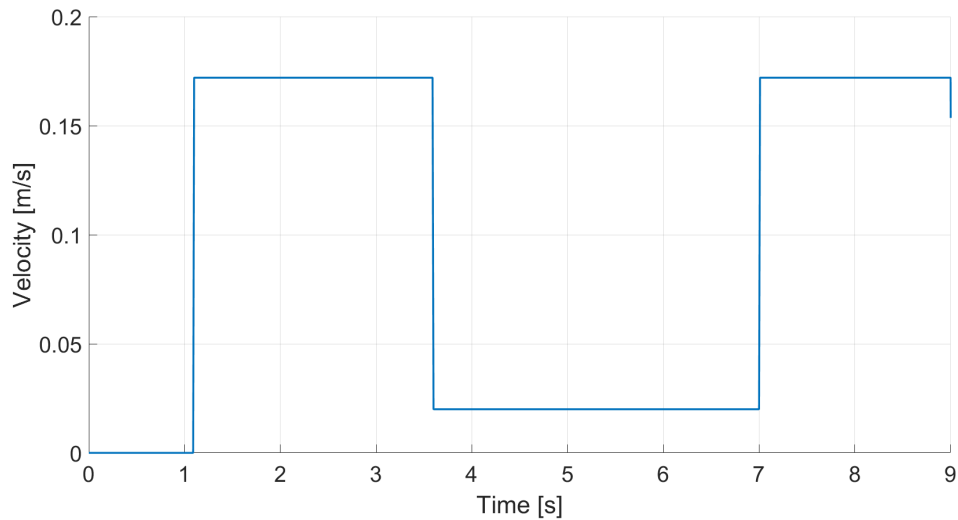


Figure 6.8: Arm actuator velocity profile during heavy duty work cycle

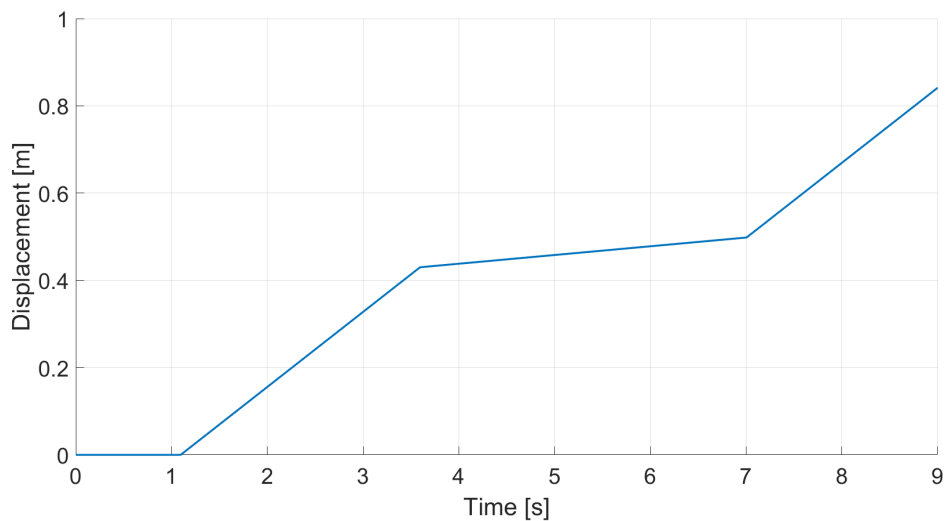


Figure 6.9: Arm actuator displacement profile during heavy duty work cycle

selected pressures for the high and medium-pressure rails have been adopted to facilitate this operation (see Table 6.1).

The process of selecting appropriate pressure settings commenced with establishing the high-pressure threshold, ensuring compliance with the specified parameters suitable for the excavator under examination. The determination of the high-pressure level was guided by the operational requirements and the performance capabilities of the excavator.

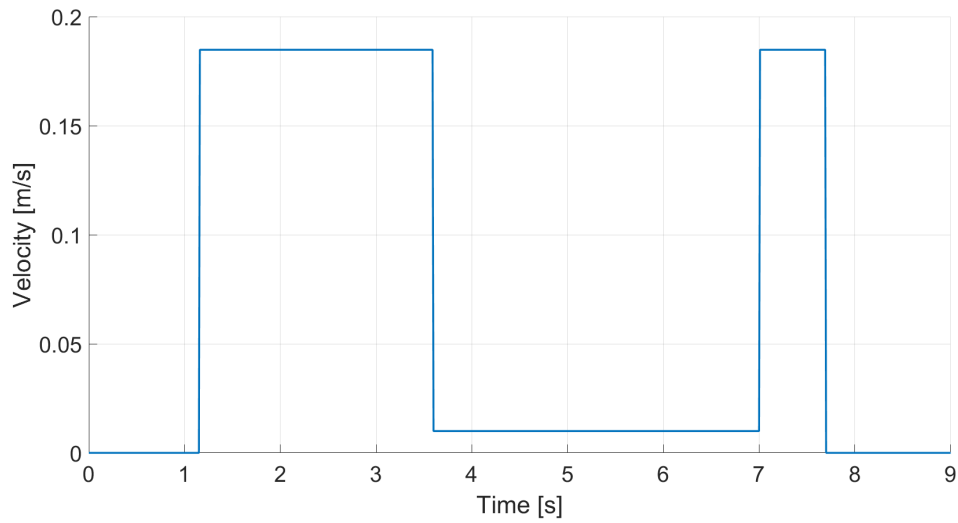


Figure 6.10: Bucket actuator velocity profile during heavy duty work cycle

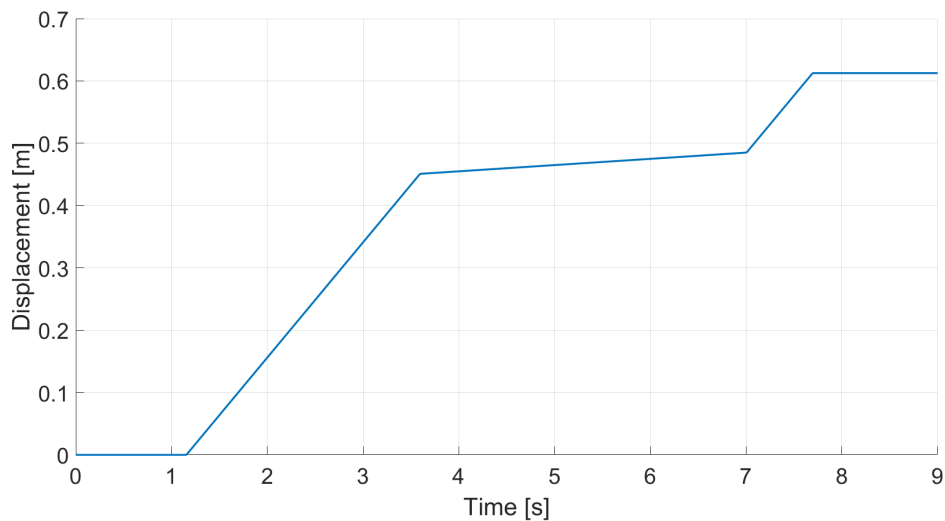


Figure 6.11: Bucket actuator displacement profile during heavy duty work cycle

For the selection of the medium-pressure setting, an intermediate value was chosen between the established high and low-pressure levels. This decision was based on the analysis of pressure trends observed during the decision-making process for the Common Pressure Rail system, particularly in the context of configurations optimized for the dig and dump cycle (see Section 3.2.3).

The operational conditions used to conduct the cycle for both the LS and CPR architectures remained consistent with those employed in the execution of the other

Accumulator	Operating Pressure [bar]	Pre-charge Pressure [bar]	Nominal Volume [L]
High Pressure	310	200	30
Medium Pressure	150	80	30

Table 6.1: Settings of accumulators for the heavy-duty work cycle

two reference cycles (see Section 5.1.1).

Comparative Analysis of Fuel Economy Between CPR and LS Architectures

The analysis now turns to the examination of the results obtained in terms of fuel consumption, comparing the Load Sensing architecture with the CPR architecture featuring increased accumulator pressures, denoted hereafter as CPR_HP. Table 6.2 displays the fuel consumption values resulting from the execution of the heavy-duty work cycle for both architectures under scrutiny. The findings from this case study indicate the CPR architecture to be notably advantageous over its Load Sensing counterpart, achieving approximately a 36% reduction in fuel usage. This suggests that the enhanced rail pressures have delivered significant benefits, enabling effective management of heavy load conditions while achieving substantial fuel savings. However, this apparent advantage requires further scrutiny. To provide a comprehensive analysis, the Common Pressure Rail architecture in the CPR_HP configuration was also evaluated across the previously described standard cycles, namely dig and dump, and air grading. Table 6.3 summarizes the corresponding fuel consumption values.

Architecture	Duty Cycle	Fuel [g]
Load Sensing	Heavy Duty	11.75
CPR_HP	Heavy Duty	7.48

Table 6.2: Comparison of fuel consumption for heavy-duty work cycle - LS vs CPR_HP

The results presented in Table 6.3 reveal a significant decline in fuel efficiency compared to the cases outlined in Section 5.1. Specifically, for the dig and dump cycle, the CPR_HP configuration shows only a marginal 4.10% improvement over Load Sensing, contrasting starkly with the earlier scenario where CPR achieved a substantial 54% reduction. Similar trends are observed in the air grading cycle,

where the CPR_HP configuration now offers a reduced advantage of 36.17% compared to the previous 64% improvement with CPR.

Architecture	Duty Cycle	Fuel [g]
Load Sensing	Dig and Dump	25.59
CPR_HP	Dig and Dump	24.54
Load Sensing	Air grading	17.58
CPR_HP	Air grading	11.22

Table 6.3: Comparison of fuel consumption for dig and dump and air grading work cycle - LS vs CPR_HP

In conclusion, while the Common Pressure Rail architecture consistently demonstrates advantages over Load Sensing, the feasibility of implementing CPR_HP with high-pressure accumulators must be carefully evaluated, especially in consideration of the specific excavator dimensions and operational requirements. Sicuramente la scelta del livello di media pressione non è ottimale in quanto l'averne un valore a metà fra l'alta pressione e la media pressione in realtà

The potential benefits of this architecture may not justify the architectural complexities and costs associated with its widespread adoption.

Comparative Analysis on Precision and Responsiveness Between CPR and LS System

For the sake of completeness in the results, the following section presents the performance outcomes of the CPR architecture in the CPR_HP configuration in terms of the error between the input velocity provided to the controller and the actual velocity generated by the actuator, as well as the error in terms of the actuator's displacement. These results aim to provide a more comprehensive overview of the performance of the developed Simulink controller, thereby determining whether more demanding conditions, compared to those previously examined, might pose challenges in managing the architecture.

Figures 6.12 and 6.13 illustrate the comparison between the reference and actual velocities and the comparison between the reference and actual displacements for the boom actuator, respectively. Similarly, Figures 6.14 and 6.15 display the comparisons of the reference and actual velocities and displacements for the arm actuator. Finally, Figures 6.16 and 6.17 show the comparisons of the reference and actual velocities and displacements for the bucket actuator.

The analysis of these figures reveals critical insights into the performance of the CPR_HP architecture under heavy-duty conditions. Specifically, the velocity error plots for the boom, arm, and bucket actuators indicate how closely the actual

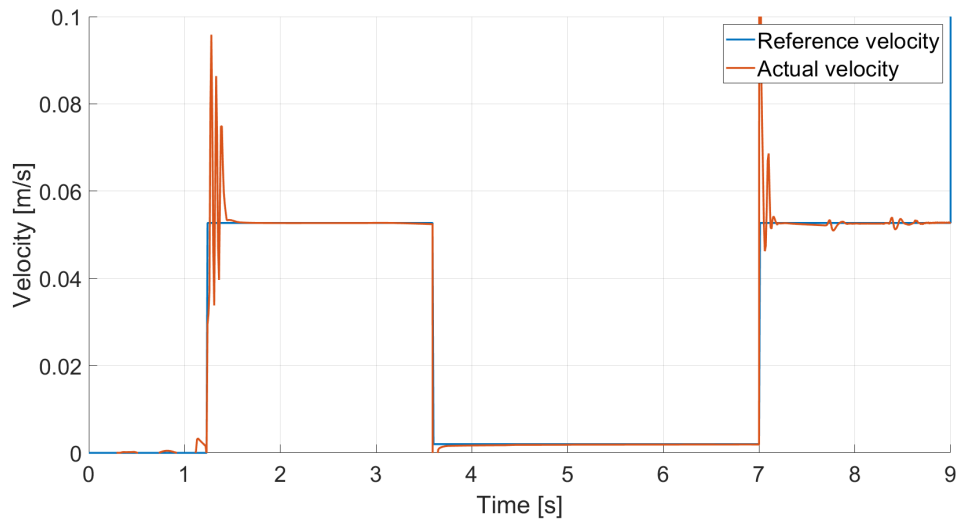


Figure 6.12: Comparison of reference and actual velocities for boom actuator during Heavy Duty cycles - CPR in CPR_HP configuration

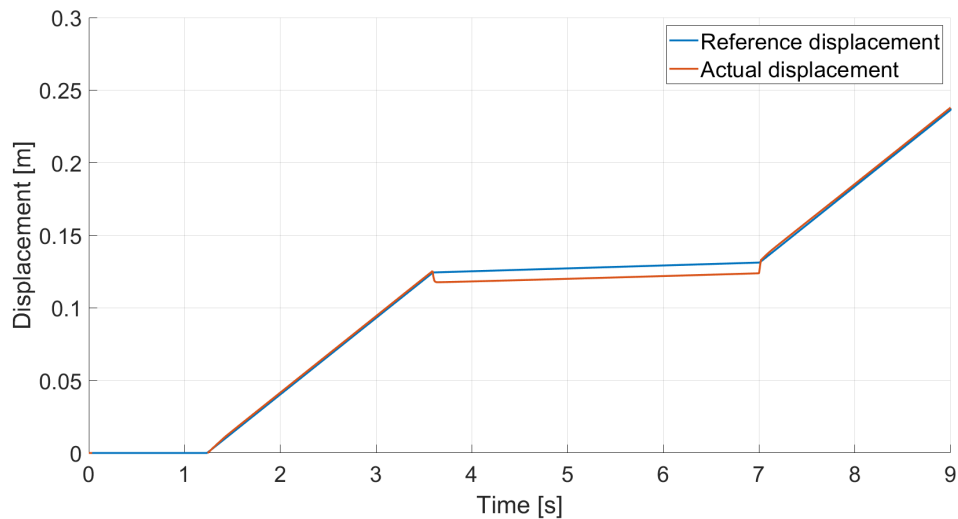


Figure 6.13: Comparison of reference and actual displacement for boom actuator during Heavy Duty cycles - CPR in CPR_HP configuration

velocities track the reference velocities provided to the controller. Focusing on the segments where the actuator encounters an obstacle, the controller effectively manages both the actuator's velocity and the required load. Similarly, the displacement error plots provide an understanding of the accuracy with which the actuators reach their desired positions, which is crucial for precision in tasks requiring fine

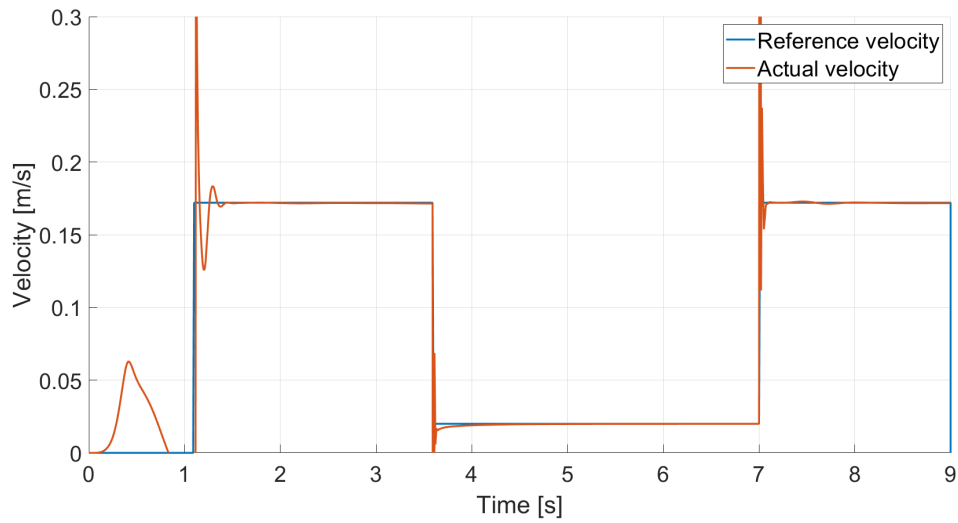


Figure 6.14: Comparison of reference and actual velocities for arm actuator during Heavy Duty cycles - CPR in CPR_HP configuration

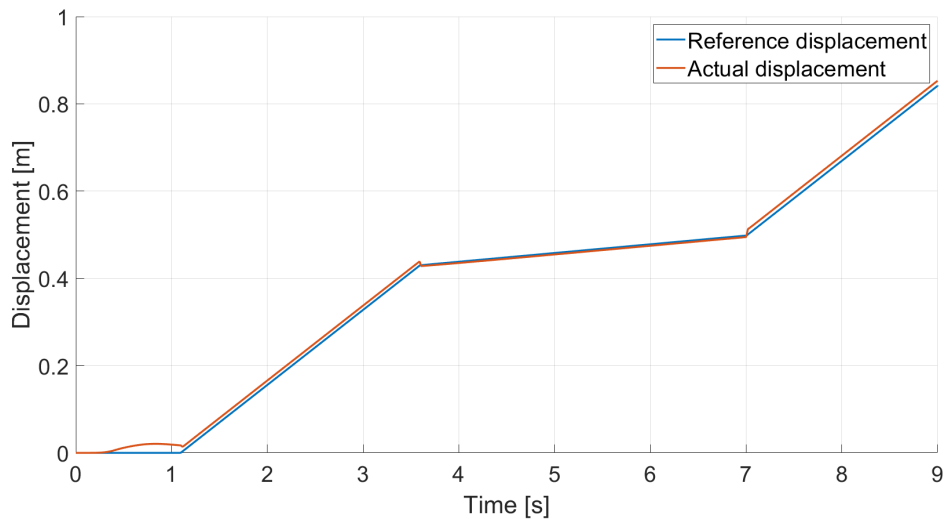


Figure 6.15: Comparison of reference and actual displacement for arm actuator during Heavy Duty cycles - CPR in CPR_HP configuration

control.

The only noticeable issue in the graphs is a slight overshoot in the velocity plots, likely caused by a somewhat elevated proportional coefficient (K_p) in the closed-loop controls of the three actuators. Unfortunately, due to the lack of an opportunity to generate optimal Design of Experiments (DOE) that could effectively determine

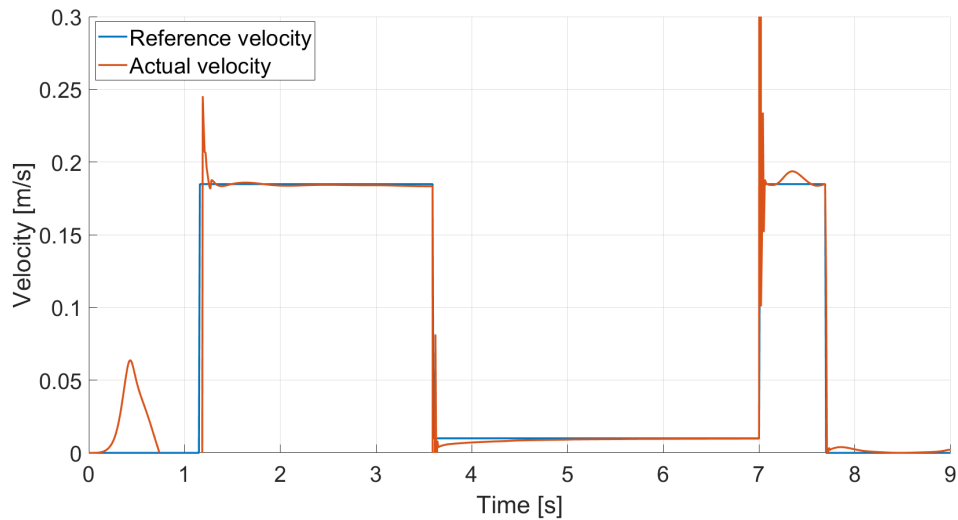


Figure 6.16: Comparison of reference and actual velocities for bucket actuator during Heavy Duty cycles - CPR in CPR_HP configuration

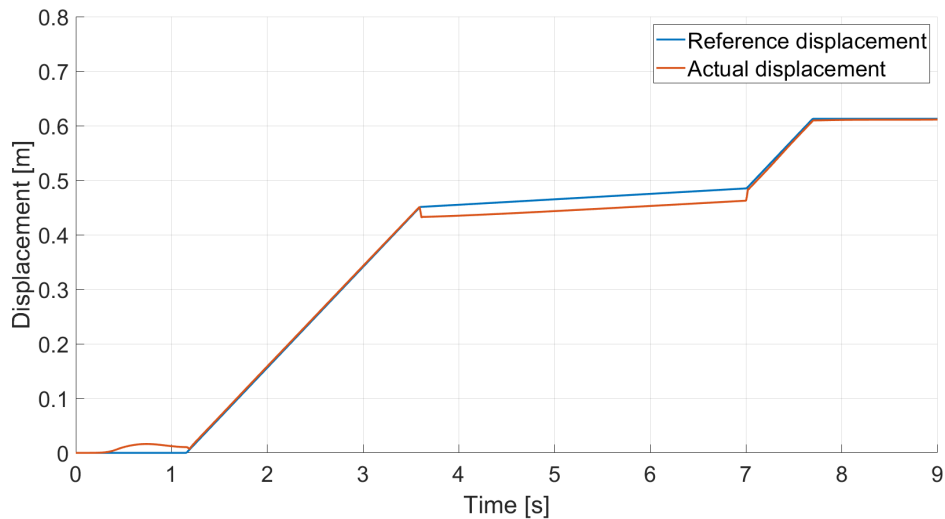


Figure 6.17: Comparison of reference and actual displacement for bucket actuator during Heavy Duty cycles - CPR in CPR_HP configuration

the closed-loop control parameters for the architecture, considering the interaction between the various actuators and the entire flow generation unit, the results are somewhat lacking. Nonetheless, they are still commendable.

To verify these observations, Table 6.4 presents the maximum errors generated by the architecture in terms of actuator displacements compared to the reference

values. Despite the lack of an adequate optimization of the closed-loop system, all values remain below 5%, demonstrating the effectiveness of the developed controller.

Actuator	Maximum Error [%]
Boom	4.81
Arm	3.16
Bucket	3.46

Table 6.4: Actuators displacements maximum errors - Heavy duty cycle

6.2 Introduction to the Common Pressure Rail plus Electronic Flow Matching

In previous sections, the performance of the Common Pressure Rail architecture was examined, with a particular focus on its significant impact on fuel economy, which is heavily influenced by rail pressures. Optimization of these pressures for specific operating cycles can lead to substantial energy savings, exceeding 50% compared to traditional Load Sensing architectures.

However, when the system operates under working cycles with rail pressures that deviate significantly from the optimal settings, the potential advantages over the Load Sensing counterpart diminish considerably. For example, in a typical dig and dump cycle, the efficiency gain may be diminished to a mere 5%. Similarly, in cycles such as air grading and heavy-duty operations, there is a significant reduction in fuel economy, with efficiency gains limited to only 36%. These figures starkly contrast with the over 50% energy savings observed when rail pressures are optimized for both the dig and dump and air grading cycles.

Given the conditions during standard operations such as dig and dump or air grading, there is no necessity to maintain high pressures as set in the CPR_HP configuration. The system inherently laminates more on the proportional valves to match the available pressures provided by the nearest operational mode to the user's working point. This necessity for constant adjustment significantly impacts the total system efficiency.

To address these challenges, a solution was conceived that combines the benefits observed in the CPR architecture optimized for the dig and dump cycle with the maximum pressure requirements necessary for the excavator's scale. This led to the development of the Common Pressure Rail plus Electronic Flow Matching (CPR+EFM) architecture. This innovative approach aims to merge the optimized rail pressure configurations of CPR with the dynamic pressure matching capabilities

required to meet the varying demands of different operational cycles, thereby enhancing overall efficiency and performance.

6.2.1 Common Pressure Rail plus Electronic Flow Matching - Hydraulic Architecture

This section provides a detailed exploration of the implementation of the Common Pressure Rail plus Electronic Flow Matching (CPR+EFM) hydraulic solution. The architecture retains the core framework of the Common Pressure Rail detailed in Section 3.2, with a significant enhancement: the integration of an on-off valve at the high-pressure accumulator outlet, as depicted in Figure 6.18.

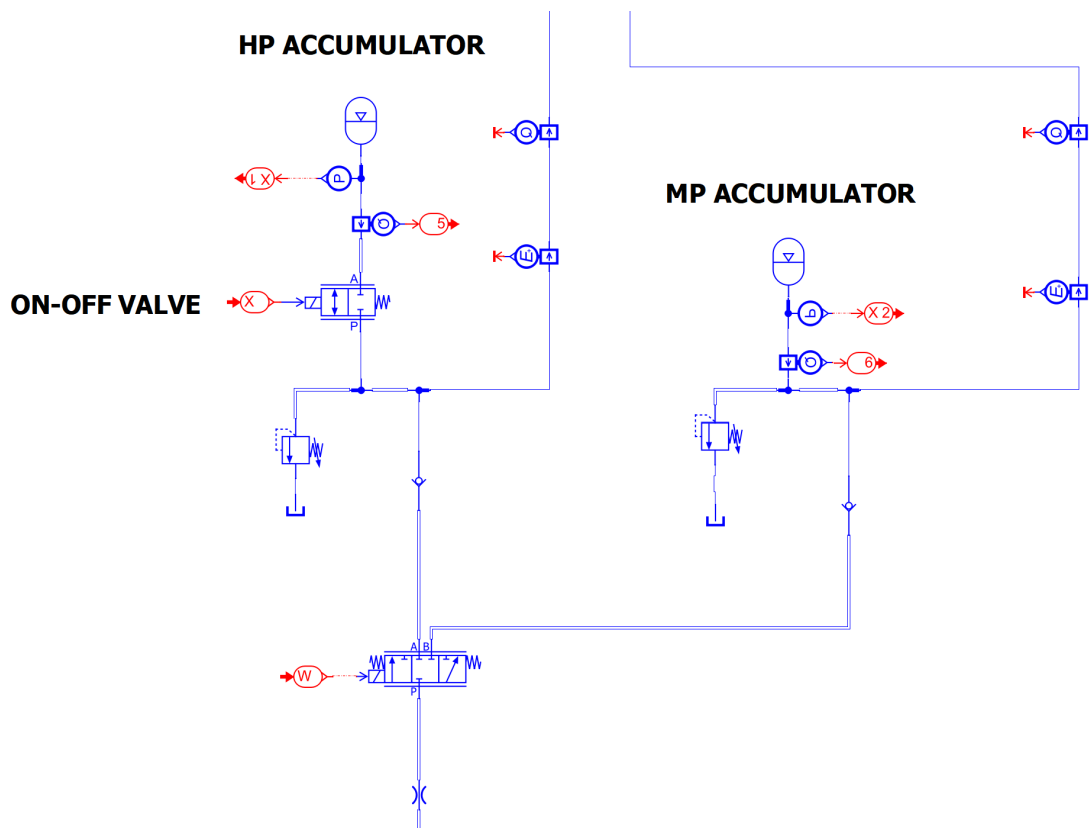


Figure 6.18: Common Pressure Rail architecture featuring Electronic Flow Matching capability

The highlighted on-off valve in Figure 6.18 serves as a crucial component enabling seamless transition between Common Pressure Rail operation and Electronic Flow Matching. Operationally, during normal conditions where accumulator pressures suffice to meet user load demands, the on-off valve remains closed, maintaining the

accumulator's connection to the high-pressure line. This configuration operates similarly to a conventional Common Pressure Rail, as discussed in earlier chapters. However, when accumulator pressures fall short of meeting user load pressure demands, the on-off valve opens, disconnecting the accumulator from the high-pressure line. Upon activation, the directional valve controlling pump discharge to the high-pressure and medium-pressure lines directs the pump discharge directly to the high-pressure line, enabling adjustment of pump displacement according to user-specified flow rates via joystick inputs. This mechanism facilitates precise control over pump flow rates, transforming the system from one where user requests are decoupled from flow generation unit (typical in traditional Common Pressure Rail) to one where the flow generation unit adapts dynamically to user demands.

In both operational modes, the medium-pressure accumulator remains connected to its rail, offering significant advantages in energy recovery. This configuration ensures that even in Electronic Flow Matching mode, where the system adjusts to meet varying load pressures, the medium-pressure accumulator remains active. If only one actuator requires higher load pressure than the standard rails can provide, the system seamlessly shifts to Electronic Flow Matching mode. Importantly, this mode allows each actuator to independently access the high-pressure, medium-pressure, and low-pressure lines based on their specific load requirements. As a result, the distribution of operational modes across the p_L/Q_L plane varies according to the highest load pressure demand at any given time. This variability ensures optimal performance and energy efficiency over the operational lifespan of the system.

The entire system is managed by a bespoke controller designed to oversee operational modes of various users, appropriately activating the on-off valves and modulating the proportional valve settings to match operating conditions. Additionally, the controller manages engine rotational speed, pump displacement, directional valve operation, and mode-selecting on-off valve, ensuring seamless operation across all modes.

6.2.2 Common Pressure Rail plus Electronic Flow Matching - Fuel Consumption Results

This section presents the results and performance evaluation in terms of fuel consumption for the implemented Common Pressure Rail plus Electronic Flow Matching hydraulic architecture, as detailed in Section 6.2, across different operational cycles.

The assessment metrics focus on three key operational cycles described in previous chapters: dig and dump, air grading, and heavy-duty operations, comparing them against traditional Load Sensing hydraulic systems.

For both systems, the same simulation parameters defined in Section 5.1.1

were used. The only modification was made to the engine rotational speed in the CPR+EFM system: it was set to a constant 1800 rpm in Electronic Flow Matching mode, while it remained at 1200 rpm in CPR mode, as in previous tests.

Architecture	Duty Cycle	Fuel [g]
Load Sensing	Dig and Dump	25.59
CPR+EFM	Dig and Dump	11.79
Load Sensing	Air grading	17.58
CPR+EFM	Air grading	6.18
Load Sensing	Heavy Duty	11.75
CPR+EFM	Heavy Duty	5.20

Table 6.5: Comparison of fuel consumption for dig and dump, air grading, and heavy duty work cycles - LS vs CPR+EFM

Table 6.5 summarizes the results. The modifications to the architecture successfully combine the benefits of the Common Pressure Rail with those of Electronic Flow Matching. The system not only performs all cycles, including heavy duty, without altering accumulator pressures (set at 175 and 85 bar for high and medium pressure accumulators, respectively), but also achieves significant fuel consumption reductions. Specifically, the CPR+EFM system shows approximately 54% and 64% fuel savings compared to the Load Sensing system for the dig and dump and air grading cycles, respectively. Notably, in the heavy duty cycle, the CPR+EFM system improves fuel consumption from a 36% to a 56% reduction compared to CPR in CPR_HP configuration.

For the dig and dump and air grading cycles, the CPR+EFM system operates in CPR mode consistently, as these cycles do not demand the high loads that require Electronic Flow Matching mode. The only potential efficiency loss in CPR+EFM compared to traditional CPR could come from the on-off valve at the high-pressure accumulator inlet, but using a valve of significant size minimizes these losses.

In the heavy duty cycle, the enhanced efficiency (from a 36% to a 56% reduction) is primarily due to improved system performance during non-peak load phases. Unlike the CPR_HP mode, which maintains high accumulator pressures throughout the cycle, the CPR+EFM system operates in CPR mode for 5.6 out of 9 total seconds, only switching to Electronic Flow Matching during the 3.4 seconds when high pressures are needed. This switch reduces fuel consumption by minimizing unnecessary high-pressure maintenance.

The heavy duty cycle, designed as an extreme condition with all three actuators fully loaded, shows fuel consumption comparable to traditional Load Sensing during peak loads. However, in scenarios where only one actuator is maximally loaded, the CPR+EFM system would demonstrate even greater fuel efficiency benefits over

Load Sensing.

To illustrate the system's behavior during the heavy duty cycle, Figure 6.19 shows the pressure on the pump discharge line. Initially, until 3.6 seconds, the pressure is approximately 83 bar, indicating CPR mode operation with the pump recharging the medium-pressure accumulator. At 3.6 seconds, the system switches to Electronic Flow Matching, and the pressure rises to about 305 bar due to the high load on the heaviest actuator. At 7 seconds, as actuator loads decrease to manageable levels, the system reverts to CPR mode, with the pump discharge pressure dropping to 177 bar to recharge the high-pressure accumulator.

Additionally, Figure 6.20 depicts the control signal sent to the on-off valve at the high-pressure accumulator inlet. Initially activated, the valve connects the high-pressure accumulator to the rail. Upon encountering a load exceeding accumulator capacity, the valve closes, disconnecting the accumulator. Once the load returns to manageable levels at 7 seconds, the valve reopens, reestablishing the accumulator connection.

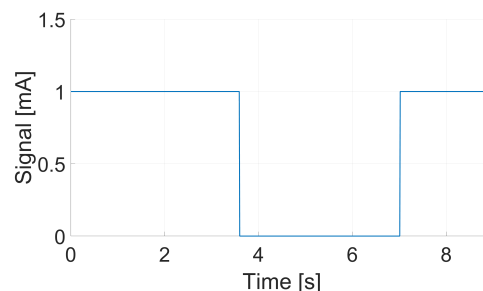
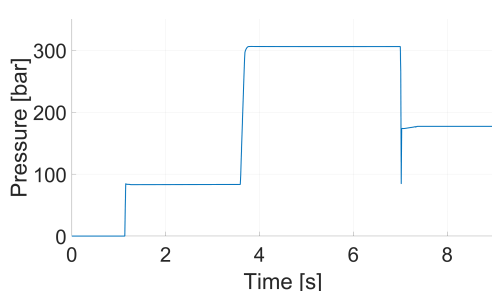


Figure 6.19: Pump discharge pressure during heavy duty cycle - CPR plus EFM **Figure 6.20:** Control signal for on-off valve at high-pressure accumulator - CPR plus EFM

In conclusion, the CPR+EFM system demonstrates significant improvements in fuel efficiency across various operational cycles compared to traditional Load Sensing systems and with respect to CPR in CPR_HP configuration.

6.3 Insights into Control of Common Pressure Rail plus Electronic Flow Matching

This section delves into the control strategies and mechanisms implemented in the Common Pressure Rail plus Electronic Flow Matching system. Understanding the control dynamics is crucial for optimizing the performance and efficiency of the hydraulic architecture, particularly in varying operational scenarios.

6.3.1 Control System Architecture

The control system for the CPR+EFM architecture, developed within the Simulink environment, is meticulously designed to manage multiple components and operational modes seamlessly. The comprehensive model is illustrated in Figure 6.21.

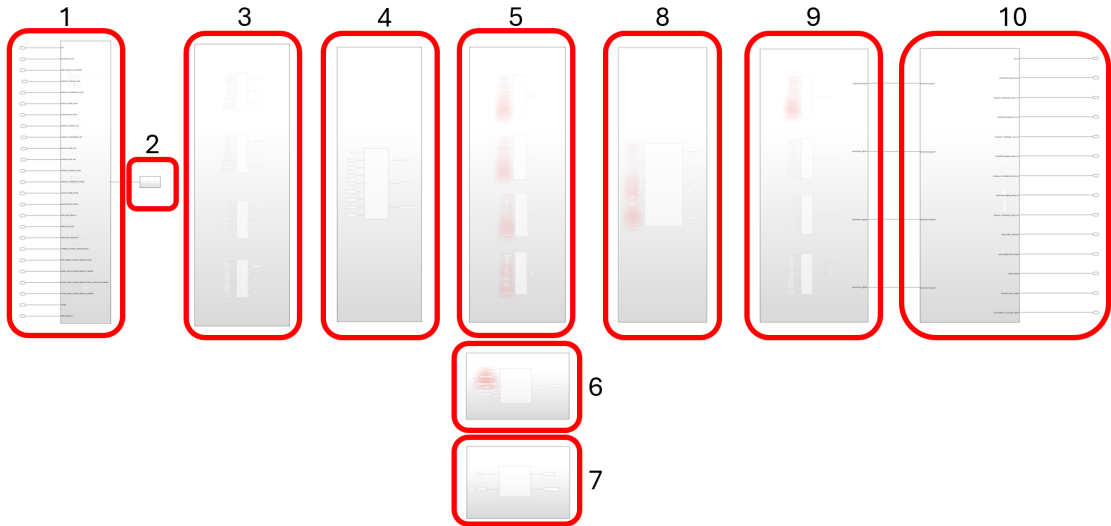


Figure 6.21: Detailed view of the Simulink controller model for managing the CPR+EFM architecture

A detailed analysis of each subcomponent within the Simulink model depicted in Figure 6.21 is provided below:

1. Input of required variables: this module handles the acquisition and processing of all necessary input variables to ensure the system operates within desired parameters. The required parameters include pressure levels, user commands, Finite state machine signal, engine data, accumulator pressure and others.
2. Electronic Flow Matching mode check: this MATLAB function verifies the operational mode of the architecture at the previous timestep. Based on this, as well as the high-pressure rail and accumulator pressures, it determines whether to switch from Electronic Flow Matching (EFM) mode to Common Pressure Rail (CPR) mode or continue with the current mode.
3. On-Off valves control: this is the initial block in the decision-making process for selecting the optimal operational mode for each utility. It is executed only if the architecture was in CPR mode at the previous timestep. This function not only selects the operational mode for each utility but also calculates

the required high pressure if the current rail pressures cannot meet the load demands.

4. Electronic Flow Matching mode trigger: this MATLAB function activates the EFM mode if necessary. It checks the outputs from the On-Off Valves Control function and, if any high pressure requirement is greater than zero, it triggers the EFM mode and returns the maximum required high pressure along with the associated actuator.
5. On-Off valves control in EFM mode: this is the second block in the decision-making process for selecting the optimal operational mode for each actuator. It is executed only if the EFM mode is on. In this function, new calculations are performed to determine the optimal operational mode for each actuator, considering that the high-pressure rail will now be set to the maximum required high pressure.
6. Engine rotational speed control: this MATLAB function regulates the engine's rotational speed based on the required torque. If the torque is zero, the engine is set to idle speed. If the torque is non-zero, the function checks whether the EFM mode has been triggered. If not, it sets the rotational speed for CPR mode. If the EFM mode has been triggered, the engine speed is set to 1800 rpm to ensure maximum performance. In both cases, the actual engine speed varies according to the applied load.
7. Accumulator on-off valve and directional valve control: this MATLAB function coordinates the operations of the accumulator's on-off valve and the directional valve, which are crucial for pressure management and flow direction based on the chosen operational mode from the previous functions.
8. Pump displacement control: this MATLAB function is active only if the EFM mode is on. During CPR mode, the pump operates at a fixed displacement controlled by the state machine. In EFM mode, the pump displacement is dynamically adjusted to align with user-specified flow rates derived from joystick inputs. It considers the maximum power output of the engine and the pump's efficiency and maximum flow characteristics. Additionally, an anti-saturation option is implemented to proportionally reduce the operator-generated signals if the pump cannot meet the required flow rate.
9. Proportional valves control: this section modulates the proportional valves to ensure precise control over flow rates and pressures within the system in both EFM and CPR modes.
10. Output generation: the final component consolidates all processed data and control signals, generating the necessary outputs to drive the system efficiently.

For the code of each function, please refer to Appendix 8.

The control system architecture for the CPR+EFM system, developed within the Simulink environment, represents a highly sophisticated and integrated approach to managing modern hydraulic systems. Through a detailed examination of each subcomponent, it is evident that the system is designed to seamlessly handle multiple operational modes and components, ensuring optimal performance and energy efficiency.

Each module within the Simulink model has been meticulously crafted to perform specific functions, from input variable acquisition to the dynamic control of pump displacement and engine rotational speed. The decision-making processes embedded within these modules enable the system to adapt dynamically to varying operational demands, maintaining high levels of precision and reliability.

The Electronic Flow Matching mode and the associated control strategies illustrate the system's capability to manage complex hydraulic scenarios, offering tailored operational modes that significantly enhance performance. Additionally, the integration of anti-saturation measures ensures that the system remains robust, even under extreme conditions.

It is noteworthy that performance graphs detailing errors in actuator speed and displacement, as well as hydraulic motor performance, have not been included in this section. This omission is due to the fact that these performance metrics are virtually identical to those presented in previous chapters. Specifically, for the dig and dump and air grading cycles, the results align closely with those obtained using the CPR architecture with high and medium pressure accumulators set at 175 and 85 bar, respectively. For the heavy-duty cycle results, reference can be made to the controller performance observed with the CPR architecture in the CPR_HP configuration.

In summary, the CPR+EFM control system architecture provides a comprehensive solution for modern hydraulic system management, combining advanced control strategies with efficient energy usage. This architecture not only improves fuel efficiency and performance but also lays the groundwork for future advancements in hydraulic technology.

Conclusion

The primary objective of this thesis was the development of a Simulink controller aimed at optimizing the performance of the Common Pressure Rail (CPR) architecture in hydraulic excavators. This intricate task involves not only selecting operational modes but also precisely modulating proportional valves for each utility, including linear actuators and the hydrostatic machine of the turret. These actions are based on inputs provided by the operator via joysticks, as well as dynamic environmental factors such as forces and torques exerted during the excavator's operation.

Upon establishing the foundational control system for the CPR architecture and recognizing its inherent limitations, the research progressed to develop an advanced Simulink controller capable of managing the CPR architecture augmented with Electronic Flow Matching. This enhanced controller extended its influence beyond the hydraulic distributor to include the hydraulic pump and internal combustion engine, thereby orchestrating a cohesive system optimization strategy.

The initial phase of the study involved creating sophisticated low-pass filters to meticulously analyze force signals derived from a reference model of an excavator utilizing Load Sensing architecture during typical operational cycles like digging and dumping. This analytical phase aimed not only to discern predominant force trends and magnitudes exchanged but also to inform design decisions that align seamlessly with the performance criteria of traditional excavator systems. Subsequent efforts concentrated on devising control logics for managing both on-off and proportional valves, initially focusing on linear actuators and subsequently expanding to encompass the hydrostatic machine of the turret. These control logics were intricately designed to respond to critical system inputs, such as actuator velocities and applied loads.

Following the successful validation of the open-loop control system, which demonstrated exemplary performance characteristics, the investigation pivoted towards implementing closed-loop control mechanisms. This phase was specifically geared towards minimizing discrepancies in linear actuator and hydrostatic machine speeds and displacements relative to operator inputs. The findings underscored the necessity to identify and address architectural constraints, leading to the innovative

introduction of a non-invasive solution: integrating an on-off valve at the high-pressure accumulator outlet. This integration effectively transformed the CPR architecture into a hybrid system, augmenting it with EFM functionality.

With the newly enhanced architecture in place, the thesis project focused on the development of a comprehensive controller capable of orchestrating the entire hydraulic system, spanning from the internal combustion engine and hydraulic pump to the intricate distribution network. Rigorous testing across various operational scenarios, including dig and dump cycles, air grading, and heavy-duty tasks, revealed a remarkable energy efficiency enhancement of over 50% compared to conventional Load Sensing architectures. Furthermore, deviations in the movements of linear actuators and the turret's hydrostatic machine from prescribed input values did not exceed 6% in any of the conducted tests, affirming the robustness of the developed control strategies.

Ongoing challenges center around optimizing parameters in the closed-loop control framework, with potential avenues for improvement explored through advanced Design of Experiments (DOE) methodologies. Additionally, while all valves within the architecture were initially modeled as ideal in terms of dynamics, the consideration of real-world valve behaviors characterized by first or second-order transfer functions holds promise for refining predictions related to fuel consumption and operational efficiency. Implementing such realistic valve models poses a significant computational challenge, warranting a careful balance between optimizing closed-loop control parameters and potentially adopting more sophisticated control strategies, such as Proportional-Derivative (PD) controllers, to accommodate valve dynamics within the open-loop control framework.

In conclusion, the Common Pressure Rail architecture emerges as a compelling alternative to existing market technologies, distinguished by its cost-effectiveness and minimally invasive implementation. However, its fuel efficiency remains intricately tied to specific operational parameters and pressure line settings, thereby presenting opportunities for further enhancement and adaptation in commercial applications. The proposal for enhanced flexibility in accumulator pressure settings, as put forth in this thesis, promises to catalyze significant advancements in industrial machinery technology, addressing longstanding efficiency challenges prevalent in contemporary market offerings.

Chapter 7

Appendix A

The co-simulation in AMESim involves developing a model in Simulink and generating a library for implementation in AMESim. The following steps outline the process:

1. Ensure compatibility by using Visual Studio 2018 alongside AMESim 2304 and Matlab 2022a.
2. Install necessary MATLAB add-ons shown in Figure 7.1:
 - Simulink Coder
 - Matlab Coder
 - Matlab Compiler
3. Set the Simulink solver to a fixed-step solver with ode4 (Runge-Kutta) before generating the library (see Figure 7.2).
4. Launch MATLAB from the AMESim environment to install required packages. TO do so navigate to Tools > MATLAB in the AMESim window.
5. Run modified MATLAB code provided below to generate the library once MATLAB opens automatically.
6. To import the library into AMESim, go to 'Sketch' > 'Category path list...' > 'User/Corporate/Managed libraries', then 'Browse...' to select and 'Add' to add your generated library.
7. Verify successful import by locating the Simulink block in the AMESim library tree under 'SL2AMECosim-Library'.

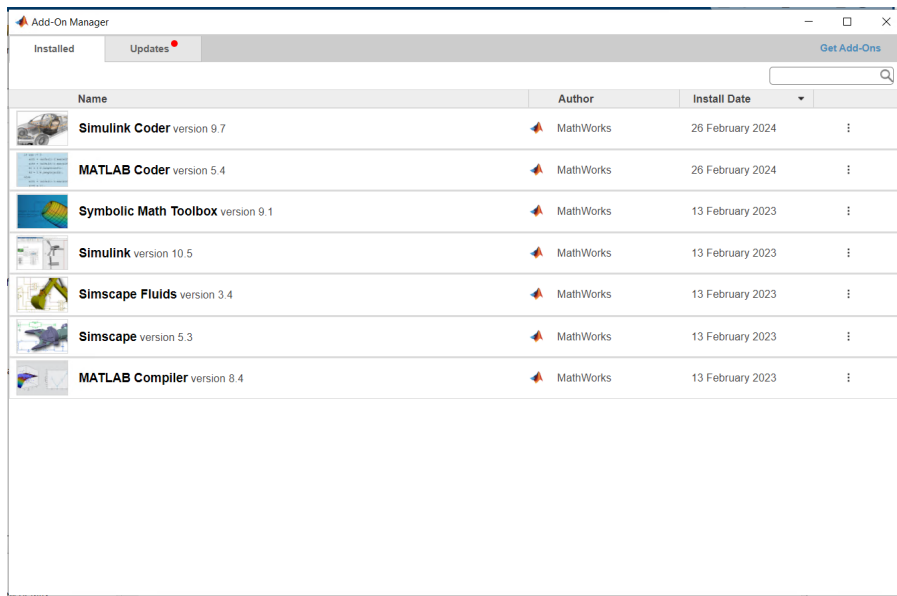


Figure 7.1: Adds-on to be installed in MATLAB

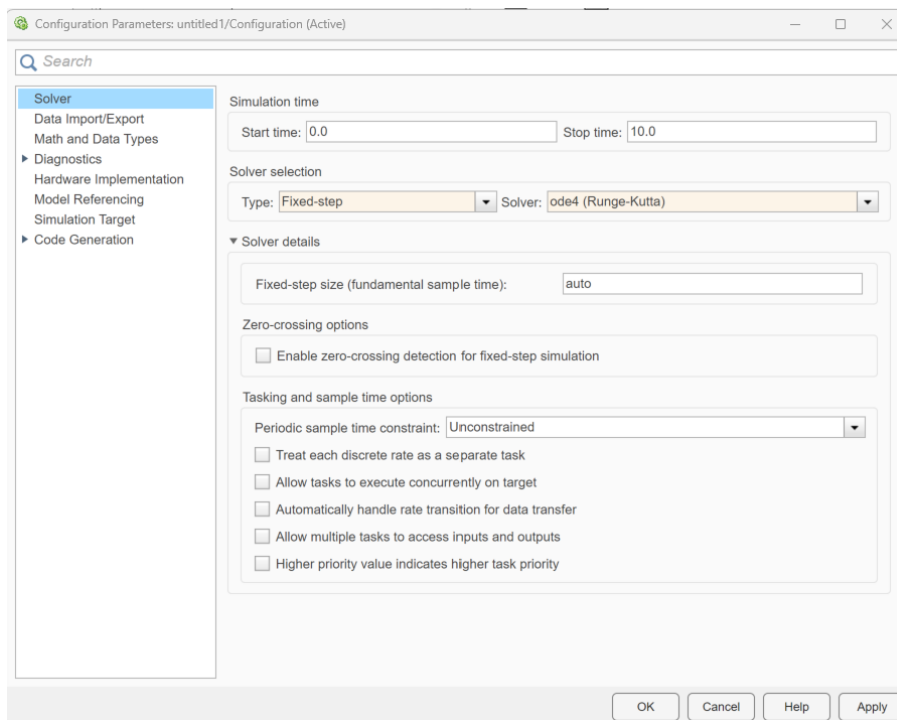


Figure 7.2: Simulink solver settings

Listing 7.1: MATLAB Script for Generating Library

```
% Each time you generate a library, some files  
% will be generated, so in this first let's clean up  
  
file = 'sl2amecosim.log';  
if exist(file, 'file') == 2  
    delete(file);  
end  
  
%Eliminate old library if existing  
folder = 'Library';  
if exist(folder, 'dir') == 7  
    % Eliminate folder and all its content  
    rmdir(folder, 's');  
end  
  
%Subtitute the * with your folder name  
folder = '*_grt_rtw';  
if exist(folder, 'dir') == 7  
    % Eliminate folder and all its content  
    rmdir(folder, 's');  
end  
  
% Create new variable  
folderName = 'Libreria';  
  
% Check if the folder exists in the current path  
if exist(folderName, 'dir') ~= 7  
    % Create folder  
    mkdir(folderName);  
end  
  
% Generate library  
sl2amecosim('Simulink_model_name', 'Libreria', 'auto')
```

Chapter 8

Appendix B

```
function [LS, high_pressure_common_rail] = fcn(high_pressure_common_rail, LS,  
accumulator_pressure, delta_pressure_switch_LS_CPR)  
  
delta_pressure_switch_LS_CPR=delta_pressure_switch_LS_CPR*10^5;  
  
if LS == 1 && high_pressure_common_rail + delta_pressure_switch_LS_CPR <  
accumulator_pressure  
  
    LS=0;  
    high_pressure_common_rail = accumulator_pressure;  
  
end  
  
end
```

Electronic Flow Matching Mode Check - Function 2

```
function [LS, high_pressure_required, actuator_imposing_high_pressure] = fcn(LS,
overpower_boom, overpower_arm, overpower_bucket, overpower_swing,
high_pressure_required_boom, high_pressure_required_arm, high_pressure_required_bucket,
high_pressure_required_swing)

high_pressure_required = 0;

actuator_imposing_high_pressure = 0;

if overpower_boom == 2 || overpower_arm == 2 || overpower_bucket == 2 ||
overpower_swing == 2

    LS=1;
    [high_pressure_required, actuator_imposing_high_pressure] =
max([high_pressure_required_boom, high_pressure_required_arm,
high_pressure_required_bucket, high_pressure_required_swing]);
end

end
```

Electronic Flow Matching Mode Trigger - Function 4

```
function engine_speed = fcn(LS, engine_speed_LS_desired,
engine_speed_min_at_torque_max_LS, engine_speed_common_pressure_rail_desired,
engine_speed_min_at_torque_max_common_pressure_rail, idle_speed,
torque_max_at_engine_speed_common_pressure_rail_desired,
torque_max_at_engine_speed_LS_desired, torque, FSM_signal)

engine_speed=0;

if LS == 0

    if FSM_signal ~= 0

        engine_speed = engine_speed_common_pressure_rail_desired +
(engine_speed_min_at_torque_max_common_pressure_rail-
engine_speed_common_pressure_rail_desired)*torque/torque_max_at_engine_speed_commo-
n_pressure_rail_desired;

    else

        engine_speed = idle_speed;

    end

elseif LS == 1

    engine_speed = engine_speed_LS_desired + (engine_speed_min_at_torque_max_LS-
engine_speed_LS_desired)*torque/torque_max_at_engine_speed_LS_desired;

end
```

Engine Rotational Speed Control - Function 6

```
function [directional_valve, accumulator_on_off_valve_signal] = fcn(LS, FSM_signal)
accumulator_on_off_valve_signal = 1;
directional_valve=0;
if LS == 1
    accumulator_on_off_valve_signal=0;
    directional_valve = 1;
elseif LS == 0
    directional_valve=FSM_signal;
end
```

Accumulator On-Off Valve and Directional Valve Control - Function 7

```
function [proportional_signal,High_pressure_small_chamber,
Medium_pressure_small_chamber, Low_pressure_small_chamber, High_pressure_big_chamber,
Medium_pressure_big_chamber, Low_pressure_big_chamber] = fcn(proportional_signal,
combination)

[High_pressure_small_chamber, Medium_pressure_small_chamber,
Low_pressure_small_chamber] = deal(0);
[High_pressure_big_chamber, Medium_pressure_big_chamber, Low_pressure_big_chamber] =
deal(0);

switch combination(1,1)
case 1, Low_pressure_small_chamber = 1;
case 2, Medium_pressure_small_chamber = 1;
case 3, High_pressure_small_chamber = 1;
end

switch combination(1,2)
case 1, Low_pressure_big_chamber = 1;
case 2, Medium_pressure_big_chamber = 1;
case 3, High_pressure_big_chamber = 1;
end
```

Output Generation - Function 10

```

function [combination, overpower, high_pressure_required] = fcn(LS, h_pressure,
m_pressure, l_pressure, stand_by_pressure, delta_pressure_switch_CPR_to_LS,
piston_diameter, rod_diameter, reference_velocity, viscous_friction_coefficient,
external_force, flow_rate_maximum_opening_on_off, corresponding_pressure_drop_on_off,
flow_rate_maximum_opening_proportional_valve,
corresponding_pressure_drop_proportional_valve,
flow_rate_maximum_opening_chock_piston_side,
corresponding_pressure_drop_chock_piston_side,
flow_rate_maximum_opening_chock_rod_side, corresponding_pressure_drop_chock_rod_side)

high_pressure_required = 0;

big_chamber_area=pi*(piston_diameter^2)/4*10^-6;
small_chamber_area=pi*(piston_diameter^2-rod_diameter^2)/4*10^-6;

stand_by_pressure = stand_by_pressure*10^5;
delta_pressure_switch_CPR_to_LS=delta_pressure_switch_CPR_to_LS*10^5;

matrix1=[l_pressure, m_pressure, h_pressure];
matrix2=matrix1;

valve_characteristic_on_off=(flow_rate_maximum_opening_on_off*10^-
3)/(60*sqrt(corresponding_pressure_drop_on_off*10^5));

valve_characteristic_proportional=(flow_rate_maximum_opening_proportional_valve*10^-
3)/(60*sqrt(corresponding_pressure_drop_proportional_valve*10^5));

choke_characteristic_piston_side = (flow_rate_maximum_opening_chock_piston_side*10^-
3)/(60*sqrt(corresponding_pressure_drop_chock_piston_side*10^5));

choke_characteristic_rod_side = (flow_rate_maximum_opening_chock_rod_side*10^-
3)/(60*sqrt(corresponding_pressure_drop_chock_rod_side*10^5));

combination=zeros(1,2);
force_diff=0;

overpower=0;

if reference_velocity ~= 0

    if LS == 0

        force_diff_min=inf;

        for k=1:length(matrix1)
            for j=1:length(matrix2)
                if k ~= 1 || j ~= 1
                    if external_force>0 && reference_velocity>0
                        big_chamber_pressure=matrix1(k)-
                        (reference_velocity*big_chamber_area/valve_characteristic_on_off)^2-
                        (reference_velocity*big_chamber_area/valve_characteristic_proportional)^2-
                        (reference_velocity*big_chamber_area/choke_characteristic_piston_side)^2;

                        small_chamber_pressure=matrix2(j)+(reference_velocity*small_chamber_area/valve_characte
                        ristic_on_off)^2+(reference_velocity*small_chamber_area/valve_characteristic_proportion
                        al)^2+(reference_velocity*small_chamber_area/choke_characteristic_rod_side)^2;

                        force_diff=big_chamber_pressure*big_chamber_area-
                        small_chamber_pressure*small_chamber_area-abs(external_force)-
                        abs(reference_velocity*viscous_friction_coefficient);
                    end
                end
            end
        end
    end
end

```

On-Off Valves Control - Linear Actuator - Function 3


```

function [combination, overpower, high_pressure_required] = fcn(LS, h_pressure,
m_pressure, l_pressure, stand_by_pressure, delta_pressure_switch_CPR_to_LS,
engine_displacement, reference_angular_velocity, reference_angular_acceleration,
engine_volumetric_efficiency, engine_mechanical_efficiency,
constant_excavator_inertia_moment, variable_excavator_inertia_moment,
diff_variable_excavator_inertia_moment, viscous_friction_coefficient, gear_ratio,
flow_rate_maximum_opening_on_off, corresponding_pressure_drop_on_off,
flow_rate_maximum_opening_proportional_valve,
corresponding_pressure_drop_proportional_valve)

matrix1=[l_pressure, m_pressure, h_pressure];
matrix2=matrix1;

engine_displacement=engine_displacement*10^-6/(2*pi);
viscous_friction_coefficient=viscous_friction_coefficient*(60/(2*pi));
stand_by_pressure = stand_by_pressure*10^5;
delta_pressure_switch_CPR_to_LS=delta_pressure_switch_CPR_to_LS*10^5;

equivalent_inertia =
constant_excavator_inertia_moment+variable_excavator_inertia_moment;

valve_characteristic_on_off=(flow_rate_maximum_opening_on_off*10^-
3)/(60*sqrt(corresponding_pressure_drop_on_off*10^5));
valve_characteristic_proportional=(flow_rate_maximum_opening_proportional_valve*10^-
3)/(60*sqrt(corresponding_pressure_drop_proportional_valve*10^5));

inertia_torque = diff_variable_excavator_inertia_moment*reference_angular_velocity;
reference_requested_torque = reference_angular_acceleration*equivalent_inertia;
viscous_torque = viscous_friction_coefficient*reference_angular_velocity;
total_requested_torque=inertia_torque+reference_requested_torque+abs(viscous_torque);
right_triangle_having_up_shaft_pressure=0;
left_triangle_having_up_shaft_pressure=0;

combination=zeros(1,2);
torque_diff=0;
overpower=0;
high_pressure_required = 0;
mode = 0;

if reference_angular_velocity ~= 0
    if LS == 0
        torque_diff_min=inf;
        %Proviamo a valutare se i carichi sono resistenti
    end
end

```

On-Off Valves Control - Turret Motor - Function 3

```

function combination = fcn(LS, combination, actuator_imposing_high_pressure,
actuator_number, h_pressure, m_pressure, l_pressure, piston_diameter, rod_diameter,
reference_velocity, viscous_friction_coefficient, external_force,
flow_rate_maximum_opening_on_off, corresponding_pressure_drop_on_off,
flow_rate_maximum_opening_proportional_valve,
corresponding_pressure_drop_proportional_valve,
flow_rate_maximum_opening_chock_piston_side,
corresponding_pressure_drop_chock_piston_side,
flow_rate_maximum_opening_chock_rod_side, corresponding_pressure_drop_chock_rod_side)

small_chamber_pressure=0;
big_chamber_pressure=0;

big_chamber_area=pi*(piston_diameter^2)/4*10^-6;
small_chamber_area=pi*(piston_diameter^2-rod_diameter^2)/4*10^-6;

matrix1=[l_pressure, m_pressure, h_pressure];
matrix2=matrix1;

valve_characteristic_on_off=(flow_rate_maximum_opening_on_off*10^-
3)/(60*sqrt(corresponding_pressure_drop_on_off*10^5));

valve_characteristic_proportional=(flow_rate_maximum_opening_proportional_valve*10^-
3)/(60*sqrt(corresponding_pressure_drop_proportional_valve*10^5));

choke_characteristic_piston_side = (flow_rate_maximum_opening_chock_piston_side*10^-
3)/(60*sqrt(corresponding_pressure_drop_chock_piston_side*10^5));

choke_characteristic_rod_side = (flow_rate_maximum_opening_chock_rod_side*10^-
3)/(60*sqrt(corresponding_pressure_drop_chock_rod_side*10^5));

matrix1=[l_pressure, m_pressure, h_pressure];
matrix2=matrix1;

force_diff=0;

if reference_velocity ~= 0
    if LS == 1 && actuator_imposing_high_pressure ~= actuator_number
        force_diff_min=inf;

        for k=1:length(matrix1)
            for j=1:length(matrix2)
                if k ~= 1 || j ~= 1
                    if external_force>0 && reference_velocity>0
                        big_chamber_pressure=matrix1(k)-
                        (reference_velocity*big_chamber_area/valve_characteristic_on_off)^2-
                        (reference_velocity*big_chamber_area/valve_characteristic_proportional)^2-
                        (reference_velocity*big_chamber_area/choke_characteristic_piston_side)^2;

                        small_chamber_pressure=matrix2(j)+(reference_velocity*small_chamber_area/valve_characte
                        ristic_on_off)^2+(reference_velocity*small_chamber_area/valve_characteristic_proportion
                        al)^2+(reference_velocity*small_chamber_area/choke_characteristic_rod_side)^2;

                        force_diff=big_chamber_pressure*big_chamber_area-
                        small_chamber_pressure*small_chamber_area-abs(external_force)-
                        abs(reference_velocity*viscous_friction_coefficient);

                    elseif external_force<0 && reference_velocity>0

```

On-Off Valves Control in EFM Mode - Linear Actuator - Function 5

```

function combination = fcn(LS, combination, actuator_imposing_high_pressure,
actuator_number, h_pressure, m_pressure, l_pressure, engine_displacement,
engine_volumetric_efficiency, engine_mechanical_efficiency, gear_ratio,
reference_angular_velocity, reference_angular_acceleration,
constant_excavator_inertia_moment, variable_excavator_inertia_moment,
diff_variable_excavator_inertia_moment, viscous_friction_coefficient,
flow_rate_maximum_opening_on_off, corresponding_pressure_drop_on_off,
flow_rate_maximum_opening_proportional_valve,
corresponding_pressure_drop_proportional_valve)

matrix1=[l_pressure, m_pressure, h_pressure];
matrix2=matrix1;

torque_diff_min=0;
torque_diff_max=0;

engine_displacement=engine_displacement*10^-6/(2*pi);

viscous_friction_coefficient=viscous_friction_coefficient*(60/(2*pi));

equivalent_inertia =
constant_excavator_inertia_moment+variable_excavator_inertia_moment;

valve_characteristic_on_off=(flow_rate_maximum_opening_on_off*10^-
3)/(60*sqrt(corresponding_pressure_drop_on_off*10^5));

valve_characteristic_proportional=(flow_rate_maximum_opening_proportional_valve*10^-
3)/(60*sqrt(corresponding_pressure_drop_proportional_valve*10^5));

inertia_torque = diff_variable_excavator_inertia_moment*reference_angular_velocity;

reference_requested_torque = reference_angular_acceleration*equivalent_inertia;
viscous_torque = viscous_friction_coefficient*reference_angular_velocity;

total_requested_torque=inertia_torque+reference_requested_torque+abs(viscous_torque);

right_triangle_having_up_shaft_pressure=0;
left_triangle_having_up_shaft_pressure=0;

torque_diff=0;
mode = 0;

if reference_angular_velocity ~= 0

    if LS == 1 && actuator_imposing_high_pressure ~= actuator_number

        torque_diff_min=inf;

        %carichi sono resistenti

        for j=1:length(matrix2)
            for k=1:length(matrix1)
                if k ~= 1 || j ~= 1

                    if reference_angular_velocity>0

                        right_triangle_having_up_shaft_pressure=matrix1(k)-
((engine_displacement*reference_angular_velocity*gear_ratio/engine_volumetric_efficienc
y)/valve_characteristic_on_off)^2-
((engine_displacement*reference_angular_velocity*gear_ratio/engine_volumetric_efficienc
y)/valve_characteristic_proportional)^2;

```

On-Off Valves Control in EFM Mode - Turret Motor - Function 5

```

function [pump_displacement_signal, reference_velocity_boom_new,
reference_velocity_arm_new, reference_velocity_bucket_new,
reference_angular_velocity_swing_new] = pump_control(LS,
speed_discretization_reduction, FSM_signal, reference_velocity_boom,
reference_velocity_arm, reference_velocity_bucket, reference_angular_velocity_swing,
combination_boom, combination_arm, combination_bucket, combination_swing,
piston_diameter_boom, rod_diameter_boom, piston_diameter_arm, rod_diameter_arm,
piston_diameter_bucket, rod_diameter_bucket, engine_displacement_swing,
engine_volumetric_efficiency, gear_ratio, shaft_speed, motor_max_power,
high_pressure_required, pump_displacement_geometric,
flow_rate_maximum_opening_choke_pump, corresponding_pressure_drop_choke_pump,
flow_rate_maximum_opening_non_return_valve_pump,
corresponding_pressure_drop_non_return_valve_pump,
flow_rate_maximum_opening_directional_valve_pump,
corresponding_pressure_drop_directional_valve_pump)

reference_velocity_boom_new = reference_velocity_boom;
reference_velocity_arm_new = reference_velocity_arm;
reference_velocity_bucket_new = reference_velocity_bucket;
reference_angular_velocity_swing_new = reference_angular_velocity_swing;

flow_rate_boom=0;
flow_rate_arm=0;
flow_rate_bucket=0;
flow_rate_swing=0;

pump_displacement_geometric = pump_displacement_geometric*10^-6/(2*pi); %m^3/rad

choke_characteristic_pump = (flow_rate_maximum_opening_choke_pump*10^-
3)/(60*sqrt(corresponding_pressure_drop_choke_pump*10^5));

valve_characteristic_non_return_pump =
(flow_rate_maximum_opening_non_return_valve_pump*10^-
3)/(60*sqrt(corresponding_pressure_drop_non_return_valve_pump*10^5));

valve_characteristic_directional =
(flow_rate_maximum_opening_directional_valve_pump*10^-
3)/(60*sqrt(corresponding_pressure_drop_directional_valve_pump*10^5));

big_chamber_area_boom=pi*(piston_diameter_boom^2)/4*10^-6;
small_chamber_area_boom=pi*(piston_diameter_boom^2-rod_diameter_boom^2)/4*10^-6;

big_chamber_area_arm=pi*(piston_diameter_arm^2)/4*10^-6;
small_chamber_area_arm=pi*(piston_diameter_arm^2-rod_diameter_arm^2)/4*10^-6;

big_chamber_area_bucket=pi*(piston_diameter_bucket^2)/4*10^-6;
small_chamber_area_bucket=pi*(piston_diameter_bucket^2-rod_diameter_bucket^2)/4*10^-6;

engine_displacement_swing=engine_displacement_swing*10^-6/(2*pi);
displacement_swing = engine_displacement_swing*gear_ratio/engine_volumetric_efficiency;

shaft_speed=shaft_speed*2*pi/60;
motor_max_torque = motor_max_power/shaft_speed;

```

Pump Displacement Control - Function 8

```

function proportional_signal = fcn(LS, actuator_number,
actuator_imposing_high_pressure, combination, stand_by_pressure,
h_pressure_common_pressure_rail, h_pressure_LS, m_pressure, l_pressure,
piston_diameter, rod_diameter, reference_velocity, viscous_friction_coefficient,
external_force, flow_rate_maximum_opening_on_off, corresponding_pressure_drop_on_off,
flow_rate_maximum_opening_proportional_valve,
corresponding_pressure_drop_proportional_valve,
flow_rate_maximum_opening_chock_piston_side,
corresponding_pressure_drop_chock_piston_side,
flow_rate_maximum_opening_chock_rod_side, corresponding_pressure_drop_chock_rod_side)

proportional_signal = 0;

big_chamber_area=pi*(piston_diameter^2)/4*10^-6;
small_chamber_area=pi*(piston_diameter^2-rod_diameter^2)/4*10^-6;

valve_characteristic_on_off=(flow_rate_maximum_opening_on_off*10^-
3)/(60*sqrt(corresponding_pressure_drop_on_off*10^5));

valve_characteristic_proportional=(flow_rate_maximum_opening_proportional_valve*10^-
3)/(60*sqrt(corresponding_pressure_drop_proportional_valve*10^5));

choke_characteristic_piston_side = (flow_rate_maximum_opening_chock_piston_side*10^-
3)/(60*sqrt(corresponding_pressure_drop_chock_piston_side*10^5));

choke_characteristic_rod_side = (flow_rate_maximum_opening_chock_rod_side*10^-
3)/(60*sqrt(corresponding_pressure_drop_chock_rod_side*10^5));

stand_by_pressure=stand_by_pressure*10^5;

matrix = zeros(1,3);

if LS == 0

    matrix = [l_pressure, m_pressure, h_pressure_common_pressure_rail];

elseif LS == 1

    matrix = [l_pressure, m_pressure, h_pressure_LS];

end

big_chamber_pressure_max=0;
small_chamber_pressure_max=0;

if reference_velocity ~= 0

    if LS == 0 || (LS == 1 && actuator_imposing_high_pressure ~= actuator_number)

        if reference_velocity>0
            big_chamber_pressure_max=matrix(combination(1,2))-
(reference_velocity*big_chamber_area/valve_characteristic_on_off)^2;

small_chamber_pressure_max=matrix(combination(1,1))+(reference_velocity*small_chamber_a
rea/valve_characteristic_on_off)^2;
            elseif reference_velocity<0

big_chamber_pressure_max=matrix(combination(1,2))+(reference_velocity*big_chamber_area/
valve_characteristic_on_off)^2;

```

Proportional Valves Control - Linear Actuator - Function 9

```

function proportional_signal = fcn(LS, actuator_number,
actuator_imposing_high_pressure, combination, stand_by_pressure,
h_pressure_common_pressure_rail, h_pressure_LS, m_pressure, l_pressure,
engine_displacement, engine_volumetric_efficiency, engine_mechanical_efficiency,
gear_ratio, reference_angular_velocity, reference_angular_acceleration,
constant_excavator_inertia_moment, variable_excavator_inertia_moment,
diff_variable_excavator_inertia_moment, viscous_friction_coefficient,
flow_rate_maximum_opening_on_off, corresponding_pressure_drop_on_off,
flow_rate_maximum_opening_proportional_valve,
corresponding_pressure_drop_proportional_valve)

proportional_signal = 0;

matrix = zeros(1,3);

if LS == 0

    matrix = [l_pressure, m_pressure, h_pressure_common_pressure_rail];

elseif LS == 1

    matrix = [l_pressure, m_pressure, h_pressure_LS];

end

engine_displacement=engine_displacement*10^-6/(2*pi);
viscous_friction_coefficient=viscous_friction_coefficient*(60/(2*pi));

equivalent_inertia =
constant_excavator_inertia_moment+variable_excavator_inertia_moment;

valve_characteristic_on_off=(flow_rate_maximum_opening_on_off*10^-
3)/(60*sqrt(corresponding_pressure_drop_on_off*10^5));

valve_characteristic_proportional=(flow_rate_maximum_opening_proportional_valve*10^-
3)/(60*sqrt(corresponding_pressure_drop_proportional_valve*10^5));

inertia_torque = diff_variable_excavator_inertia_moment*reference_angular_velocity;

reference_requested_torque = reference_angular_acceleration*equivalent_inertia;
viscous_torque = viscous_friction_coefficient*reference_angular_velocity;

total_requested_torque=inertia_torque+reference_requested_torque+abs(viscous_torque);

right_triangle_having_up_shaft_pressure_max=0;
left_triangle_having_up_shaft_pressure_max=0;

stand_by_pressure=stand_by_pressure*10^5;

if LS == 0 || (LS == 1 && actuator_imposing_high_pressure ~= actuator_number)

    if total_requested_torque<-1 || total_requested_torque>1

        if reference_angular_velocity>0
            right_triangle_having_up_shaft_pressure_max=matrix(combination(1,1))-
((engine_displacement*reference_angular_velocity*gear_ratio/engine_volumetric_efficienc
y)/valve_characteristic_on_off)^2;

```

Proportional Valves Control - Turret Motor - Function 9

Bibliography

- [1] T. Virvalo and M. Vilenius. «The Influence of Pumps and Valves on the Efficiency of a Hydraulic Boom, Chapter 8». English. In: *Developments in Fluid Power Control of Machinery and Manipulators*. Ed. by A. Garbacik and J. Stecki. Fluid Power Net Publication, 2000, pp. 183–207 (cit. on p. 1).
- [2] J. H. Lumkes Jr. and J. Andruch III. «Hydraulic Circuit for Reconfigurable and Efficient Fluid Power Systems». In: *The Twelfth Scandinavian International Conference on Fluid Power*. Tampere, Finland, 2011 (cit. on p. 1).
- [3] Milos Vukovic and Roland Leifeld. «STEAM-a hydraulic hybrid architecture for excavators». In: pp. 151–162 (cit. on pp. 1, 19, 20, 42, 69, 70, 128, 130).
- [4] Masakazu Haga, Watanabe Hiroshi, and Kazuo Fujishima. «Digging control system for hydraulic excavator». In: *Mechatronics* 11.6 (2001), pp. 665–676 (cit. on pp. 3, 7).
- [5] Volvo Construction Equipment. «Different excavator types, sizes, and purposes explained 2021». In: (Apr. 2024). URL: <https://www.volvoce.com/asia/en-as/about-us/news/2021/different-excavator-types-sizes-and-purposes-explained-2021/> (cit. on pp. 4, 5).
- [6] Milos Vukovic, Roland Leifeld, and Hubertus Murrenhoff. «Reducing Fuel Consumption in Hydraulic Excavators—A Comprehensive Analysis». In: *Energies* 10 (May 2017), p. 687. DOI: 10.3390/en10050687 (cit. on pp. 6, 19).
- [7] Susan Philpott. *12 main reasons Hyundai excavator cabs are so comfortable*. Aug. 2020. URL: <https://na.hd-hyundaice.com/12-main-reasons-hyundai-excavator-cabs-are-so-comfortable/> (cit. on p. 7).
- [8] Construction Equipment Parts. *Main Control Valve - 723-47-14800 - Construction equipment parts*. Mar. 2024. URL: <https://ceparts.com/product/main-control-valve-723-47-14800/> (cit. on p. 7).

- [9] Damiano Padovani, Massimo Rundo, and Gabriele Altare. «The working hydraulics of valve-controlled mobile machines: Classification and review». In: *Journal of Dynamic Systems, Measurement and Control, Transactions of the ASME* 142 (7 July 2020). ISSN: 15289028. DOI: 10.1115/1.4046334/1074597 (cit. on pp. 12, 13).
- [10] Nicola Nervegna and Massimo Rundo. «Passi nell'oleodinamica. Vol. 1-2». In: (2020) (cit. on p. 13).
- [11] Gabriele Altare. «Analisi e simulazione di circuiti idraulici per macchine movimento terra». PhD thesis. Politecnico di Torino, 2013 (cit. on pp. 14, 15, 22, 28).
- [12] *Perni e Boccole Komatsu PC75-1*. RB Bonomi. URL: <https://rbbonomi.com/macchinario/komatsu/pc75-1/> (visited on 06/19/2024) (cit. on p. 23).
- [13] Edward McKyes. *Soil Cutting and Tillage*. Elsevier, 1985. ISBN: 0444419403 (cit. on p. 28).
- [14] Howard N. Cannon. «Extended Earthmoving with an Autonomous Excavator». Master's Thesis. Carnegie Mellon University, 1999 (cit. on p. 28).
- [15] Siemens Digital Industries Software. *Amesim Help Page*. 2023 (cit. on pp. 28, 29).
- [16] Sem Zarotti, Eugenio Leati, and Roberto Paoluzzi. «Hydraulic Excavator Working Cycle: From Field Test to Simulation Model». In: Mar. 2010, p. 2 (cit. on p. 42).
- [17] Paolo Stefano Crovetto. *Analog to Digital Conversion - Acquisition Frontend*. Lecture for the course: Electronic systems for vehicles, Politecnico di Torino. 2023 (cit. on p. 55).
- [18] Carlo Novara. *Proportional Integral Derivative control*. Lecture for the course: Driver assistance system design A, Politecnico di Torino. 2023 (cit. on p. 120).